Cranfield University

Kristian Petterson

The Aerodynamics of Slender Aircraft Forebodies at High Angle of Attack

2001

College of Aeronautics
Flow Control & Prediction Group

EngD Thesis

Cranfield University
College of Aeronautics
Flow Control & Prediction Group

EngD Thesis
Academic Year 2000-2001

Kristian Petterson

The Aerodynamics of Slender Aircraft Forebodies at High Angle of Attack

Academic Supervisor: Professor D.I.A.Poll
Industrial Supervisors: M.Sillén & B.Arlinger (Saab AB)

August 2001

This thesis is submitted in partial fulfilment of the requirements for the Degree of Doctor of Engineering

To my Parents

Abstract

High angle-of-attack aerodynamics has been the focus of much attention as a result of the drive to increase combat aircraft manoeuverability and thereby improve survivability. A key factor in this regime is the behaviour of the complex vortical wake generated by the forebody. Even at zero yaw, the shear layers and vortex pairs which are symmetric at moderate angles of attack (alpha) can become highly asymmetric as alpha is increased. This can lead to large sideforces and yawing moments which may exceed available control power.

Computationally simulating high-alpha forebody flowfields is known to be a challenging problem. This thesis details the evaluation and enhancement of the CFD code NSMB with the objective of improving qualitative and quantitive predictions of the flowfield around fighter-type forebodies throughout the angle-of-attack range.

Results on a tangent-ogive body confirmed that computing asymmetric flow required the introduction of a space- and time-fixed surface excrescence or the use of a non-symmetric solution algorithm to simulate flow instabilities via transient numerical error. Although solution stability problems were encountered, results with the non-symmetric algorithm showed promise. Suspected turbulence modelling issues were addressed by implementing the k-ω family.

Having established a methodology, solutions were obtained for the forebody of a current fighter aircraft, the Saab JAS-39 Gripen. The computed data shows excellent experimental agreement for $0^o \leq \alpha \leq 50^o$ over the clean geometry but the inclusion of a nose pitot probe was seen to destabilise the calculation and prevent convergence. Finally, a single vertical nose strake or 'rhino horn' was added. When undeflected, this stabilised the flowfield, reduced solution oscillation and negated sideforce. Deflecting the horn produced a stable flowfield with non-zero sideforce. Similar devices may be used, together with engine thrust-vectoring, in the next generation of combat aircraft and may also be added to existing airframes as a MLU.

Acknowledgements

The work presented in this thesis would not have been possible without the help of several individuals and organisations.

Firstly, I would like to thank the EPSRC for financial support and Saab Aerospace, Linköping, Sweden for agreeing to participate on the Engineering Doctorate Program and proposing such an interesting technical challenge. In particular I would like to thank all the members, past and present, of the CFD group within Saab Future Products and Technology with whom I was involved during the work: Bert Arlinger, both for initially organising the project and the help and encouragement given before his well-earned retirement; Mattias Sillén, for taking over on Bert's departure; and Ingemar Persson, Per Weinerfelt, Stefan Ledin and Yngve Sedin for some interesting discussions over coffee.

Saab sponsorship came about through my links to Flygteknik at Kungliga Tekniska Högskolan, Stockholm. Thanks to all the staff and students who made me feel so welcome on each of my visits there but especially to Dr. Nathalie Duquesne and Professor Arthur Rizzi for sharing some of their technical knowledge and for organising HPC access.

Supercomputer time for the project was generously provided by Parallel Dator Centrum at KTH and by the Swedish National Supercomputing Centre at Linköpings Universitetet. Special thanks go to Göran Magnusson at Saab Combitech Networks for help and advice regarding the T3E.

Back at Cranfield, thanks in particular to Dr. Kevin Garry and Professor Ian Poll for their academic guidance and Dr. Les Oswald for lending a hand whenever I needed assistance with my somewhat non-standard computing needs. Thanks are also due to the many friends I've made during my time at the University, all of whom contributed to making my time there memorable.

I reserve the final thanks for my Parents, who have supported and encouraged me in my studies ever since I first started school.

Contents

List of Figures

List of Tables

Nomenclature

C_x	Axial force coefficient
C_y	Side force coefficient
C_z	Normal force coefficient
C_μ	Momentum blowing coefficient, $\dot{m}v_j/q_\infty S$
E	Total energy, (J)
M	Mach number
Pr	Prandtl number, $\mu C_p/\lambda$ (= 0.72 for air)
R	Gas constant (= 287 $Jkg^{-1}K^{-1}$ for air)
Re	Reynolds number, $\rho Ul/\mu$
T	Temperature, (K)
U	Overall magnitude of velocity vector, (ms^{-1})
α	Angle of attack, $(^o)$.
β	Angle of yaw, $(^o)$.
δ_{ij}	Kronecker delta
$\dot{m}$	Mass flow rate through slot or port, (kgs^{-1})
γ	Ratio of specific heats, c_p/c_v
λ	Conductivity, $(Wm^{-1}K^{-1})$
μ	Dynamic viscosity, (Nsm^{-2})
μ_t	Eddy viscosity, (Nsm^{-2})
ρ	Density, (kgm^{-3})
τ	Shear stress tensor

τ_{ij}	Reynolds stress tensor
θ	Nose semi apex angle *or* Angle from leeward meridian, clockwise looking aft, $(^o)$.
$\tilde{u}, \tilde{v}, \tilde{w}$	Favre-averaged velocity components in Cartesian directions, (ms^{-1})
c_p	Specific heat (constant pressure), $(Jkg^{-1}K^{-1})$
c_v	Specific heat (constant volume), $(Jkg^{-1}K^{-1})$
e	Specific internal energy, (J)
f, g, h	Inviscid flux components in Cartesian directions
f_v, g_v, h_v	Viscous flux components in Cartesian directions
p	Pressure, (Pa)
q_∞	Freestream dynamic pressure, (Pa)
t	Time (s)
u'', v'', w''	Favre fluctuating velocity components in Cartesian directions, (ms^{-1})
u''_i	Favre fluctuating velocity components in tensor notation
u', v', w'	Fluctuating velocity components in Cartesian directions, (ms^{-1})
u'_i	Fluctuating velocity in tensor notation
u, v, w	Instantaneous velocity components in Cartesian directions, (ms^{-1})
u_i	Instantaneous velocity in tensor notation
v_j	Jet velocity, (ms^{-1})
x, y, z	3-dimensional Cartesian coordinate system
x_i	Coordinate vector in tensor notation
D	Tangent-ogive base diameter, (m)
d	Local diameter, (m)
i,j,k	Unit vectors in x, y, z directions
l	Characteristic length, (m)
S	Reference (wing) area, (m^2)

Introduction

"[It] climbed like a monkey and manoeuvered like the devil."

- Rittmeister Manfred von Richthofen (on the Fokker DR.1 *Dreidecker*)

"Float like a butterfly, sting like a bee."

- Muhammad Ali

Subsonic high angle of attack aerodynamics has been the focus of considerable research effort over the last few years, driven by the desire of industry to increase combat aircraft effectiveness by improving manoeuverability. Modern combat aircraft are capable of extreme agility, but both pilots and aircraft designers have understood the importance of combat manoeuverability since the First World War. In simple terms, the more manoeuverable the aircraft, the easier it is to get into a tactically advantageous position and the easier it is to avoid a threat, whether it be from the air or the ground.

By the end of the Great War, the fighter aircraft had come of age. Stable weapons platforms such as the Vickers FB5 'Gunbus' had been replaced by small, fast, agile machines such as the Sopwith Camel and the S.E.5a, whilst the Germans moved from Igor Etrich's *Taube* to aircraft such as the Pfalz D.XII and the Fokker DR.1, von Richthofen's favourite mount. Fighter development slowed during the inter-war years, but World War Two saw the emergence of machines such as the Spitfire and Messerschmitt Me109, beloved of their pilots for their close-combat capabilities. The trend for small, light, and fast continued after the War, with aircraft such as the Soviet MiG-15 pushing the limit of what was achievable at the time. However, the advent of air-to-air missiles in the early 1960s seemed, for a while, to make visual range engagement an unlikely event and hence low-speed handling of reduced importance. Contemporary air-combat doctrine stated that extended dogfights were obsolete, replaced by short, high-speed, missile-based engagements. Indeed, Phantom pilots initially went into combat in Vietnam with no fixed gun, so confident were McDonnell that all future engagements would be beyond-visual-range, stand-off affairs. This proved not to be the case, and during the Falklands War in 1982 the value of high subsonic manoeuverability was once again demonstrated by the Harrier pilots of the RAF and RN. 22 Argentine aircraft were downed in air-to-air combat without the loss of a single Harrier, largely due to the skill of the British pilots in exploiting the aircraft's exceptional agility.

Upwardly spiralling development and purchase costs mean that airforces today can no longer rely on large numbers for superiority. Modern fighter and strike aircraft have to be capable of operating successfully in a number of roles, and so it is clear why combat aircraft manufacturers retain subsonic manoeuverability as a major design goal alongside stealth and survivability. To this end, several new technologies have been investigated in recent years, examples being the addition of engine thrust-vectoring, extra aerodynamic control surfaces and total wing/fuselage blending as per the MiG-29 and Su-27. This increased emphasis on high manoeuverability is pushing aircraft into previously unexplored areas of the flight envelope, one of the most interesting of which is extremely high angle-of-attack (α), or post-stall, flight, generally seen as $\alpha > 30^o$. In the late 1980s, NASA instigated a comprehensive High Alpha Technology Program, (HATP). The HATP brought together a fleet of aircraft including an F/A-18 aircraft modified as a High Alpha Research Vehicle, (HARV), see Fig.(1), the AFTI[1] F-16, F-16XL and F-16 MATV[2], the F-15 ACTIVE[3] and the X-29 and X-31 research prototypes to investigate thoroughly how aircraft manoeuverability can be improved in the high alpha regime.

Figure 1: *Forebody vortex flow visualisation using smoke on the NASA F-18 High Alpha Research Vehicle (HARV) at $\alpha = 42^o$. NASA photograph.*

Incorporating thrust-vectoring paddles around the nozzle, the X-31 prototypes were the first aircraft to be designed from the outset for operation in the post-stall arena. The

---

[1] Advanced Fighter Technology Integration

[2] Multi-Axis Thrust vectoring

[3] Advanced Control Technology for Integrated Vehicles

benefits of this approach quickly became apparent when mock combat engagements were flown against a F/A-18 adversary. Reporting to the NASA 4th High Alpha Conference, Canter [7], stated that whilst none of the pilots involved in the X-31 program thought the aircraft represented a revolution in air combat, '*...the enhanced pitch pointing and velocity vector manoeuvering provided by post stall opened new options for the pilot to use in close in combat. These options involved using post stall manoeuvering as a repositioning tool to drive the fight, or as a way to optimally rotate and point the vehicle for a weapons employment when the opponent can't counter you*'. One of the most impressive of these new options is the minimum-radius, 180° turn known as the Herbst Manoeuver, see Fig.(2). After increasing alpha to approximately 70° so that the entire airframe is acting as a speed brake, using thrust vectoring to maintain control, the pilot rapidly rolls the aircraft to reverse the direction of flight, completing the manoeuver with acceleration back to high speed in the opposite direction. The ability to manoeuver in this way could reduce the turning time of a fighter aircraft by 30 percent. Extending the flight envelope in this manner clearly has its benefits but unfortunately it also brings associated problems. Few current aircraft, including the fourth-generation combat aircraft now entering service, were explicitly designed for effective operation at high angles of attack, say $\alpha = 50^o$, hence certain aerodynamic deficiencies become apparent when high-alpha manoeuvers are attempted.

One of the most interesting aerodynamic problems being encountered is that of the side-force that is generated by a slender combat aircraft forebody when placed at moderately high angles of attack, typically $\gtrsim 30^o$. This sideforce, which also results in a yawing moment, can occur even when the forebody is completely symmetric and at zero sideslip. Wind-tunnel tests on a simplified, but representative, 3.5D[4] tangent-ogive/cylinder geometry by Keener et al., [60], revealed the local sideforce to be up to 1.5 times greater than the local normal force. In addition, the non-uniform distribution of this sideforce along the forebody and the substantial moment-arm results in a yawing moment which may be too severe for the available rudder control power to counter, [109]. It should be remembered that rudder authority is often extremely limited at high-α by wing and fuselage blanking of the tail. Hence, at high angle-of-attack, the controllability of the aircraft is largely dictated by the nose.

Clearly, the possibility of such large sideforces and yawing moments being generated on the forebodies of manoeuvering combat aircraft raises several important questions: Why do the sideforces arise; what physical factors influence them; can they be controlled or harnessed to improve high angle-of-attack manoeuverability?

Concerning the first of the above questions, one of the first to note the generation of sideforce on symmetric slender bodies at high angle of attack and zero sideslip was Letko, [72]. Letko's results '*showed that the fuselage experienced a large increase in yawing moment as the angle of attack increased, owing to asymmetrical disposition of the pair of trailing vortices emanating from the nose*'. Subsequent research confirmed this and then focussed on trying to define the effects of the flow parameters and model

---

[4] 3.5D denotes the fineness ratio (length/maximum diameter) to be 3.5.

Dryden Flight Research Center EC94-42478-4 Photographed 1994
X-31: Demonstrating entry into the high angle of
attack Herbst Maneuver. NASA photo by Jim Ross

Figure 2: *The NASA X-31 at* $\alpha = 70^o$ *demonstrating the Herbst manoeuver. NASA photograph.*

geometry on the vortex wake. Much work has been done in this area and generalities are now known, although the exact reason for the asymmetry is still a topic for debate: some argue, based upon computational, [14], and experimental data, [130, 19], that the asymmetry is the result of a convective instability of an originally symmetric flow, whilst others cite a vortex crowding effect as a possible reason, [8].

When experimentalists began to investigate the flow around slender forebodies at high angles of attack and zero sideslip, it was rapidly established that repeatability was poor and duplication of the results of others difficult to achieve. However, the general structure and development of the flow with increasing α has now been agreed upon:

1. At very low α the flow remains attached to the body.

2. As α is increased, primary separation lines appear on either side of the body, vorticity feeding into separated shear layers on either side of the pitching plane.

3. Initially, the shear layers seprate symmetrically and roll up into two symmetric vortices running along the leeside of the body. Re-attachment of these primary vortices occurs along two lines near the leeside meridian, the re-attachment lines merging to form a single line as the vortices grow in size and strength.

4. As α exceeds the *onset angle*, the vortices become asymmetric, one becoming dominant and moving closer to the body whilst the other moves further away from the surface. The onset angle for this asymmetric flow is approximately twice the semi-apex angle, [58, 61].

5. The move to an asymmetric flow state results in a side-force and accompanying yawing moment being generated. The sideforce is directed towards the vortex lying closest to the forebody surface, this vortex generating the lowest pressure, hence greater suction, of the two. The flow can now be approximately described using the impulsive flow analogy - this states that the flow at successive streamwise stations from the nose develops in the same manner as the flow about a two-dimensional cylinder started impulsively from rest, [2].

6. A slight further increase in α and the vortices become bi-stable. Disturbing the flow momentarily with, for example, an air jet, can cause the vortices to switch handedness.

7. Increasing α further causes the vortex asymmetry to strengthen. This then develops into a steady multiple vortex flowfield with vortices shedding from alternate sides of the body as downstream distance increases. This alternate shedding results in the sideforce distribution also alternating in sign moving aft from the apex. In addition, the sideforce distribution compresses towards the apex of the forebody.

8. The steady alternate vortex shedding then degenerates with further increases in α, unsteadiness spreading towards the apex from the rear of the body. Nearing 90^o, it resembles a von Karman vortex street.

The general flowfield described above occurs on a variety of slender forebodies. These range from cones to tangent-ogives to paraboloids but the flow is not restricted to bodies of revolution. A similar asymmetric shedding can be seen from slender delta wings, [59], (where the separation point is fixed at the leading edge) and, importantly, non-circular forebodies typical of modern-era combat aircraft, for example the F-5, [24, 109], or F-16, [40, 112].

From trying solely to explain and quantify forebody vortex flowfields, research in recent years has moved increasingly into their prediction and control. Initial thoughts were simply to eliminate the non-zero sideforces and moments entirely, thereby improving high-α stability and departure resistance. However, as mentioned above, conventional yaw-control authority is often extremely limited at high angles-of-attack and it was soon realised that controlled manipulation of the vortex system might provide an alternative means of control. Methods since investigated range from simple nose-tip strakes, [98], to boundary-layer trips and pneumatic control techniques, [36, 97].

Whilst flight test constituted a major part of the NASA HATP, an extensive wind-tunnel and computational test program ran alongside. Many aspects of high alpha flight were investigated but a large part was aimed at forebody vortex control: tested systems including tangential slot blowing and static and actuated nose strakes. This program, and several other smaller studies, have been extremely successful in demonstrating the benefits that such systems can bring and that, in refined form, it is possible and desirable that they be integrated into the next generation of combat aircraft. Indeed, the F-15 Forebody Vortex Control (FVC) Program was initiated in the US with the goal of developing a production FVC system for the F-15. This should improve yaw control at high alpha, and improve departure resistance as well as general manoeuverability. The system will either take the form of a mechanically actuated device such as the deployable twin strakes developed in the HARV program, or a pneumatic device such as the port blowing system tested on the X-29 airframe.

Research Objectives & Thesis Structure

From the short introduction above, it is clear that it is desirable for the aerodynamicist to have a predictive capability for forebody flowfields in order to minimise any problems as early in the design cycle as possible. Wind-tunnel tests are expensive, time-consuming and do not necessarily tell the truth. Computational fluid dynamics (CFD) methods may provide a viable alternative if a sufficiently accurate physical model can be simulated. Solution techniques are continually improving and available supercomputer power increasing year on year, so forebody flow may now be an ideal candidate for computational solution.

Saab have a longstanding committment towards R&D and a vested interest in keeping abreast of modern computational aerodynamic techniques. To this end, since 1992 they have been members in the pan-European NSMB Consortium, a grouping of two universities (IMHEF/EPFL, Lausanne, Switzerland, and KTH, Stockholm, Sweden), one research establishment (CERFACS, Toulouse, France) and two aerospace companies (Aerospatiale, Toulouse, France, and Saab, Linköping, Sweden), aiming to develop the NSMB structured multi-block Navier-Stokes code to the stage where it can be used confidently for industrial configuration design and evaluation. In 1996, the Future Products and Technology Group, Saab Aerospace, agreed to part-fund the author through an Engineering Doctorate (EngD) at Cranfield College of Aeronautics with the broad technical objective of developing a more physically coherent approach towards the forebody vortex problem centred around the NSMB code and the nose geometry of the JAS-39 Gripen, Fig.(3). This was then defined further to produce the following:

- Investigate methods of capturing high-α asymmetries computationally.
- Assess requirements for successful simulation: grid, solver, turbulence model, transition, computer power etc.
- Implement improvments to the existing code where necessary.
- Compute high-α flow about the clean JAS-39 forebody.
- Assess the effect of adding a *rhino-horn*-type forebody tip strake.
- Define a computational strategy for modelling high-α forebody flows. Is it worth trying to capture the flow physics or better to concentrate on the macro effects?

The four year duration of the Engineering Doctorate has permitted a detailed study to be made of the problems involved in the computational simulation of forebody flows and most of the initial objectives to be achieved. The thesis starts with a survey of existing literature pertinent to the problem and the contributing physical factors. Chapter 2 covers the numerical aspects of the simulation, before dealing with the additional turbulence models implemented in the code and their validation, grid-generation and data-reduction techniques and concluding with a summary of the computational hardware used. Chapter 3 details preliminary computations on the tangent-ogive/cylinder geometry and attempts to produce asymmetry whilst computations on the clean JAS-39 nose are covered in Chapter 4. Forebody vortex control techniques are reviewed in Chapter 5 before results on the JAS-39 and rhino-horn are presented in Chapter 6.

Since most fighter aircraft currently in service are not capable of any measure of controlled post-stall flight, the retro-fitting of forebody vortex-control devices and other manoeuverability and lethality enhancements may be a viable alternative to the purchase of new-build fourth-generation aircraft for many poorer countries with ageing airforces. A brief investigation into this and other purchasing options available to airforces around the world follows an assessment of the changing requirements of airpower to constitute the non-technical aspect of the work in Chapter 7. Some brief concluding remarks follow to complete the thesis.

__Figure 3:__ Saab JAS-39 Gripen over northern Sweden. Saab photograph.

1. Literature Review

This chapter presents a review of the available literature on the subject of slender forebody aerodynamics, a substantial body of work. Experimental studies of the behaviour of slender forebodies at high angles of attack have, to date, delivered almost all the qualitative information on factors contributing to the flow. Hence, the first section of the chapter discusses the relevant flow physics, the influence of geometric shape and flow conditions. The problem of modelling high-alpha asymmetries numerically is dealt with in the second section. Problems have arisen largely as a result of fundamental uncertainty regarding the relative importance of the various mechanisms driving the flow. This is examined together with the physical assumptions and simplifications that have been necessary in previous simulations. Literature pertaining to forebody flow control is covered separately in Chapter 5.

1.1 Flow Physics

The sharp cone is the simplest forebody which can be considered. Ignoring base flow, the flow parameters are constant along rays originating at the apex[1]. A tangent-ogive forebody, see Fig.(1.1), has added complexity owing to the curvature of the surface in the streamwise direction. However, on local scales, the tip region can be regarded as being very nearly conical and, since this region has been found to have a large bearing on the nature of the flow, the flow asymmetry develops much as it does for a cone. Indeed, the onset of asymmetry occurs at an angle of attack approximately twice the semi apex angle as it does for a cone, see Keener & Chapman, [61].

1.1.1 Influence of fineness ratio

The onset of asymmetry for sharp-nosed slender bodies occurs at an angle approximately equal to twice the semi apex angle. Clearly, the more slender the forebody, the lower the angle of attack at which asymmetry begins to occur. This may give a clue as to the cause of the asymmetry. As the apex angle of the forebody is reduced, the resultant nose-tip vortices are positioned closer and closer to each other. Keener and Chapman, [59], and later Chen *et al.*, [8], postulated that once the vortices reach a particular strength it is impossible for them to co-exist symmetrically in such close proximity. Thus, the flow is excited into a stable asymmetric mode, one vortex moving inboard and closer to the body whilst the other moves further away.

---

[1] All flows having this property are mathematically regarded as being *'conical'*.

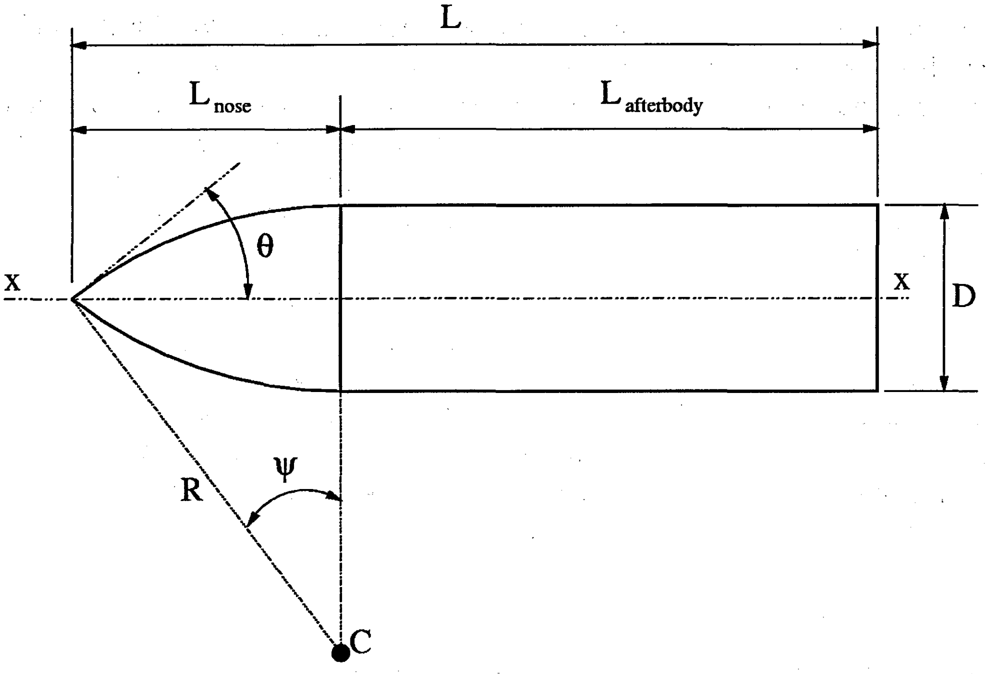

Figure 1.1: Plan view of a tangent-ogive/cylinder combination. The ogive is formed by rotating an arc of a circle (centre C, radius R) through 360^o *about the axis* xx. *θ is the nose semi apex angle; L_{nose}/D is the tangent-ogive fineness ratio or calibre.*

Moir, [85], conducted a study into the effect of overall fineness ratio (L/D) of tangent-ogive/cylinder combinations on the resultant asymmetric forces. He concluded that low overall L/D and small apex angles coupled to reduce the effect of afterbody shedding and make the onset angle almost entirely apex-angle dependent. For the opposite case of high overall L/D and high apex angle i.e. a long afterbody with a short forebody, the onset angle becomes dependent solely on overall L/D. For this latter case, the asymmetry was seen to develop near the base of the afterbody and progress forward, reaching the tip at an angle of incidence close to the apex angle of the nose. For the former case, micro-asymmetries at the nose would cause the flow to switch to either of two mirror image asymmetric conical tip vortex pairs, these states becoming stable at angles of attack greater than the onset angle, see Fiddes, [31]. However, Moir concluded that further tests would have to be performed before it could be stated categorically that two different mechanisms for asymmetry could act depending on model geometry.

1.1.2 Mach number

The effect of Mach number on the flowfield is well documented, for example Pick, [102]. Despite problems with wind-tunnel turbulence at the higher end of the Mach number range, it is agreed that increasing Mach number reduces the sideforce. Wardlaw and Morrison, [120], show that a reduction in sideforce begins when the crossflow Mach number, defined for a body of revolution as the Mach number of the component of the freestream velocity vector normal to the axis of revolution, reaches approximately 0.4. At this point, the crossflow accelerating around either side of the forebody becomes supersonic and the resulting shock-induced separations dominate the flow, forcing symmetry. Increasing forebody fineness ratio has the effect of delaying the onset of fall off in sideforce to slightly higher Mach numbers.

It should be noted that an asymmetric wake can exist with a sideforce distribution giving a net value of $C_Y = 0$. Keener and Chapman, [61], observed an asymmetric vortex wake for an ogive-cylinder combination at a crossflow Mach number of 1.28. Hunt, [49], explains that high crossflow Mach number causes narrowing of the wake. Furthermore, the asymmetric wake becomes more isolated from the body because of the supersonic crossflow, although the separating shear layers still feed into the vortex structure and the trailing vortices will still force re-attachment.

1.1.3 Reynolds number

For any complex three-dimensional flow with separation and re-attachment, a strong dependency on Reynolds number would be expected due to the transition from laminar to turbulent flow. Much data which has been gathered has been taken for flow conditions where the crossflow Reynolds number would mean boundary-layer transition if dealing with a circular cylinder. The ogive-cylinder combination has added complications, however, due to the varying cross-sectional area.

Keener *et al.*, [60], as part of their detailed study on forebody flows, tested a 3.5D[2] tangent-ogive forebody for $0.3 \times 10^6 \leq Re_D \leq 3.8 \times 10^6$ (based on base diameter) at $M = 0.25$. They noted that, at very low Reynolds number, increasing Re increased the sideforce acting on the body. This sideforce reached as high as 1.4 times the maximum normal force. However, increasing above $Re_D = 0.8 \times 10^6$ reduced the sideforce in a similar manner to boundary-layer trips, [102]. As the Reynolds number increased above $Re_D \approx 2 \times 10^6$, the magnitude of the sideforce was seen to increase again but the direction of the sideforce was reversed. This would correlate with the existence of an increasing region of turbulent flow on the windward side of the body. The normal force acting on the body showed definite Reynolds number dependency, with $C_{N_{max}} = 2.9$ at the lowest Re_D, decreasing to 2 as Re_D increased. Generally, $\frac{\partial C_N}{\partial \alpha}$ increased when sideforce increased, hence C_N may be increased by increasing flow asymmetry. Changing the Reynolds number had little effect on the onset angle.

Lamont, [67], studied a shorter 2.0D ogive coupled to a long cylindrical afterbody. This should reduce the complexity of the flow since the cross-sectional area increases rapidly to the maximum and any problems with multiple flow regimes on the forebody are minimised. With sideforce data gathered for Reynolds numbers between 0.2×10^6 and 4.0×10^6 and $20^o \leq \alpha \leq 90^o$, Lamont plotted overall sideforce coefficient C_Y at $\alpha = 55^o$ against Reynolds number (based on base diameter). The result is shown in Fig.(1.2).

---

[2] L_{nose}/D=3.5

The huge reduction in sideforce in what Lamont refers to as the transitional regime[3]was present across the entire angle of attack range. The reason stated for this is degradation in the coherency of the vortex wake structure as the boundary-layer transitions.

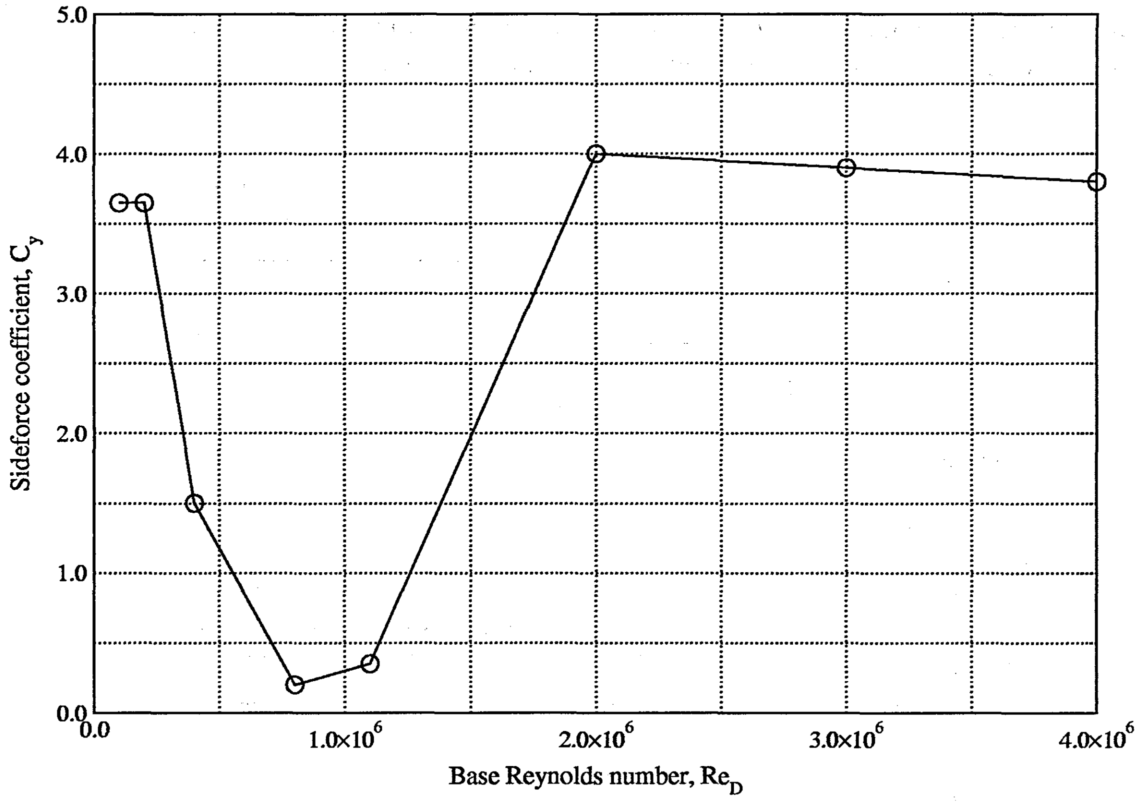

Figure 1.2: *The effect of Reynolds number on the maximum sideforce generated on a 2.0D tangent-ogive/cylinder combination, $\alpha = 55^o$. Data from Lamont, [67].*

The conclusions of Lamont are contested by Ericsson and Reding, [27], who claim that differential transition on either sides of the body amplified by existing wake vorticity leads to the greatest sideforces across the Reynolds number range. Much of the data claimed to support this view has to be taken in context but some, for example that of Nelson and Fleeman, [95], undoubtedly proves that under certain flow conditions this can be the case. However, differential transition should be regarded as the weakest mechanism for production of asymmetry and not the primary cause.

As mentioned above, the direction of the sideforce reverses with increasing Reynolds number. The differing pressures on either side of the body that cause the sideforce also result in turbulent re-attachment occurring on one side, that with the lower pressure, before the other. This is due to the higher velocities and accompanying higher local *Re*.

---

[3] Described as covering the range of Re_D where a laminar bubble is present, the flow undergoing laminar separation, transition and subsequent turbulent re-attachment. He defines the fully turbulent regime to be when the flow transitions before separation and the laminar regime to be absence of transition.

The pressure on this side then rises due to the re-attachment, moving the vortex and causing a reduction in the asymmetry. This mechanism is probably helped by a reduction in the coherency of the vortex structure and together with this may be enough to push the primary pair into their mirrored state. Unfortunately, there is little evidence strongly supporting the above argument and the problem is further compounded by a second change in sideforce direction if Re_D is increased to fairly high values (approx 4×10^6).

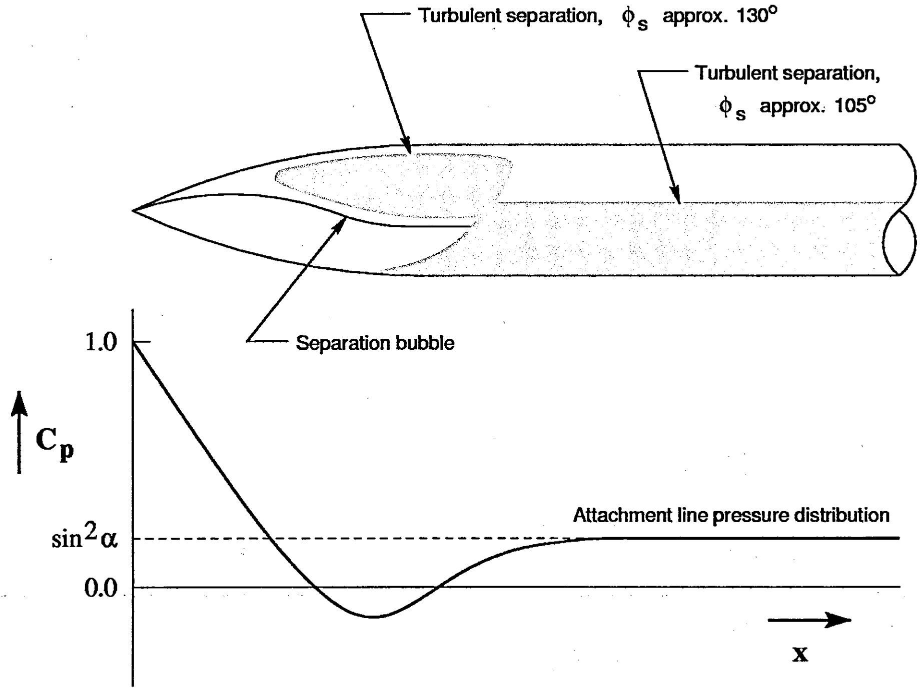

Figure 1.3: Orientation of transition fronts and separation lines when attachment-line contamination occurs. Figure from Poll, [104].

Drawing on the experimental work of Lamont regarding critical Reynolds number versus incidence boundaries, Poll, [104], seeks to clarify the transition physics for bodies of revolution, expanding on earlier work which focusses on yawed cylinders. Relating Lamont's boundaries to what is known of three-dimensional flows, Poll establishes the likely transition mechanisms and formulates criteria to define the critical Reynolds number versus incidence boundaries based upon the transition physics. He notes that, for smooth bodies with no surface discontinuities immersed in uniform fluid flow with low free-stream turbulence, transition is usually a result of boundary-layer instability: free shear-layer instability; attachment-line instability; cross-flow instability; streamwise-flow (Tollmien-Schlichting) instability.

Extremely susceptible to instabilities aside at extremely low Re, a laminar free shear-layer may transition and re-attach if the transition point is close enough to the surface, forming a bubble. The thicker, more energetic turbulent boundary layer is more resistant to the leeside adverse pressure gradients than a laminar boundary layer with the result that the separation point moves towards the leeward generator, see Fig.(1.3). (c.f. drag-reduction in two-dimensional cylinder flow).

Attachment-line transition is dealt with in detail by Poll in [103]. For a tangent-ogive/cylinder, a point of minimum pressure exists just aft of the ogive/cylinder junction. At a sufficiently high Reynolds number, the subsequent adverse pressure gradient experienced by the flow along the attachment line aft of this point results in a point source of turbulence forming, convecting aft and developing into a wedge, again see Fig.(1.3). Given that the flow in such a situation becomes turbulent at the attachment line (i.e. at the windward meridian), no separation bubble is formed and turbulent separation occurs at $\phi_s \approx 105^o$.

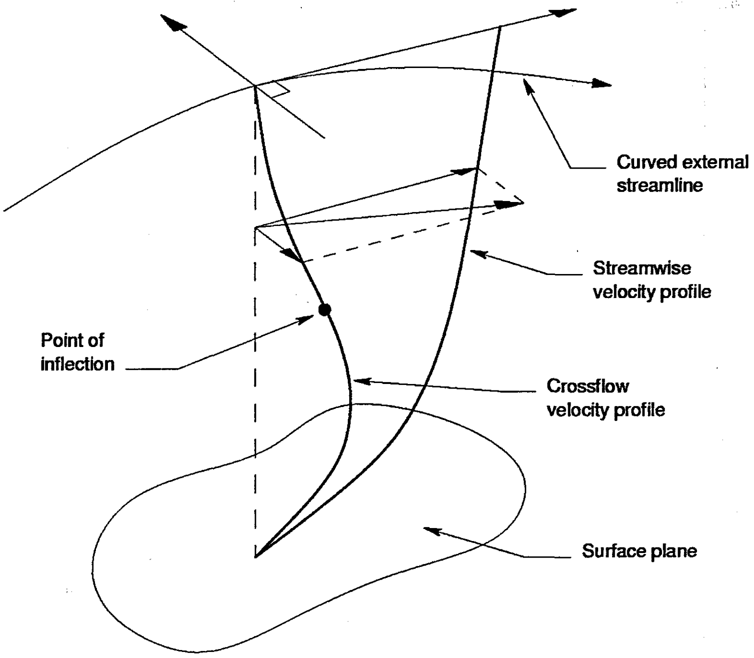

Figure 1.4: *Typical velocity distribution for a three-dimensional boundary-layer flow. Figure from Poll, [104].*

Cross-flow transition is again described in detail by Poll, see [105]. Either side of the attachment line, the streamlines marking the edge of the boundary layer are curved in planes lying parallel to the surface of the body. Moving down through the boundary layer towards the wall, the flow is slowed by viscosity but the cross-stream pressure gradients remain constant. The effect of this excessive pressure gradient is to induce a crossflow boundary-layer velocity component, see Fig.(1.4). This crossflow is far more susceptible to instabilities resulting from flow disturbances than the main velocity profile and thus is liable to transition at a far lower Reynolds number. Small streamwise vortices begin to form in the boundary layer, stationary with respect to the surface, their axes aligned with the external streamlines and, at high enough Reynolds number, a distinctive saw-tooth transition front forms. As with attachment-line contamination, transition occurs within the attached boundary layer, without bubble formation, thereby shifting the locus of separation of the turbulent shear layer which feeds the wake vortices.

Where the associated Reynolds numbers are low enough to preclude the three mechanisms above, Tollmien-Schlichting instability of the streamwise flow may act.

By considering each transition mechanism in turn, Poll establishes a set of Reynolds number versus incidence transition boundaries which are plotted with the data from Lamont in Fig.(1.5). Clearly, with four transition mechanisms possible, each capable of significantly altering the locus of separation for the shear layer feeding the vortex wake, Reynolds number is a critical factor in defining the character of the flow.

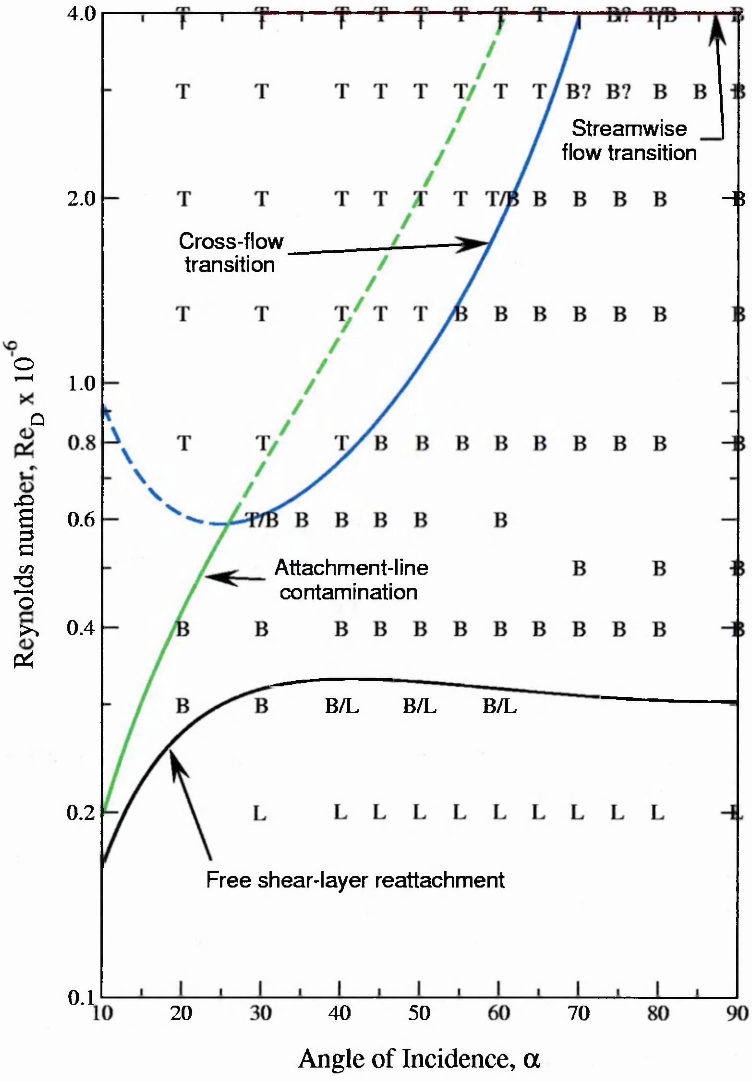

Figure 1.5: Predicted vs. experimental transition boundaries for a tangent-ogive/ cylinder. Figure from Poll, [104], with data from Lamont, [67, 69].

1.1.4 Roll angle effects

The roll angle of the model is known to have a significant effect on the normal force and the distribution and magnitude of the sideforces through altering the vortex disposition. Dexter & Hunt, [20, 50], performed a series of tests in which the roll orientation of the apex was systematically altered. They observed that the position in roll of the nose dominated the flow development - this also being shown by Peake *et al.*, [100]. These results indicate that asymmetric imperfections in the geometry of the nose close to the apex dictate the sense of the vortex asymmetry. Lamont, [67, 69], used a sophisticated experimental rig which enabled a full range of roll angles to be investigated. The sideforce varied between approximately equally positive and negative limits through a complete sweep of roll angle. Both amplitude and span of the sideforce distribution varied at different roll orientations. By making efforts to minimise support interference and flow unsteadiness, Lamont confirmed that any asymmetry at the nose can infuence the whole flow. Despite changing Reynolds number and α, the dependency on roll angle persisted and a pattern was discerned when plotting $C_y/|C_{y_{max}}|$ *vs.* roll angle within the laminar and fully turbulent separation regimes. This pattern takes the form of a square waveform with the magnitude of the sideforce corresponding to a *'regular state'* occurring with either handedness and the same vortex wake structure down the length of the body. These regular states appear to be well defined for sharp noses at high α but no similar pattern could be found when laminar separation/turbulent re-attachment was present, Lamont's transitional regime. Variation of normal force with roll angle was most marked in the fully turbulent separation regime, whilst normal forces in the transitional regime varied little with roll angle.

The above studies generally found the orientation of the cylindrical afterbody to have little effect on the sideforce. However, the results of Kruse *et al.*, [66], and Keener, [57] contradict this. Both studies employed a multi-piece model and showed that the sideforce could vary significantly while varying the roll angle of the afterbody and keeping the forebody/tip fixed. An attempt to explain this discrepancy was made by Zilliac *et al.*, [128]. They proposed that a perturbation downstream of the nose might be able to trigger asymmetry in a similar manner to the way that nose micro-asymmetries trigger asymmetry. Clearly, however, any perturbation on the afterbody capable of generating a disturbance strong enough to propagate upstream towards the tip and provoke asymmetry would have to be much larger scale.

1.1.5 Freestream turbulence level

The effect of freestream turbulence on the character of the vortex flowfield has received relatively little consideration. Ericsson and Reding, [26], acknowledged that the Reynolds number at which maximum sideforce is experienced would vary between tunnels owing to the degree of freestream disturbance and tunnel noise. Regarding surface pressures, Dexter and Hunt, [20, 50], showed that freestream turbulence could have a significant effect. Their results indicate that turbulence of a particular scale and strength might induce switching of the asymmetric vortices into their mirror image. Dexter and Hunt operated with an ambient turbulence level of 0.01%. However, taking measurements with and without a turbulence screen (providing levels of about 2%), Wardlaw and Yanta, [121], demonstrated that surface pressures and sideforce distribution changed little.

A study of the effect of different levels of freestream turbulence on asymmetric vortex formation was performed by Howard *et al.*, [48]. The study focussed particularly on whether or not the degree of freestream turbulence could be made to influence vortex switching. With a Reynolds number (calculated with respect to base-diameter) of 1.1×10^5, symmetric laminar separation was assumed, although this was not verified. Four grids were used to vary turbulence levels between the ambient level of 0.23% and a maximum of 3.8%. The addition of high-intensity, large-scale turbulence was found to reduce the induced side forces and also to move the range of the asymmetric regime to slightly higher angles of attack. The ogive forebody of fineness ratio 2.29 had an apex angle of approximately 50^o. However, the overall model fineness ratio 13 was large enough to result in asymmetric shedding on the afterbody below 50^o, the angle at which the asymmetric forebody vortices began to dominate. Generally, increasing turbulence levels reduced the magnitude of the yawing moments, although they still remained significant. However, the afterbody generated yawing moments at low α were, for the most part, removed. Regarding the primary aim of researching the switching phenomenon, no correlation between levels of turbulence and switching could be established. Overall, Howard *et al.* concluded that the interaction between the vortices and freestream turbulence cannot be regarded as a linear problem and that there is a high dependence on the turbulence scale.

1.2 CFD Predictions

The database of existing numerical work on high alpha flows around slender forebodies only extends back fifteen years or so. Indeed, fine-grid Navier Stokes solutions around tangent-ogive type forebodies only became possible as recently as the late 1980's.

Zilliac, [129], ran a parallel computational and towing-tank study of the incompressible flow around a tangent-ogive/cylinder combination at $Re_L = 1000$. For the computations, a full-grid was used with no symmetry plane being enforced and the symmetric results compared well with experiment, displaying such features as the separation lines, saddle points and well-defined vortex cores. In the same year, Degani and Schiff, [17], ran time-accurate Navier-Stokes computations of the laminar flow about a slender ogive-cylinder at $M = 0.2$, $\alpha = 40^o$. These computations showed the vortical flowfield to be symmetric in nature, whereas experimental results taken at the same flow conditions gave the flow as being highly asymmetric. Introducing a small perturbation at the nose, Degani and Schiff saw the computational flowfield become asymmetric but, when the disturbance was removed, the flowfield returned to its original, symmetric state.

Whilst Degani and Schiff found that a small, space-fixed and time-invariant perturbation was necessary to obtain an asymmetric computational result, Siclari and Marconi, [108], achieved asymmetry without any disturbance but with the addition of a conical flow assumption. Since that paper was published, engineers researching the high-alpha flow regime around forebody-type geometries have fallen into one of two camps. The first camp subscribes to the belief that with a perfectly symmetric geometry in zero sideslip, no asymmetry can be computationally attained unless a space-fixed time-invariant perturbation is added. This simulates the tip asymmetry inherent in any experimental model which generates a flowfield disturbance which in turn rapidly amplifies to produce an asymmetric flowfield. The second camp, however, believes that the phenomena is fundamentally inviscid, with two equally valid solutions (one symmetric and the other comprising two mirror-image asymmetric solutions) becoming feasible at high angles of attack. In this case, any tip asymmetries which are present serve only to tip the symmetric flow into one or other of the asymmetric solutions.

1.2.1 Asymmetry through geometric disturbance

Following on from their earlier work, mentioned above, Degani and Schiff, [18], studied the effect of spatial disturbances on vortex asymmetry. They ran time-accurate fine-grid Navier-Stokes computations over the same geometries as previously, *i.e.* a 3.5D tangent-ogive forebody with varying lengths of cylindrical afterbody. A small jet was added, acting normal to the plane of incidence, at either $x/D \approx 0.12$ or $x/D \approx 1.20$. The conclusions drawn were that a space-fixed, time-invariant perturbation was indeed necessary to induce vortex asymmetry at high α. Importantly, at lower angles of attack, the symmetric flowfield that was produced proved to be stable to time-varying perturbations, this being consistent with experimental observations. Where asymmetry was produced, the degree of asymmetry was shown to be a function of the disturbance strength: this corresponds to the different asymmetric flowfields and sideforces produced when rolling an experimental model which, due to machining limitations, will always have slight tip asymmetry. It was also demonstrated that, as has been noted experimentally, any perturbation at the nose induces the greatest asymmetry. However, whilst the above results imply that the nature of any vortex asymmetry is caused by space-fixed surface roughness, agreeing with Hall, [39], and Moskovitz *et al.*, [86], it does not imply that the asymmetric state becomes stable above the onset angle.

The above work was continued in subsequent papers, [130, 14, 15], and in all cases, it was found necessary to introduce and maintain a small perturbation near the tip to induce asymmetry. Accordingly, the authors all suggest that the origin of the vortex asymmetry is a convective-type instability of an originally symmetric flow.

1.2.2 Asymmetry through conical flow assumption

As discussed above, Siclari and Marconi, [108], achieved flow asymmetry purely by using the conical flow equations instead of the full, compressible, three-dimensional Navier-Stokes Equations. However, their paper followed earlier work by Fiddes, [32, 30, 31], Dyer, Fiddes and Smith, [22], and later that of Marconi, [78].

Fiddes work was centred on small disturbance calculations with vortex sheets modelled by vortex filaments and gave an asymmetric result for the incompressible flow about a slender cone. He showed that two sets of solutions are possible for a symmetrically separating flow: the first possible solution is valid for all α and is a symmetric flowfield with two primary vortices; the second solution becomes feasible at high angles of attack and comprises two mirror-image asymmetric flowfields. Computations performed subsequently by Marconi using an Euler solver coupled to a flow separation model also produced asymmetric solutions. The symmetric solution, however, proved to be unstable.

Siclari and Marconi, [108], computed the flow about a $\theta = 5^o$ circular cone at $M = 1.8$ for various high angles of attack (i.e. $\alpha \geq 2\theta$). Convergence was continued down to machine zero, with a 14 or 15 order drop in residual. For $\alpha = 2\theta$, a symmetric flowfield was produced, the calculation being allowed to continue for 1000 multigrid cycles once reaching machine zero to demonstate the stability of the solution. For 20^o angle of attack, the calculation was initially stopped after the error had decreased by about 9 orders. Normally, convergence to a greater degree than this produces a negligible change in the result. However, when the calculation was continued in order to demonstrate the stability of the evolving symmetric solution, the residual dropped slightly before climbing 8 orders and then converging 11 orders down to machine zero with an asymmetric solution. Similar results were obtained at several other high angles of attack and the flowfields proved stable when perturbed, but, interestingly, when $\alpha = 6\theta$ was computed, the result was a stable symmetric solution. It was later found that the initial convergence towards the symmetric flowfield could be bypassed by initialising the entire flowfield, except the outer boundaries, with freestream conditions under a small degree of sideslip. Whilst the computations were laminar and at low Reynolds number, ($Re_D = 1 \times 10^5$), the only possible experimental comparison that could be made used data taken at a higher Reynolds number where the flow was probably turbulent, so no conclusions could be drawn as to how physical the results actually were.

Similar results to the above were published by Kandil, Wong and Liu, [55], who also employed a conical flow assumption. Thomas, [115], however, published data which casts doubt on the validity of this approximation. He employed a three-dimensional Navier-Stokes code which gave a fully symmetric solution when running with symmetric boundary conditions. On the addition of a conical flow assumption, an asymmetric solution was produced.

Levy, Hesselink and Degani, [73], suggest that assuming conical flow fundamentally alters the problem. They argue that, by eliminating one coordinate direction, the problem becomes quasi two-dimensional and the crossflow hence becomes susceptible to the instability that leads to vortex asymmetry in the flow past a circular cylinder. Furthermore, Levy *et al.*, question why, if a symmetric base solution is not generated by the solver, does it have a preferred orientation, or handedness, of asymmetry? The reason that they propose is that certain solution algorithms may contain inherent asymmetries. If this is the case, then a symmetric base solution will be bypassed and a non-physical asymmetric solution result. The next important question to be asked is clearly whether or not an asymmetry introduced into the problem in this manner is a good way of numerically simulating what physically happens in the flow.

1.2.3 Non-symmetric solution algorithm

The differences possible when using an inherently asymmetric algorithm instead of a fully symmetric algorithm were highlighted by Levy, Hesselink and Degani, [73]. They computed the flow over a tangent-ogive/cylinder combination using three different algorithms: the Beam and Warming algorithm; a flux-split algorithm; a diagonal algorithm. Ignoring the usual slight differences that will be present between results from different codes, the clear difference between the three sets of results was that the diagonal algorithm produced vortex asymmetry with a symmetric grid, symmetric boundary conditions and no geometric perturbations. The other two algorithms predicted a symmetric flowfield. Levy *et al.* then go on to analyse the diagonal algorithm and demonstrate that the diagonalisation process breaks the symmetry-preserving properties of the original Beam and Warming algorithm on which it is based. They show that *'every time an inversion is performed, in any cross section, at any radial distance from the body, and in each of the three factors, a small asymmetric error is introduced'*. This error is very small, being similar in order to numerical rounding errors at low angles of attack, but, at higher angles of attack, it becomes capable of triggering instability mechanisms in the same manner as added geometric disturbances. The difference is that, when a geometric disturbance is introduced into the flowfield to induce asymmetry, it is a single perturbation placed on the body near the tip and not a series of perturbations spread throughout the flowfield. Levy *et al.* therefore believe that an asymmetric solution generated by an asymmetric algorithm is, in fact, spurious, and cannot match with experiment.

The findings of Levy *et al.* correlate with the earlier work of Vanden, [117], and Vanden and Belk, [118]. Vanden obtained asymmetric solutions using a second-order Roe scheme with a two-pass implicit approximate factorisation - this introducing an asymmetric error in the transient solution. Having re-written the algorithm with symmetric factorisation in the crossflow plane, Vanden and Belk initially found that the solutions converged symmetrically. However, when a flux limiter was introduced to improve stability, an asymmetric solution emerged *regardless of the factorisation employed.* In these cases, they established that numerical asymmetries were magnified from 10^{-12} to 10^{-5}. This appeared to be independent of the actual limiter used. Both the location of the vortex cores and the core total pressures were seen to be dependent on solver configuration.

In contrast to the above, Hwang and Rho, [51], produced some interesting results comparing solutions obtained using three differing algorithms: the symmetric ADI method; asymmetric steady LU-SGS[4]; asymmetric unsteady LU-SGS. As expected, the ADI algorithm remained symmetric throughout the solution process and produced a symmetric result. Both the LU-SGS computations produced asymmetric flowfields due to the asymmetric factorisation error in the crossflow plane with the unsteady LU-SGS calculation showing markedly reduced magnitude of oscillation in sideforce during convergence. Surprisingly, when the LU-SGS calculations were re-run with the sweep direction flipped, the handedness of the vortex wake remained unchanged.

In order to assess the stability of each solution, Hwang and Rho restarted the con-

---

[4] Lower-Upper Symmetric Gauss-Seidel ..... something of a misnomer as the scheme is non-symmetric.

verged asymmetric LU-SGS solution with ADI and converged symmetric ADI solution with LU-SGS. The flowfields remained largely unchanged, demonstrating both converged solutions to be unaffected by factorisation method. Hwang and Rho conclude that the factorisation error occurs mainly in the early stages of iteration and decays to zero as the solution converges. The transient nature of the disturbance and the stability of the resulting solution even with the perturbation removed points to absolute instability of the flow being the mechanism driving the asymmetry.

1.2.4 Transition & turbulence modelling

It will have been noted that computational studies thus far have focussed on capturing asymmetric flow around simplified geometries with the importance of one major physical complication being hugely underplayed: turbulence. Given the influence that transition and turbulence have on the nature of the flowfield, as shown in Subsection 1.1.3, the majority of work has either been at very low Reynolds number with the assumption of wholly laminar flow or at high Reynolds number with the flow assumed to be wholly turbulent. When included, turbulence modelling has largely been limited to either the original algebraic Baldwin-Lomax model, [4], or the Degani-Schiff version, [16], which includes modifications to take into account the presence of separated shear layers.

In reality, it has been shown that several transition mechanisms may be acting and, even at high Re_D, there may be a sizeable laminar region on the underside of the body near the apex of the nose. At the time of writing, this problem has only been tackled by Hartwich and Hall, [41], and Hartwich, Hall and Hemsch, [42], who employed a modified Baldwin-Lomax model which could simulate crossflow transition. Their results show slightly improved agreement with the experimental reference but the technique has not been developed.

2. Computational Method

This chapter covers the numerical details of the research. Commencing with a brief description of NSMB, the governing equations, turbulent closure and existing one- and two-equation turbulence models are covered. This is followed by details of the k-ω *family of models, including the blended* k-ω-SST *model, together with their implementation and testing within NSMB. The finite-volume formulation of the code is then briefly discussed, along with descriptions of the time-integration methods employed. The chapter finishes with sections dealing broadly with computational hardware issues, NSMB database generation and the grid-generation and post-processing techniques and software utilised in the research.*

Computational flow analysis tools have existed for several years now that are useable by the industrial aerodynamicist or designer alongside wind-tunnel or analytical methods. Increased accessibility to the techniques has resulted in a rapidly increasing user-base which, in turn, has meant application to an ever widening range of fluids problems. Driven by the demands of industry, commercial CFD solvers such as Fluent or StarCD have become increasingly capable and are suitable for a variety of aerospace work. However, commercial CFD solvers are, by necessity, not optimised for any particular class of problem and consequently occasionally show weaknesses when applied to complex or unusual geometries or severe flow conditions. On the other-hand, whilst user-friendliness may be relatively low, an in-house code can be kept up to date easily, tweaked as and when required for a particular case, and eliminates any reliance on a third-party software vendor.

As mentioned in the Introduction, NSMB is a state-of-the-art Multi-Block Navier-Stokes finite-volume code ostensibly being developed by a pan-European consortium including two universities (IMHEF/EPFL, Lausanne, Switzerland, and KTH, Stockholm, Sweden), one research establishment (CERFACS, Toulouse, France) and two aerospace manufacturers (Aerospatiale, Toulouse, France, and Saab, Linköping, Sweden). Given Saab's involvement and the author's prior experience of NSMB, it was the logical choice as the basis for the EngD research: Saab had a vested interest in improving the code; the source code was open, enabling modification; the development team easily contactable should any problems arise.

2.1 The Navier-Stokes Equations

NSMB numerically solves the unsteady compressible Navier-Stokes equations, equations that accurately describe the conservation of mass, momentum and energy for any fluidic system. The derivation of these equations can be found in any standard aerodynamics or computational fluid dynamics text, good examples being Refs. [3, 46], hence it will not be covered here. Using a 3-dimensional Cartesian coordinate system, (x, y, z), the Navier-Stokes equations in conservative form are as follows:

$$\frac{\partial W}{\partial t}+\frac{\partial}{\partial x}(f+f_v)+\frac{\partial}{\partial y}(g+g_v)+\frac{\partial}{\partial z}(h+h_v)=0 \tag{2.1}$$

where the state vector, W, is given by

$$W=\begin{pmatrix}\rho\\ \rho u\\ \rho v\\ \rho w\\ \rho E\end{pmatrix} \tag{2.2}$$

and the inviscid (convective) fluxes f, g and h and the viscous fluxes f_v, g_v and h_v are given by

$$\begin{gathered}
f=\begin{pmatrix}\rho u\\ \rho u^2+p\\ \rho uv\\ \rho uw\\ u(\rho E+p)\end{pmatrix},\quad f_v=\begin{pmatrix}0\\ -\tau_{xx}\\ -\tau_{xy}\\ -\tau_{xz}\\ -u\tau_{xx}-v\tau_{xy}-w\tau_{xz}+q_x\end{pmatrix}\\
g=\begin{pmatrix}\rho v\\ \rho vu\\ \rho v^2+p\\ \rho vw\\ v(\rho E+p)\end{pmatrix},\quad g_v=\begin{pmatrix}0\\ -\tau_{yx}\\ -\tau_{yy}\\ -\tau_{yz}\\ -u\tau_{yx}-v\tau_{yy}-w\tau_{yz}+q_y\end{pmatrix}\\
h=\begin{pmatrix}\rho w\\ \rho wu\\ \rho wv\\ \rho w^2+p\\ w(\rho E+p)\end{pmatrix},\quad h_v=\begin{pmatrix}0\\ -\tau_{zx}\\ -\tau_{zy}\\ -\tau_{zz}\\ -u\tau_{zx}-v\tau_{zy}-w\tau_{zz}+q_z\end{pmatrix}
\end{gathered} \tag{2.3}$$

The components of the shear stress tensor, τ, are

$$\begin{aligned}
\tau_{xx} &= 2\mu\frac{\partial u}{\partial x}+\lambda\left(\frac{\partial u}{\partial x}+\frac{\partial v}{\partial y}+\frac{\partial w}{\partial z}\right)\\
\tau_{yy} &= 2\mu\frac{\partial v}{\partial y}+\lambda\left(\frac{\partial u}{\partial x}+\frac{\partial v}{\partial y}+\frac{\partial w}{\partial z}\right)\\
\tau_{zz} &= 2\mu\frac{\partial w}{\partial z}+\lambda\left(\frac{\partial u}{\partial x}+\frac{\partial v}{\partial y}+\frac{\partial w}{\partial z}\right)
\end{aligned} \tag{2.4}$$

$$\begin{aligned}
\tau_{xy} = \quad \tau_{yx} = &\quad \mu\varepsilon_{xy} = \mu\left(\frac{\partial v}{\partial x} + \frac{\partial u}{\partial y}\right) \\
\tau_{xz} = \quad \tau_{zx} = &\quad \mu\varepsilon_{xz} = \mu\left(\frac{\partial w}{\partial x} + \frac{\partial u}{\partial z}\right) \\
\tau_{yz} = \quad \tau_{zy} = &\quad \mu\varepsilon_{yz} = \mu\left(\frac{\partial v}{\partial z} + \frac{\partial w}{\partial y}\right)
\end{aligned} \tag{2.5}$$

The quantities τ_{xx}, τ_{yy}, τ_{zz} in Equations (2.4) only arise if the gradients of velocity $\frac{\partial u}{\partial x}$, $\frac{\partial v}{\partial y}$ and $\frac{\partial w}{\partial z}$ are extremely large, such as in the region of a shock. These normal stress terms compress or expand the fluid and hence can be seen as acting in addition to pressure. λ is termed the bulk viscosity coefficient. Equations (2.5) define the tangential stresses, ε_{ij} denoting time rate of strain. For both Equations (2.4) and (2.5), μ denotes viscosity (Stokes hypothesis). The viscous dissipation in the energy equation is calculated from

$$\begin{aligned}
(\tau U)_x &= \tau_{xx}u + \tau_{xy}v + \tau_{xz}w \\
(\tau U)_y &= \tau_{yx}u + \tau_{yy}v + \tau_{yz}w \\
(\tau U)_z &= \tau_{zx}u + \tau_{zy}v + \tau_{zz}w
\end{aligned} \tag{2.6}$$

The conductive heat flux is found using Fourier's Law,

$$\begin{aligned}
q_x &= -k\frac{\partial T}{\partial x} \\
q_y &= -k\frac{\partial T}{\partial y} \\
q_z &= -k\frac{\partial T}{\partial z}
\end{aligned} \tag{2.7}$$

T denoting temperature and k the thermal conductivity. Assuming a calorifically perfect gas, the viscosity, μ, is found *via* Sutherland's Law. This takes two differing forms depending on the freestream static temperature of the flow,

$$\begin{aligned}
\mu(T) &= \left\{ \begin{array}{ll} \mu_\infty \frac{(T_\infty + S_1)}{T + S_1} \frac{T}{T_\infty}^{3/2} & if \quad T \geq 120K \\ \mu(120) \frac{T}{120} & if \quad T \leq 120K \end{array} \right\} \quad for \quad T_\infty \geq 120K \\
\mu(T) &= \left\{ \begin{array}{ll} \mu(120) \frac{(120 + S_1)}{T + S_1} \frac{T}{120}^{3/2} & if \quad T \geq 120K \\ \mu_\infty \frac{T_\infty}{120} & if \quad T \leq 120K \end{array} \right\} \quad for \quad T_\infty < 120K
\end{aligned} \tag{2.8}$$

μ_∞ denotes viscosity at the reference temperature T_∞ and S_1 is a constant, taken to be 100.3 for air. Thermal conductivity, k, is calculated from the Prandtl number, which is assumed to be constant.

$$k = \mu \frac{c_p}{Pr} \tag{2.9}$$

The specific heats at constant volume and constant pressure are constant for a calorifically perfect gas at room temperatures and are calculated from $c_v = R/(\gamma - 1)$ and $c_p = \gamma c_v$. R is the universal gas constant, equal to 287 J/kgK for air, and $\gamma = 1.4$. The system of equations is closed by a relation linking the pressure to the state vector, this relation depending on the thermodynamic model being used. Since a calorifically perfect gas is being considered, the relation employed is

$$p = \rho e \left(\gamma - 1\right) = \rho c_v T \left(\gamma - 1\right) = \rho R T \tag{2.10}$$

where e denotes the internal energy. This is related to the total energy of the fluid by the following equation,

$$e = E - \frac{1}{2}\left(u^2 + v^2 + w^2\right) \tag{2.11}$$

2.2 Turbulence Modelling

Turbulent flow is, by nature, complex and time-dependent. Direct numerical simulation is possible, but is currently far too computationally expensive for large-scale aerodynamics problems to be solved. The engineering approach, as always, has been to simplify the problem to the stage where an acceptable estimate can be obtained. In the case of turbulence modelling, this has meant taking a statistical approach and trying to model the macroscopic effects of the flow turbulence rather than attempting to capture the behaviour of each and every turbulent eddy. This is achieved by expressing each of the flow variables as the sum of a mean and a fluctuating part. The governing equations of mass, momentum and energy can then be time- and mass-averaged. However, there still remains the problem of the momentum fluxes that are present due to the non-linearity of the system. These appear as additional stress terms and present a closure problem since there are now more unknown terms than there are equations. Hence, the requirement for some type of turbulence closure model.

The following sections briefly cover the equations and principles behind turbulence modelling before looking at three existing models in the code: the one-equation model of Spalart & Allmaras and the two-equation models of Hoffman and Chien. For more background, and information on the turbulence modelling infrastructure within NSMB, the reader is directed towards the standard text by Wilcox, [124], the NSMB handbook, [119], and the final report for Swedish NFFP Project 2.246, [21], from which some of the following Favre averaging theory has been adapted.

2.2.1 Favre averaging

The concept of time-averaging the instantaneous Navier-Stokes equations for incompressible flow was first proposed by Osborne Reynolds in 1895, [106]. Unfortunately, allowing flow compressibility results in additional density and temperature fluctuations that, if time-averaging is employed, increase significantly the difficulty of finding suitable closure relations. This problem can be circumvented by applying the density-weighted averaging procedure of Favre, [28].

In order to demonstrate the benefit of Favre averaging the Navier-Stokes equations when considering compressible flow, it is helpful to consider what happens when time-averaging is attempted. The instantaneous values of the flow variables are split into mean and fluctuating components, $\bar{\phi}$ and $\phi'(t)$ respectively. Thus, for an arbitrary flow variable, $\phi(t)$

$$\phi(t) = \bar{\phi} + \phi'(t) \tag{2.12}$$

where $\bar{\phi}$, the mean value for the flow variable, is defined by

$$\bar{\phi} = \lim_{T \to \infty} \frac{1}{T} \int_t^{t+T} \phi(t)dt \tag{2.13}$$

Consider the continuity equation,

$$\frac{\partial \rho}{\partial t} + \frac{\partial \rho U_i}{\partial x_i} = 0 \tag{2.14}$$

This becomes, with the density and velocity terms rewritten in this manner,

$$\frac{\partial}{\partial t}(\bar{\rho} + \rho') + \frac{\partial}{\partial x_i}(\bar{\rho} U_i + \rho' U_i + \bar{\rho} u_i' + \rho' u_i') = 0 \tag{2.15}$$

Time averaging the above equation gives the Reynolds-averaged continuity equation for compressible flow,

$$\frac{\partial \bar{\rho}}{\partial t} + \frac{\partial}{\partial x_i}\left(\bar{\rho} U_i + \overline{\rho' u_i'}\right) = 0 \tag{2.16}$$

Clearly, in order to obtain closure for this equation, some kind of relationship between ρ' and u_i' is necessary. The problem becomes even more acute when considering the time averaged momentum equation for a compressible flow since there is a triple product of $\rho u_i v_j$ before the averaging is performed. Favre averaging overcomes the above problems by defining a mass-averaged velocity, $\tilde{u}_i$ as

$$\tilde{u}_i = \frac{1}{\bar{\rho}} \lim_{T \to \infty} \int_t^{t+T} \rho(\tau) u_i(\tau) d\tau \tag{2.17}$$

Hence, if an overbar represents standard Reynolds averaging,

$$\bar{\rho} \tilde{u}_i = \overline{\rho u_i} = \bar{\rho} U_i + \overline{\rho' u_i'} \tag{2.18}$$

which allows the continuity equation to be rewritten as follows,

$$\frac{\partial \bar{\rho}}{\partial t} + \frac{\partial}{\partial x_i}\left(\bar{\rho}\tilde{u}_i\right) = 0 \tag{2.19}$$

The form of Eqn.(2.19) is identical to a laminar continuity equation and thus it can be seen that the Favre averaging procedure effectively treats momentum per unit volume as a single dependent variable, a physically sound solution.

Now, if the instantaneous velocity is split into mass-averaged and fluctuating components,

$$u_i = \tilde{u}_i + u_i'' \tag{2.20}$$

the Favre average can be formed by multiplying by density and then time-averaging the result to give

$$\overline{\rho u_i} = \bar{\rho}\tilde{u}_i + \overline{\rho u_i''} \tag{2.21}$$

However, Eqn.(2.18) gives the result $\overline{\rho u_i''} = 0$, which would not be true if time-averaging had been employed. If Favre averaging is used for all variables with the exception of density, pressure and heat flux, the resultant mass-averaged Navier-Stokes equations can be written as follows.

$$\frac{\partial \overline{W}}{\partial t} + \frac{\partial}{\partial x}\left(\bar{f} + \bar{f}_v\right) + \frac{\partial}{\partial y}\left(\bar{g} + \bar{g}_v\right) + \frac{\partial}{\partial z}\left(\bar{h} + \bar{h}_v\right) = 0 \tag{2.22}$$

where the state vector, (cf. Eqn.(2.2)), has now become

$$\overline{W} = \begin{pmatrix} \bar{\rho} \\ \bar{\rho}\tilde{u} \\ \bar{\rho}\tilde{v} \\ \bar{\rho}\tilde{w} \\ \bar{\rho}\tilde{E} \end{pmatrix} \tag{2.23}$$

with the inviscid and viscous fluxes becoming, in tensor notation for simplicity,

$$\overline{f_i} = \begin{pmatrix} \bar{\rho}\tilde{u}_i \\ \bar{\rho}\tilde{u}_i\tilde{u}_1 + \delta_{i1}\bar{p} \\ \bar{\rho}\tilde{u}_i\tilde{u}_2 + \delta_{i2}\bar{p} \\ \bar{\rho}\tilde{u}_i\tilde{u}_3 + \delta_{i3}\bar{p} \\ \bar{\rho}\tilde{u}_i\tilde{E} + \tilde{u}\bar{p} \end{pmatrix}, \quad \overline{f_i^v} = \begin{pmatrix} 0 \\ -\tilde{\tau}_{i1} + \overline{\rho u_i'' u_1''} \\ -\tilde{\tau}_{i2} + \overline{\rho u_i'' u_2''} \\ -\tilde{\tau}_{i3} + \overline{\rho u_i'' u_3''} \\ -\tilde{u}_j\bar{\tau}_{ij} + \bar{q}_i + \overline{\rho E'' u_i''} - \overline{\tau_{ij} u_i''} + \overline{p u_i''} \end{pmatrix} \tag{2.24}$$

where δ_{ij} is the Kronecker delta. The stress tensor, $\bar{\tau}_{ij}$, is equivalent to

$$\bar{\tau}_{ij} = \bar{\mu}\left(\frac{\partial \tilde{u}_i}{\partial x_j} + \frac{\partial \tilde{u}_j}{\partial x_i}\right) - \frac{2}{3}\delta_{ij}\bar{\mu}\frac{\partial \tilde{u}_k}{\partial x_k} \tag{2.25}$$

Using the perfect gas relations,

$$\overline{\rho E'' u_i''} \equiv c_v \overline{\rho T'' u_i''} + \overline{\rho u_i'' u_j''}\tilde{u}_j + \frac{1}{2}\overline{\rho u_j'' u_j'' u_i''} \tag{2.26}$$

and, using $p = \rho RT$,

$$\overline{pu_i''} + \overline{p'u_i''} = (\gamma - 1)\, c_v \overline{\rho \left(\tilde{T}u_i'' + T''u_i''\right)} = (\gamma - 1)\, c_v \overline{\rho T''u_i''} \tag{2.27}$$

Which results in the viscous flux contributions being written as

$$\overline{f_i^v} = \begin{pmatrix} 0 \\ -\tilde{\tau}_{i1} + \overline{\rho u_i'' u_1''} \\ -\tilde{\tau}_{i2} + \overline{\rho u_i'' u_2''} \\ -\tilde{\tau}_{i3} + \overline{\rho u_i'' u_3''} \\ -\tilde{u_j}\bar{\tau}_{ij} + \bar{q}_i + \gamma c_v \overline{\rho T'' u_i''} + \overline{\rho u_i'' u_j''}\tilde{u}_i + \frac{1}{2}\overline{p u_i'' u_j'' u'' j} - \overline{\tau_{ij} u_i''} + \overline{p' u_i''} \end{pmatrix} \tag{2.28}$$

The compressibility terms written in red have been shown to be negligible for Mach numbers less than about 5, which, when compared to the instantaneous, unaveraged, equations, leaves the following additional terms:

1. Reynolds-stress tensor: $-\overline{\rho u_i'' u_j''}$
2. turbulent heat flux: $-\gamma c_v \overline{\rho T'' u_i''}$
3. triple correlation term $-\frac{1}{2}\overline{\rho u_j'' u_j'' u_i''}$

Closure of the averaged equations thus requires these unknown quantities to be accounted for by some type of turbulence model.

2.2.2 The Boussinesq approximation

At the time of writing, the majority of turbulence models in common use are first-order models based around the Boussinesq eddy-viscosity approximation, [6]. The approximation relates the Reynolds stress tensor to the strain-rate tensor by way of introducing the concept of turbulent viscosity, μ_t. Wilcox, [124], rationalises this well by considering the molecular transport of momentum in a two-dimensional shear flow, with streamwise velocity a function of cross-stream location,

$$U = U(y) \tag{2.29}$$

The momentum posessed by molecules within the fluid is thus dependent on their y-location and so the Brownian motion within the flow gives rise to shear stress, t_{xy}. The molecular velocities can now be split into mean and fluctuating parts, similar to before,

$$u = U + u''' \tag{2.30}$$

with u''' the fluctuating velocity due to Brownian motion. As any flux across the plane $y = 0$ is related to the normal velocity, v''', the instantaneous x-momentum flux across the area dS can be written as

$$dp_{xy} = \rho\,(U + u''')\, v'''dS \;\rightarrow\; dP_{xy} = \overline{\rho u''' v'''} dS \tag{2.31}$$

for all molecules. Since the stress at $y = 0$ is

$$\sigma_{xy} = \frac{dP_{xy}}{dS} \tag{2.32}$$

and

$$\sigma_{ij} = p\delta_{ij} - t_{ij} \tag{2.33}$$

Eqn.(2.31) thus becomes

$$t_{xy} = -\overline{\rho u''' v'''} \tag{2.34}$$

which is of an identical form to the Reynolds-stress tensor, the turbulent fluctuations having been replaced by those due to Brownian motion. Now, the kinetic theory of gases can be shown to produce the result

$$t_{xy} = \mu \frac{dU}{dy} \tag{2.35}$$

with the molecular viscosity given by

$$\mu = \frac{1}{2} \rho v_{th} l_{mfp} \tag{2.36}$$

where v_{th} is the internal thermal velocity of the fluid molecules and l_{mfp} the mean free path.

Prandtl proposed that momentum transfer due to turbulence was analogous to the molecular transport of momentum and that turbulent mixing length, l_{mix}, and mixing velocity, v_{mix} could replace l_{mfp} and v_{th} in Eqn.(2.36) to give

$$\tau_{xy} = \frac{1}{2} \rho v_{mix} l_{mix} \frac{dU}{dy} \tag{2.37}$$

where

$$v_{mix} = const \cdot l_{mix} \left| \frac{dU}{dy} \right| \tag{2.38}$$

Eqn.(2.37) can then be simplified to give

$$\tau_{xy} = \mu_t \frac{dU}{dy} \tag{2.39}$$

with μ_t, the eddy viscosity, equivalent to

$$\mu_t = \rho l_{mix}^2 \left| \frac{dU}{dy} \right| \tag{2.40}$$

Turbulence models based upon Prandtl's mixing-length hypothesis are termed algebraic or zero-equation models. Whilst adequate for simple two-dimensional flows, zero-equation models take no account of turbulence history. To rectify this, rather than assuming a relation between v_{mix} and l_{mix}, Prandtl proposed that μ_t be dependent on the turbulent kinetic energy, k, with an additional k equation added to the system, the basis of one-equation models, but a turbulent length scale must still be specified.

Kolmogorov, [62], proposed the first complete model of turbulence by adding a second turbulence equation to solve for ω, the *specific rate of dissipation.* Subsequent turbulence researchers have refined Kolmogorov's initial ideas, the most notable being the addition of a production term and allowance for molecular dissipation, and in recent years models in the k-ω family have enjoyed renewed attention after being overshadowed for a long time by k-ε two-equation models.

To conclude, the Boussinesq approximation with compressibility corrections gives the following relation between the Reynolds-stress tensor, τ_{ij}, and eddy viscosity, μ_t:

$$\tau_{ij} \equiv -\overline{\rho u_i'' u_j''} = 2\mu_t \left(S_{ij} - \frac{1}{3}\frac{\partial \tilde{u}_k}{\partial x_k} - \delta_{ij} \right) - \frac{2}{3}\rho k \delta_{ij} \tag{2.41}$$

where S_{ij} is the mean strain-rate tensor.

$$S_{ij} = \frac{1}{2}\left(\frac{\partial \tilde{u}_i}{\partial x_j} + \frac{\partial \tilde{u}_j}{\partial x_i} \right) \tag{2.42}$$

The turbulent heat-flux vector is dealt with in the same way,

$$q_{tj} = \overline{\rho u_j'' h''} = -\frac{\mu_t c_p}{Pr_t}\frac{\partial \tilde{T}}{\partial x_j} = -\frac{\mu_t}{Pr_t}\frac{\partial \tilde{h}}{\partial x_j} \tag{2.43}$$

where Pr_t is the turbulent Prandtl number, usually regarded as constant for subsonic flows at 0.72. The final unknown in the Favre-averaged equations is the triple correlation, often referred to as a turbulent diffusion term, which is treated as a function of the gradient of k,

$$-\overline{\rho u_j'' u_j'' u_i''} = \frac{\mu_t}{\sigma_k}\frac{\partial \tilde{k}}{\partial x_i} \tag{2.44}$$

2.3 Existing Turbulence Models in NSMB

Only three of the available turbulence models within NSMB have been used within the context of this research: the one-equation model of Spalart & Allmaras and the two-equation models of Hoffman and Chien.

2.3.1 The Spalart-Allmaras model

The one-equation Spalart-Allmaras turbulence model, [113], was formulated as a robust and practical alternative to simple zero-equation, algebraic, models and the far more complex and grid-sensitive two-equation models. The model has four nested versions, the simplest being suitable for free-shear flows and the most complex adequate for treatment of viscous flows past solid bodies or flows incorporating transition. This is achieved by the addition of new terms in the model as the flow increases in complexity. The basic model formulation is given below but for information on the implementation within NSMB, including linearisation for the implicit LU-SGS algorithm, the reader is directed towards the NSMB Handbook, [119].

One-equation models such as Spalart-Allmaras require, as the name implies, solution of one additional turbulence equation. The additional variable is usually $\tilde{\nu}$, giving the following system of six averaged equations (cf. Equations 2.1-2.3):

$$\frac{\partial W}{\partial t} + \frac{\partial}{\partial x}(f + f_v) + \frac{\partial}{\partial y}(g + g_v) + \frac{\partial}{\partial z}(h + h_v) = S \tag{2.45}$$

$$W = \begin{pmatrix} \bar{\rho} \\ \bar{\rho}\tilde{u} \\ \bar{\rho}\tilde{v} \\ \bar{\rho}\tilde{w} \\ \bar{\rho}\tilde{E} \\ \tilde{\nu} \end{pmatrix} \tag{2.46}$$

with the inviscid (convective) fluxes f, g and h and the viscous fluxes f_v, g_v and h_v now given by

$$\begin{gathered}
f = \begin{pmatrix} \bar{\rho}\tilde{u} \\ \bar{\rho}\tilde{u}^2 + \bar{p} \\ \bar{\rho}\tilde{u}\tilde{v} \\ \bar{\rho}\tilde{u}\tilde{w} \\ \tilde{u}\left(\bar{\rho}\tilde{E} + \bar{p}\right) \\ \tilde{u}\tilde{\nu} \end{pmatrix}, \quad f_v = \begin{pmatrix} 0 \\ -\tau_{xx} \\ -\tau_{xy} \\ -\tau_{xz} \\ -\tilde{u}\tau_{xx} - \tilde{v}\tau_{xy} - \tilde{w}\tau_{xz} + \bar{q}_x \\ D_{\tilde{\nu}x} \end{pmatrix} \\
g = \begin{pmatrix} \bar{\rho}\tilde{v} \\ \bar{\rho}\tilde{v}\tilde{u} \\ \bar{\rho}\tilde{v}^2 + \bar{p} \\ \bar{\rho}\tilde{v}\tilde{w} \\ \tilde{v}\left(\bar{\rho}\tilde{E} + \bar{p}\right) \\ \tilde{v}\tilde{\nu} \end{pmatrix}, \quad g_v = \begin{pmatrix} 0 \\ -\tau_{yx} \\ -\tau_{yy} \\ -\tau_{yz} \\ -\tilde{u}\tau_{yx} - \tilde{v}\tau_{yy} - \tilde{w}\tau_{yz} + \bar{q}_y \\ D_{\tilde{\nu}y} \end{pmatrix} \\
h = \begin{pmatrix} \bar{\rho}\tilde{w} \\ \bar{\rho}\tilde{w}\tilde{u} \\ \bar{\rho}\tilde{w}\tilde{v} \\ \bar{\rho}\tilde{w}^2 + \bar{p} \\ \tilde{w}\left(\bar{\rho}\tilde{E} + \bar{p}\right) \\ \tilde{w}\tilde{\nu} \end{pmatrix}, \quad h_v = \begin{pmatrix} 0 \\ -\tau_{zx} \\ -\tau_{zy} \\ -\tau_{zz} \\ -\tilde{u}\tau_{zx} - \tilde{v}\tau_{zy} - \tilde{w}\tau_{zz} + \bar{q}_z \\ D_{\tilde{\nu}z} \end{pmatrix}
\end{gathered} \tag{2.47}$$

and the additional turbulent source term S given by

$$S_{\tilde{\nu}} = \begin{pmatrix} 0 \\ 0 \\ 0 \\ 0 \\ 0 \\ P_{\tilde{\nu}} - \Phi_{\tilde{\nu}} \end{pmatrix} \tag{2.48}$$

The eddy viscosity ν_T is, in turn, given by the following relations:

$$\nu_T = \tilde{\nu} f_{v1}, \quad f_{v1} = \frac{\chi^3}{\chi^3 + c_{v1}^3}, \quad \chi \equiv \frac{\tilde{\nu}}{\nu} \tag{2.49}$$

In Eqn.(2.49), ν denotes molecular viscosity. The term $\tilde{\nu}$ obeys the following transport equation:

$$\begin{aligned} \frac{D\tilde{\nu}}{Dt} &= c_{b1}\left[1 - f_{t2}\right]\tilde{S}\tilde{\nu} \\ &+ \frac{1}{\sigma}\left[\nabla.\left(\left(\nu + \tilde{\nu}\right)\nabla\tilde{\nu}\right) + c_{b2}\left(\nabla\tilde{\nu}\right)^2\right] \\ &- \left[c_{w1} f_w - \frac{c_{b1}}{\kappa^2} f_{t2}\right]\left[\frac{\tilde{\nu}}{d}\right]^2 + f_{t1}\Delta U^2 \end{aligned} \tag{2.50}$$

Where

$$\tilde{S} \equiv S + \frac{\tilde{\nu}}{\kappa^2 d^2} f_{v2}, \quad f_{v2} = 1 - \frac{\chi}{1 + \chi f_{v1}} \tag{2.51}$$

S denotes the magnitude of the vorticity,

$$S = \left[\left(\frac{\partial V}{\partial x} - \frac{\partial U}{\partial y}\right)^2 + \left(\frac{\partial W}{\partial y} - \frac{\partial V}{\partial z}\right)^2 + \left(\frac{\partial U}{\partial Z} - \frac{\partial W}{\partial x}\right)^2\right]^{1/2} \tag{2.52}$$

and d is the distance to the closest wall. The function f_w is given by

$$f_w = g\left[\frac{1 + c_{w3}^6}{g^6 + c_{w3}^6}\right]^{1/6}, \quad g = r + c_{w2}\left(r^6 - r\right), \quad r \equiv \frac{\tilde{\nu}}{\tilde{S}\kappa^2 d^2} \tag{2.53}$$

The wall boundary condition is taken to be $\tilde{\nu} = 0$ and this is generally taken as the freestream value as well. The function f_{t2} is given as

$$f_{t2} = c_{t3} e^{\left(-c_{t4}\chi^2\right)} \tag{2.54}$$

f_{t1} is the *trip function* and can be written as

$$f_{t1} = c_{t1} g_t exp\left(-c_{t2}\frac{\omega_t^2}{\Delta U^2}\left[d^2 + g_t^2 d_t^2\right]\right) \tag{2.55}$$

where d_t is the distance from the point in question to the trip point (on a wall), ω_t is the wall vorticity at the trip point, ΔU is the difference between velocity at the point in question and at the trip. $g_t \equiv min\,(0.1, \Delta U/\omega_t \Delta x_t)$, where Δx_t is the wall grid-spacing at the trip point. Other constants are:

$$\left.\begin{aligned} c_{b1} &= 0.1355 \\ \sigma &= 2/3 \\ c_{b2} &= 0.622 \\ \kappa &= 0.41 \\ c_{w1} &= \tfrac{c_{b1}}{\kappa} + \tfrac{1+c_{b2}}{\sigma} \\ c_{w2} &= 0.3 \\ c_{w3} &= 2 \\ c_{v1} &= 7.1 \\ c_{t1} &= 1 \\ c_{t2} &= 2 \\ c_{t3} &= 1.2 \\ c_{t4} &= 0.5 \end{aligned}\right\} \tag{2.56}$$

2.3.2 The Hoffman k-ε model

The following two sub-sections present the two low Reynolds number k-ε models already in NSMB prior to this research. Neither model solves for the actual turbulent dissipation, ε, but uses instead

$$\tilde{\varepsilon} = \tilde{\varepsilon}_{real} + W_k \tag{2.57}$$

where $\tilde{\varepsilon}$ denotes the isotropic component of the turbulent dissipation and W_k gives $\tilde{\varepsilon}_{wall} = 0$. Further details of their implementation and testing can be found in Ref. [21]. The Hoffman k-ε model is formulated as follows:

Eddy Viscosity

$$\mu_t = C_\mu f_\mu \frac{\bar{\rho}\tilde{k}^2}{\tilde{\varepsilon}} \tag{2.58}$$

Turbulence Kinetic Energy

$$\frac{D\bar{\rho}\tilde{k}}{Dt} = \tau_{ij}\frac{\partial U_i}{\partial x_j} - \bar{\rho}\tilde{\varepsilon} - \frac{\bar{\mu}}{x_j}\frac{\partial \tilde{k}}{\partial x_j} + \frac{\partial}{\partial x_j}\left[\left(\bar{\mu} + \frac{\mu_t}{\sigma_k}\right)\frac{\partial \tilde{k}}{\partial x_j}\right] \tag{2.59}$$

Dissipation Rate

$$\frac{D\bar{\rho}\tilde{\varepsilon}}{Dt} = C_{\varepsilon 1} f_1 \frac{\tilde{\varepsilon}}{\tilde{k}}\tau_{ij}\frac{\partial U_i}{\partial x_j} - C_{\varepsilon 2} f_2 \bar{\rho}\frac{\tilde{\varepsilon}^2}{\tilde{k}} + \frac{\partial}{\partial x_j}\left[\left(\bar{\mu} + \frac{\mu_t}{\sigma_\varepsilon}\right)\frac{\partial \tilde{\varepsilon}}{\partial x_j}\right] \tag{2.60}$$

Auxiliary Relations

$$C_\mu = 0.09, \quad C_{\varepsilon 1} = 1.81, \quad C_{\varepsilon 2} = 2.00, \quad \sigma_k = 2.00, \quad \sigma_\varepsilon = 3.0$$

$$f_\mu = e^{-1.75\left(1+\frac{Re_t}{50}\right)^{-1}}, \quad f_1 = 1.00, \quad f_2 = 1.0 - 0.3e^{-Re_t^2}$$

At the wall,

$$\tilde{k}_{wall} = \tilde{\varepsilon}_{wall} = 0$$

2.3.3 The Chien k-ε model

The Chien k-ε model is formulated as follows:

Eddy Viscosity

$$\mu_t = C_\mu f_\mu \frac{\bar{\rho}\tilde{k}^2}{\tilde{\varepsilon}} \tag{2.61}$$

Turbulence Kinetic Energy

$$\frac{D\bar{\rho}\tilde{k}}{Dt} = \tau_{ij}\frac{\partial U_i}{\partial x_j} - \bar{\rho}\tilde{\varepsilon} - \frac{2\bar{\mu}\tilde{k}}{x_j^2} + \frac{\partial}{\partial x_j}\left[\left(\bar{\mu} + \frac{\mu_t}{\sigma_k}\right)\frac{\partial \tilde{k}}{\partial x_j}\right] \tag{2.62}$$

Dissipation Rate

$$\frac{D\bar{\rho}\tilde{\varepsilon}}{Dt} = C_{\varepsilon 1} f_1 \frac{\tilde{\varepsilon}}{\tilde{k}}\tau_{ij}\frac{\partial U_i}{\partial x_j} - C_{\varepsilon 2} f_2 \bar{\rho}\frac{\tilde{\varepsilon}^2}{\tilde{k}} - \frac{2\bar{\mu}\tilde{\varepsilon}}{x_j^2}e^{-0.5y^+} + \frac{\partial}{\partial x_j}\left[\left(\bar{\mu} + \frac{\mu_t}{\sigma_\varepsilon}\right)\frac{\partial \tilde{\varepsilon}}{\partial x_j}\right] \tag{2.63}$$

Auxiliary Relations

$$C_\mu = 0.09, \quad C_{\varepsilon 1} = 1.35, \quad C_{\varepsilon 2} = 1.80, \quad \sigma_k = 2.00, \quad \sigma_\varepsilon = 3.0$$

$$f_\mu = 1.0 - e^{-0.0115y^+}, \quad f_1 = 1.00, \quad f_2 = 1.0 - 0.22e^{-Re_t^2 \cdot 36^{-1}}$$

At the wall,

$$\tilde{k}_{wall} = \tilde{\varepsilon}_{wall} = 0$$

2.4 The k-ω Family of Models

No turbulence model has yet been proposed that performs well for all aerodynamic configurations and flow conditions. For external aerodynamics, at the time of writing the model of choice is the k-ω-SST model, a hybrid model that attempts to overcome the respective deficiencies of the k-ε and k-ω models by blending them together. This model is known to be particularly capable in capturing flowfields featuring large separated shear layers. Hence, after the first stage of the research was completed, concerning the tangent-ogive geometry, it was decided to implement the k-ω family of models of NSMB and assess their performance for high angle-of-attack forebody flows.

Six versions of the k-ω turbulence model were introduced into NSMB. The standard Wilcox, [122], model is the simplest of these and has being included in both the high *Re* form, with fixed closure coefficients, and the low *Re* form, [11, 123], with closure coefficients dependent on the turbulent Reynolds number. Whilst the k-ω model is extremely accurate and robust in the near-wall region in comparison to the more commonly used k-ε models, it suffers from high dependency on the chosen freestream values of k, the turbulent kinetic energy, and ω, the specific dissipation rate. Menter, [82], attacked this problem by first transforming the k-ε model into a k-ω type formulation before introducing a blending function dependent, among other things, on distance from the nearest wall. The result is a model which acts like k-ω near the wall and k-ε in the freestream. Further to this baseline (BSL) model, Menter then added a shear-stress transport correction to form the k-ω-SST model. The final two k-ω models are simply low-Reynolds number versions of the Menter models, the original Wilcox high Reynolds number coefficients for the inner region being replaced by those from his low Reynolds number model.

2.4.1 The Wilcox k-ω model

The Wilcox k-ω two-equation model is formulated as follows:

Eddy Viscosity

$$\mu_T = \alpha^* \frac{\bar{\rho}\tilde{k}}{\tilde{\omega}} \tag{2.64}$$

Turbulence Kinetic Energy

$$\frac{\partial \bar{\rho}\tilde{k}}{\partial t} + U_j \frac{\partial \bar{\rho}\tilde{k}}{\partial x_j} = \tau_{ij} \frac{\partial U_i}{\partial x_j} - \beta^* \bar{\rho}\tilde{k}\tilde{\omega} + \frac{\partial}{\partial x_j}\left[(\mu + \sigma^* \mu_T)\frac{\partial \tilde{k}}{\partial x_j}\right] \tag{2.65}$$

Specific Dissipation Rate

$$\frac{\partial \bar{\rho}\tilde{\omega}}{\partial t} + U_j \frac{\partial \bar{\rho}\tilde{\omega}}{\partial x_j} = \alpha \frac{\tilde{\omega}}{\tilde{k}} \tau_{ij} \frac{\partial U_i}{\partial x_j} - \beta \bar{\rho}\tilde{\omega}^2 + \frac{\partial}{\partial x_j}\left[(\mu + \sigma \mu_T)\frac{\partial \tilde{\omega}}{\partial x_j}\right] \tag{2.66}$$

Auxilliary Relations

$$\tilde{\varepsilon} = \beta^* \tilde{\omega}\tilde{k}, \quad l = \tilde{k}^{1/2}/\tilde{\omega} \tag{2.67}$$

For the high Reynolds number version of the model, denoted by *2eq-kwwh* in *NSMB*, the closure coefficients are as follows:

$$\alpha^* = 1, \quad \alpha = 5/9, \quad \beta = 3/40, \quad \beta^* = 9/100, \quad \sigma = 1/2, \quad \sigma^* = 1/2 \tag{2.68}$$

The closure coefficients for the low Reynolds number version of the Wilcox model, *2eq-kwwl*, are obtained from the following relations:

$$\begin{aligned}
\alpha^* &= \frac{\alpha_0^* + Re_T/R_k}{1 + Re_T/R_k} \\
\alpha &= \frac{5}{9} \cdot \frac{\alpha_0 + Re_T/R_\omega}{1 + Re_T/R_\omega} \cdot (\alpha^*)^{-1} \\
\beta^* &= \frac{9}{100} \cdot \frac{5/18 + (Re_T/R_\beta))^4}{1 + (Re_T/R_\beta))^4} \\
\beta = 3/40, &\quad \sigma^* = 1/2, \quad \sigma = 1/2, \quad \alpha_0^* = \beta/3 \\
\alpha_0 = 1/10, &\quad R_\beta = 8, \quad R_k = 6, \quad R_\omega = 27/10
\end{aligned} \tag{2.69}$$

where Re_T is the turbulence Reynolds number, defined as:

$$Re_T = \frac{\tilde{k}}{\tilde{\omega}\nu} \tag{2.70}$$

2.4.2 The Menter k-ω-BSL and k-ω-SST models

The philosophy of the blended models of Menter, [82, 83] is to keep the robust and accurate near-wall formulation of the original Wilcox k-ω model whilst improving free-stream independence through use of the k-ε model in the outer part of the boundary-layer. This is done by first rewriting the k-ε model in k-ω form. Compared to the original k-ω model, the differences are the values of the model constants and the presence of an additional (cross-diffusion) term[1]. The two models are then combined by multiplying the original k-ω model by a function F_1, the transformed model by $(1 - F_1)$, and then adding. Obviously the function F_1 is composed so as to be 1 near the wall and zero in the freestream.

Original Wilcox k-ω:

$$\frac{\partial \bar{\rho}\tilde{k}}{\partial t} + U_j \frac{\partial \bar{\rho}\tilde{k}}{\partial x_j} = \tau_{ij}\frac{\partial \tilde{u}_i}{\partial x_j} - \beta^* \bar{\rho}\tilde{\omega}\tilde{k} + \frac{\partial}{\partial x_j}\left[(\mu + \sigma_{k1}\mu_t)\frac{\partial \tilde{k}}{\partial x_j}\right] \tag{2.71}$$

$$\frac{\partial \bar{\rho}\tilde{\omega}}{\partial t} + U_j \frac{\partial \bar{\rho}\tilde{\omega}}{\partial x_j} = \frac{\gamma_1}{\nu_t}\tau_{ij}\frac{\partial \tilde{u}_i}{\partial x_j} - \beta_1 \bar{\rho}\tilde{\omega}^2 + \frac{\partial}{\partial x_j}\left[(\mu + \sigma_{\omega 1}\mu_t)\frac{\partial \tilde{\omega}}{\partial x_j}\right] \tag{2.72}$$

Transformed k-ε:

$$\frac{\partial \bar{\rho}\tilde{k}}{\partial t} + U_j \frac{\partial \bar{\rho}\tilde{k}}{\partial x_j} = \tau_{ij}\frac{\partial \tilde{u}_i}{\partial x_j} - \beta^* \bar{\rho}\tilde{\omega}\tilde{k} + \frac{\partial}{\partial x_j}\left[(\mu + \sigma_{k2}\mu_t)\frac{\partial \tilde{k}}{\partial x_j}\right] \tag{2.73}$$

$$\frac{\partial \bar{\rho}\tilde{\omega}}{\partial t} + U_j \frac{\partial \bar{\rho}\tilde{\omega}}{\partial x_j} = \frac{\gamma_2}{\nu_t}\tau_{ij}\frac{\partial \tilde{u}_i}{\partial x_j} - \beta_2 \bar{\rho}\tilde{\omega}^2 + \frac{\partial}{\partial x_j}\left[(\mu + \sigma_{\omega 2}\mu_t)\frac{\partial \tilde{\omega}}{\partial x_j}\right] + 2\bar{\rho}\sigma_{\omega 2}\frac{1}{\tilde{\omega}}\frac{\partial \tilde{k}}{\partial x_j}\frac{\partial \tilde{\omega}}{\partial x_j} \tag{2.74}$$

---

[1] Menter discards a small additional diffusion term during the transformation.

Blending the above equations using the function F_1 gives the new baseline model, referred to hereafter as k-ω-BSL:

$$\frac{D\bar{\rho}\tilde{k}}{Dt} = \tau_{ij}\frac{\partial \tilde{u}_i}{\partial x_j} - \beta^* \bar{\rho}\tilde{\omega}\tilde{k} + \frac{\partial}{\partial x_j}\left[\left(\mu + \sigma_k \mu_t\right)\frac{\partial \tilde{k}}{\partial x_j}\right] \tag{2.75}$$

$$\frac{D\bar{\rho}\tilde{\omega}}{Dt} = \frac{\gamma_2}{\nu_t}\tau_{ij}\frac{\partial \tilde{u}_i}{\partial x_j} - \beta\bar{\rho}\tilde{\omega}^2 + \frac{\partial}{\partial x_j}\left[\left(\mu + \sigma_\omega \mu_t\right)\frac{\partial \tilde{\omega}}{\partial x_j}\right] + 2\bar{\rho}\left(1 - F_1\right)\sigma_{\omega 2}\frac{1}{\tilde{\omega}}\frac{\partial \tilde{k}}{\partial x_j}\frac{\partial \tilde{\omega}}{\partial x_j} \tag{2.76}$$

The new constants are generated using the relation:

$$\phi = F_1\phi_1 + (1 - F_1)\phi_2 \tag{2.77}$$

where ϕ_1 and ϕ_2 represent constants in the original Wilcox model and transformed k-ε models respectively. The ϕ_1 constants (Wilcox k-ω) are:

$$\sigma_{k1} = 0.5, \quad \sigma_{\omega 1} = 0.5, \quad \beta_1 = 0.0750$$

$$\beta^* = 0.09, \quad \kappa = 0.41, \quad \gamma_1 = \beta_1/\beta^* - \sigma_{\omega 1}\kappa^2/\sqrt{\beta^*}$$

The ϕ_2 constants (standard Launder-Sharma k-ε) are:

$$\sigma_{k2} = 1.0, \quad \sigma_{\omega 2} = 0.856, \quad \beta_2 = 0.0828$$

$$\beta^* = 0.09, \quad \kappa = 0.41, \quad \gamma_2 = \beta_2/\beta^* - \sigma_{\omega 2}\kappa^2/\sqrt{\beta^*}$$

Other definitions are as follows:

$$\nu_t = \frac{\tilde{k}}{\tilde{\omega}} \tag{2.78}$$

$$\tau_{ij} = \mu_t\left(\frac{\partial \tilde{u}_i}{\partial x_j} + \frac{\partial \tilde{u}_j}{\partial x_i} - \frac{2}{3}\frac{\partial \tilde{u}_k}{\partial x_k}\delta_{ij}\right) - \frac{2}{3}\bar{\rho}\tilde{k}\delta_{ij} \tag{2.79}$$

$$F_1 = tanh\left(arg_1^4\right) \tag{2.80}$$

$$arg_1 = min\left[max\left(\frac{\sqrt{\tilde{k}}}{0.09\tilde{\omega}y}; \frac{500\nu}{y^2\tilde{\omega}}\right); \frac{4\bar{\rho}\sigma_{\omega 2}\tilde{k}}{CD_{k\omega}y^2}\right] \tag{2.81}$$

where y is the distance to the closest surface and $CD_{k\omega}$ is the positive part of the cross-diffusion term in the blended specific turbulence dissipation equation:

$$CD_{k\omega} = max\left(2\bar{\rho}\sigma_{\omega 2}\frac{1}{\tilde{\omega}}\frac{\partial \tilde{k}}{\partial x_j}\frac{\partial \tilde{\omega}}{\partial x_j}, 10^{-20}\right) \tag{2.82}$$

The SST model is identical to to the BSL model bar the set 1 constants and the definition of the eddy viscosity. The new constants (SST ϕ_1) are:

$$\sigma_{k1} = 0.85, \quad \sigma_{\omega 1} = 0.5, \quad \beta_1 = 0.0750, \quad a_1 = 0.31$$

$$\beta^* = 0.09, \quad \kappa = 0.41, \quad \gamma_1 = \beta_1/\beta^* - \sigma_{\omega 1}\kappa^2/\sqrt{\beta^*}$$

and the eddy viscosity is now defined as:

$$\nu_t = \frac{a_1\tilde{k}}{max\left(a_1\tilde{\omega};\, |\Omega| F_2\right)} \tag{2.83}$$

where $|\Omega|$ is the absolute value of the vorticity,

$$|\Omega| = \sqrt{\left(\frac{\partial \tilde{w}}{\partial y} - \frac{\partial \tilde{v}}{\partial z}\right)^2 + \left(\frac{\partial \tilde{u}}{\partial z} - \frac{\partial \tilde{w}}{\partial x}\right)^2 + \left(\frac{\partial \tilde{v}}{\partial x} - \frac{\partial \tilde{u}}{\partial y}\right)^2} \tag{2.84}$$

F_2 is given by

$$F_2 = tanh\left(arg_2^2\right) \tag{2.85}$$

where

$$arg_2 = max\left(2\frac{\sqrt{\tilde{k}}}{0.09\tilde{\omega}y};\, \frac{500\nu}{y^2\tilde{\omega}}\right) \tag{2.86}$$

Modifications to the Menter Model have been proposed by Hellsten, [56, 44], to allow inclusion of rough walls and improve the resolution of flows with high streamline curvature but add further complications and have not been considered in this study.

2.5 Implementation of k-ω

2.5.1 Linearisation

Implicit time-integration methods can provide accelerated convergence rates over explicit methods, however, the near-wall grid requirements of two-equation turbulence models mean that pointwise implicit treatment of the source-terms is useful to maintain solution stability. This requires linearisation of the source terms[2]. The source terms are:

$$S_k = P_k - \beta^*\bar{\rho}\tilde{k}\tilde{\omega} \tag{2.87}$$

$$S_\omega = \alpha\frac{\tilde{\omega}}{\tilde{k}}P_k - \beta\bar{\rho}\tilde{\omega}^2 \tag{2.88}$$

where

$$P_k = \tau_{ij}\frac{\partial \tilde{u}_i}{\partial x_j} \tag{2.89}$$

---

[2] As discussed by Duquesne [21], in NSMB the only linearised terms treated implicitly are the negative parts of the terms in the source-Jacobian matrix.

The source-Jacobian matrix is defined as follows:

$$J = \frac{\partial S}{\partial U} = \begin{bmatrix} \frac{\partial S_k}{\partial \bar{\rho}\tilde{k}} & \frac{\partial S_k}{\partial \bar{\rho}\tilde{\omega}} \\ \frac{\partial S_\omega}{\partial \bar{\rho}\tilde{k}} & \frac{\partial S_\omega}{\partial \bar{\rho}\tilde{\omega}} \end{bmatrix} \tag{2.90}$$

In order to linearise the terms within the source-Jacobian, some assumptions have to be made, see Wilcox, [124]:

1. $\tilde{\omega}/\tilde{k}$ remains constant over a timestep.
2. The production term is a direct function of μ_t and is treated as a constant. i.e. $P_k \propto \mu_t$.

Utilising the standard expression for eddy viscosity, Eqn.(2.64),

$$\frac{\partial}{\partial \bar{\rho}\tilde{k}} \left(\bar{\rho}\tilde{k}\tilde{\omega}\right) \equiv \frac{\partial}{\partial \bar{\rho}\tilde{k}} \left[\frac{\bar{\rho}^2\tilde{k}^2}{\mu_t}\right] \equiv \frac{2\bar{\rho}\tilde{k}}{\mu_t} \equiv 2\tilde{\omega} \tag{2.91}$$

and

$$\frac{\partial}{\partial \bar{\rho}\tilde{\omega}} \left(\bar{\rho}\tilde{\omega}^2\right) \equiv \frac{\partial}{\partial \bar{\rho}\tilde{\omega}} \left(\frac{\bar{\rho}^2\tilde{\omega}\tilde{k}}{\mu_t}\right) \equiv \frac{\partial}{\partial \bar{\rho}\tilde{\omega}} \left[\left(\bar{\rho}\tilde{\omega}\right)^2 \frac{const.}{\mu_t}\right] \equiv \frac{2\bar{\rho}\tilde{\omega}const.}{\mu_t} \equiv 2\tilde{\omega} \tag{2.92}$$

Hence the terms in the Jacobian can be written as follows:

$$\begin{aligned} \frac{\partial S_k}{\partial \bar{\rho}\tilde{k}} &= \frac{P_k}{\bar{\rho}\tilde{k}} - 2\beta^*\tilde{\omega} \\ \frac{\partial S_k}{\partial \bar{\rho}\tilde{\omega}} &= 0 \\ \frac{\partial S_\omega}{\partial \bar{\rho}\tilde{k}} &= 0 \\ \frac{\partial S_\omega}{\partial \bar{\rho}\tilde{\omega}} &= \frac{P_k}{\bar{\rho}\tilde{\omega}} - 2\beta\tilde{\omega} \end{aligned} \tag{2.93}$$

2.5.2 Boundary conditions, limits and reference values of k & ω

Choice of the boundary conditions, limits and reference values for k and ω has long been known to be one of the largest obstacles to producing a robust, accurate implementation of the model[3]. The sensitivity to freestream values is well documented, for example [81]. As a result, a large part of the post implementation validation of the k-ω models in NSMB involved ensuring that these key parameters were suitable.

Three validation cases were used to assess the implementation of each of the turbulence models in the k-ω family. These test-cases cover a range of physical conditions

---

[3] Note that superscripts denoting averaged quantities are henceforth omitted for reasons of clarity.

and were also used by Duquesne, [21], in the previous phase of turbulence model implementation. Where possible, solver parameters were kept consistent with these earlier calculations. Appendix A gives the full results from the code validation: data generated with the k-ω models is presented and compared with runs using the one-equation model of Spalart and Allmaras and the low Reynolds-number, two-equation k-ε models of Hoffman and Chien.

Wall boundary conditions For a smooth wall, the value of ρk is simply set to 1×10^{-30} due to the no-slip condition eliminating any velocity fluctuation. However, the boundary condition for $\rho\omega$ is more complicated. Theoretically, as shown by Wilcox, [122, 124], $\omega \to \infty$ approaching a smooth wall since

$$\omega = \frac{2\nu}{\beta^* d^2} \tag{2.94}$$

where d is the distance from the wall and β^* is a model constant (see above). In fact, the Wilcox (and Menter) k-ω models asymptote to

$$\omega \to \frac{7.2\nu}{\beta^* d^2} = \frac{6\nu}{\beta d^2} \tag{2.95}$$

where β is a model constant. The high gradient of ω near the wall can be the source of much numerical error and excessive grid dependence and several methods for determining appropriate wall values have been suggested, see [124, 43]. The method used, however, is that suggested by Menter, [82, 83], where ω at the point adjacent to the wall is evaluated using Eqn.(2.95) and then multiplied by 10 to provide a surface value,

$$\omega_w = 10\frac{6\nu}{\beta d_{1/2}^2} \tag{2.96}$$

A simple extrapolation is then performed to calculate ω for the first ghost-cell, this value also being copied into the second layer.

Freestream Values & lower limits of k and ω Freestream values of k and ω were initially calculated using the method proposed by Menter, [82, 83],

$$\begin{aligned} \omega_\infty &= \mathit{constant} \times U_\infty / L_{ref} && (2.97)\\ \nu_{t\infty} &= 10^{-3}\nu && (2.98)\\ k_\infty &= \nu_{t\infty}\omega_\infty && (2.99) \end{aligned}$$

where the constant is taken to be 1.0 by default but is user-defineable if need be. L_{ref} is also user-defineable but by default is set to 1. After testing it was found that this simple setup was inadequate, with a massive over-prediction of boundary-layer thickness. The problem was eliminated by first setting a minimum value of 10 for ω_∞. Turbulent Reynolds number is then calculated and, if greater than 10^{-10}, k_∞ is divided by 10 until

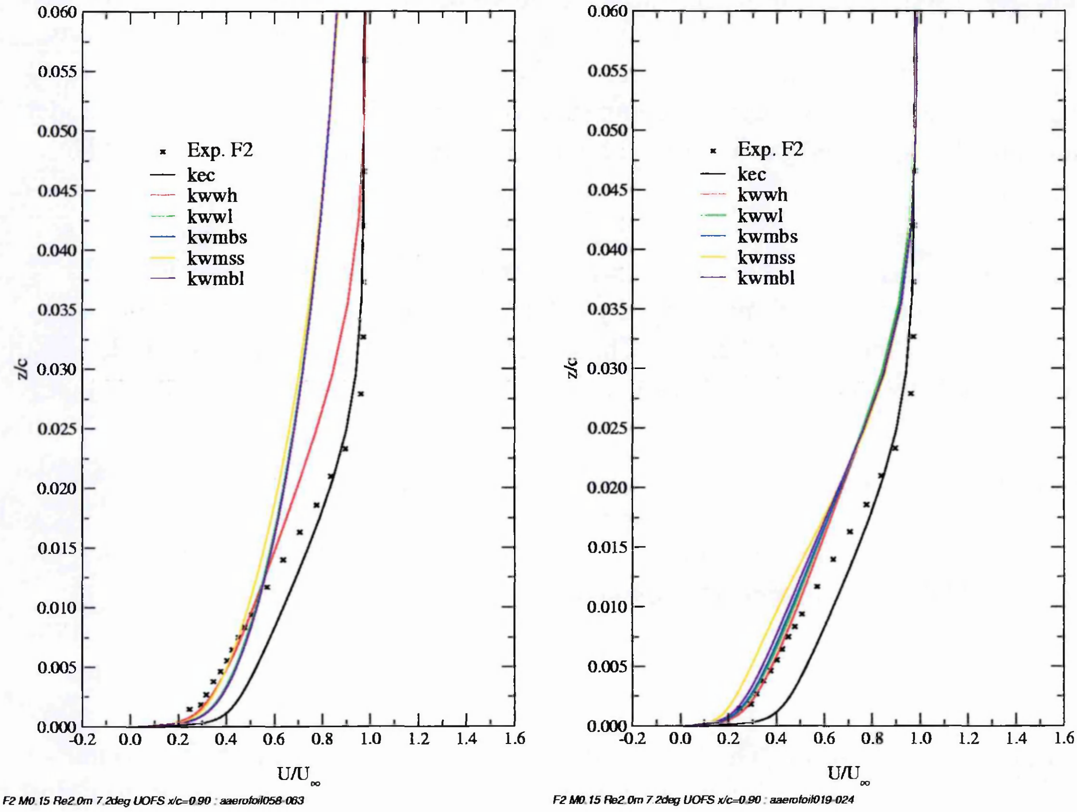

(**a**) Original method (Menter)

(**b**) Modified method

Figure 2.1: *Comparison of original Menter method for calculating freestream values with adjusted method including restrictions on minimum* ω_∞ *and* Re_t. *A-aerofoil,* M=0.15, *Re*=2.0*m*, α=7.2°, *x/c*=0.9.

$Re_t < 10^{-10}$. Boundary-layer profiles for the A-aerofoil illustrating these two freestream treatments are shown in Fig.(2.1). It should be noted when viewing these figures that no transition position was prescribed for the calculations.

In order to aid code stability and robustness, it is common practice to impose certain upper and lower limits on the turbulent variables. NSMB employs a μ_t limitation as an upper limiter but the choice of the lower limits and the treatment of the variable updating is worth mentioning. Initial thoughts were to simply reset both k and ω to freestream values should either of them fall below these levels. This method is used for the k-ε and k-τ two-equation models in the code without any problems. However, it was found that using dual updating of the turbulence variables for k-ω could cause convergence problems for some cases. No differences were evident between the two methods when running the flat plate testcases but, as can be seen from Fig.(2.2), dual updating resulted in major oscillations in the residuals. Switching to individual updating stabilised the convergence markedly.

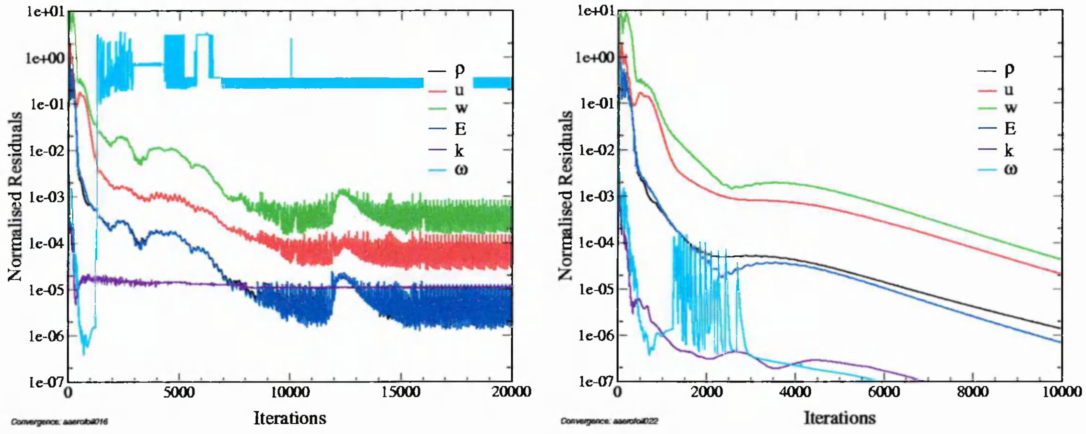

(a) A-aerofoil, dual updating

(b) A-aerofoil, individual updating

Figure 2.2: Comparison of the effect of dual and individual updating of the k and ω variables at their lower limits. A-aerofoil, F2 tunnel conditions, $\alpha = 7.2^o$, k-ω-SST model.

2.5.3 Other notes on implementation

Other implementation details worth noting are the omission of a production term limiter, the treatment of the cross-diffusion term and the method of calculation for the convective flux in the k and ω equations.

For the k-ε models, NSMB limits the turbulence production term to 10 times the dissipation in order to aid code stability. It was assumed that this would also be necessary for the Wilcox k-ω models and the baseline Menter model without the SST limitation. However, testing showed this not to be the case and no production limiter was included.

The method of calculation of the cross-diffusion term $CD_{k\omega}$ in the original Menter blended models was found by Hellsten, [44], to lead to a rise in the blending function F1 back towards 1.0 at the outer edge of the boundary-layer. Hellsten linked this behaviour to the use of $CD_{k\omega_{min}} = 10^{-20}$ and proposed instead that $CD_{k\omega_{min}} = 10^{-8} \times CD_{k\omega_{max}}$. This minor modification was included in the NSMB implementation with the blockwise value of $CD_{k\omega_{max}}$ being used rather than the maximum for the whole flowfield for ease of coding.

Finally, it is worth noting that testing showed the models to be far more stable when utilising first-order upwind differencing for the convective parts of the k and ω equations instead of second-order central differencing. As shown previously by Jongen, [54], and confirmed by Duquesne, [21], this results from the elimination of transient negative values of k or ω. Hence, first-order upwind differencing has been set as the default for the k-ω family, central differencing being retained as a user-specified option.

2.6 Numerical Method

2.6.1 Spatial discretisation

NSMB employs the finite-volume method as devised by McDonald, [80], and MacCormack & Paullay, [74], and extended into three-dimensions by Rizzi & Inoue, [107]. A number of spatial discretisation approaches are available in the code including standard central differencing and variations on the upwind Roe Scheme. Full details of these methods are given in the NSMB Handbook, [119].

2.6.2 Boundary conditions

As is usual for finite-volume codes, boundary conditions in NSMB are imposed using *ghost cells* existing outside the actual computational domain. The Navier-Stokes equations are not solved in these exterior cells, the values of W, the state vector, being calculated from the user specified boundary conditions, whether physical or numerical. If the central differencing used for the physical boundary condition is considered, it is clear that only one exterior cell is necessary in order to evaluate all the interior cells. However, two layers of ghost cells are required due to the use of artificial dissipation terms in the scheme.

NSMB has a large variety of boundary conditions available to cope with most flow situations. The conditions that were used in this research are as follows:

bc130: Freestream conditions As would be expected, when a freestream boundary condition is applied at a boundary, the ghost cells are filled with freestream values of the state vector.

bc131: Characteristic variables bc131 is a freestream or artificial far-field boundary condition. It has the necessary property that waves leaving the computational domain are, for the most part, not reflected - this being important for convergence to steady state. This is achieved by extrapolating the physical variables using characteristic variables. The method will not be discussed here, for further information consult either the NSMB Handbook, [119], or Hirsch, [47].

bc220: Linear extrapolation When linear extrapolation is employed as a boundary condition, the variables in the ghost cells at the boundary are calculated by linearly extrapolating values from the two cells immediately inside the domain. This is generally used as a subsonic boundary condition.

bc300: Solid wall bc300 comprises the standard slip condition that should be applied to a solid boundary. This simply specifies that for Euler calculations the normal component of the velocity at the wall is zero or for Navier-Stokes calculations that the velocity component in each direction at the wall is zero and is the only physical boundary condition required. The pressure in the first layer of ghost cells is found by linear extrapolation for inviscid flows and for viscous flows is set equal to the pressure in the first interior cell, thus setting the normal pressure gradient to zero. These values are then copied into the second layer of ghost cells.

When considering the correct numerical boundary condition for the artificial dissipation, problems arise due to there being no 'physical' values. The solution is to set the surface dissipative flux to zero.

bc450: Degenerated face The degenerated face boundary condition can be used to specify a singular line in a C-O type grid. Values in the two layers of ghost cell are simply set to be identical to the corresponding two layers of cells inside the block boundary.

2.6.3 Time integration

Time integration of the equations is achieved using either an explicit multi-stage Runge-Kutta scheme or an implicit LU-SGS or LU-SSOR scheme. The Runge-Kutta scheme has good stability and is symmetric, a valuable property in the context of this research. Unfortunately, solution times are too great to make it a practical proposition on large three-dimensional geometries.

NSMB also allows use of the implicit LU-SGS scheme of Yoon and Jameson, [126, 52, 53], LU-SGS standing for Lower-Upper Symmetric-Gauss-Seidel. Separate space- and time-discretisation ensures that the steady-state solution evolves independently of the time-step which, in turn, allows use of extremely high CFL numbers. Both scalar and full matrix versions of the scheme are available. Full details are available in the NSMB Handbook, [119].

2.7 The Solution Process

2.7.1 Computational hardware

For CFD to be a viable design and evaluation tool, it is necessary to have solution turn-around times of the order of a day or, preferably, overnight. This requirement has always limited the complexity of the problems for which industry can use the techniques. However, computer power has (in 2001) now advanced to the level where numerical solution of viscous three-dimensional flow over complex aerodynamic configurations is possible using high-powered multi-processor supercomputers.

At the start of this research program, the only available 'high-performance' computing facility was the Cranfield J916. This, rather feeble machine, comprised four processing elements (PEs) with 512Mb RAM with performance of 200Mflop/PE and proved adequate at best for the initial work: solutions on the preliminary tangent-ogive test-grid of 333,684 cells were obtained after between one and two weeks of continuous run-time on one PE. The situation improved at the beginning of April 1998 when access was granted to a 3 processor Fujitsu VX/3 vector supercomputer at KTH, Stockholm, and the Cray T3E at the Swedish National Supercomputer Centre, Linköping.

The Fujitsu VX/3 has 3 processing elements each comprising a scalar and vector unit with a peak performance of 2.2 Gflop/s and 2Gb memory. Memory throughput is 36.4 Gb/s. The operating system is UXP/V, based on UNIX System V rel. 4, with queuing managed by NQS.

Unlike the Fujitsu, the T3E is a massively parallel system comprising lower powered processors connected together via a high bandwidth network in a 3-dimensional torus. The processors are DEC Alpha EV5 300MHz which are capable of two floating point operations per cycle to give peak performance of 600Mflop/s per PE used. 256 application PEs are available on the NSC machine, of which 100 are equipped with 256 Mb memory and the remainder with 128Mb.

Aside from the numerical solution process, computer power is also required for the pre- and post-processing of data. Pure CPU speed is of reduced importance for these applications, however, the requirement for high-performance graphics with rapid refresh-rates means that specialised graphics workstations with memory capable of handling the large 3-D grids and solution datasets are vital. For this research, all pre- and post-processing of data was performed on an SGI Octane workstation equipped with twin 195Mhz R10000 processors, SI graphics and 1Gb RAM.

For completeness, it can be noted that the implementation and initial testing of the k-ω models was carried out on a 350 MHz Linux PC with 256Mb RAM.

2.7.2 Grid generation

The grid generation process for the tangent-ogive grids was carried out using Geomesh, a licenced version of the ICEMCFD suite of packages produced specifically for Fluent Inc.. Subsequently, withdrawal of Fluent support for Geomesh led to the purchase of the full ICEMCFD software and its use for all the JAS-39 Gripen meshes. As mentioned above, grid-generation was performed on an SGI Octane graphics workstation.

Geometry definition and development of the surfaces was done within the ICEMCFD DDN module, a fully featured CAD package. In the case of the JAS-39 meshes, this stage was simplified by the provision by Saab of an IGES file containing a CAD surface model of the clean forebody. This was cleaned up to remove surface holes and overlaps before the block structure and outer domain were developed.

Within P-Cube, the structured multi-block meshing module, block faces were mapped to the relevant CAD surfaces to produce a mesh accurately following the body contours. For the more complex curvatures of the JAS forebody, the success of this operation proved to be heavily dependent on the block topology and edge-of-face node clustering chosen. Where necessary, faces were split down into subfaces to increase the level of control possible.

2.7.3 Database generation & domain decomposition

In the majority of computational fluid dynamic codes data is handled using a series of files, each one covering one aspect such as surface grid geometry, mesh coordinates or flow solution. NSMB is different from such codes in that it uses a database system called MEM-COM, [1]. MEM-COM is a data management system for memory and memory-to-disk data handling. It contains several data access tools, including a database manager, a relational table manager and a network manager. With the MEM-COM system, all data pertaining to any particular calculation, or series of calculations on the same problem, is stored in a single binary database file. This file contains several datasets which may be accessed independently and are of two types: datasets used to store variables such as velocity data or pressure; relational table datasets used to store key parameters. Hence all the information necessary to describe fully the flow simulation is kept together readily available.

The main advantage of the MEM-COM system is that all data for a simulation is stored in one file. Data exchange during the solution generation and visualisation process is performed using the database. Modification of data contained within the database is also fairly simple using the *monitor* tool.

When using ICEMCFD for grid-generation, creation of the MEM-COM database for NSMB is carried out using the NSMB utilities *nsmbtopo* and *icemtomemcom*. These utilities take the ICEM topo_mulcad_out and domain files and, after user-input definition of the non block-connectivity boundary-conditions, produce a clean database file containing coordinate and topology information.

Domain decomposition for computation on parallel machines is achieved using MB-Split, [127], a multi-block partitioning and load-balancing tool for structured grids. MB-Split allows any grid to be partitioned and optimally load-balanced according to the performance of the computational facilities on which the problem is to be run. The existing blocks are split and a load-balance file produced which can be read by NSMB in the run-initialisation phase. Alternatively, the load-balance file can be omitted and NSMB allowed to distribute the blocks around the desired number of computational nodes using internal routines. The parallelisation of NSMB was initially facillitated using PVM but all versions since NSMB 4.5 employ MPI.

2.7.4 Problem definition

Having generated the problem database and performed any necessary domain decomposition, the problem itself can be defined. NSMB requires a single main input file containing information on the database to be used, the flow conditions, viscous model and various solver parameters. The input file is organised on a *keyword: value* basis and, aside from parameters such as Mach number and Reynolds number which, obviously, have to be included, default values are used for all other options unless otherwise specified. This has the benefit of keeping input files short and minimising setup error. Sample input files can be found in Appendix A.

When required, additional input files are used for prescribing transition locations, time-dependent boundary-conditions and so on.

2.7.5 Flow visualisation & data reduction

The visualisation of the computational results and their extraction and reduction into forms suitable for comparison with wind-tunnel or empirical data was achieved using several different packages over the course of the research. Of these, the simplest was the NSMB utility *rensmb*, useful for rapid extraction of two-dimensional data such as boundary-layer profiles or circumferential pressure coefficient distributions. Whilst convenient, this utility is restricted to extraction along coordinate directions with no capacity for interpolation. For visualisation of the three-dimensional results, the commercial packages *Fieldview* and, in the later stages of the work, *EnSight* were employed. Features such as particle path tracing and the generation of surface streaklines, comparable to the oil-flow wind-tunnel visualisation technique, prove invaluable in assessing three dimensional flows. Both these packages are tremendously powerful tools and the use of restart files enabled identical data extraction and visualisation procedures to be performed quickly in batch-mode on multiple datasets. Two-dimensional graphing was entirely carried out using the freeware packages *Gnuplot* and *Grace* for IRIX or Linux.

3. Tangent-Ogive Forebody

Computational fluid dynamics solvers vary tremendously in their capability. Differences in the choice of numerical method or its implementation within the software can result in superficially similar codes behaving quite differently when applied to the same problem. The initial literature review, carried out before any computational work was attempted, highlighted several areas where potential difficulties might arise. As a result, the first stages of the research comprised a thorough evaluation of the capabilities of the existing code for the high-α flow about a simplified representative geometry, the tangent-ogive/cylinder. The following chapter covers this work, including attempts to generate asymmetry through the addition of tip excrescences and the use of a non-symmetric solution algorithm.

Rather than attempting to model mixed laminar/turbulent, asymmetric, vortical flow on a realistic combat-aircraft forebody geometry from the start, it was thought that a more sensible approach would be to increase the difficulty of the problem in stages. Simplification of the problem geometry to the ubiquitous tangent-ogive/cylinder combination was the obvious first step. As can be seen from the literature survey in Chapter 1, this particular body of revolution has been utilised many times before as a generic forebody. As well as being geometrically simple, it demonstrates all the aerodynamic characteristics that might be found on more realistic forebodies and is easy to machine, in the case of wind-tunnel models, or mesh, in the case of computational models. Additionally, when dealing with a realistic fighter forebody, flow characteristics may result which are particular to that one specific geometry and reduce the global relevance of the results.

Unfortunately, the nature of the forebody problem means that no further spatial simplifications are possible. Whilst the streamwise development of the vortical wake of a cone/cylinder or ogive/cylinder in planes normal to the axis of the body of revolution has been likened to the time-development of Kármán shedding from a circular cylinder, it was felt that two-dimensional cylinder calculations would achieve little. Similarly, use of a fully three-dimensional FANS code, such as NSMB, was seen as the only solver option. As discussed in Chapter 1, although Siclari & Marconi, [108], and Kandil, Wong & Liu, [55], computed asymmetric forebody flow using a Conical RANS code, the work of Thomas, [115], introduced the possibility that this was only achieved because of the effective elimination of the three-dimensional terms, a view shared by Levy *et al.*, [73][1].

---

[1] Although not of concern here, the same could be said to be true of results obtained at higher Mach numbers using PNS solvers.

3.1 Experimental Reference

Surprisingly, given the number of aeronautical applications where tangent-ogive-type forebodies are employed, very few comprehensive experimental databases exist in the public domain. Most computational work on this type of forebody geometry has thus been benchmarked against the work of Lamont, [67, 69], which has, as a consequence, become a standard experimental reference for the problem.

Lamont's experiments of the late 1970's and early 1980's were carried out in the 12ft low turbulence wind tunnel at NASA Ames Research Centre. The first phase of the work, documented in [67], involved tests on a 2.0D tangent-ogive of 152.4mm (6in) diameter mated to a 13.0D afterbody, the pitching axis located at 8 diameters from the nose. The second phase, documented in [69], involved the same cylindrical afterbody used in the first series of tests but this time with a tangent-ogive of increased fineness ratio, 3.5D. The model included 420 pressure tappings distributed at 12 axial locations at a separation of 0.5 diameters: 24 tappings (15^o intervals) at 0.5D from the nose and 36 pressure tappings (10^o intervals) at each subsequent downstream station, see Fig.(3.1). An alpha sweep of $20 \leq \alpha \leq 90^o$ was made for 9 Reynolds numbers with respect to base diameter between $2 \times 10^5 \leq Re_D \leq 4 \times 10^6$. With knowledge of the importance of the tip geometry, Lamont also tested at least 12 different roll orientations for most combinations of α and Re_D. It is this second phase of tests, on the more slender 3.5D ogive, which was chosen as the experimental reference for this part of the research.

It should be noted at this point that the data taken by Lamont was earmarked for a NASA report where it would have been presented in tabulated form. This, unfortunately, was never released. Much of the recent research into forebody aerodynamics has been carried out under the auspices of NASA and, as a result, access to the raw Lamont data was not a problem. This was not the case with this research, thus all experimental pressure and force data was extracted from the two original Lamont papers and other reports referencing his data that are available in the public domain.

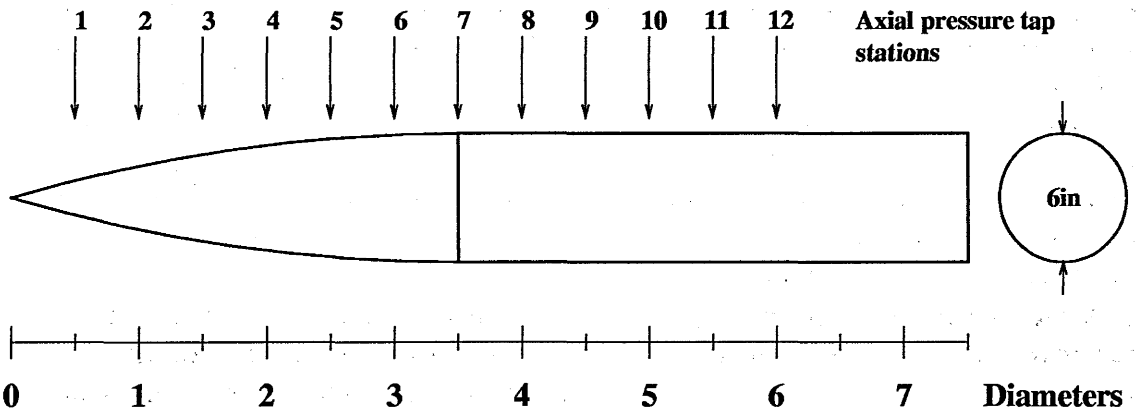

Figure 3.1: The tangent-ogive/cylinder geometry of Lamont, [69].

3.2 Computational Details

3.2.1 Grid generation

Computational facilities at the first stage in the research were initially limited to use of a single node on the Cranfield Cray J916 computer, hence limiting the number of finite-volume cells was of paramount importance in order to reduce job turn-around times to acceptable levels. For this reason, the first grid generated which was actually used in a calculation, this grid hereafter being referred to as ogive3, should be regarded as a development grid. For grid ogive3, Lamont's full test geometry was truncated to a 3.5D tangent-ogive forebody mated to a 3.5D afterbody giving a total model length of 1066.8mm. To keep things simple at this early stage, the chosen topology was H-O with the upstream extent of the domain 1.75D from the apex of the nose and the rear of the domain extending 15 diameters from the surface of the body. Grid size was 62 × 69 × 78 cells in the axial, radial and circumferential directions respectively to give a total grid size of 333,684 cells, see Fig.(3.2(a)).

As mentioned in Chapter 2, meshing for this stage of the work was performed using Geomesh, the Fluent Inc. version of the ICEMCFD structured grid generation package. For ogive3 and all subsequent tangent-ogive meshes, a half-forebody grid was generated and then mirrored to produce a single-block grid with a periodic boundary-condition. Thus, whilst not axisymmetric, all the tangent-ogive meshes are symmetric about the pitching plane. In retrospect, generating a 2-dimensional slice and then rotating it through 360^o to generate a full 3-dimensional mesh might have been easier and eliminated the possibility of any small geometric discrepancies arising due to the surface mapping process. However, given the results subsequently obtained with the controlled insertion of surface excrescences, it is felt that use of this method would have had little bearing on the solution.

The choice of an H-O topology made modification of ogive3 to model the effect of small tip excrescences relatively simple. A small *fortran* routine was written to take the mirrored grid and introduce a geometric perturbation by radially displacing two surface vertices at the first station downstream of the apex of the forebody, see Fig.(3.3). Three modified grids were created with a small bump at 90^o to the windward meridian, the cell vertices being displaced 0.1mm, 0.5mm and 1.0mm respectively. Vertex displacement was continued into the farfield to increase grid smoothness, the amount of movement being reduced with distance away from the axis. A close-up of the modified nose with a 1.0mm bump is shown in Fig.(3.4).

After several calculations using ogive3, it was decided that the outer boundary might be suppressing any possible asymmetric solution and/or distorting the vortex flowfield. It was felt that the farfield boundary was positioned far too close to the body for the Mach numbers being calculated and so a new grid, ogive4, was generated with a significantly extended farfield, see Fig.(3.2(b)). The main differences between this grid and its predecessor are the increase in domain extent forward of the apex and the increase of grid frontal area. Grid dimensions were 66 × 68 × 77 to give a total of 345,576 cells.

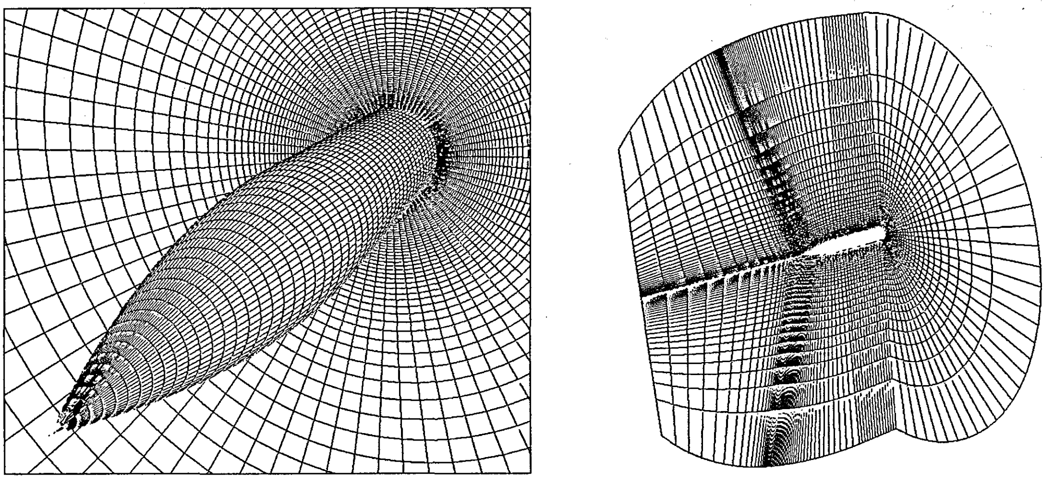

(a) Ogive3, H-O type.

(b) Ogive4. H-O type.

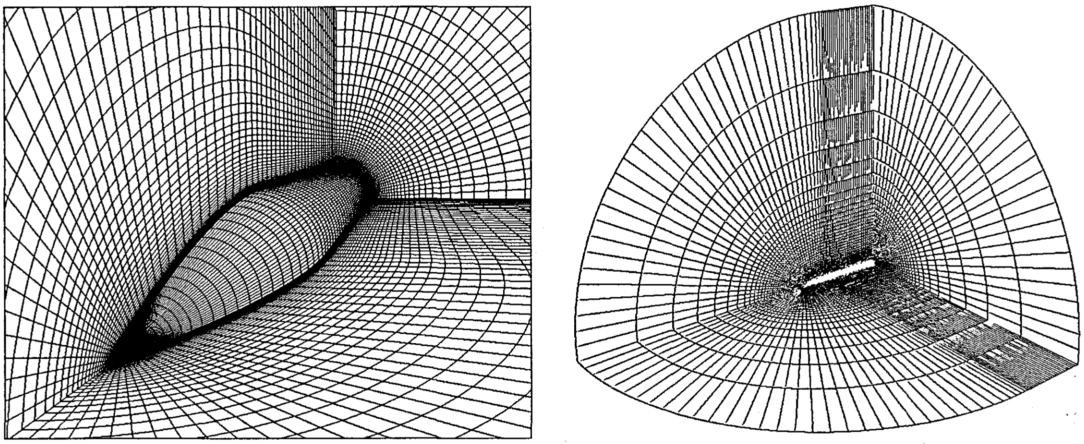

(c) Ogive5, C-O type, close-up.

(d) Ogive5, C-O type, farfield.

Figure 3.2: *Comparison of tangent-ogive/cylinder grids: Ogive3, H-O type,* 62 × 69 × 78 *cells; Ogive4, H-O type,* 66 × 68 × 77 *cells; Ogive5, C-O type,* 60 × 80 × 120 *cells.*

For the final iteration of the tangent-ogive grid, ogive5, a C-O topology was employed. Choosing this topology had the benefit of allowing increased cell density near the surface of the body whilst reducing the numbers of 'wasted' cells in the farfield. It was at this point in the research that access was made available to high-performance computing facilities at Kungliga Tekniska Högskolan (KTH), The Royal Institute of Technology, Stockholm, Sweden. With the prospect of increased job-throughput, ogive5 was generated with an increased resolution of 60 × 80 × 120 to give a grid size of 576,000 cells. At the same time, the cylindrical afterbody was extended by 3 base-diameters and the farfield boundary was formed as a hemisphere-cylinder with a radius of $R_{max}/D = 30$ to allow the use of a freestream farfield boundary condition. Cells were clustered axially as well as radially but circumferentially they were maintained at a fixed 3^o separation. Two views of the grid are shown in Figs.(3.2(c)) & (3.2(d)).

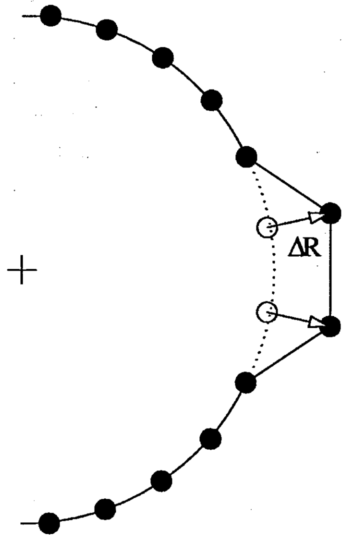

Figure 3.3: Schematic of radial node movement to produce bump.

3.2.2 Coordinate system

The orientation of the axes was consistent between all tangent-ogive grids and is shown in Fig.(3.5). The periodic boundary was located in the x-y plane. Angular position θ is measured clockwise from top dead-centre looking aft.

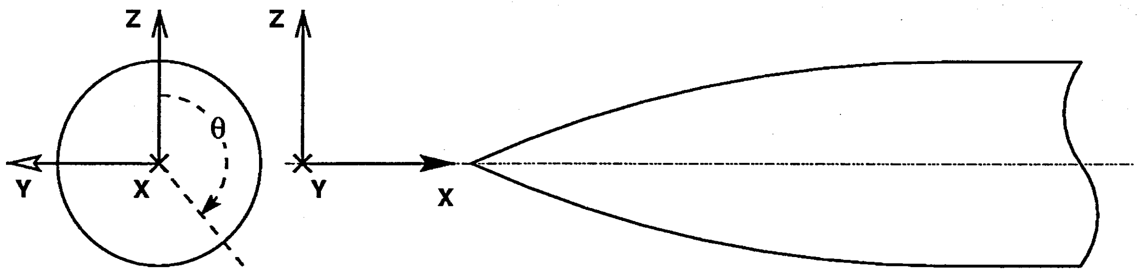

Figure 3.5: Axes orientation, tangent-ogive grids.

3.2.3 Boundary conditions

For the H-O type grids, ogive3 and ogive4, a characteristic variables boundary condition was applied at the farfield boundary with a linear extrapolation at the exit. For the later

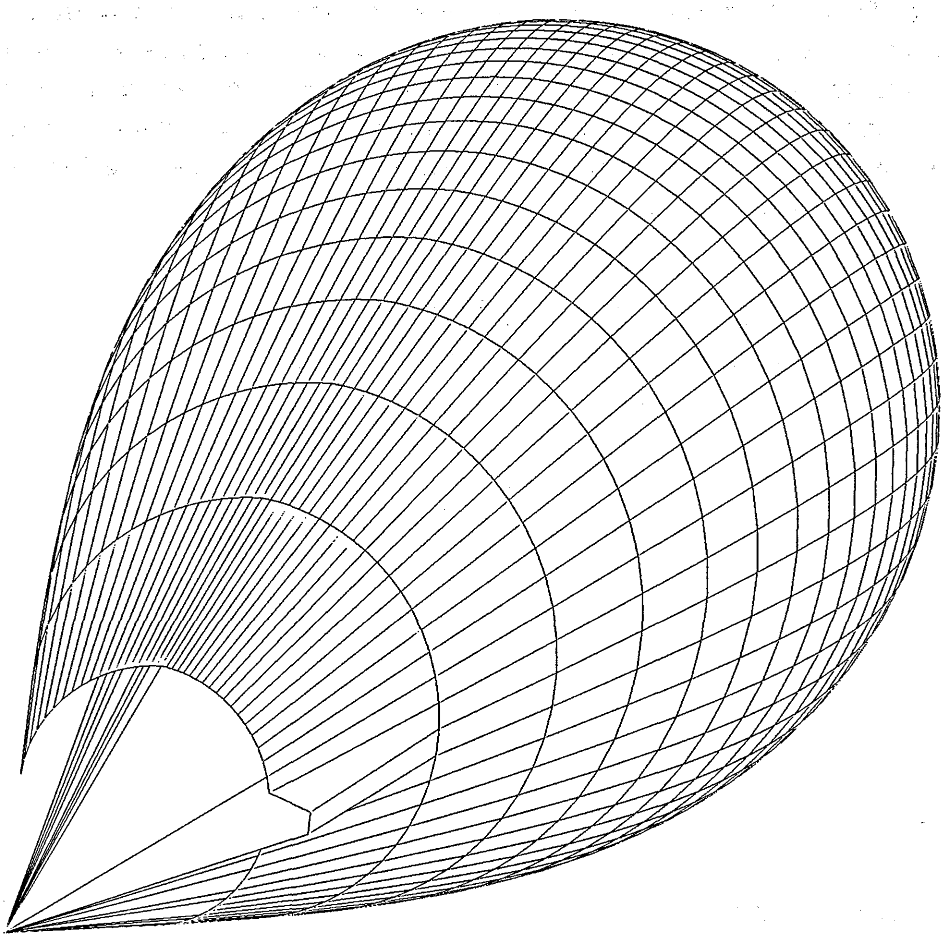

Figure 3.4: Close-up of ogive3 nose-region modified with 1mm bump (h/D=0.0066).

calculations, run on the larger C-O type grid, ogive5, the outer domain was extended sufficiently to enable freestream values to be set as the farfield boundary condition. The exit condition was again a simple linear extrapolation but, as mentioned above, the cylindrical afterbody was extended by a further 3.0 diameters to minimise the influence of this on the formation and development of the vortices. A characteristic variables condition at the exit proved to be unsuitable.

3.2.4 Flow conditions

Two sets of flow conditions for the tangent-ogive computations were chosen from the experimental database of Lamont, [67, 69], and are tabulated in Table (3.1). According to the critical Reynolds number-incidence boundaries experimentally defined by Lamont and discussed further by Poll, [104], Case 1 conditions correspond to laminar flow at separation, see Fig.(1.5). It can be seen from the same figure that, for $\alpha = 40^o$, Case 2 conditions lie on the cross-flow transition boundary, where it can be assumed that the flow has transitioned to turbulence before separation. It should be noted that the above refers solely to the Reynolds number calculated with respect to base diameter, Re_D, and does not take into account the axial variation in Reynolds number based on local body diameter, Re_d - see Subsection (1.1.3).

	Case 1	*Case 2*
Re_D	200,000	800,000
Re/m	1,312,336	5,249,344
$Mach\ No.$	0.2	0.2
$\rho_\infty\ (kg/m^3)$	0.300	1.198
$P_\infty\ (Pa)$	24629	98514
$T_\infty\ (K)$	286.6	286.6
$a_\infty\ (m/s^2)$	339.346	339.346
$U_\infty\ (m/s)$	67.9	67.9

Table 3.1: *Flow conditions, tangent-ogive computations.*

3.3 Preliminary Calculations

Before investigating methods of achieving a stable asymmetric solution, it was decided that the first calculations should use a basic solver setup and a simple, symmetric grid in order to provide a baseline for the subsequent work. Having generated the single-block ogive3 grid, four computations were run under Case 1 conditions: two at 40^o; two at 60^o. The first computation at each angle was run with α being set to the desired value of incidence and β, the sideslip angle, being kept at zero. This put the periodic boundary on one side of the body, normal to the x-z pitching plane. For the second run at each angle-of-attack, the sideslip angle β was used to angle the body into the wind, α being set to zero, moving the periodic boundary to lie along the pitching plane. This would eliminate a possible source of asymmetry in the problem setup and allow evaluation of the effect, if any, of the positioning of the periodic boundary.

Although Case 1 conditions should mean laminar flow at separation, it was decided to run fully turbulent with the Spalart-Allmaras model due to the high angles-of-attack being considered. This model was expected to prove superior to the Baldwin-Lomax/Degani-Schiff model commonly used for this problem. The explicit RK-4 time-stepping algorithm was selected together with central spatial discretisation. The standard artificial dissipation model was used until the normalised density residual had dropped to approximately 0.5×10^{-3} when it was replaced by the Martinelli model, [79]. Despite the low Mach number, the artificial viscosity coefficients were set relatively high in order to aid convergence. The effect of reducing these values to more reasonable levels was examined later.

As can be seen from the force and moment figures tabulated in Table (3.2), all four solutions were symmetric, variation of the location of the periodic boundary having no appreciable effect.

In order to ensure the solution was totally stable, the $\beta = 40^o$ ogive3001 calculation was continued to a total of 105000 iterations, about 14 days run time on the single J916 node, as ogive3005. The value of *resl2*, the normalised density residual, reached 0.2354e-08, the maximum residual being 0.8006e-01. The convergence history is shown in Fig.(3.7(a)). At this point, convergence at about 4 orders beyond what is usual, the solution was stable and symmetric. This was expected given the explicit RK4 time-stepping algorithm. Forces and moments for this continued calculation are tabulated in Table (3.3).

Run No.	α	β	Boundary	Initialised	# Its.	Resl2
ogive3001	40^o	0^o	side	freestream	55,000	0.2843E-04
ogive3002	60^o	0^o	side	ogive3001	60,000	0.8029E-04
ogive3003	0^o	40^o	bottom	freestream	45,000	0.3104E-04
ogive3004	0^o	60^o	bottom	freestream	30,000	0.9006E-03
Run No.	C_x	C_y	C_z	C_{Mx}	C_{My}	C_{Mz}
ogive3001	0.0353	0.0000	0.0485	0.0000	-0.0694	0.0000
ogive3002	0.0783	0.0003	0.0589	0.0003	-0.1138	0.0002
ogive3003	0.0354	0.0486	0.0000	0.0000	0.0000	0.0695
ogive3004	0.0757	0.0572	0.0000	0.0000	0.0000	0.1073

***Table 3.2:** Preliminary tangent-ogive computational details.*

3.4 Addition of Surface Excrescence

Having computed a symmetric flowfield on the symmetric grid at 40^o[2], three computations were run to investigate the effect of adding small geometric perturbations of varying magnitudes near the apex of the forebody. As discussed in Chapter 1, this method of promoting vortex asymmetry was first used by Degani *et al.*, (following on from the small air jet they had initially tried), and works by causing the tip vortex on the side of the excrescence to separate from the surface immediately after formation. Degani *et al.* found that the addition of a surface anomaly, large locally but small compared to the maximum body diameter, could cause large-scale asymmetry over the entire length of the body.

NSMB was then run past each grid, using the highly converged symmetric grid solution as the starting point and an unchanged solver setup. Each computation was continued until the *resl2* value had dropped to below 0.1e-7, a level of convergence much greater than that required for stable force coefficients as previously demonstrated. Density residual convergence histories for the three calculations are shown in Fig.(3.6(a)).

---

[2] Henceforth, incidence will be referred to as α, regardless of grid orientation.

Calculations ogive3001-ogive3004 were made with the second order artificial viscosity set to 0.5 in all three directions. Under the flow conditions used, this should not have been necessary to aid convergence but may have had some effect on the final flow solution. As a result, the four computations listed in Table (3.3) were all run with the second order viscosity removed. This seemed to have no effect on convergence speed or the nature of the final solution: forces for run ogive3003 (with second order artificial viscosity) and ogive3005 (the continuation of the ogive3003 calculation with second order artificial viscosity removed) are identical to within 10^{-4}.

Run no.	α	Bump	% D	Total # Its.	Resl2	C_y	C_z
ogive3005	40°	No	-	105,000	0.2354E-08	0.0000	0.0486
ogive3006	40°	1.0mm	0.66	153,000	0.3302E-08	-0.0452	0.0594
ogive3007	40°	0.5mm	0.33	150,000	0.5194E-08	-0.0476	0.0593
ogive3008	40°	0.1mm	0.07	150,000	0.1833E-08	-0.0125	0.0491

Table 3.3: *Comparison of forces for the clean 3.5D tangent-ogive geometry and those obtained with 0.1mm, 0.5mm and 1.0mm tip excrescences.*

3.4.1 Results

First consideration should be given to the overall force and moment values generated by each configuration. Comparing data between the 'clean' and modified configurations in Table (3.3), with C_z the normal force coefficient and C_y the sideforce coefficient, two things become readily apparent: normal force has increased by 22% over the 'clean' value and sideforce is generated almost equal in magnitude to the normal force for the unmodified geometry. These figures are purely due to the disruption in the boundary layer and vortex structure.

Graphs of the calculated pressure coefficients around the body at 0.5, 2.0 and 3.5 diameter axial intervals are shown in Figs.(3.6(b)) - (3.6(d)). C_p data is taken from all four calculated cases to allow comparisons to be made. Starting with Fig.(3.6(b)), at x/D=0.5, differences are already visible between the pressure distributions around the clean ogive and those for the two larger excrescences. Little difference can be ascertained, however, between the C_p distribution for the clean geometry and that for the smallest bump case, 0.1mm. Moving further downstream to 2.0 diameters, it can be seen how the addition of the larger bumps has caused the port-side primary vortex to move further outboard and away from the body, flattening the pressure distribution, whilst the starboard vortex has moved inboard and closer to the surface, producing a greater negative C_p. A slight reduction in gradient before the primary separation on the port side may also indicate that a secondary vortex is forming. This secondary vortex becomes the primary vortex further downstream once the initial primary vortex has been shed. Continuing aft, differences become more apparent between the solution for the clean configuration and for that with the 0.1mm bump, although sideforce figures are approximately one third of those caused by the larger bumps. The much smaller sideforce generated by the 0.1mm bump compared to the almost equal sideforces generated by the 0.5mm and 1mm bumps indicates that there may be a critical bump size in order to produce meaningful solutions.

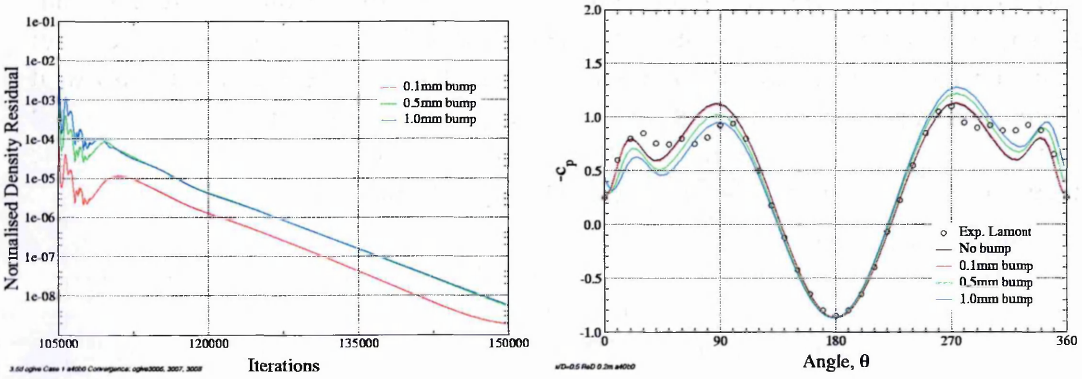

(a) Density residual

(b) x/D=0.5

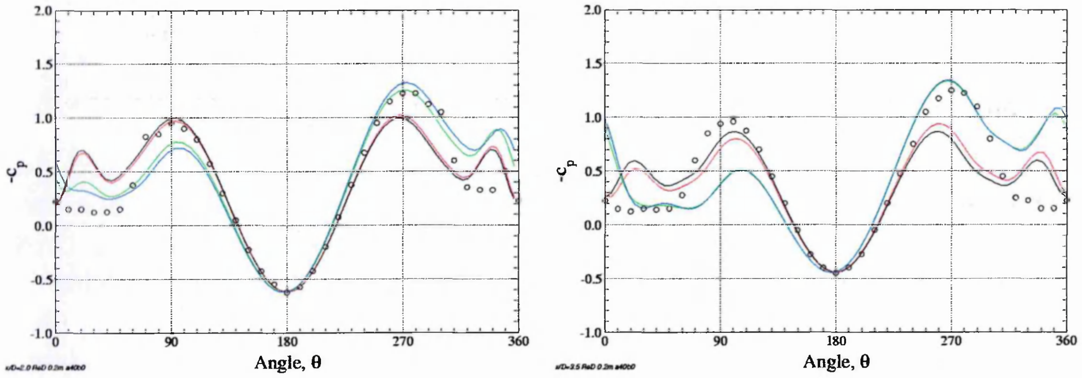

(c) x/D=2.0

(d) x/D=3.5

Figure 3.6: *Tangent-ogive grid ogive3 with and without tip excrescence,* M=0.2, Re_D=0.2 × 10^6, α=40^o. *Comparison of density residual convergence history and comparative effect of increasing bump size on surface* C_p.

To give a better idea of how the flow develops moving aft from the tip, and how the asymmetric vortices evolve and develop in the cases where an excrescence is present, Figs.(3.8) - (3.11) show pitot pressure ratio contours, looking downstream, taken at half-diameter intervals down the body. The initiation of asymmetric flow by the port-side bump is already clearly visible after 0.5 diameters for the two larger bumps, see Figs.(3.10(a)) & (3.11(a)). As expected, the addition of the excrescence at the tip causes early separation on the side on which it is located. This results in the entire vortex structure becoming asymmetric *ab initio* via convection. The strong influence of the tip region becomes apparent on considering contours taken at stations further downstream, the flow failing to stabilise itself into a symmetric form with vortices being shed from alternate sides.

As discussed in Subsection 1.2.1, the experience of Degani and his co-workers has been that the asymmetric solutions generated by addition of tip excrescences or air-jets are not stable for a symmetric grid and symmetric conditions. In other words, a time-invariant space-fixed perturbation is required to produce and maintain asymmetry through convective means. This was tested by running a calculation on the symmetric grid with the flowfield initialised with the fully converged asymmetric solution generated by the ogive with 1.0mm tip excrescence. Unsurprisingly, with the removal of the geometric asymmetry, the solution quickly lapsed back to the symmetric state.

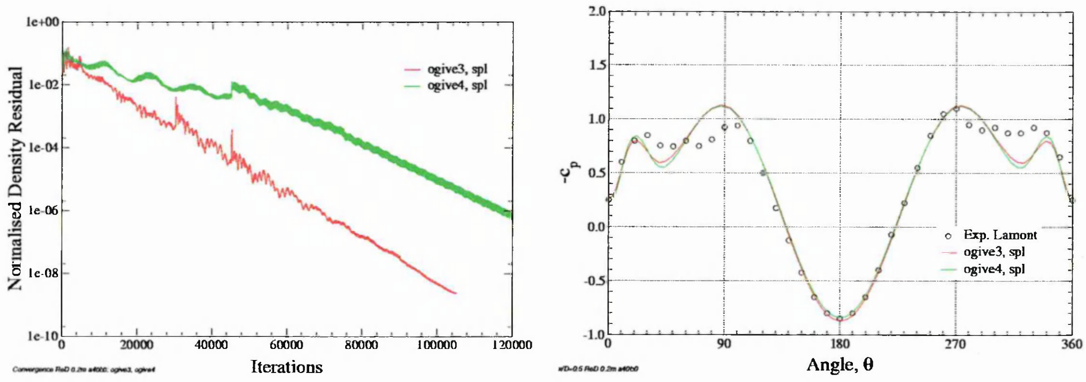

(a) Density residual

(b) x/D=0.5

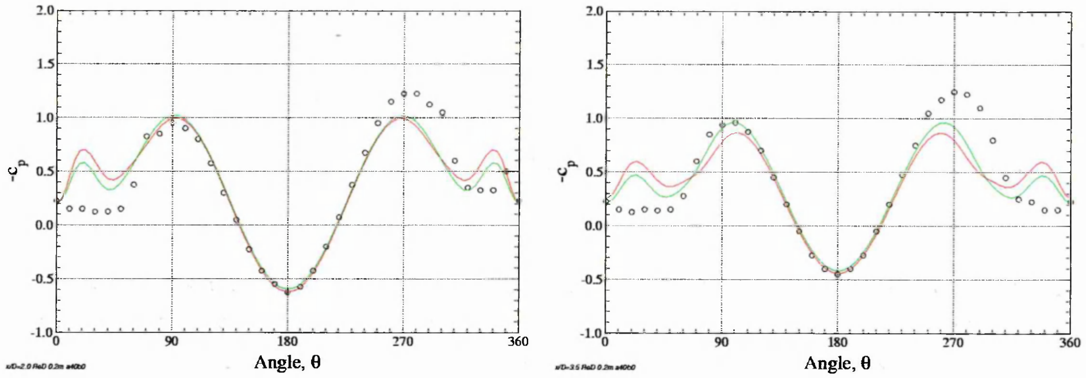

(c) x/D=2.0

(d) x/D=3.5

Figure 3.7: *Tangent-ogive grids ogive3 & ogive4 with no tip excrescence,* M=0.2, Re_D=0.2 × 10^6, α=40°. *Comparison of density residual convergence history and surface* C_p.

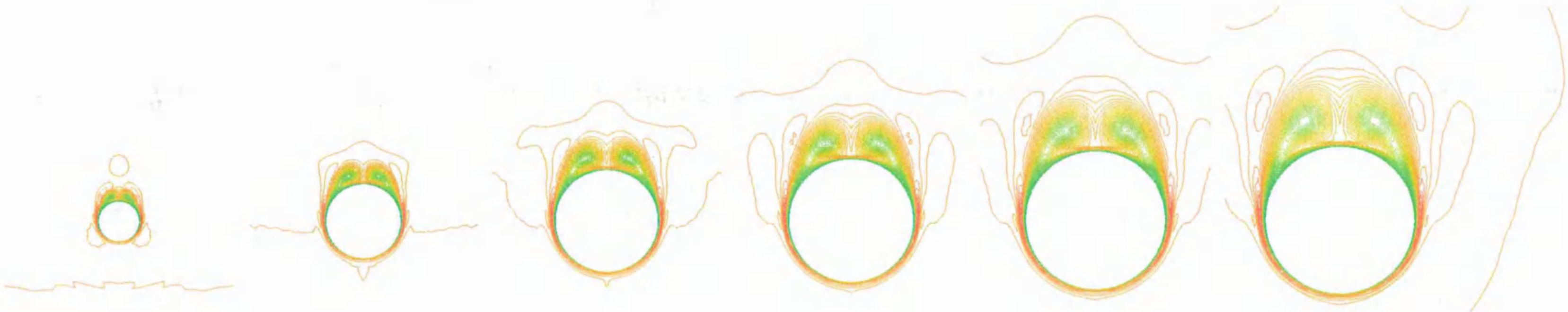

(a) x/D=0.5 (b) x/D=1.0 (c) x/D=1.5 (d) x/D=2.0 (e) x/D=2.5 (f) x/D=3.0

(g) x/D=3.5 (h) x/D=4.0 (i) x/D=4.5 (j) x/D=5.0 (k) x/D=5.5 (l) x/D=6.0

Figure 3.8: *Tangent-ogive grid ogive3 with no tip excrescence, M=0.2, Re=1.31 × 10^6, α=40°. Contours of pitot pressure ratio, Spalart-Allmaras model.*

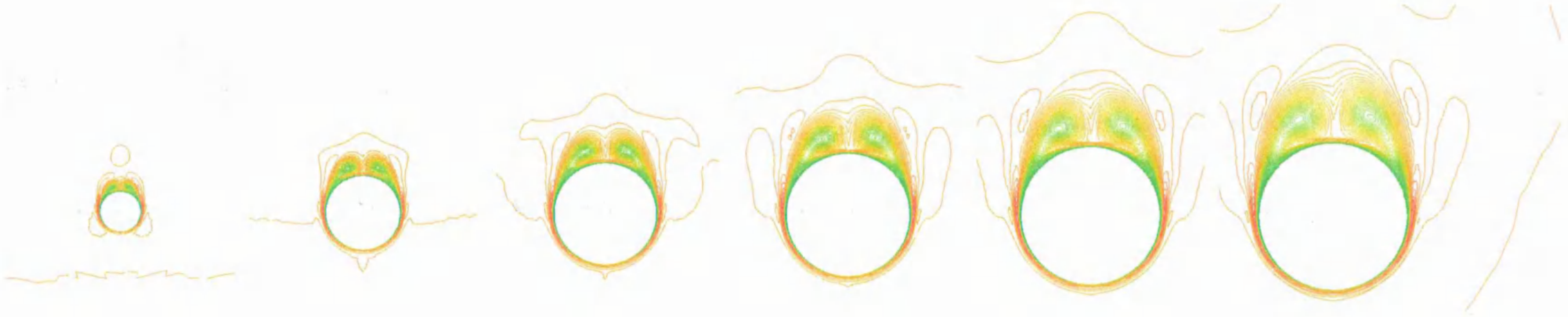

(a) x/D=0.5 **(b)** x/D=1.0 **(c)** x/D=1.5 **(d)** x/D=2.0 **(e)** x/D=2.5 **(f)** x/D=3.0

(g) x/D=3.5 **(h)** x/D=4.0 **(i)** x/D=4.5 **(j)** x/D=5.0 **(k)** x/D=5.5 **(l)** x/D=6.0

Figure 3.9: *Tangent-ogive grid ogive3 with 0.1mm tip excrescence,* M=0.2, Re=1.31 × 10^6, α=40^o. *Contours of pitot pressure ratio, Spalart-Allmaras model.*

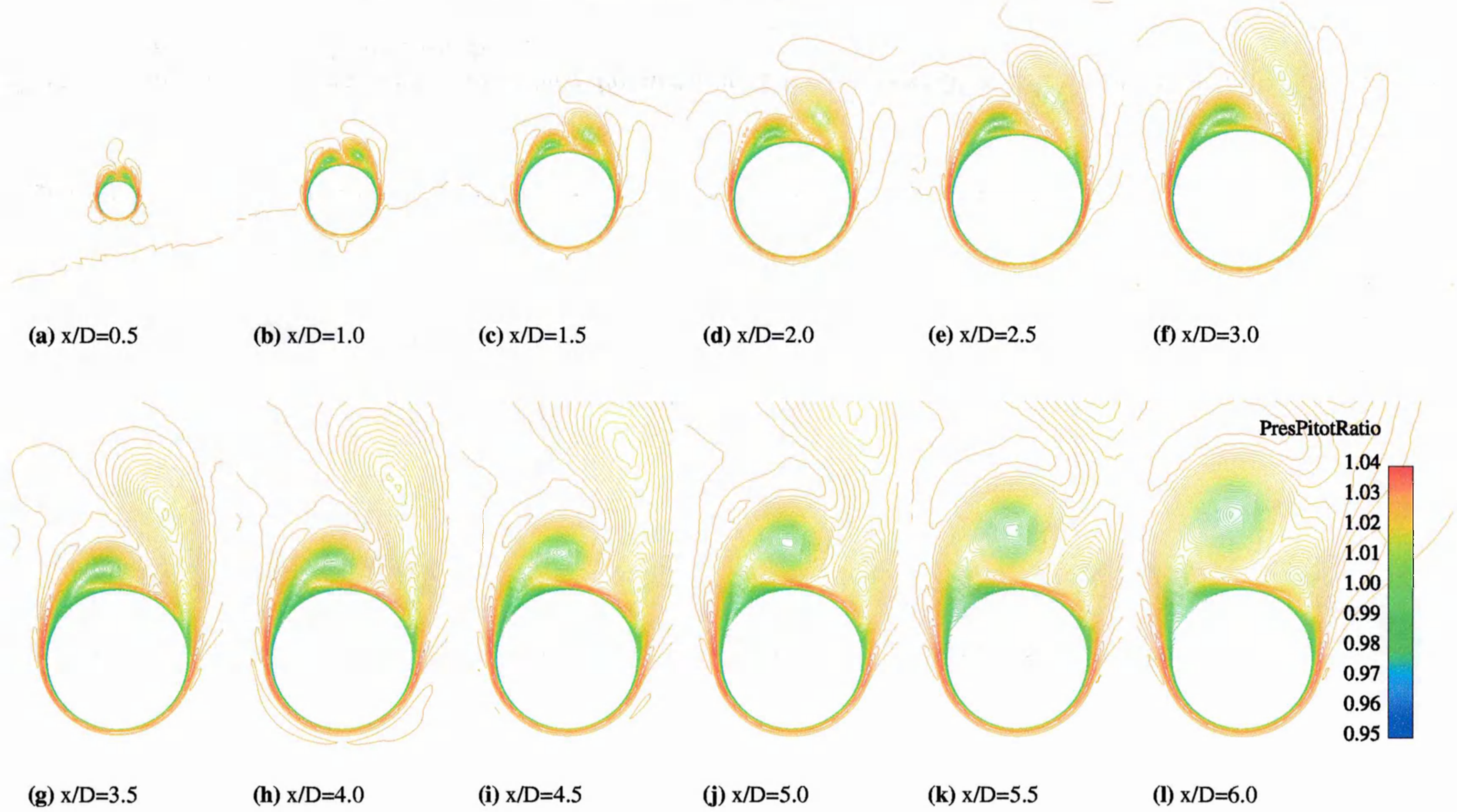

(a) x/D=0.5 **(b)** x/D=1.0 **(c)** x/D=1.5 **(d)** x/D=2.0 **(e)** x/D=2.5 **(f)** x/D=3.0

(g) x/D=3.5 **(h)** x/D=4.0 **(i)** x/D=4.5 **(j)** x/D=5.0 **(k)** x/D=5.5 **(l)** x/D=6.0

Figure 3.10: *Tangent-ogive grid ogive3 with 0.5mm tip excrescence,* M=0.2, Re=1.31 × 10^6, α=40^o. *Contours of pitot pressure ratio, Spalart-Allmaras model.*

(a) x/D=0.5 **(b)** x/D=1.0 **(c)** x/D=1.5 **(d)** x/D=2.0 **(e)** x/D=2.5 **(f)** x/D=3.0

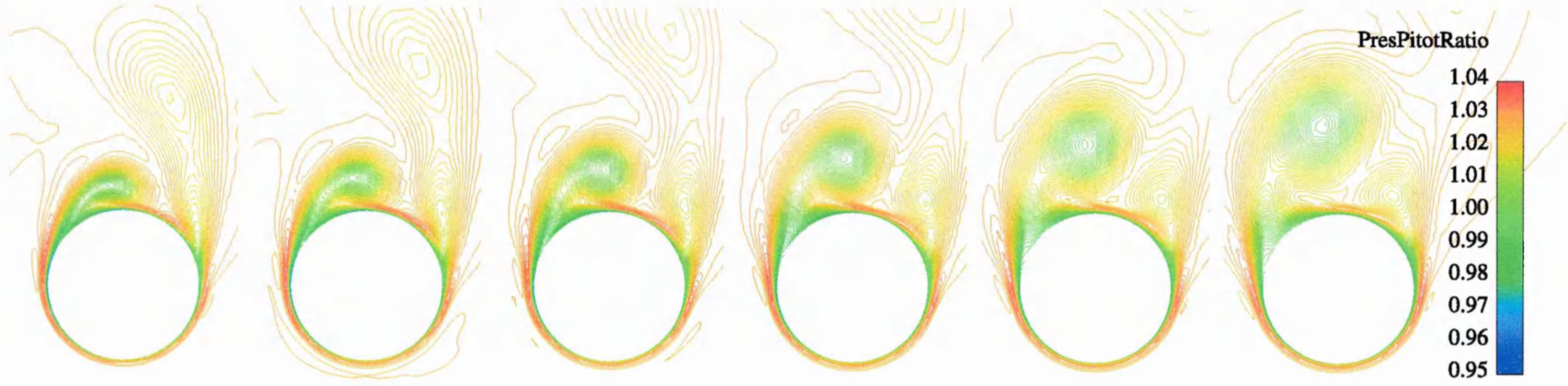

(g) x/D=3.5 **(h)** x/D=4.0 **(i)** x/D=4.5 **(j)** x/D=5.0 **(k)** x/D=5.5 **(l)** x/D=6.0

Figure 3.11: *Tangent-ogive grid ogive3 with 1.0mm tip excrescence, M=0.2, Re=1.31 × 10^6, α=40^o. Contours of pitot pressure ratio, Spalart-Allmaras model.*

3.5 Non-symmetric Solution Algorithm

As discussed in Subsection 1.2.3, an alternative to the surface excrescence approach has been to employ a non-symmetric solution algorithm. Certain implicit time-integration methods such as the LU-SGS scheme of Jameson and Yoon, [53], are known to introduce small asymmetric numerical errors into the solution process as a result of the factorisation process. These errors can be shown to be transient, see [51], hence disappear as the iterative procedure progresses and the solution converges.

Undeniably, the above implicit schemes have been shown to be capable of producing asymmetric flowfields for symmetric forebodies at high alpha. However, questions remain regarding the stability of the solutions and, as for the tip excrescence method, the physical realism and validity of the approach. Therefore, as a logical next step in the research, it was decided to investigate the performance of LU-SGS as implemented in NSMB.

3.5.1 Results

Case 1, at a Reynolds number of 200,000, was categorised by Lamont [69] as being borderline laminar/transitional. Researchers in the past, for example Degani, [14], have run this case as fully laminar and so it was decided to begin testing on the new, more refined C-O type grid ogive5 using this case and without any turbulence modelling. Due to the sensitive nature of the flowfield, it was also decided to run with the upwind third-order Roe spatial discretisation and the minmod4 limiter: this combination is agreed to have low dissipation. The flow was computed for an angle of attack of 20° since it is most important that any method be able to predict the symmetric flow which occurs at lower angles of attack. The convergence history and sideforce history for this calculation, ogive5001, are shown in Fig.(3.12).

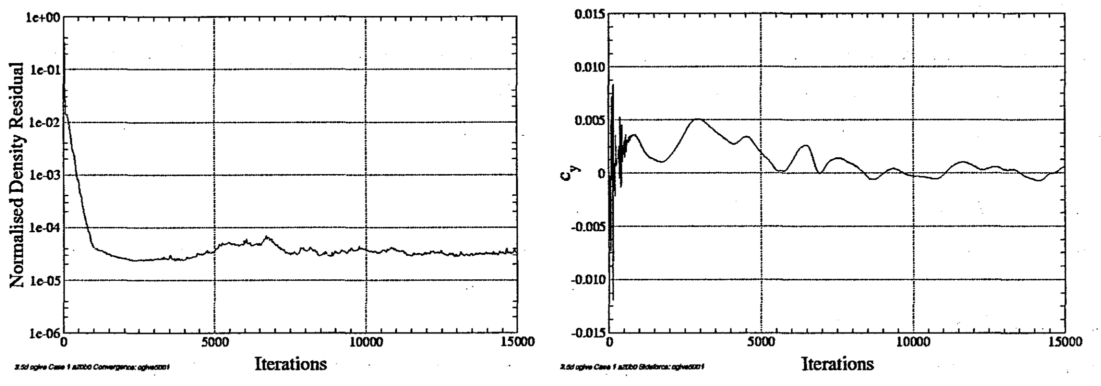

(a) Density residual

(b) Sideforce

Figure 3.12: Convergence history for the normalised density residual and sideforce coefficient, Case 1, $\alpha = 20^0$, laminar, upwind third-order Roe scheme, minmod4 limiter, 15,000 iterations.

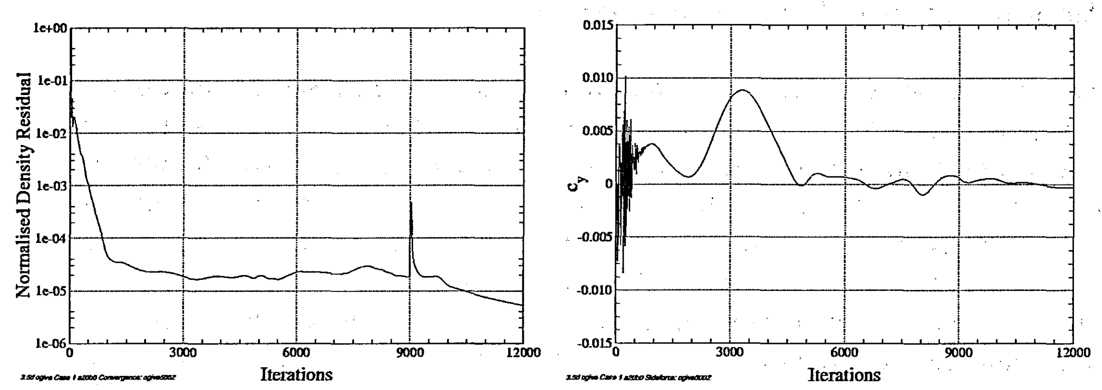

(a) Density residual

(b) Sideforce

Figure 3.13: *Convergence history for the normalised density residual and sideforce coefficient, Case 1, $\alpha = 20^0$, laminar, central scheme, fourth-order artificial dissipation 0.01 (0.05 after 9,000 iterations). 12,000 iterations.*

Whilst the sideforce has clearly not settled at the zero-value that it should be at this low angle of attack, the calculation was not continued since no further convergence seemed likely given the residual plot. Circumferential C_p profiles at two stations downstream of the tip are presented in Fig.(3.16), where they are compared with experimental data from Lamont and the results from two subsequent calculations. Looking at these profiles, one reason for the lack of further convergence becomes clear: the computed C_p profile matches well with the experimental one at the nose, 0.5 diameters downstream, but at 5.0 diameters the flowfield is fundamentally wrong. The computed C_p is accurate round to approximately 90^o either side of the windward meridian ($\theta = 180^o$), but from there on round to the leeward meridian ($\theta = 0^o$) there are large pressure peaks and troughs which are not present in the real flow. This can be explained purely by the imposition of uniformly laminar flow in the calculation. In reality, the flow appears to be laminar on the underside of the body along most (or all) of its length for $90^o < \theta < 270^o$, Re_D being too low for there to be any attachment-line contamination, see Fig.(1.5). It then separates and, apart from in the nose region where the Reynolds number based on local diameter is too low, transitions to turbulence. Although the number of data points is not really sufficient to make a judgement, the experimental C_p profiles possibly also indicate the presence of some secondary separation.

In order to ascertain whether the poor agreement with experiment of the upwind third-order Roe computation was due mainly to the laminar assumption, several other laminar calculations were run. Two were run using LU-SGS and the more dissipative central spatial-discretisation, varying the fourth-order artificial viscosity with each run, and one using explicit fourth-order Runge-Kutta time-stepping with the central scheme. Force and residual convergence histories for the two implicit calculations are shown in Figs.(3.13) & (3.14) while the C_p profiles from the initial upwind calculation can be compared with those obtained using LU-SGS, the central scheme and a fourth-order dissipation of 0.01 in Fig.(3.16). It is clear from the convergence history graphs that the central scheme is considerably more stable for this problem than the third-order upwind scheme, even when the fourth-order dissipation is set at a relatively low value of 0.01. If this is increased to 0.03, accepted as a more realistic value for calculation of a subsonic problem using *NSMB*, then convergence is even faster and smoother. However, as can be seen in Fig.(3.16) changing to the central scheme does not produce any marked improvments to the flowfield. Assuming that there are sufficient points circumferentially to resolve the various separations and re-attachments, the assumption of laminar flow would seem to be wholly inappropriate even for this low Re_D, low α case.

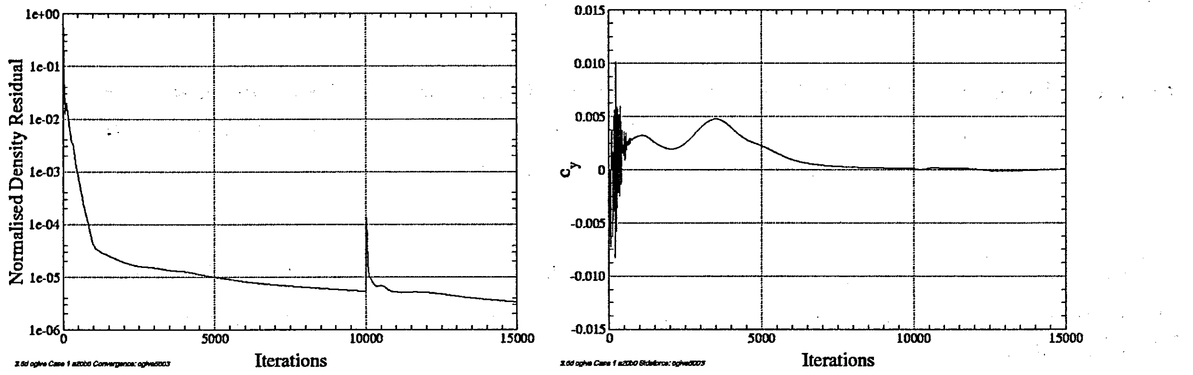

(a) Density residual

(b) Sideforce

Figure 3.14: *Convergence history for the normalised density residual and sideforce coefficient, Case 1, $\alpha = 20^0$, laminar, central scheme, fourth-order artificial dissipation 0.03 (0.05 after 10,000 iterations). 15,000 iterations.*

The one-equation turbulence model of Spalart-Allmaras has developed a reputation for being considerably more robust than two-equation models whilst also being capable of resolving complicated flowfields reasonably well. The calculation made utilising this model converged fast and monotonically to a zero sideforce solution, see Fig.(3.15). It can be seen from the resulting C_p profiles, again shown in Fig.(3.16), that the laminar calculation produced a better agreement with experiment near the nose but that the turbulent solution captures the overall character of the flowfield slightly better further downstream. The agreement with experimental data is, however, still not good. Whereas the suction peaks are correctly predicted by the laminar calculations, flow in the turbulent solution stays attached further round the body from the windward meridian, overpredicting peak suction. From the experimental data at 5.0 diameters, see Fig.(3.16(b)), it would appear that flow is laminar until approximately $\theta = 80^o$, then separates, transitions to turbulence and reattaches, forming a separation bubble. Turbulent separation then occurs again at $\theta \approx 120^o - 130^o$.

A two-equation k-ε (Chien) calculation was also run, initialised with the Spalart-

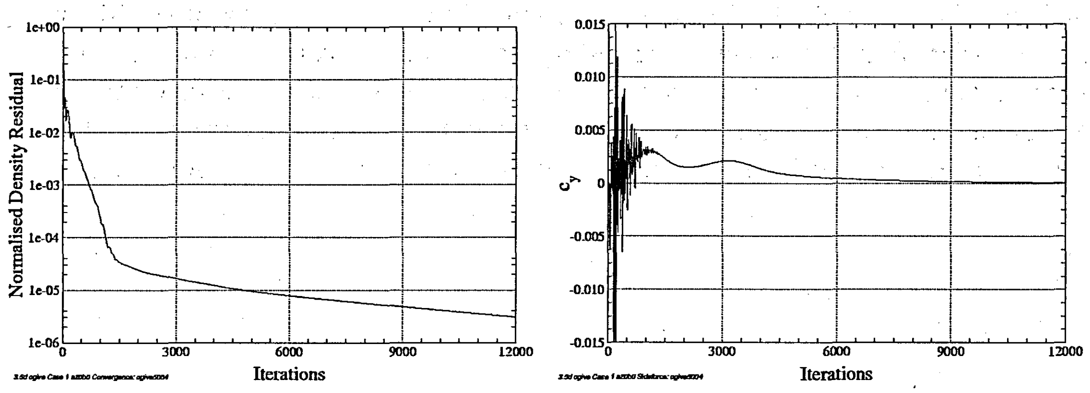

(a) Density residual (b) Sideforce

Figure 3.15: *Convergence history for the normalised density residual and sideforce coefficient, Case 1, $\alpha = 20^0$, Spalart-Allmaras, central scheme, fourth-order artificial dissipation 0.03. 12,000 iterations.*

Allmaras solution. No major differences were visible after a further 6,000 iterations had been made. However, problems were encountered with convergence and the CFL had to be held at a very low value in order to avoid a crash.

Although $\alpha = 20^o$ was proving problematical, a single turbulent calculation using Spalart-Allmaras was made at $\alpha = 40^o$ for the case 1 conditions. Whereas the wake from a 3.5D tangent-ogive should be symmetric at $\alpha = 20^o$, the wake at $\alpha = 40^o$ should be asymmetric. Time histories for the density residual and sideforce for this are shown in Fig.(3.17).

Clearly, convergence to a steady value of sideforce does not occur, indeed the oscillations seem completely random in nature and the solution is not even switching between bistable states. Literature indicates that convergence for these conditions and this value of α is possible using the LU-SGS scheme, although, as previously noted, most researchers have utilised the algebraic Baldwin-Lomax model with the Degani-Schiff modification for turbulent closure rather than the one-equation Spalart-Allmaras model. As has been mentioned before, the asymmetry is produced because the scheme itself is directionally biased to some extent but it has been shown by Hwang and Rho, [51], that the unsymmetric factorisation error occurs mainly in the early stages of computation before decaying to zero. The resulting asymmetric wake persisted even when the algorithm was switched to one with known symmetric factorisation.

Laminar and turbulent (Spalart-Allmaras) computations were also run with Case 2 flow conditions, both using the central scheme with 4th order dissipation set to 0.03 as before. Convergence histories for these are shown in Figs.(3.18) & (3.21) and C_p profiles extracted at the end of these two runs are compared in Fig.(3.22). Although neither solution converged, the C_p profiles shown were extracted from the database after 10,000 and 20,000 iterations respectively and therefore provide a snapshot of the flow at that point in the calculation. Shown in Figs.(3.19) & (3.20) are pitot pressure ratio contours for these two runs. On comparing the two sets of contours, the delayed separation and narrower wake of the turbulent solution are immediately visible. Also of note are the additional secondary and tertiary vortices captured in the laminar solution and which can be related to the extra pressure peaks and troughs visible in the circumferential C_p profiles.

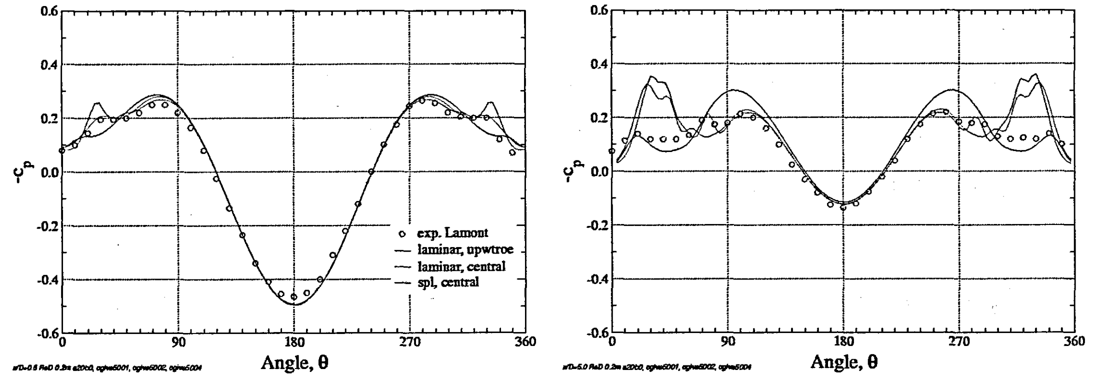

(a) x/D=0.5

(b) x/D=3.5

Figure 3.16: *Effect of numerical schemes and turbulence modelling on surface C_p. Case 1, $\alpha = 20^o$.*

With the convergence difficulties being experienced, there then followed extensive testing of flowfield initialisation methods and solver options.

Firstly, Siclari and Marconi, [108], report that initialising the flowfield with a solution obtained at yaw could aid convergence, albeit they were using a conical RANS code. First attempts for a solution at $\beta = \pm 1^o$ resulted in more oscillations and so $\beta = 5^o$ was tried. As can be seen in Fig.(3.23), this converged towards a steady sideforce. The solution obtained after 12,000 iterations was then used to initialise an $\alpha = 40^o$, $\beta = 0^o$ calculation and run for a further 12,000 iterations. Fig.(3.24) depicts the convergence histories of normalised density residual and sideforce for this calculation. No convergence was achieved, although the sideforce appears to be settling into a regular pattern of oscillation.

Secondly, the effect of the location of the periodic boundary condition was investigated and found to be negligible.

Thirdly, a sequence of runs was made using the converged $\alpha = 20^o$ solution as a starting point and increasing the angle of attack incrementally every few thousand iterations. This technique avoids exposing the body to a high-alpha onset flow immediately, allowing the solution to develop and build in complexity gradually as α increases. Unfortunately, once above $\alpha = 30^o$, convergence degraded as before.

Lastly, the upwind second-order Roe scheme was employed with a selection of limiters. This was found to be significantly more unstable than the central scheme and, when solutions were obtained without the solver crashing, no vortices were generated, although sideforces were non-zero, see Fig.(3.25). Changing limiter, or running without one, gave no improvement and so it appears that the vorticity was dissipated by the numerical scheme. However, central discretisation was used previously with no similar problems and should be more dissipative than the upwind Roe method. Hence, errors in the implementation of Roe are suspected.

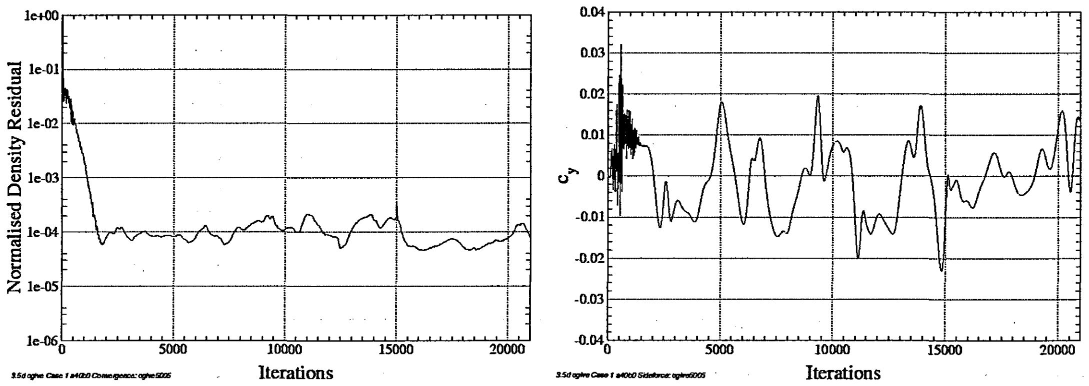

(a) Density residual

(b) Sideforce

Figure 3.17: Convergence history for the normalised density residual and sideforce coefficient, Case 1, $\alpha = 40^0$, Spalart-Allmaras, central scheme, fourth-order artificial dissipation 0.03. 21,000 iterations.

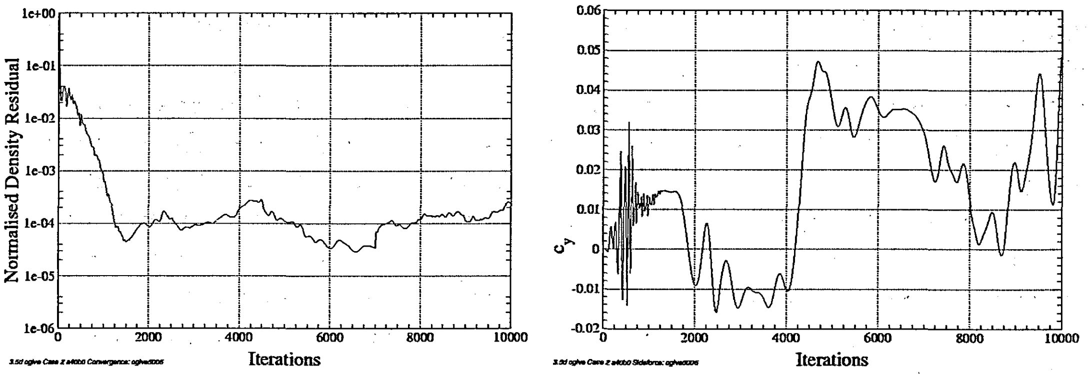

(a) Density residual

(b) Sideforce

Figure 3.18: Convergence history for the normalised density residual and sideforce coefficient, Case 2, $\alpha = 40^0$, laminar, central scheme, fourth-order artificial dissipation 0.03. 10,000 iterations.

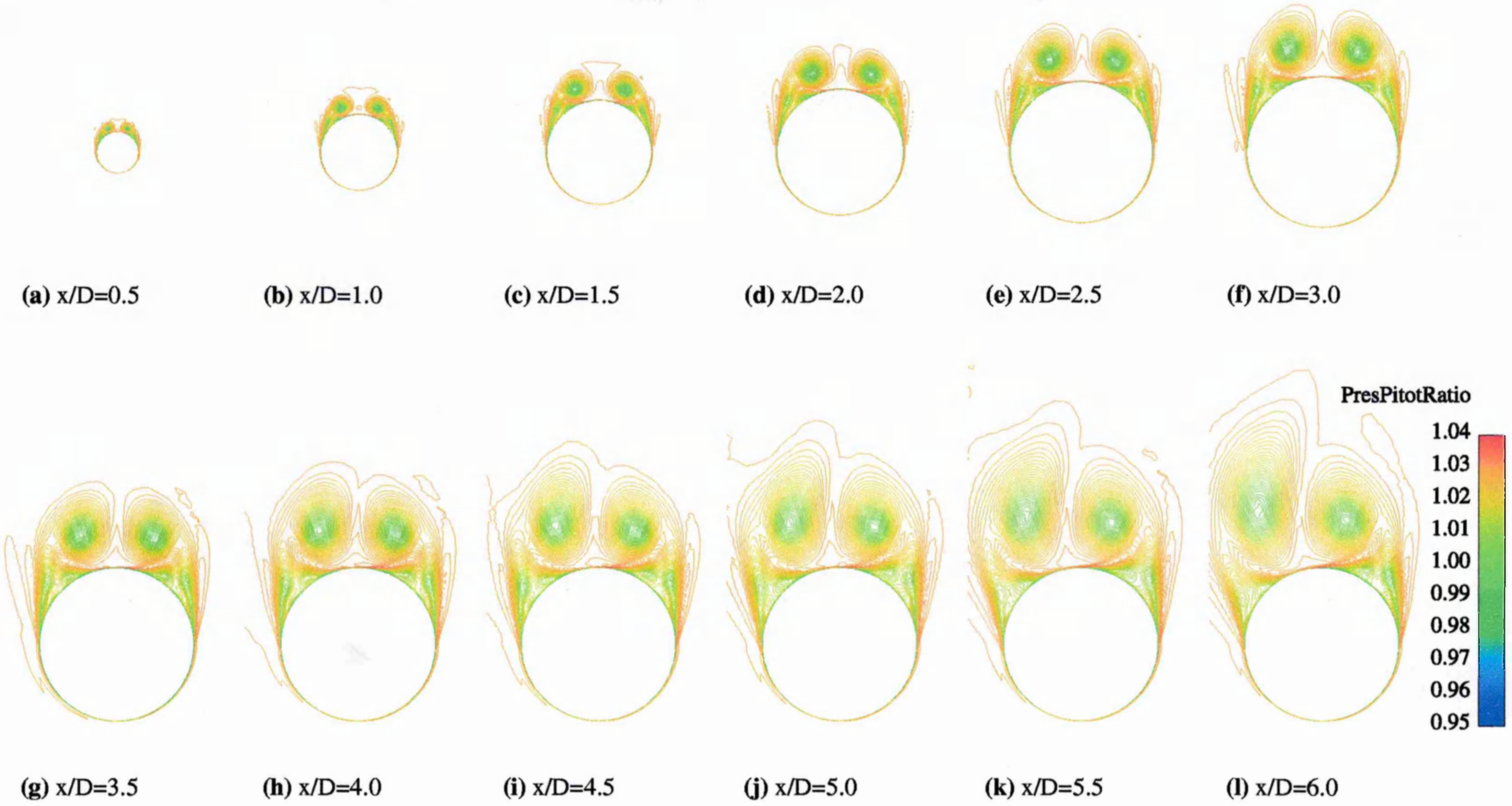

(a) x/D=0.5 **(b)** x/D=1.0 **(c)** x/D=1.5 **(d)** x/D=2.0 **(e)** x/D=2.5 **(f)** x/D=3.0

(g) x/D=3.5 **(h)** x/D=4.0 **(i)** x/D=4.5 **(j)** x/D=5.0 **(k)** x/D=5.5 **(l)** x/D=6.0

Figure 3.19: *Tangent-ogive grid ogive5, Case 2,* α=40°. *Contours of pitot pressure ratio, laminar computation.*

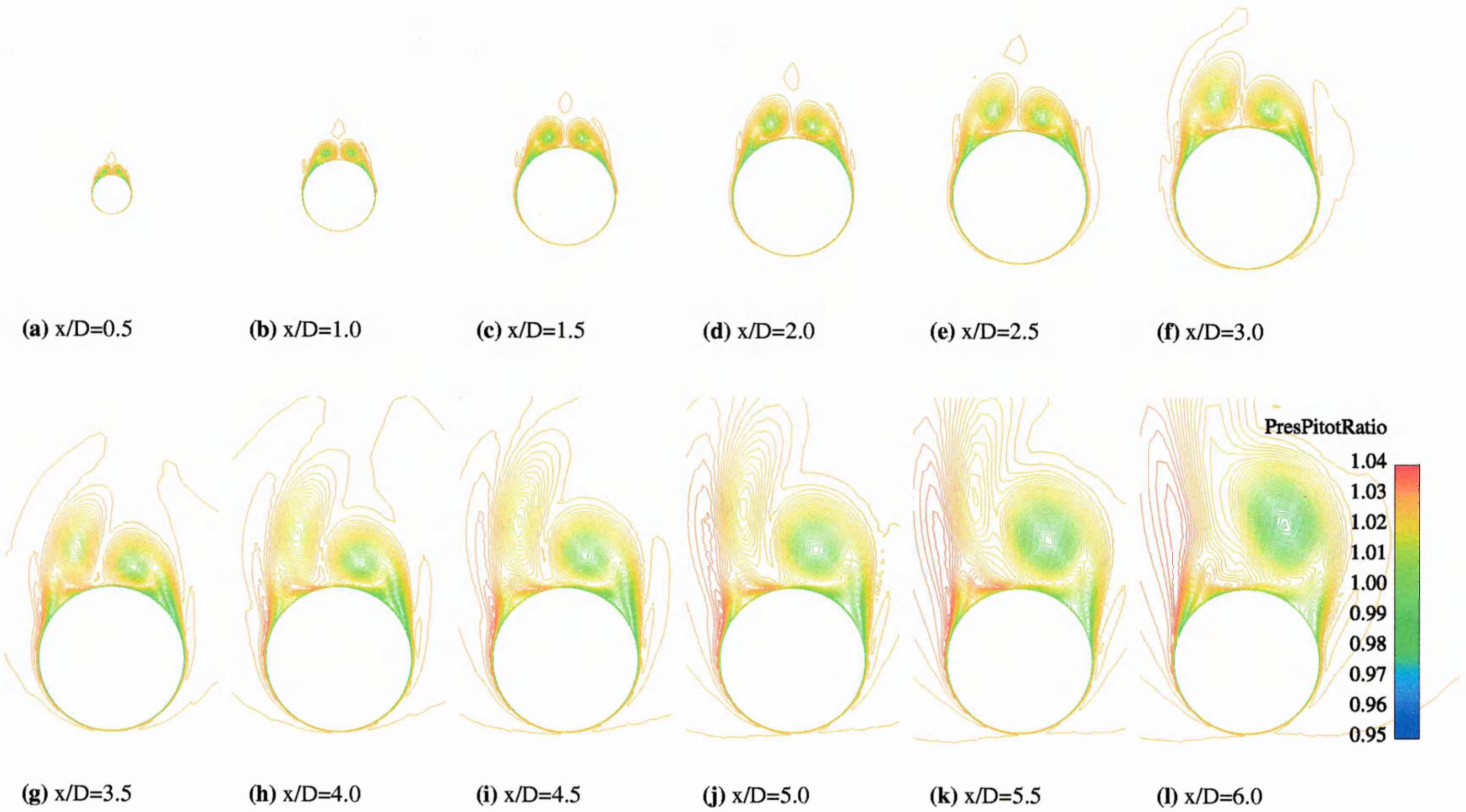

(a) x/D=0.5 (b) x/D=1.0 (c) x/D=1.5 (d) x/D=2.0 (e) x/D=2.5 (f) x/D=3.0

(g) x/D=3.5 (h) x/D=4.0 (i) x/D=4.5 (j) x/D=5.0 (k) x/D=5.5 (l) x/D=6.0

Figure 3.20: *Tangent-ogive grid ogive5, Case 2, α=40°. Contours of pitot pressure ratio, Spalart-Allmaras.*

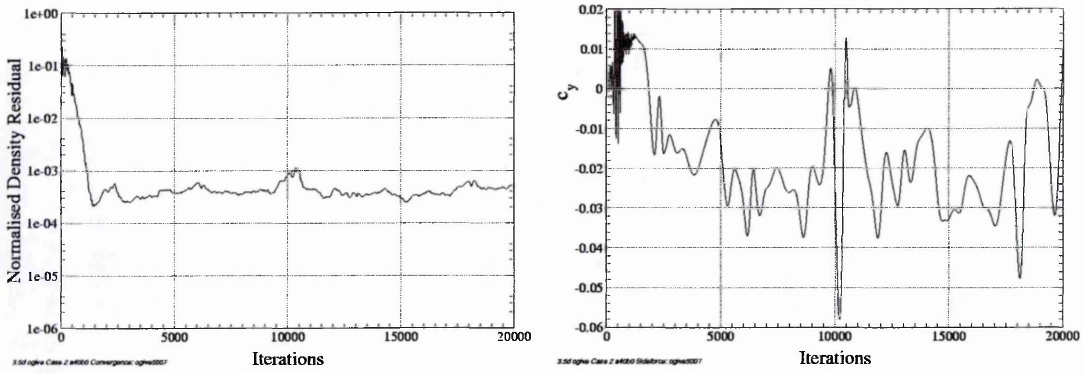

(a) Density residual

(b) Sideforce

Figure 3.21: *Convergence history for the normalised density residual and sideforce coefficient, Case 2, $\alpha = 40^0$, Spalart-Allmaras, central scheme, fourth-order artificial dissipation 0.03. 15,000 iterations.*

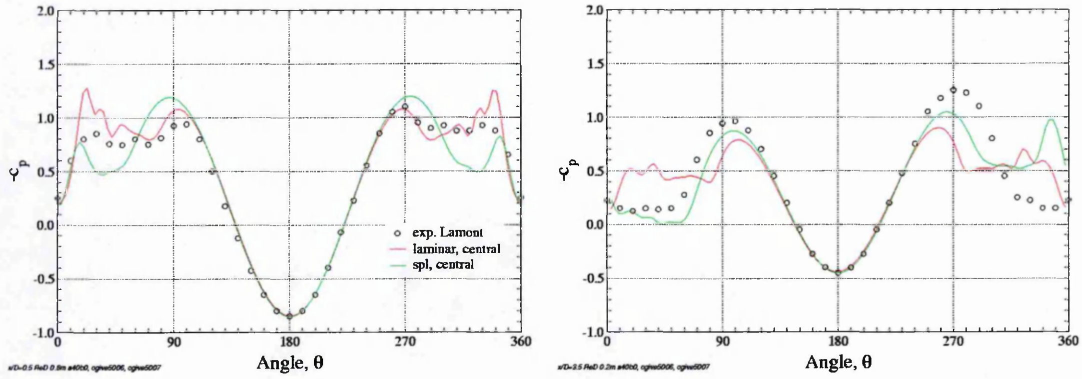

(a) x/D=0.5

(b) x/D=3.5

Figure 3.22: *Comparison of surface C_p for turbulent and laminar calculations. Case 2, $\alpha = 40^o$.*

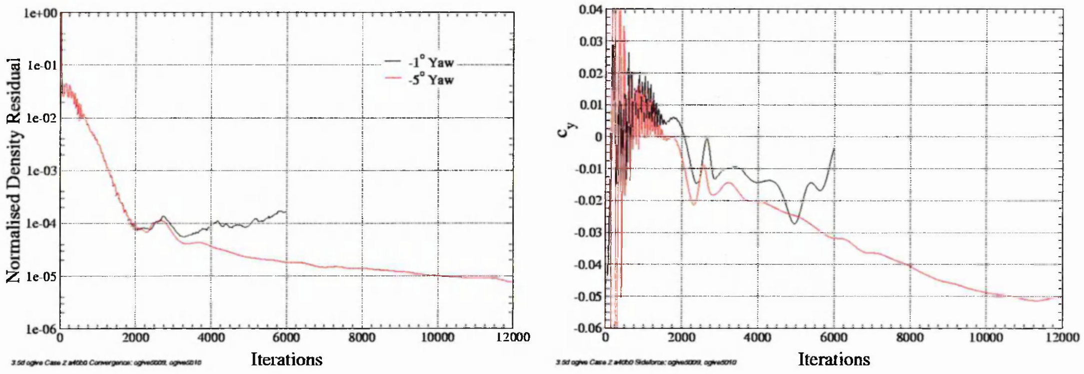

(a) Density residual

(b) Sideforce

Figure 3.23: *Comparison of convergence history for the normalised density residual and sideforce coefficient, Case 2, $\alpha = 40^0$, yaw angles $\beta = -1^o$ & $\beta = -5^o$. Spalart-Allmaras, central scheme, fourth-order artificial dissipation 0.03. 12,000 iterations.*

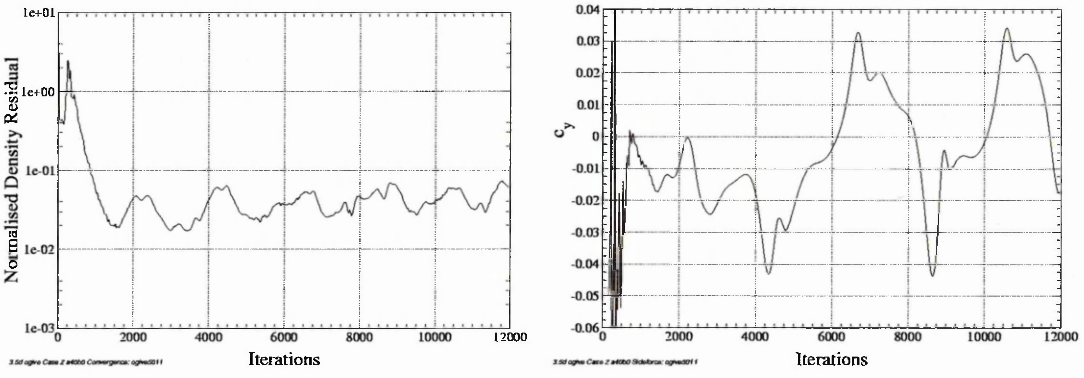

(a) Density residual

(b) Sideforce

Figure 3.24: *Convergence history for the normalised density residual and sideforce coefficient, Case 2, $\alpha = 40^0$. Initialised with flowfield from $\beta = -5^o$, Spalart-Allmaras, central scheme, fourth-order artificial dissipation 0.03. 12,000 iterations (24,000 iterations total).*

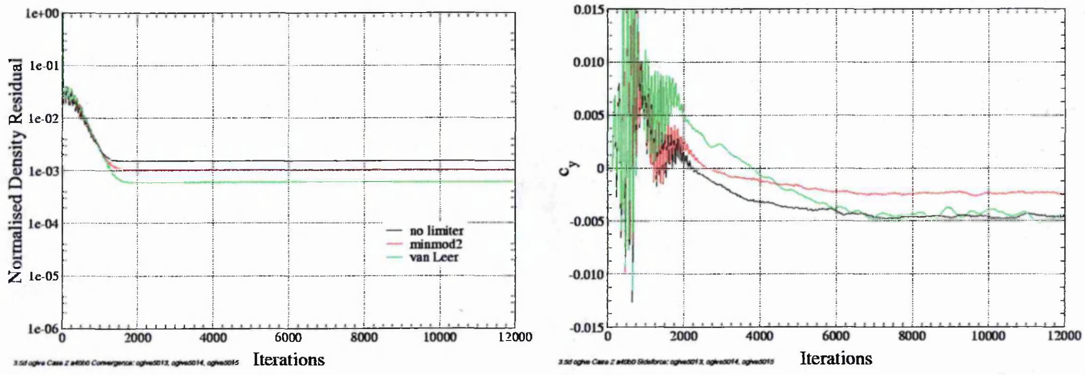

(a) Density residual

(b) Sideforce

Figure 3.25: *Effect of choice of limiter on convergence history for the normalised density residual and sideforce coefficient, Case 2,* $\alpha = 40^0$*, Spalart-Allmaras, second-order upwind Roe scheme. 12,000 iterations.*

3.6 Hardware Performance Timings

Model	Time	Spatial	Machine	CPUs	μCPUsec/It./cell
S-A	R-K4	central	Cray J916	1	32.340
Lam.	LU-SGS	upwtroe	Fujitsu VX/3	1	17.635
Lam.	LU-SGS	central	Fujitsu VX/3	1	11.048
S-A	LU-SGS	central	Fujitsu VX/3	1	15.167
S-A	LU-SGS	central	Cray T3E	16	11.585
S-A	LU-SGS	central	Cray T3E	32	5.627

Table 3.4: *Selected timings, tangent-ogive computations.*

For completeness, performance timings for the hardware used for the calculations shown in this chapter are shown above in Table (3.4). The figures in the final column can be factored by grid size and number of iterations to give an idea of run time for each case. For example, 15,000 iterations on ogive5 using 32 processors on the T3E would take $5.627 \times 10^{-6} \times 15,000 \times 576,000 = 48,617$ seconds or approximately 13.5 hours.

3.7 Summary of Results

- Fully turbulent solutions were obtained for the 3.5D tangent-ogive geometry of Lamont, [67, 69], at $\alpha = 40^o$ and $\beta = 0^o$ using the explicit RK-4 algorithm and the Spalart-Allmaras model. The flow remained symmetric unless a space- and time-fixed surface excrescence was introduced near the tip of the ogive. The degree of flow asymmetry was dependent on the size of the excrescence and removal of the disturbance caused the flow to lapse back to symmetry.

- Laminar and fully turbulent Spalart-Allmaras calculations were run on a refined tangent-ogive grid at $\alpha = 20^o, 40^o$ and $\beta = 0^o$ using the non-symmetric implicit LU-SGS algorithm. Both laminar and turbulent solutions were stable and fairly symmetric at $\alpha = 20^o$, with convergence improved by switching from the third-order Roe scheme to the more dissipative central spatial discretisation. Correlation between experimental surface pressures and the computed laminar profiles degrades moving aft, the opposite being the case for the turbulent solutions.

- Stable solutions could not be achieved at $\alpha = 40^o$ for either laminar or turbulent flow. Side force convergence plots show large-scale, non-periodic oscillations. Solution stability could be achieved neither by initialising the domain with a converged solution obtained at yaw nor by variation of spatial scheme.

- Flowfield snapshots of the unconverged $\alpha = 40^o$ calculations show the solutions to be highly asymmetric. The laminar case exhibits additional non-physical vortices over the lee-side of the body but good experimental correlation near the nose prior to separation. Pitot pressure ratio contours for the turbulent case show the port vortex to be highly dominant but agreement with experimental surface pressures is poor.

4. Baseline JAS-39 Gripen Forebody

The first stages of the research, discussed in the previous chapter, involved computations around a tangent-ogive forebody coupled to a cylindrical afterbody. This geometry proved to be a perfectly adequate initial representation and the difficulties associated with computing high alpha flows around slender forebodies were clearly demonstrated, even for such an apparently simple case. Realistic combat aircraft forebody geometries, however, have complex surface curvatures and, importantly, canopies. Literature shows these differences to be significant, thus subsequent stages of the work centred around the JAS-39 Gripen forebody geometry. The following chapter covers computations performed for the clean forebody and the slightly more complex case of the forebody with nose-mounted pitot tube.

Following a comprehensive evaluation of the existing capabilities of the code around the 3.5 calibre tangent-ogive/cylinder of Lamont, one key area was identified for potential improvement. As described in Chapter 1, a characteristic of the problem is the strong influence of the various transition mechanisms which may be acting depending on Reynolds number and angle of attack. For the flow conditions concerned, although a majority of the forebody can be assumed to be turbulent, sizeable regions of laminar flow may exist along the underside of the body and near the nose. The problems associated with crossflow transition can be reduced by moving to higher Reynolds numbers, but the range $0.2 \times 10^6 < Re_D < 1 \times 10^6$ is representative of the Re_D that combat aircraft forebodies operate at during slow, high-α manoeuvering flight. For example, flight testing during the NASA F-18 HARV program demonstrated the existence of sizeable laminar separation bubbles as far back as 1000mm from the apex of the nose at $\alpha \approx 47^o$, see [34, 35]. This leaves the modelling of turbulence as a major obstacle towards attaining realistic representation of high α flowfields. Prior to this study, most researchers utilised the algebraic Baldwin-Lomax turbulence model with modifications by Degani and Schiff to better account for separated shear layers. While turbulent closure for the tangent-ogive computations described in Chapter 3 was achieved using the one-equation Spalart-Allmaras model, it was decided to implement the two-equation k-ω family of turbulence models for subsequent stages of the work. The basic Wilcox model is known to suffer high dependence on the values of freestream k and ω but the blended variants developed by Menter, [82], are currently regarded as the two-equation models of choice for complex external flows. Details of the implementation are included in Chapter 2 and the validation of the models using standard two-dimensional NSMB test cases can be found as Appendix A.

On completion of the turbulence model validation, the focus of computational work shifted to the JAS-39 Gripen forebody geometry supplied by Saab Aerospace.

4.1 Experimental Reference

The JAS-39 Gripen is the latest in a long line of Saab fighter aircraft. The forebody geometry supplied by Saab was of a pre-production nose tested at 1:6.5 scale by the company in the mid 1980s. Fig.(4.1) shows the side profile of the forebody together with the x_{nos} coordinate system which will be used henceforth. Also marked, and tabulated in Table (4.1), are the axial locations of 14 sets of cross-sectional pressure tappings down the body. These cross-sections are shown fully in Figs.(4.3) & (4.4). Pressure taps were fitted at 10 angular locations for sections 01-05 with taps at an additional 8 angles for sections 06-14, see Fig.(4.4(f)), to give a total of 212 taps distributed over the surface of the model. Model length was 782mm.

The model was tested in three configurations: clean forebody; forebody with pitot; forebody with pitot and short nose strakes, similar to those on the production aircraft. The forebody as shown in Fig.(4.1) is in the clean configuration with the nose-mounted pitot tube of the production aircraft replaced by a conical nose cap. When fitted, the pitot tube, a simple body of revolution shown in Fig.(4.2), was mounted so as to be aligned centrally with the x_{nos} axis.

Comprehensive pressure data was gathered for each configuration across a full sweep of pitch and yaw angles but it was decided to concentrate effort on the first two configurations only.

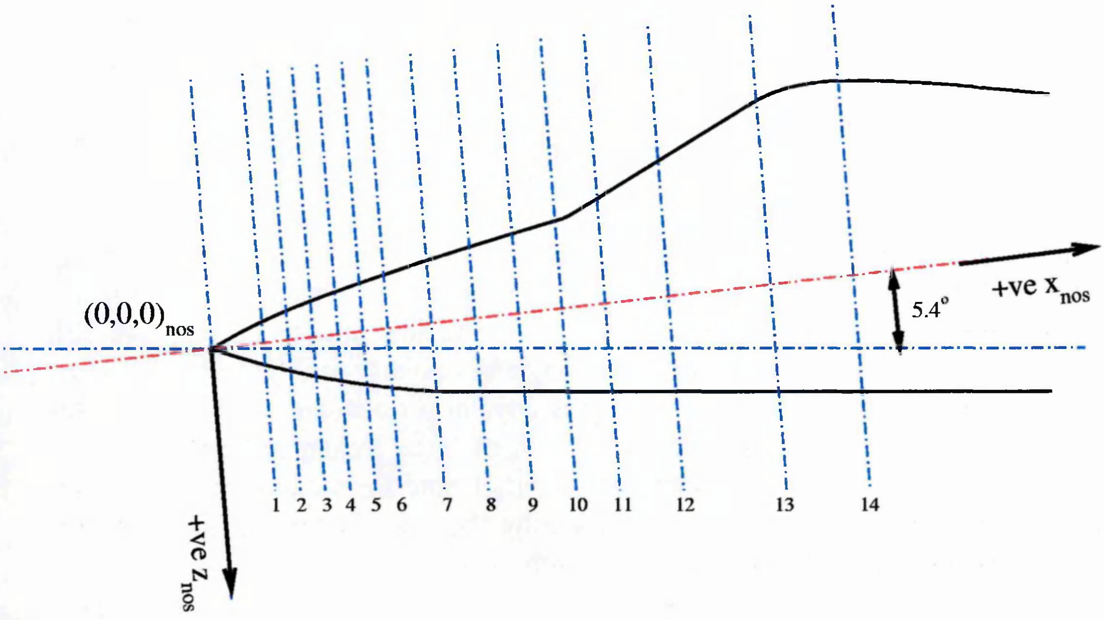

Figure 4.1: *Side elevation of the baseline JAS-39 model geometry with axial locations of cross-sectional pressure tappings.*

Section	01	02	03	04	05	06	07
X_{nos}	48.1	71.2	94.2	117.3	140.4	163.5	203.9
Section	08	09	10	11	12	13	14
X_{nos}	244.2	284.6	325.0	365.4	424.3	519.2	596.2

Table 4.1: *Location of circumferential pressure tappings in x_{nos} coordinate system. All dimensions are mm modelscale.*

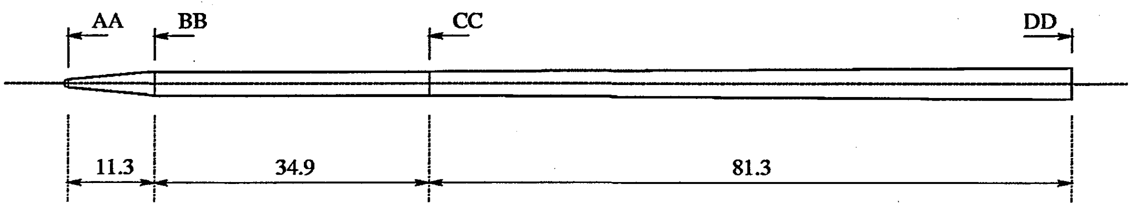

Figure 4.2: *Pitot-tube geometry definition. $AA = \phi 1.15$, $BB = \phi 2.93$, $CC = \phi 2.93$, $DD = \phi 4.00$, all dimensions mm modelscale.*

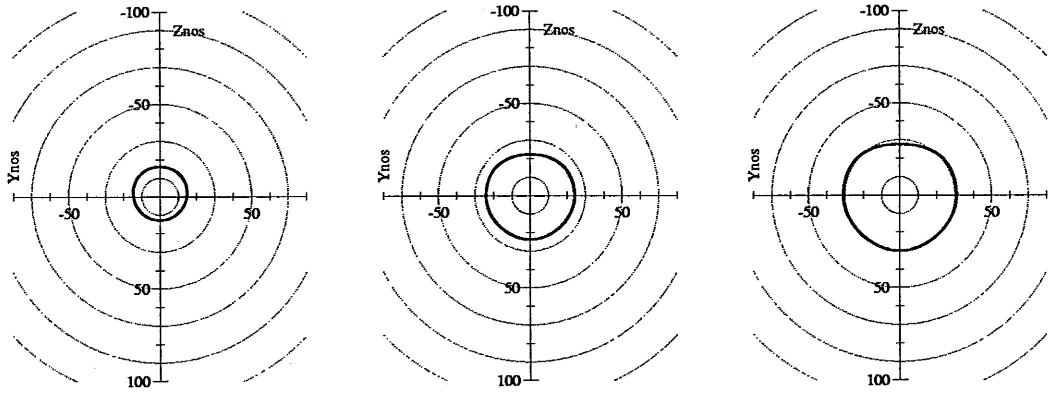

(a) Section 01 (b) Section 02 (c) Section 03

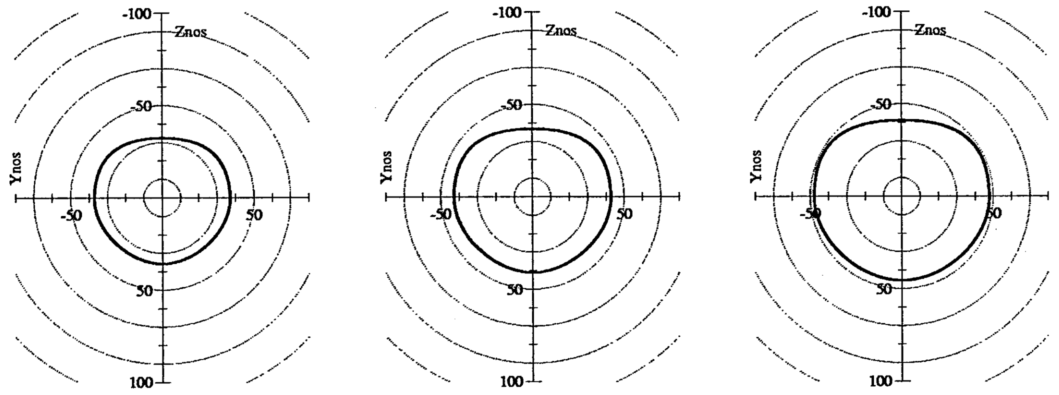

(d) Section 04 (e) Section 05 (f) Section 06

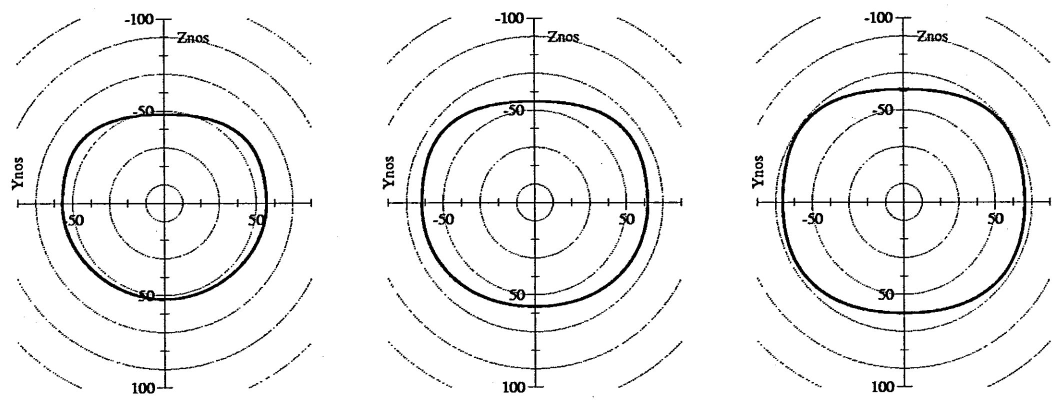

(g) Section 07 (h) Section 08 (i) Section 09

Figure 4.3: Forebody cross-sections 01-09. Dimensions in mm modelscale.

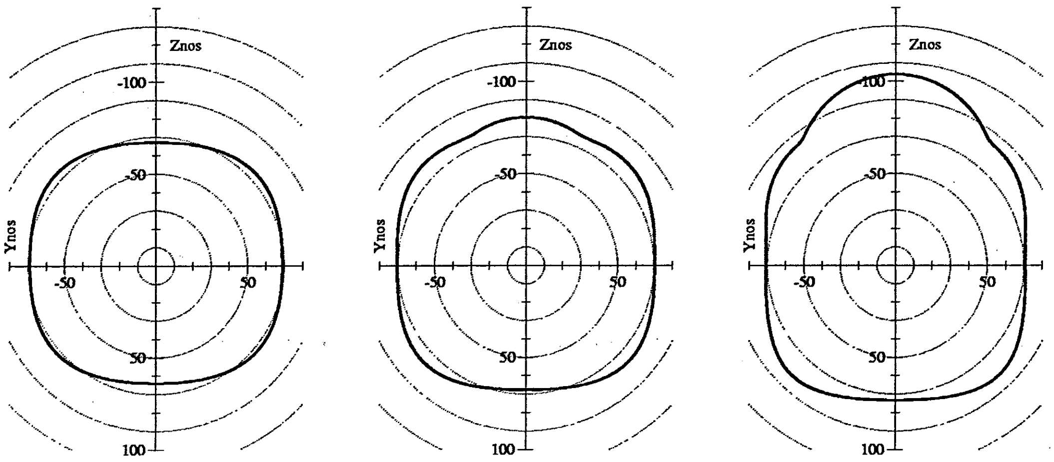

(a) Section 10 (b) Section 11 (c) Section 12

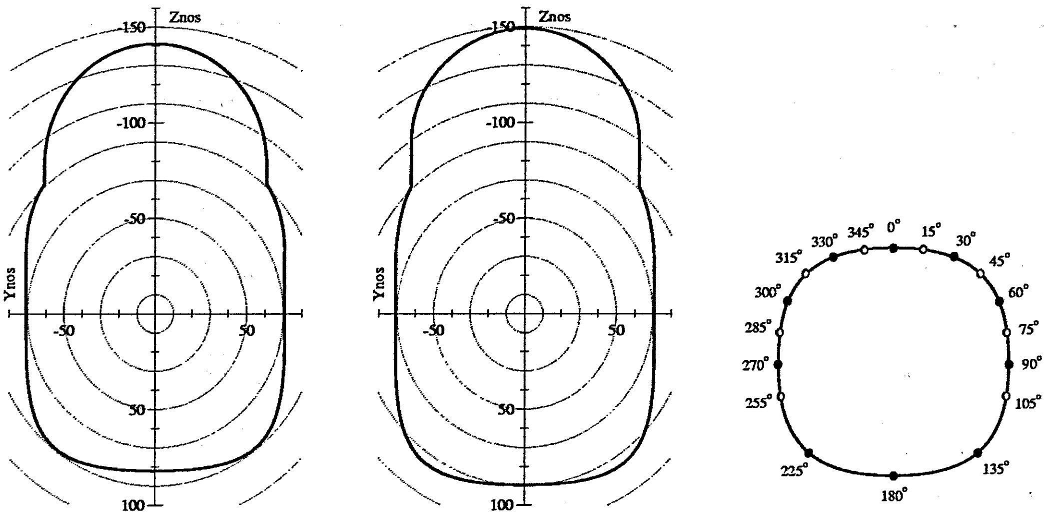

(d) Section 13 (e) Section 14 (f) Pressure tap location

Figure 4.4: *Forebody cross-sections 10-14 and experimental pressure-tap location. Black dots denote angular locations of pressure taps used for all cross-sections, red dots denote locations used solely for cross-sections 06-14. Dimensions in mm modelscale.*

4.2 Computational Details

4.2.1 Grid generation

The size of the tangent-ogive grids used for the first stage of the research was severely limited by the available computer power. By the start of this second stage of the work, time had been negotiated on the Cray T3E supercomputer at the Swedish National Supercomputer Centre, Linköping. The availability of large-scale computational resources allowed the grids for the JAS-39 forebody to be substantially more refined than was previously possible whilst still giving decreased job turn-around time.

The JAS-39 geometry was supplied in IGES format and required cleaning and patching in ICEM DDN before meshing. However, a question arose over how to treat the exit boundary. For low angle-of-attack calculations it would be appropriate to extend the rearmost cross-section of the forebody prismatically. However, at high angles-of-attack this extension would generate additional vortices which would interact with those on the forebody. Extending the domain rearwards but not the forebody would result in undesirable baseflow effects. Although not ideal, the answer was to simply truncate the domain at the rear of the forebody.

It was decided to generate all the JAS-39 grids as C-O type with a combination hemispherical/cylindrical outer domain. As before, a half-body mesh was generated and then mirrored to produce a full-body grid symmetric about the pitching plane. The first grid for the forebody without pitot was a single-block grid designated bsl1, where bsl denotes the baseline or 'clean' forebody. Grid size was 74 × 120 × 85 cells in the streamwise, circumferential and radial directions giving 754,800 cells in total. The radius of the hemispherical/cylindrical outer domain was set at 50m full-scale - scaling of all the JAS-39 grids to match model dimensions was done when generating the NSMB database from the ICEM output. Despite being a relatively uncomplicated geometry in terms of topology requirements, considerable time was taken to subdivide the face mapping onto the forebody surface in order that the complex curvature be correctly captured. A view of the bsl1 surface mesh is shown in Fig.(4.5).

Two other baseline grids were subsequently generated. Grid bsl2 shared the same surface mesh as bsl1 but differed in having an improved boundary-layer mesh as well as the farfield extended to 100m radius full-scale. Mesh size was also increased to 74 × 120 × 100, a total of 888,000 cells. Grid bsl3 was generated following convergence problems using grid bsl1 at $\alpha = 60^o$. As angle of attack was increased, the vortex system was exiting the domain further away from the surface of the forebody in regions with much reduced cell densities. It was felt that this was resulting in inadequate resolution of the vortex cores and might be contributing to the poor convergence. The farfield was extended to 100m, more cells were included streamwise on the top of the canopy and at the windscreen/forebody junction and the high cell density region was continued further away from the forebody surface. The resulting grid size was 97 × 140 × 115, a total of 1,561,700 cells.

The addition of the pitot tube to the geometry necessitated a further increase in mesh size due to the scale difference with the main body and the need to capture the vortex wake which would be develop behind the pitot as α increased. A symmetric, single block C-O topology was maintained and, after one test grid had been tried, grid pitot2 was generated, see Fig.(4.6(a)). Grid size was 183 × 148 × 115, a total of 3,114,660 cells. Rather than attempting to model the tip of the pitot accurately at first, a hemispherical cap was positioned over the end for simplicity, see Fig.(4.6(b)). Given the expected importance of pitot tip geometry on the formation of the wake vortices, for grid pitot3 this end-cap was replaced with an additional block which also extended some distance inside the actual pitot. Grid size was increased to 3,321,860.

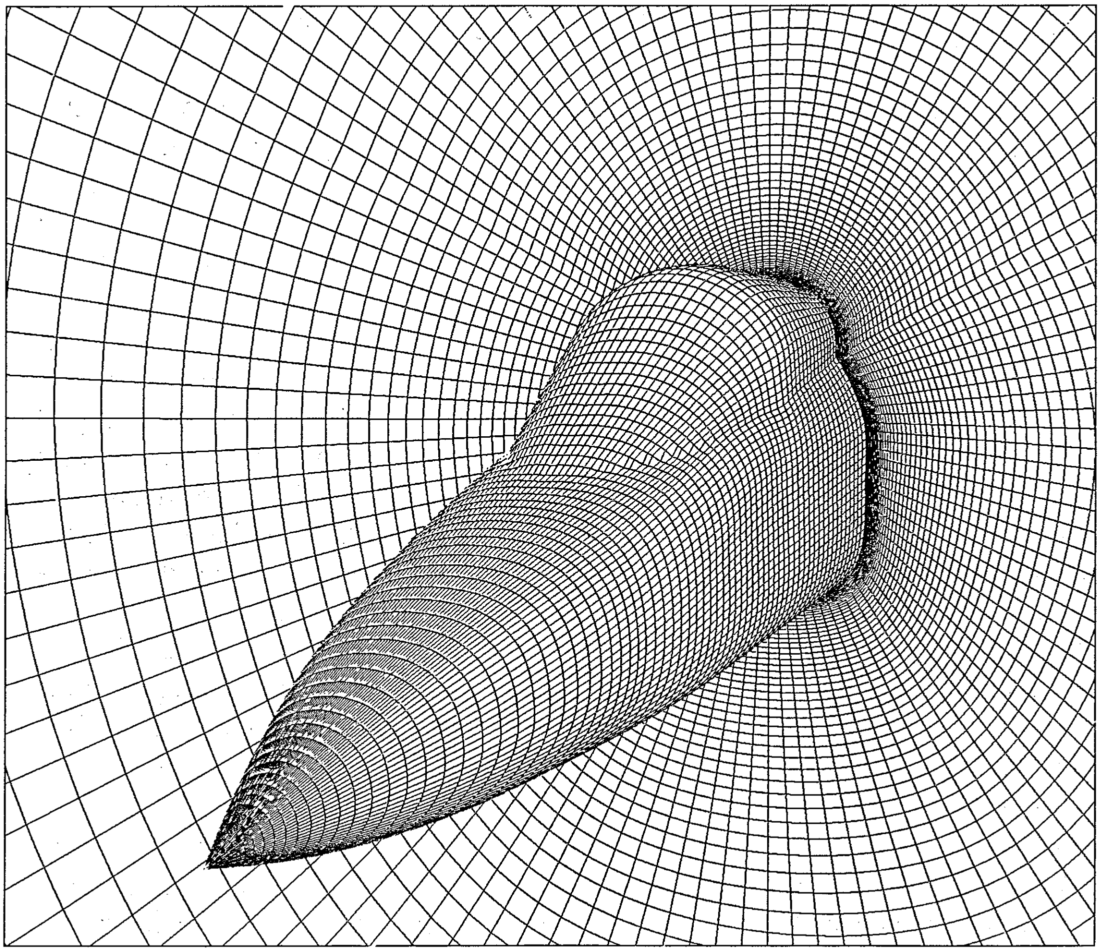

Figure 4.5: Grid bsl2, surface and exit plane mesh.

4.2.2 Boundary conditions

Boundary conditions were unchanged from the final tangent-ogive calculations. The outer domain was judged to be sufficiently far away from the body to allow freestream values

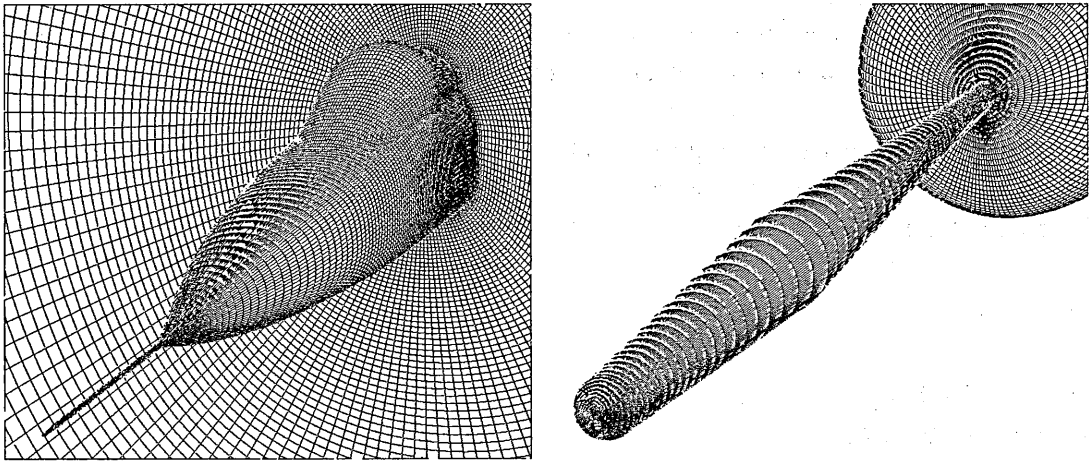

(a) pitot2, surface mesh

(b) pitot2, close-up of pitot

Figure 4.6: Grid pitot2. Surface mesh and close-up view of pitot.

to be applied with the exit condition a simple linear extrapolation. Although not strictly valid as a subsonic exit condition since it does not allow transmission of wake information back upstream, this did not appear to cause major problems in earlier computations and was deemed to be the best of a limited set of options.

4.2.3 Flow conditions

Flow conditions were chosen to match the Saab wind-tunnel experiments described in Section 4.1 and are tabulated in Table (4.2).

Re/m	4,058,823
$Mach\ No.$	0.176
$\rho_{\infty}\ (kg/m^3)$	1.225
$P_{\infty}\ (Pa)$	101325
$T_{\infty}\ (K)$	288.2
$a_{\infty}\ (m/s^2)$	340.3
$U_{\infty}\ (m/s)$	59.89

Table 4.2: Flow conditions, JAS-39 Gripen computations.

4.2.4 Solver setup

The results from the tangent-ogive calculations confirmed that it is possible to generate asymmetric flowfields with NSMB either through the use of geometric tip excrescences or with the asymmetric LU-SGS implicit scheme. Given that the size and placement of the tip excrescence has such an efect on the resulting flowfield, it was decided to continue with the LU-SGS algorithm[1] and central spatial discretisation for all forthcoming calculations on the JAS-39 forebody. The remainder of the solver configuration was established at as close to an optimum as possible using information from the previous testing and was also kept constant for all calculations, changes being limited to CFL numbers and turbulence modelling parameters. A sample input file is included in Appendix B.

4.3 Results

For the clean forebody, fully turbulent computations were made using grids bsl1 and bsl2 for $\alpha = 0^o$, 20^o, 40^o and 50^o with the Spalart-Allmaras and the Menter k-ω-SST models. Computations were also made on grid bsl1 at $\alpha = 0^o$ and 40^o with the standard Wilcox k-ω model, the Wilcox k-ω-LRN model and the baseline Menter k-ω model so that a full comparison could be made as to their relative performance on a complex three-dimensional problem. The data from these additional runs is included as Appendix B. A single, partially converged solution was obtained at $\alpha = 60^o$ using the highly refined grid bsl3 and Spalart-Allmaras.

On addition of the pitot tube, three solutions were obtained using grid pitot2 with the hemispherical end-cap: two at $\alpha = 0^o$ with Spalart-Allmaras and the Menter k-ω-SST models and one at $\alpha = 40^o$ using Spalart-Allmaras. No solution could be obtained using the SST model at the higher angle of attack. Similarly, it proved impossible to achieve any measure of code stability with the more complex geometry of grid pitot3, even at $\alpha = 0^o$. For more detailed information on the computations made see Table (4.3).

The sections that follow cover force and residual convergence and flow structure and development with increasing α including comparison with experiment.

For each case the following graphical information is shown: the normalised density-residual convergence history; comparison of computed and experimental surface C_p at 14 cross-sections[2]; pitot pressure ratio contours at 12 selected cross-sections.

4.3.1 Convergence

As mentioned in the description of the code, NSMB is continually being developed and improved. One weak point of versions of the code used in the first stages of this research was the lack of convergence information that could be output or saved. The normalised residual of one of the flow variables could be monitored and force information was limited to C_L, C_D and C_M. Grid orientation allowed β to be used instead of α to set incidence for the tangent-ogive calculations in Chapter 3 and meant that the C_L convergence history actually represented evolution of side force rather than lift. This version of the code was used for most computations using grid bsl1 but subsequent calculations employed a

---

[1] Scalar implicit was used rather than full matrix-implicit due to the 256Mb/node memory limitation on the T3E.

[2] n.b. $-C_p$ is plotted to give suction peaks, rather than troughs.

later version of the code with full convergence history reporting for the flow variables, forces and moments. This enables time-evolution graphs of normal and side force to be presented. n.b. Force plots show pressure forces only and with respect to body axes.

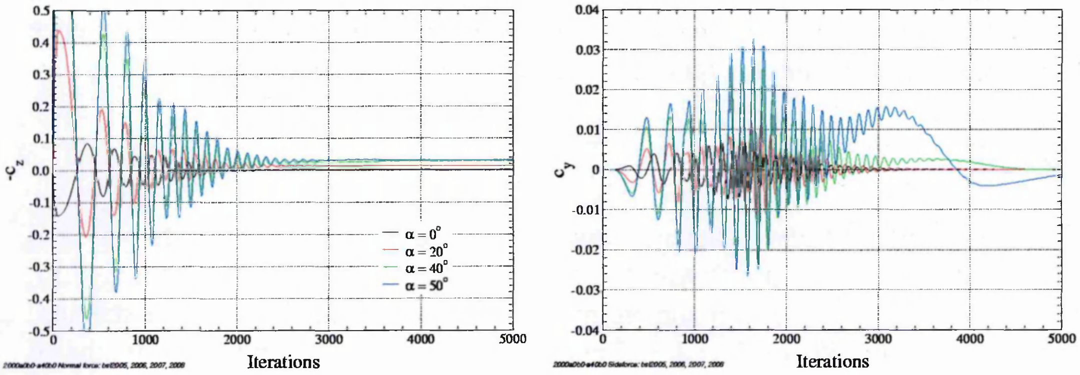

(a) Normal force

(b) Side force

Figure 4.7: *JAS-39 grid bsl2 M=0.176, Re=4.06 × 10^6, α=0^o - 50^o, Menter k-ω-SST turbulence model. Comparison of convergence of normal and side-force coefficients with increasing α for the clean (baseline) forebody.*

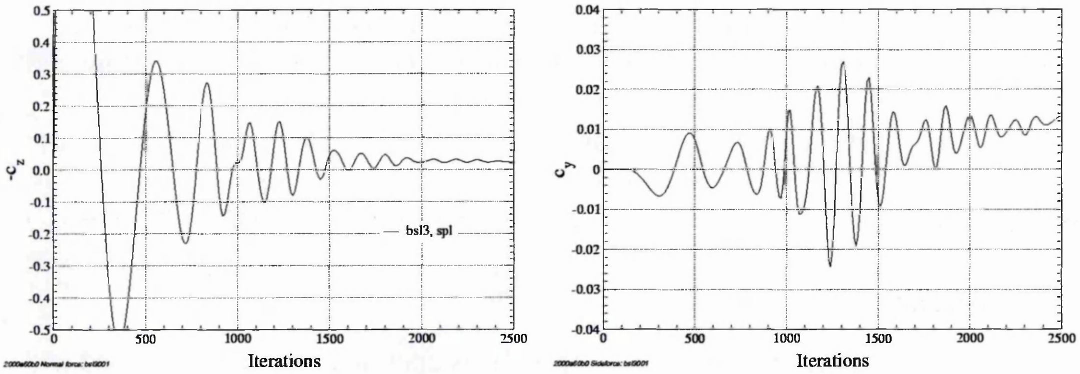

(a) Normal force

(b) Side force

Figure 4.8: *JAS-39 grid bsl3 M=0.176, Re=4.06 × 10^6, α=60^o, Spalart-Allmaras turbulence model. Convergence history of normal-force and side-force coeffcients prior to crash.*

The normal force and sideforce convergence histories for grid bsl2, $0^o \leq \alpha \leq 50^0$ are shown in Fig.(4.7). Each of these k-ω-SST computations was run for 5000 iterations and then checked for force and residual convergence. Although the side force at $\alpha = 50^o$

has not fully settled, CPU time was at a premium and unfortunately it was not possible to continue the calculation. It can be seen that the magnitude of the oscillations in both normal and side force during convergence grows as α is increased but that, with the exception of the $\alpha = 0^o$ run, the period remains constant . The equivalent graphs for the $\alpha = 60^o$ run on grid bsl3 are shown in Fig.(4.8). Following failure with the smaller grids bsl1 and bsl2 at $\alpha = 60^o$, this calculation was run with the more stable Spalart-Allmaras model and checkpointed every few hundred iterations in anticipation of a problem. Consequently, the presented results are a snapshot of the flow after 2500 iterations and prior to the code crash. No indications of imminent problems can be seen - the normal force is settling and the side force value is behaving in a similar manner to the bsl2 calculations at lower α. After investigation, it appears that the convergence problem stemmed from the turbulence variable, see Fig.(4.36), but could not be solved. The fact that no k-ω-SST solution could be obtained whatsoever is surprising given the relative performance of the models at $\alpha = 50^o$, see Fig.(4.31).

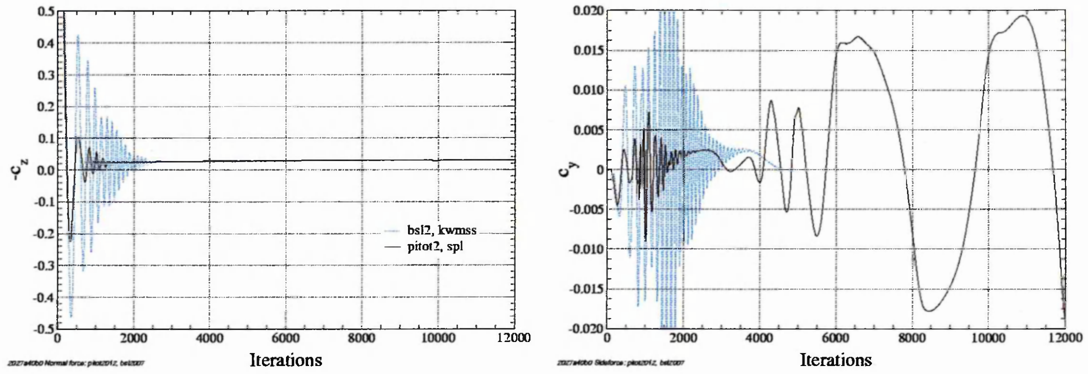

(a) Normal force

(b) Side force

Figure 4.9: *JAS-39 grids bsl2, pitot2, M=0.176, Re=4.06 × 10^6, α=40°. Comparison of normal and side-force coefficients for the clean (baseline) forebody, grid bsl2, and the forebody with pitot-tube and hemispherical end-cap.*

For almost all cases, bsl2 solutions converged significantly better than bsl1 solutions regardless of turbulence model. This can be attributed to a number of improvements in the second grid: the cell distribution in the boundary layer was improved with the minimum y^+ increasing from a rather low 0.1 to a more acceptable 0.8-1.0 and the growth factor away from the wall becoming less severe; more cells were placed in the near body region with the hope of increased location stability for the vortex cores; lastly, the cells were smoothed around the canopy/windscreen junction with the forebody. These improvements equated to approximately half an order reduction in residual after 5000 iterations, see Fig.(4.26).

The effect on convergence of the addition of the pitot tube to the problem is shown in Fig.(4.9) for $\alpha = 40^o$. The normal force settles to a steady value faster than for the baseline geometry, although this may be due to the different turbulence models, but the side force enters into non-sinusoidal oscillations of increasing magnitude. This can be attributed to the vortical wake from the pitot influencing the main forebody flowfield. Unfortunately, this computation could not be continued further due to CPU time constraints.

Global force coefficients are tabulated in Table (4.3). Agreement between the models is generally good, although some scatter appears at the higher angles.

Configuration	Grid	α (°)	Model	Run	C_x	C_y	C_z
Clean	bsl1	0	spl	001	0.00220	0.00000	-0.00070
			kwwh	054	0.00177	0.00000	-0.00055
			kwwl	055	0.00183	0.00001	-0.00042
			kwmbs	056	0.00165	0.00000	-0.00071
			kwmss	057	0.00151	0.00000	-0.00074
	bsl2	0	spl	001	0.00260	0.00000	-0.00060
			kwmss	005	0.00156	0.00000	-0.00076
	bsl1	20	spl	002	0.00450	0.00000	-0.01270
			kwmss	063	0.00378	0.00002	-0.01257
	bsl2	20	spl	002	0.00500	0.00000	-0.01280
			kwmss	006	0.00388	0.00002	-0.01258
	bsl1	40	spl	003	0.01290	-0.00020	-0.02790
			kwwh	058	0.01220	0.00016	-0.02785
			kwwl	059	0.01236	0.00017	-0.02722
			kwmbs	060	0.01221	0.00040	-0.02786
			kwmss	061	0.01231	0.00019	-0.02825
	bsl2	40	spl	003	0.01340	-0.00010	-0.02750
			kwmss	007	0.01184	-0.00013	-0.02682
	bsl1	50	spl	005	0.02010	-0.00500	-0.03430
			kwmss	062	0.01898	0.00136	-0.03339
	bsl2	50	spl	004	0.01950	-0.00210	-0.03160
			kwmss	008	0.01761	-0.00143	-0.03076
	bsl3	60	spl	001	0.01605	0.01300	-0.02382
			kwmss	002	- crash -		
Pitot (Rounded-tip)	pitot2	0	spl	002	0.00187	0.00000	-0.00079
			kwmss	006	0.00151	0.00000	-0.00084
	pitot2	40	spl	004	0.01356	-0.00789	-0.02893
			kwmss	008	- crash -		
Pitot (Actual tip)	pitot3	0	spl	001	- crash -		
			kwmss	002	- crash -		

Table 4.3: JAS-39 forebody forces. Comparison for grids and turbulence models. All forces comprise pressure and viscous components and are with respect to wind axes.

4.3.2 Baseline body

$\alpha = 0^o$, Figs.(4.16) - (4.20) Computed C_p generally follows the character of the flow but is consistently higher than experimental values at all cross-sections. Aside from an inexplicable bsl1 Spalart-Allmaras result at section 01, Fig.(4.17(a)), no variation can be discerned between the four sets of computed data. The profiles around the canopy region are generally well predicted but the suction peaks at $\theta \approx 30^o, 330^o$ are underpredicted at Section 13, Fig.(4.19(e)), which co-incides with the windscreen/canopy junction, a region of high curvature hence rapid flow acceleration. Slight oscillations in C_p are also visible at $\theta \approx 45^o, 315^o$ at sections 13 and 14, see Figs.(4.19(e)) & (4.19(f)), indicating a cell resolution problem at the canopy/forebody junction.

$\alpha = 20^o$, Figs.(4.21) - (4.25) It can be seen from Fig.(4.22(a)) that, at section 01, C_p along the windward meridian is overpredicted and experimental data show signs that the flow should be laminar at this point. For sections 02-07, Figs.(4.23(e)) - (4.23(e)), there is a visible kink in the pressure distribution at $\theta \approx 90^o, 270^o$ corresponding to a flattening of the forebody sides, see Fig.(4.3). Moving further aft, the computed C_p profiles generally agree well with each other and with the experimental data between sections 09 and 13 but the Menter SST model predicts slightly higher pressure for $\theta \approx \pm 30^0$ of the leeward meridian for sections 10 and 11. This corresponds to the high pressure region at the base of the windscreen. Grid and turbulence model effects are negligible forward of the cockpit region. Flow structure at section 14, Fig.(4.24(f)), is well predicted but the vortices are clearly weaker than the experimental data shows: the suction peaks at $\theta \approx 30^0, 330^o$ are at 0.1 below experimental values. The secondary peaks at $\theta \approx 60^0, 300^o$, corresponding to the shoulder of the cross-section, are almost resolved but there is interference from the canopy/body junction.

$\alpha = 40^o$, Figs.(4.26) - (4.30) The four computations are well converged and the attachment line C_p is well predicted at all sections. Unlike at lower α, however, differences are visible between the models from section 01, Fig.(4.27(a)). Whereas the computed profiles are fully turbulent and predict peak suction at $\theta \approx 110^o$, the experimental data clearly show laminar separation occurring at $\theta \approx 90^o$ followed by a possible reattachment after transition to form a laminar bubble. A primary vortex has been picked up by all four cases, with the bsl2 SST giving the greatest vortex strength. Both bsl2 profiles show marginally greater suction than the bsl1 results, possibly due to the improved boundary-layer and near-wall meshing. By section 04, Fig.(4.28(b)), there are clear double peaks at $\theta \approx 70^o, 90^o$ and $\theta \approx 270^o, 290^o$, these probably corresponding to flow reattachment. Not enough experimental data points exist to enable fine-scale comparisons to be made, but the double peaks are repeated at successive streamwise stations and appear to match well the shape of the experimental profiles, although suction is slightly underpredicted. Moving further aft, from section 06 onwards the primary vortex suction peak is slightly better matched by the bsl2 results, but overall the computed profiles compare reasonably well with experiment.

The effect of the canopy in reducing the interaction between the two primary vortices can clearly be seen in the pitot pressure ratio contours, see Fig.(4.30). At this angle, $\alpha = 40^o$, the vortices remain close to the forebody and so the canopy acts as a mild splitter, helping to maintain symmetry.

As an additional aid to visualising of the flow, surface particle pathlines, equivalent to what would be obtained from oilflow in the wind tunnel, are shown in Fig.(4.10). The pathlines clearly show the locii of both primary and secondary separations running the length of the body almost symmetrically and a tertiary separation line beginning to form towards the rear of the canopy.

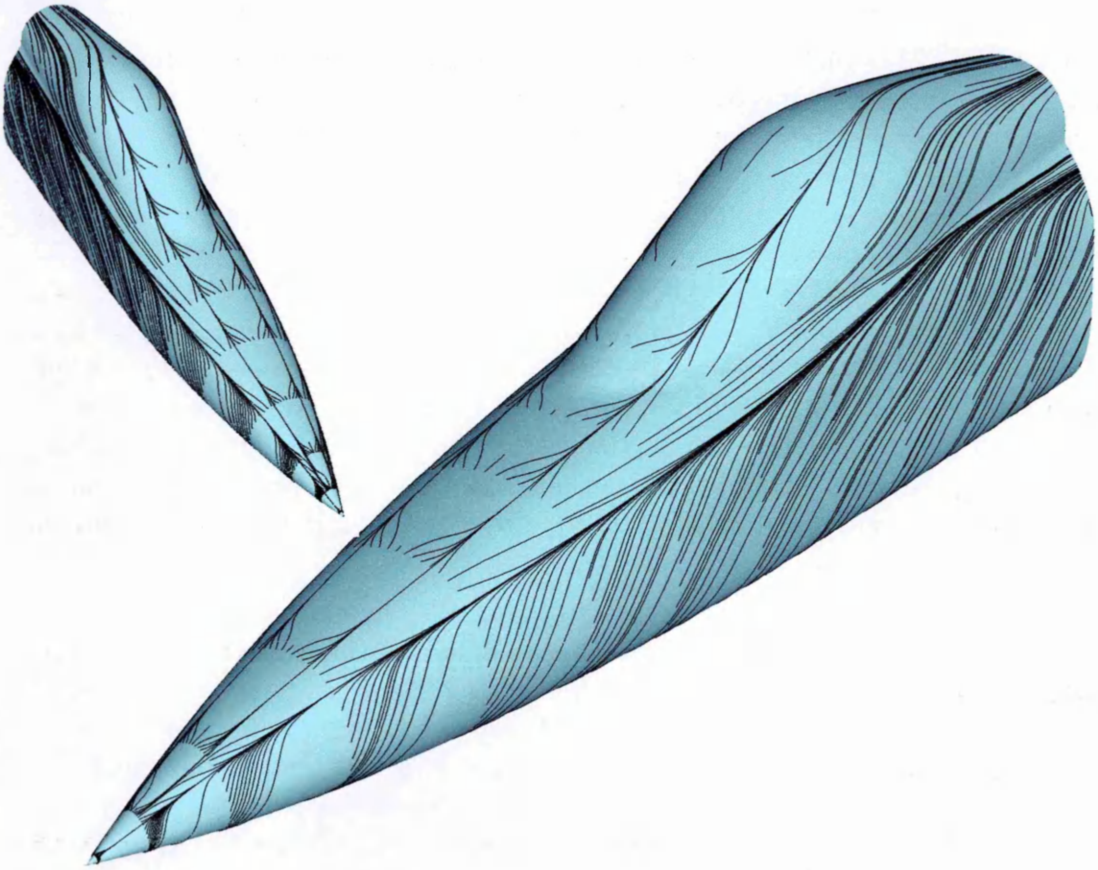

Figure 4.10: *JAS-39 grid bsl2,* M*=0.176,* Re*=4.06 × 10^6,* α*=40°. Surface particle pathlines showing the locii of separation.*

$\alpha = 50^o$, **Figs.(4.31) - (4.35)** Once again, there is very poor correlation over the top half of the forebody at section 01, see Fig.(4.32(a)). The experimental C_p values show a sharp drop off in suction at $\theta \approx 90^o, 270^o$ followed by rises at $\theta \approx 30^o, 330^o$ generated by the suction from the primary vortices. These secondary peaks remain in the computed solutions at all forebody sections, but disappear from the experimental data until section 06, Fig.(4.33(d)). It is assumed that this is due to inadequate numbers of pressure taps leading to poor resolution. Interestingly, despite the strong suction of the primary vortex pair and growing complexity of the wake at this relatively high angle, *the dominant suction peaks still result from the boundary layer.* Grid differences are once again manifested with the bsl1 calculations overpredicting the suction from the primary vortices as before. Greater differences are also visible between the two turbulence models on the earlier grid. All four computed solutions show a degree of asymmetry, unlike at lower α, although there is a poor match with the experimental data. From the contours of pitot pressure ratio, Fig.(4.35), it is clear that the primary vortices have lifted away from the surface substantially more than at $\alpha = 40^o$. This has reduced the influence of the canopy, allowing the vortices to interact more with each other, reducing the stability of the wake and resulting in increased oscillations during convergence, see Fig.(4.31) (c.f. Fig.(4.26)).

$\alpha = 60^o$, **Figs.(4.36) - (4.40)** No solution could be attained with the k-ω-SST model, even on grid bsl3, thus all data comes from a successful Spalart-Allmaras bsl3 computation. Noticeable asymmetry is visible from section 01 in the experimental data and, after flipping the computed profile to match the orientation of the flowfield, the magnitudes of the primary suction peaks are matched by the calculation. However, as at lower α, prediction of the secondary suction peaks is very poor both in terms of location and magnitude. The poor correlation with experiment continues moving further aft, improvements beginning after section 06. Although the experimental data for sections 09-14 show suction over the leeward meridian, this is not picked up in the computed solution, no doubt due to under-developed secondary vortices and boundary-layer structure either side of $\theta = 0^o$. However, given that this is a partially converged solution and the viscous features have not had time to be fully resolved, the agreement with experiment towards the rear of the forebody is still remarkably good.

4.3.3 Addition of pitot tube

$\alpha = 0^o$, **Figs.(4.41) - (4.45)** Very little can be said about this zero-incidence calculation since the turbulence models produced almost identical results with the computed profiles agreeing well with experiment. However, as with the clean forebody, the C_p is consistently underpredicted the length of the forebody. Cell resolution along the canopy/forebody junction is evidently still an issue for this grid, with minor oscillations in the pressure coefficients at $\theta \approx 45^o, 315^o$.

$\alpha = 40^o$, **Figs.(4.46) - (4.50)** As modelled, the JAS-39 pitot tube is effectively a gently tapering cylinder of aspect ratio ≈ 30 with a hemispherical end. As would be expected, when placed at 40^o incidence, the pitot develops a complex, and in reality probably time-dependent, vortical wake which envelops the nose of the aircraft. Consequently, whereas convergence and side force for the clean configuration were relatively stable at $\alpha = 40^o$, the addition of the pitot tube resulted in the calculation being destabilised and an asymmetric solution evolving. No k-ω-SST solution could be obtained at this higher angle of attack.

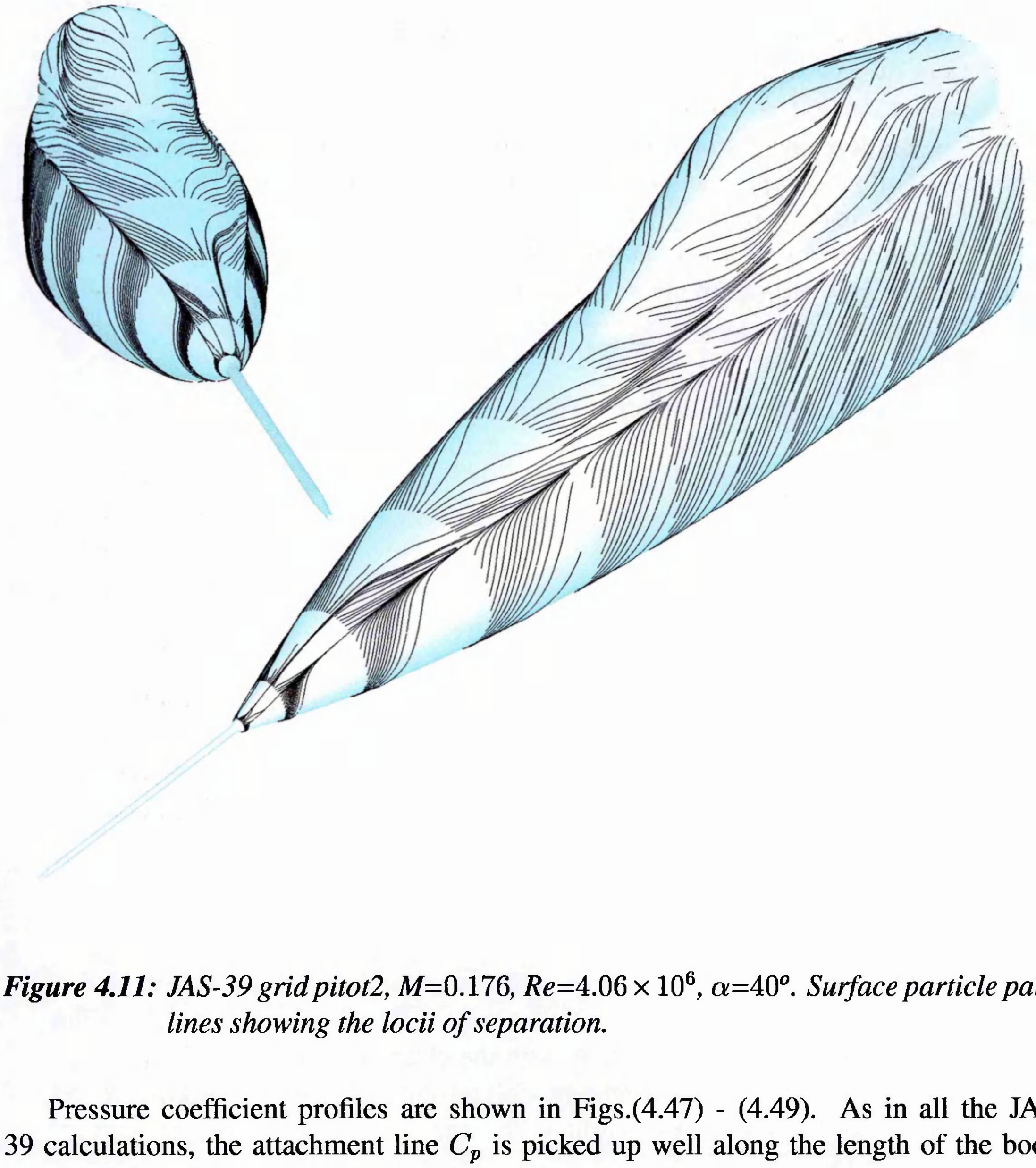

Figure 4.11: *JAS-39 grid pitot2, M=0.176, Re=4.06 × 10^6, α=40°. Surface particle pathlines showing the locii of separation.*

Pressure coefficient profiles are shown in Figs.(4.47) - (4.49). As in all the JAS-39 calculations, the attachment line C_p is picked up well along the length of the body. In contrast to the clean forebody, without the pitot tube, the experimental data shows visible asymmetry in the first few sections, mainly on the upper surface rather than in the boundary layer. The reason for this becomes clear on examination of the corresponding pitot pressure ratio contour plots, Fig.(4.50). As expected, the vortical wake from the pitot tube immerses the nose and causes a highly asymmetric flowfield to develop over the length of the body, see Fig.(4.12). Detachment of the shear layer becomes pronounced on the port side, with the starboard shear layers and vortex system remaining attached to the body, see Figs.(4.50(g)) - (4.50(l)), generating high suction forces. Interestingly, although side force for this configuration is significantly higher than for the baseline geometry, Table (4.3), there is little increase in normal force, presumably since the port-side vortex is so detached from the surface of the forebody that it counter-balances the increased suction from the starboard system. Encouragingly, despite the complexity of the flowfield and the solution being only partially converged, the computed pressure coefficient profiles appear to match the experimental data well.

Surface particle pathlines for the case are shown in Fig.(4.11). When compared to Fig.(4.10), Fig.(4.11) reveals the symmetric nature of the primary and secondary separations present on the baseline configuration to have changed considerably, particularly in the nose region. Although the primary separation lines remain roughly symmetric, there are secondary separation locii briefly visible just aft of the pitot. Further downstream, stronger secondary separations appear over the canopy. Figs.(4.14) - (4.15) depict

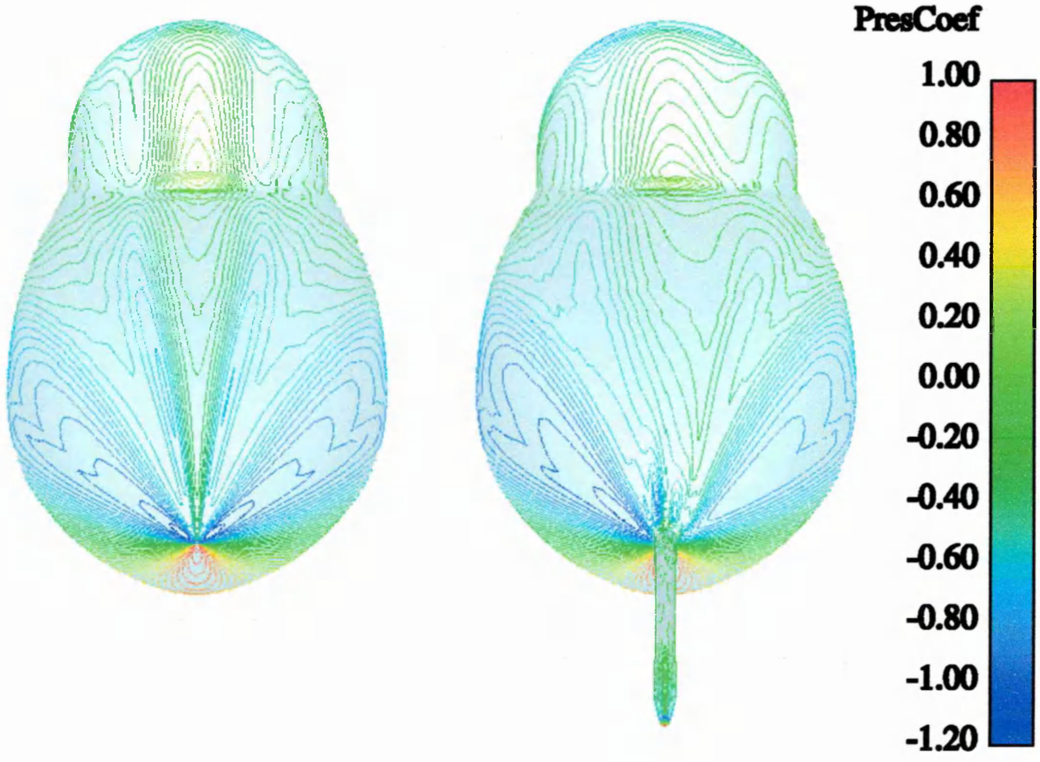

(a) bsl2, k-ω-SST (b) pitot2, Spalart-Allmaras

Figure 4.12: *JAS-39 grids bsl2, & pitot2,* M=0.176, Re=4.06 × 10^6, α=40^o. *Effect of pitot on surface pressure coefficient.*

velocity vector arrows at cross-sections down the body for the clean geometry and the forebody with pitot tube respectively for an incidence of 40^o. When considered alongside Figs.(4.10) - (4.11), these plots allow a more complete visualisation to be made of the three-dimensional flow development down the length of the forebody. It also becomes possible to generate schematic representations of the flow cross-sections using the rules of topology, see [116]. Fig.(4.13), reproduced from Peake and Tobak, [101], shows examples of the changing cross-sectional flow topology for a slender forebody with increasing relative incidence. As previously mentioned, it is possible for any asymmetric disturbance originating at the apex to be amplified at the enclosing saddle point due to the inherent instability of the inflecting velocity vectors. Given an initial left-hand asymmetric bias, the vorticity on that side increases, the primary vortex enlarges and moves away from the surface of the body, see Fig.(4.13(a)). Increasing α causes the shear layer feeding the primary to stretch, Fig.(4.13(b)), until the secondary vortices become unsteady and the primary is shed, see Fig.(4.13(c)). At this point, the third complete vortex becomes fully formed, with the two co-rotating left-hand vortices separated by an internal saddle point, Fig.(4.13(d)). The right-hand primary then increases in strength and the cycle begins again on that side, Fig.(4.13(e)). Whilst the flow around the baseline JAS-39 geometry is still largely symmetric at $\alpha = 40^o$, therefore approximating Fig.(4.13(a)) in cross-sectional topology, the asymmetric forebody flow induced by the addition of the pitot tube is clearly more akin to Fig.(4.13(b)).

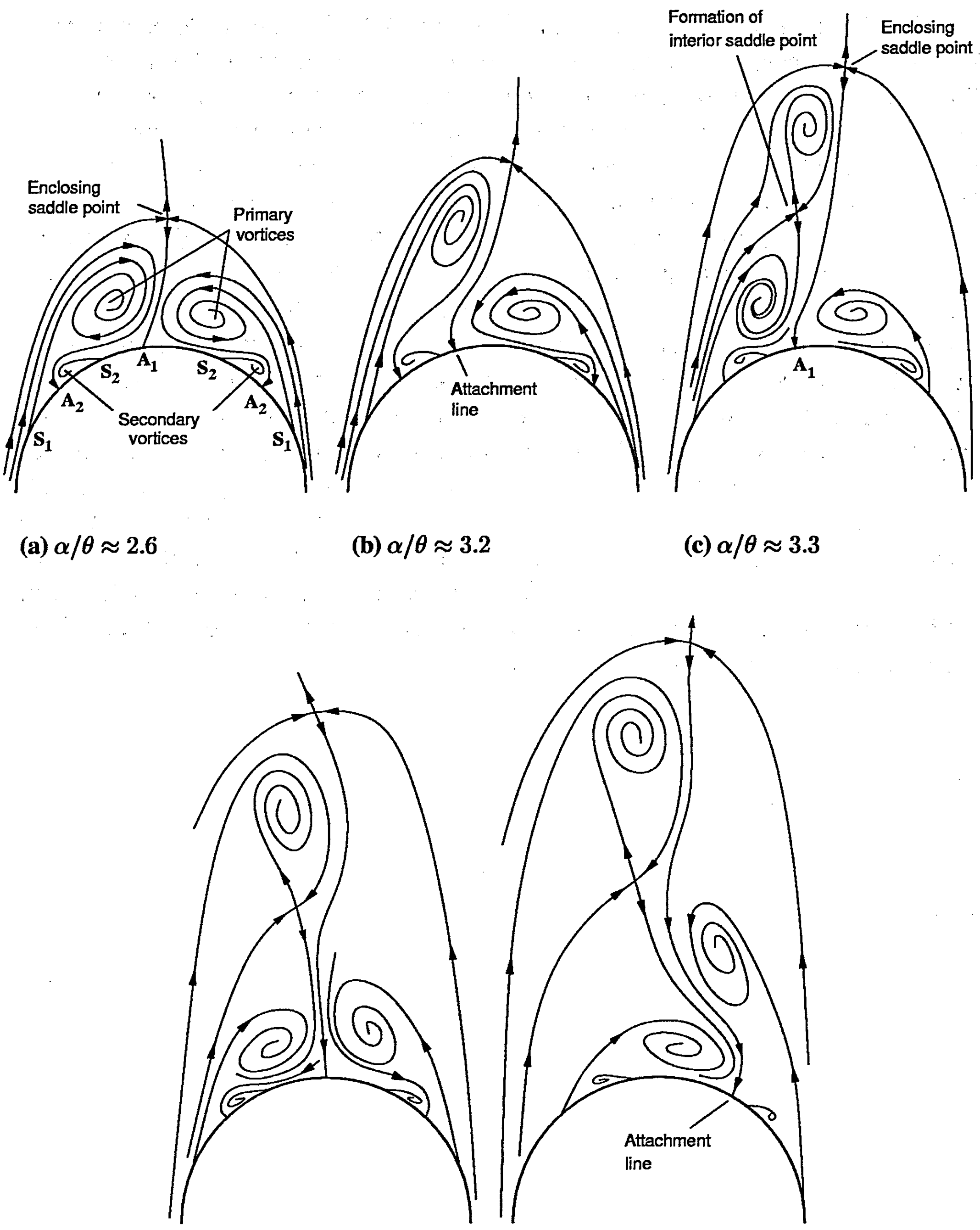

(a) $\alpha/\theta \approx 2.6$ (b) $\alpha/\theta \approx 3.2$ (c) $\alpha/\theta \approx 3.3$

(d) $\alpha/\theta \approx 3.4$ (e) $\alpha/\theta \approx 3.6$

Figure 4.13: *Schematic representation of the changing cross-sectional flow topology of a slender forebody with increasing incidence. θ denotes nose semi-apex angle. Figure from Peake & Tobak, [101].*

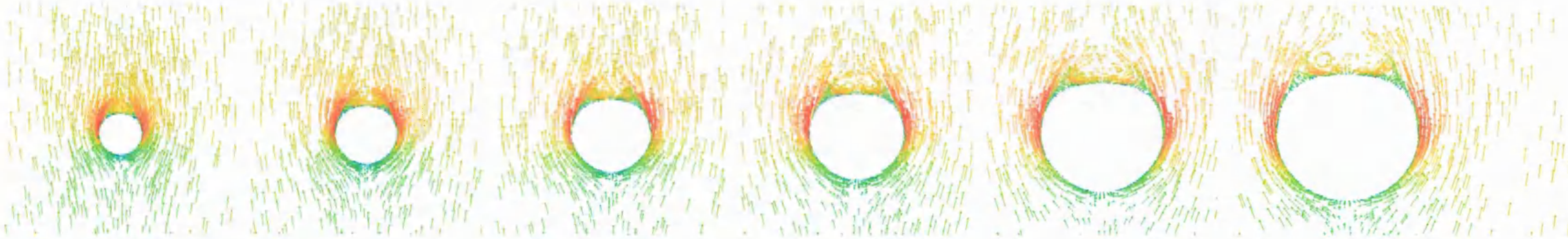

(a) Section 01 (b) Section 02 (c) Section 03 (d) Section 04 (e) Section 06 (f) Section 07

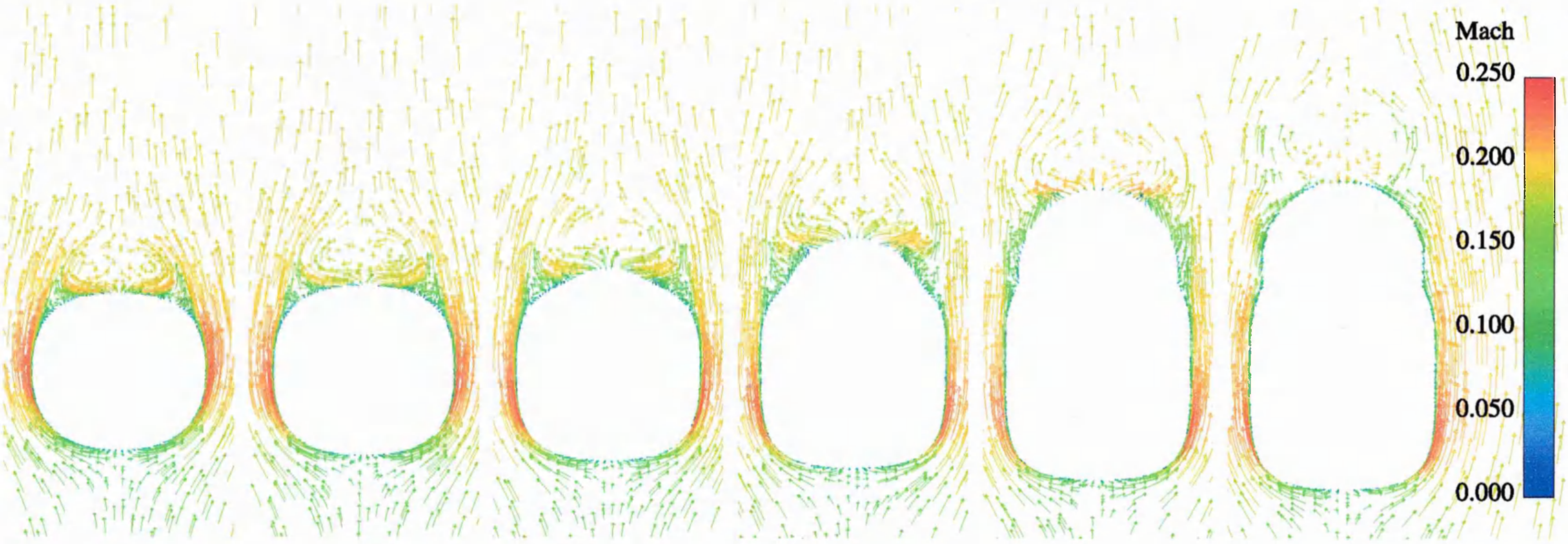

(g) Section 09 (h) Section 10 (i) Section 11 (j) Section 12 (k) Section 13 (l) Section 14

Figure 4.14: *JAS-39 grid bsl2, M*=0.176, *Re*=4.06 × 10^6, α=40°. *Velocity vectors, Menter k-ω-SST model.*

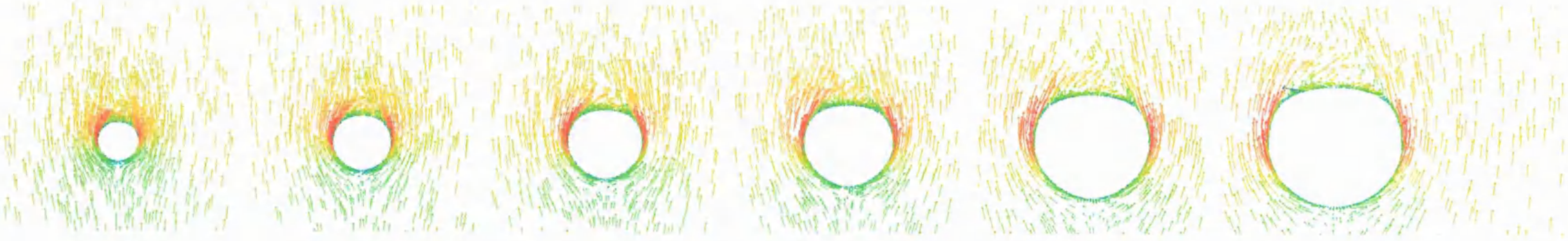

(a) Section 01 (b) Section 02 (c) Section 03 (d) Section 04 (e) Section 06 (f) Section 07

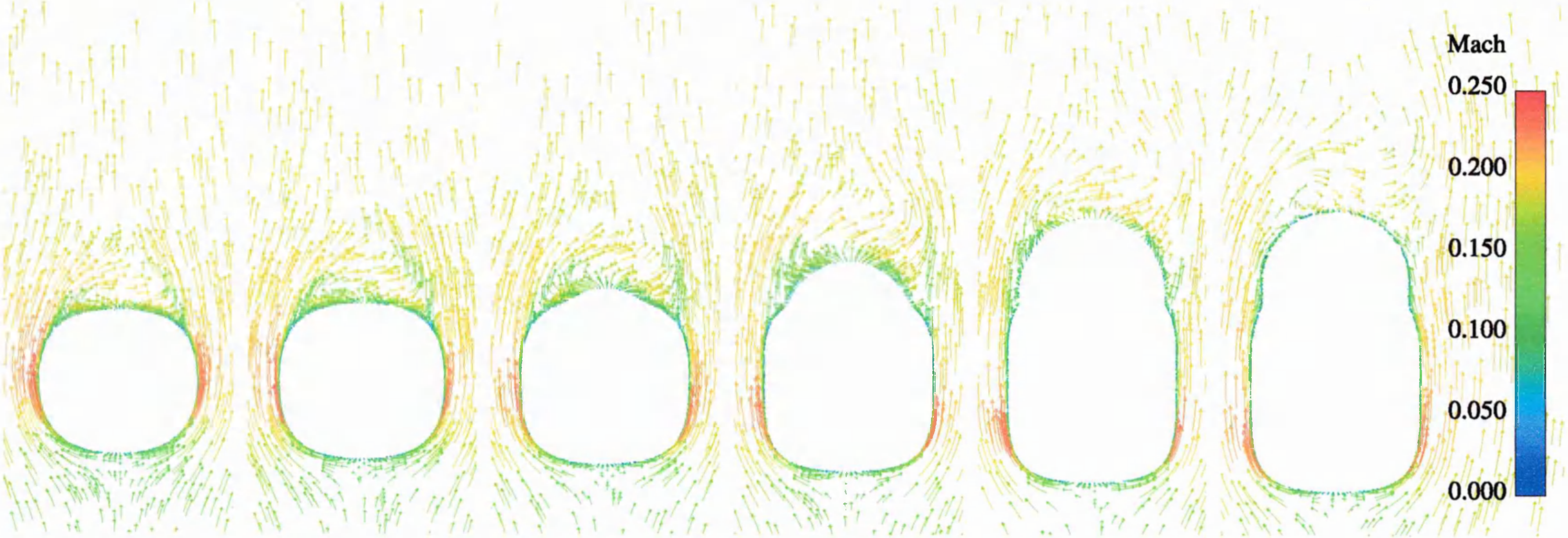

(g) Section 09 (h) Section 10 (i) Section 11 (j) Section 12 (k) Section 13 (l) Section 14

Figure 4.15: *JAS-39 grid pitot2,* M=0.176, Re=4.06 × 10^6, α=40^o. *Velocity vectors, Spalart-Allmaras model.*

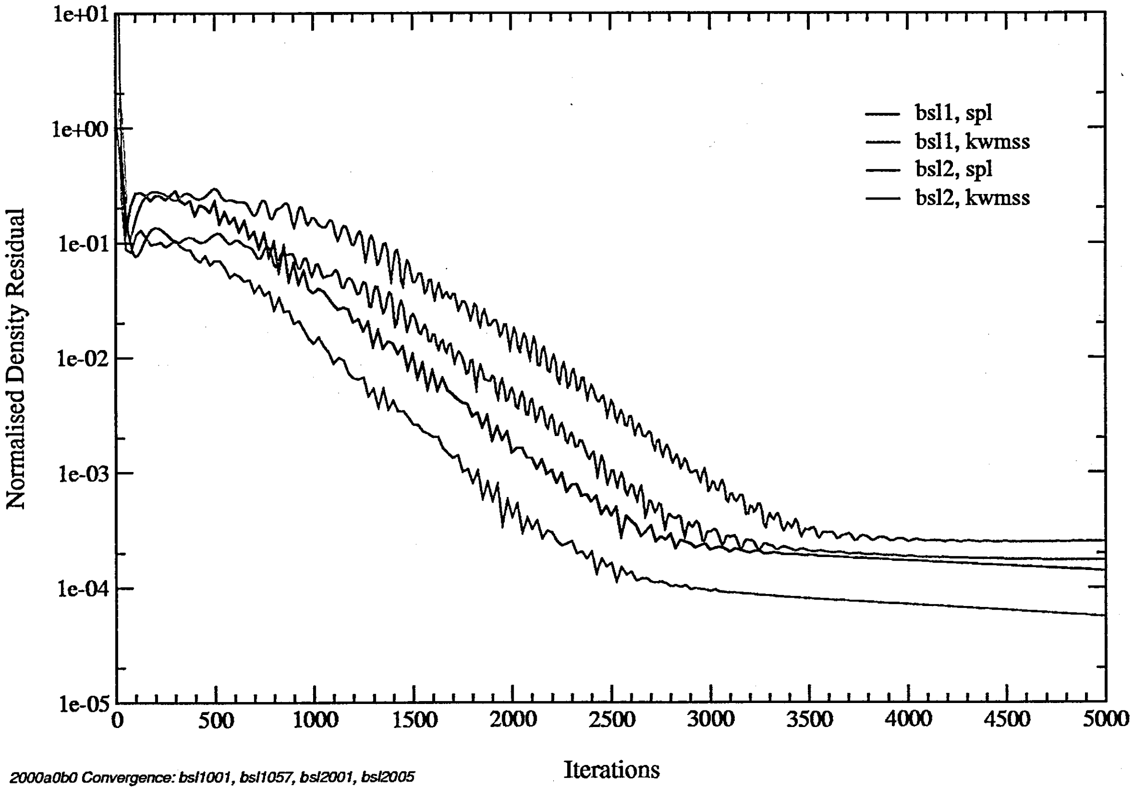

Figure 4.16: *JAS-39 grids bsl1 & bsl2, M=0.176, Re=4.06 × 10^6, α=0°. Comparison of turbulence model density residual convergence history.*

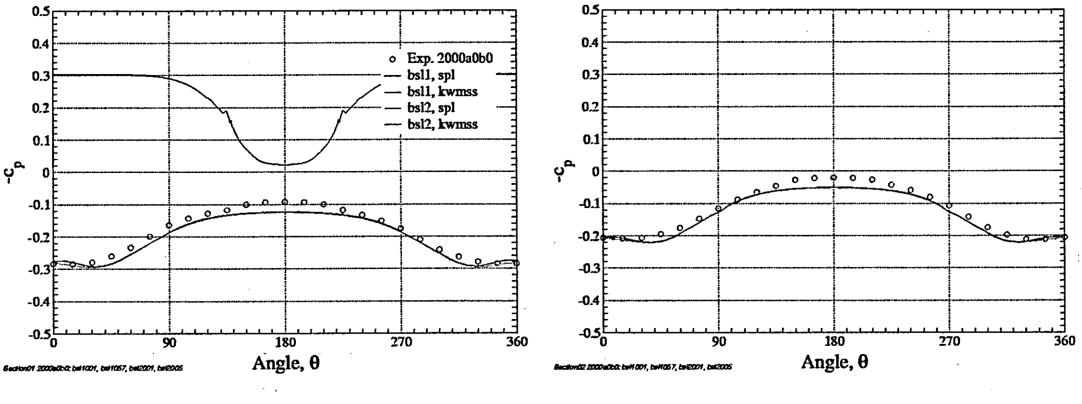

(a) Section 01

(b) Section 02

Figure 4.17: *JAS-39 grids bsl1 & bsl2, M=0.176, Re=4.06 × 10^6, α=0°. Circumferential c_p distributions, sections 01 & 02. Comparison of turbulence models and grid effects.*

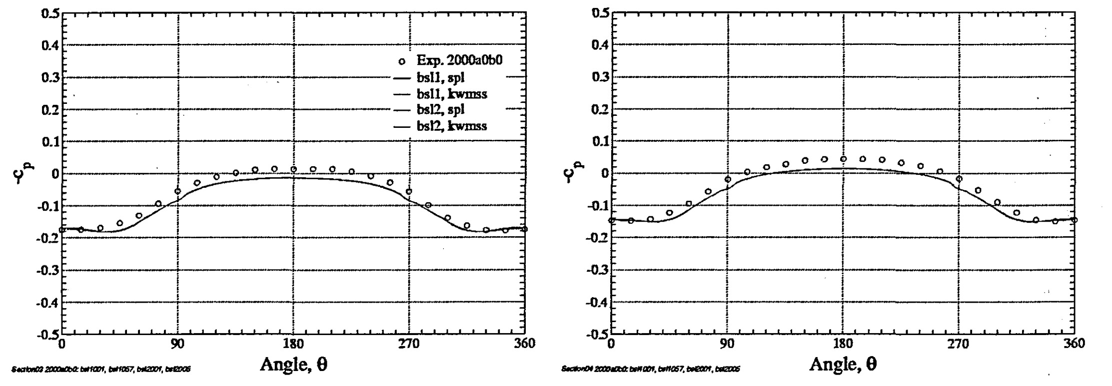

(a) Section 03

(b) Section 04

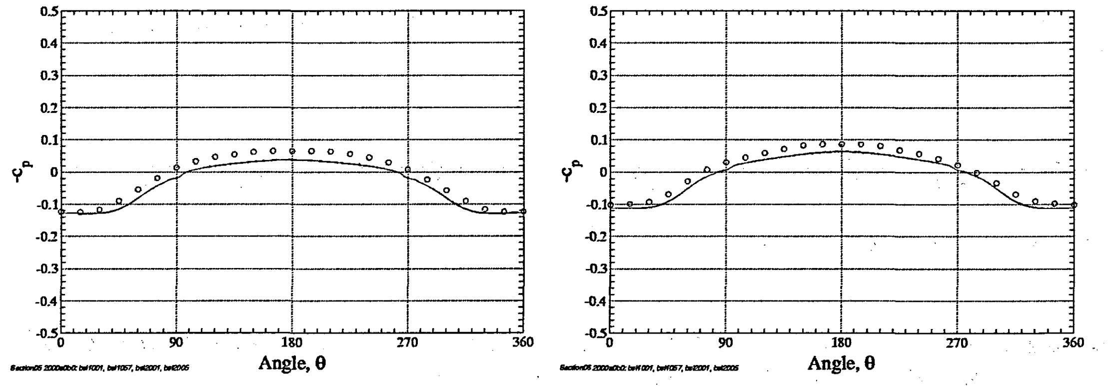

(c) Section 05

(d) Section 06

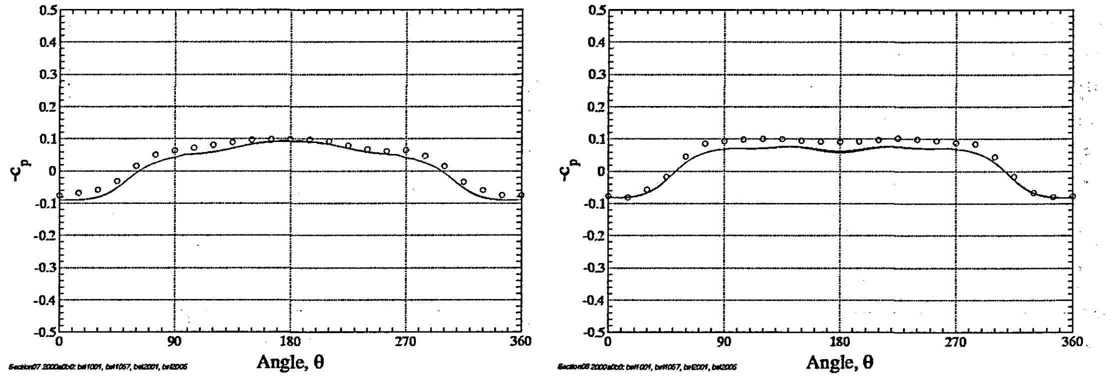

(e) Section 07

(f) Section 08

Figure 4.18: ***JAS-39 grids bsl1 & bsl2, M=0.176, Re=4.06×10^6, $\alpha=0^o$. Circumferential c_p distributions, sections 03-08. Comparison of turbulence models and grid effects.***

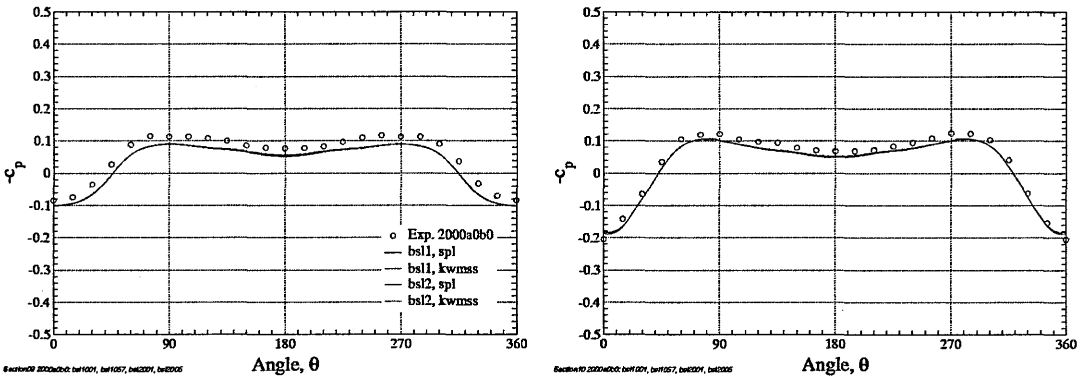

(a) Section 09

(b) Section 10

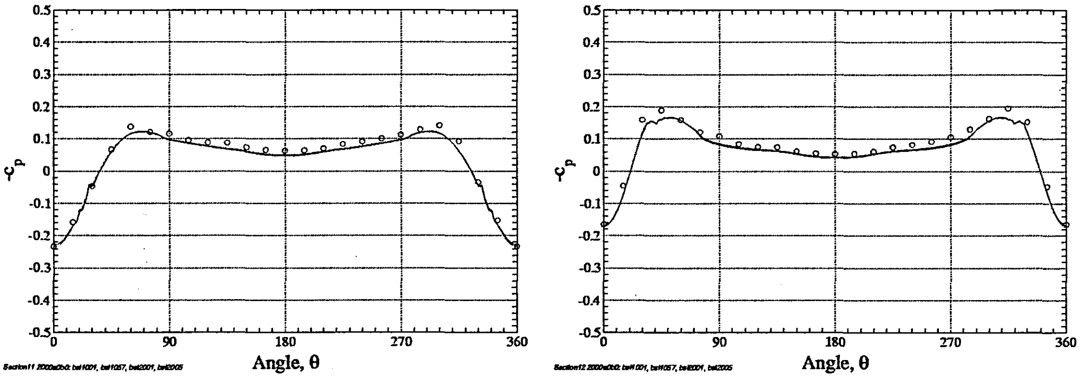

(c) Section 11

(d) Section 12

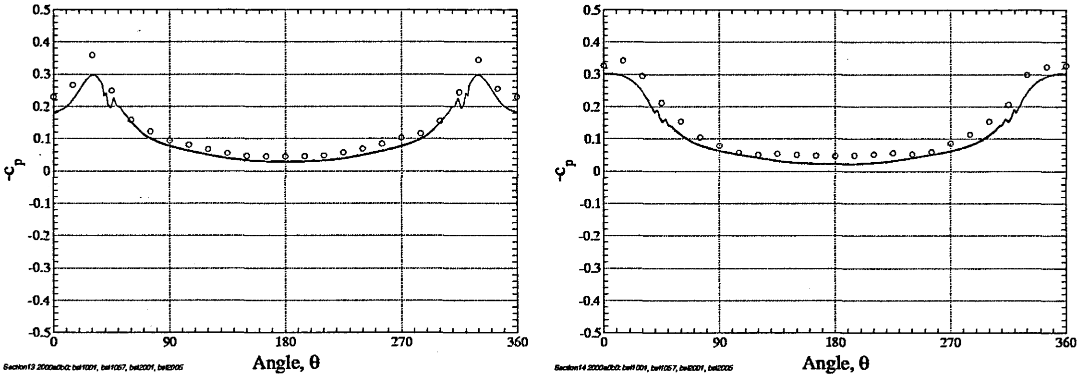

(e) Section 13

(f) Section 14

Figure 4.19: ***JAS-39 grids bsl1 & bsl2, $M=0.176$, $Re=4.06\times10^6$, $\alpha=0^o$. Circumferential c_p distributions, sections 09-14. Comparison of turbulence models and grid effects.***

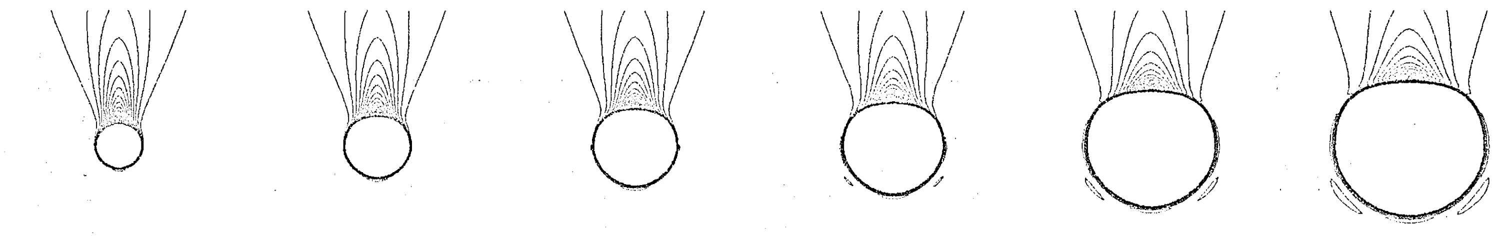

(a) Section 01 (b) Section 02 (c) Section 03 (d) Section 04 (e) Section 06 (f) Section 07

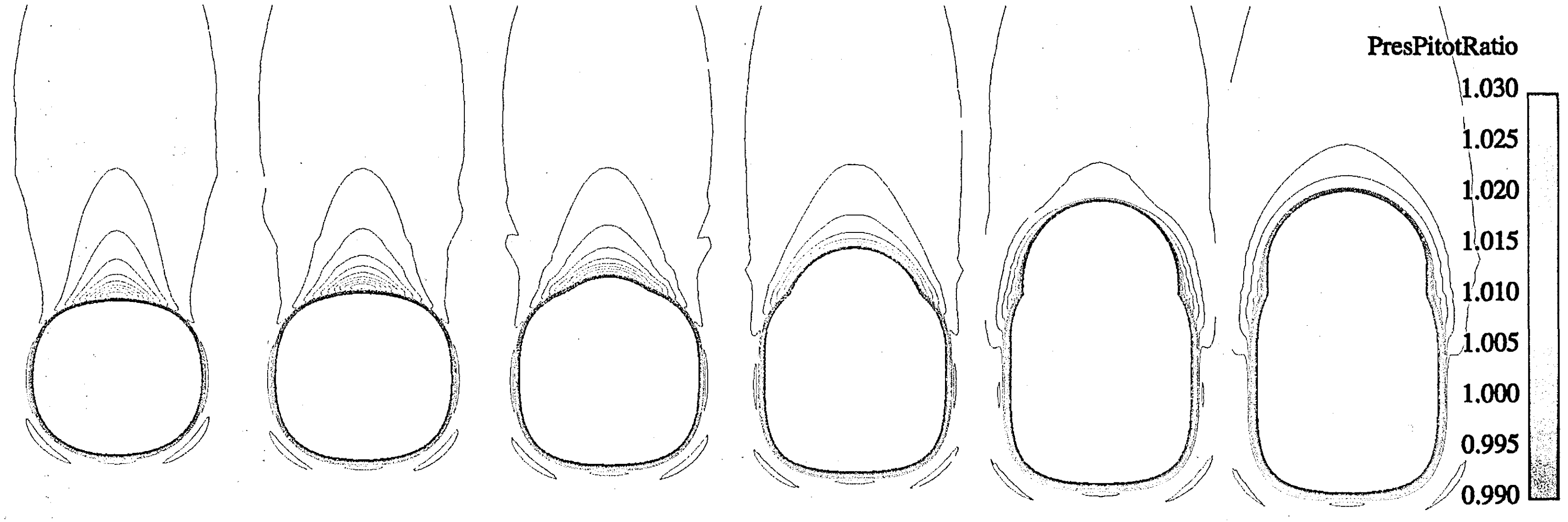

(g) Section 09 (h) Section 10 (i) Section 11 (j) Section 12 (k) Section 13 (l) Section 14

Figure 4.20: *JAS-39 grid bsl2,* M=0.176, Re=4.06 × 10^6, α=0°. *Contours of pitot pressure ratio, Menter* k-ω-SST *model.*

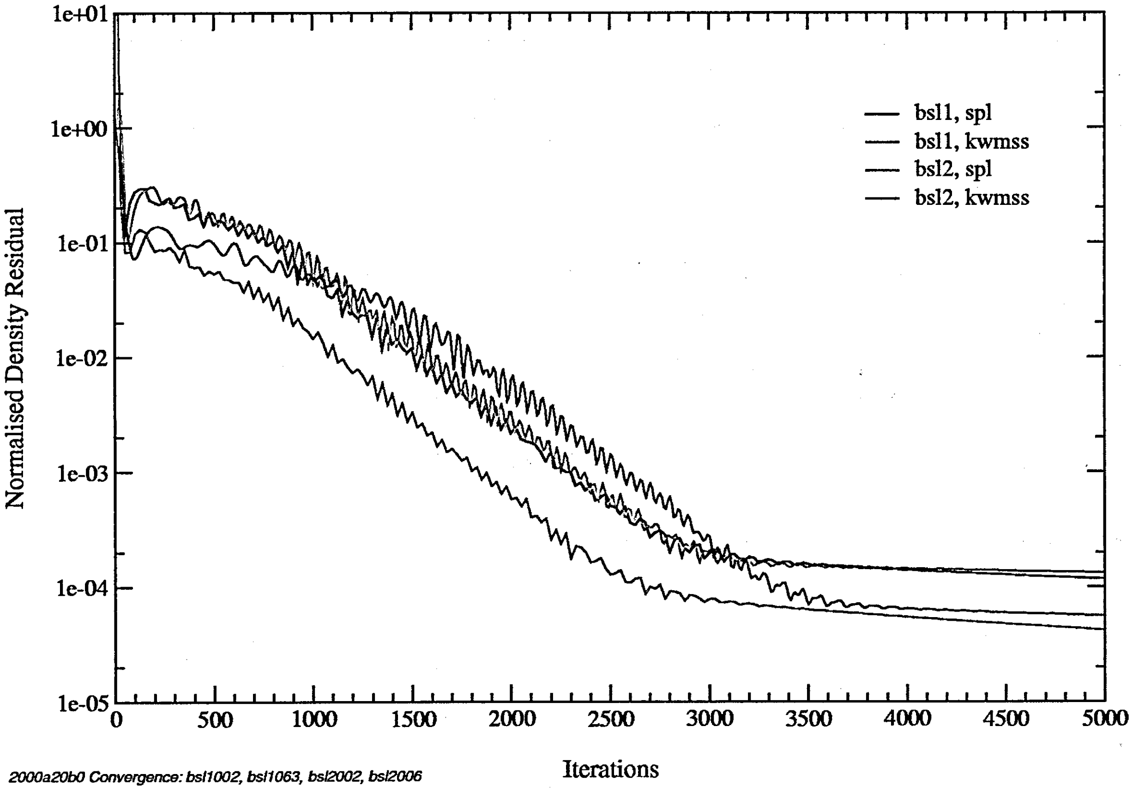

2000a20b0 Convergence: bsl1002, bsl1063, bsl2002, bsl2006

Figure 4.21: *JAS-39 grids bsl1 & bsl2, M=0.176, Re=4.06 × 10^6, α=20°. Comparison of turbulence model density residual convergence history.*

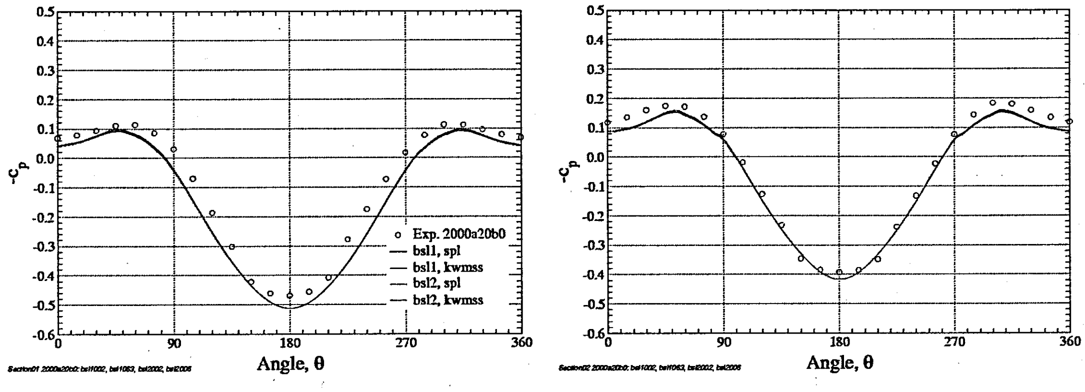

(a) Section 01

(b) Section 02

Figure 4.22: *JAS-39 grids bsl1 & bsl2, M=0.176, Re=4.06×10^6, α=20°. Circumferential c_p distributions, sections 01 & 02. Comparison of turbulence models and grid effects.*

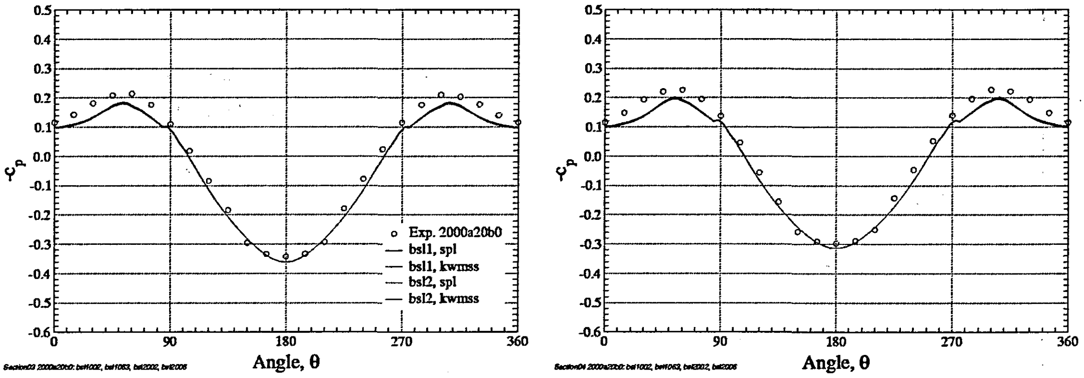

(a) Section 03

(b) Section 04

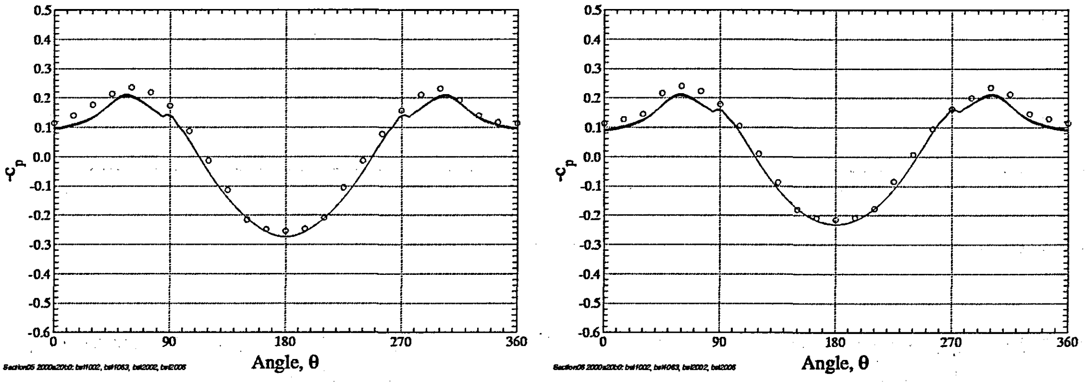

(c) Section 05

(d) Section 06

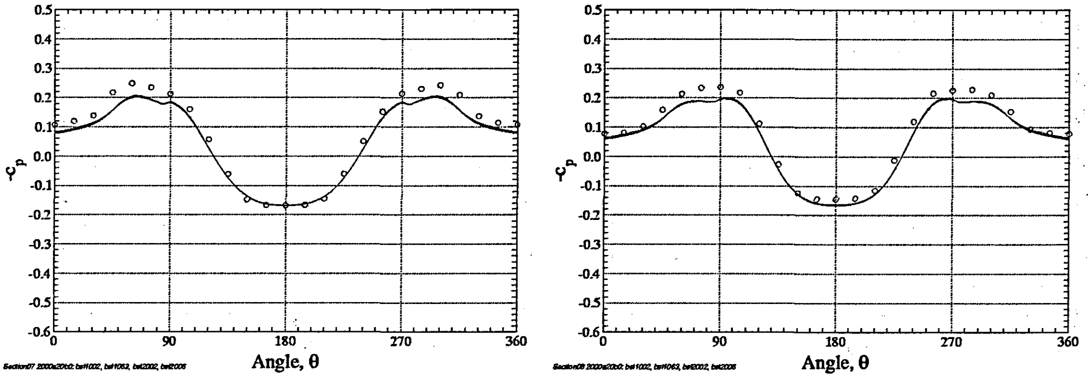

(e) Section 07

(f) Section 08

***Figure 4.23:** JAS-39 grids bsl1 & bsl2, M=0.176, Re=4.06×10^6, α=20°. Circumferential c_p distributions, sections 03-08. Comparison of turbulence models and grid effects.*

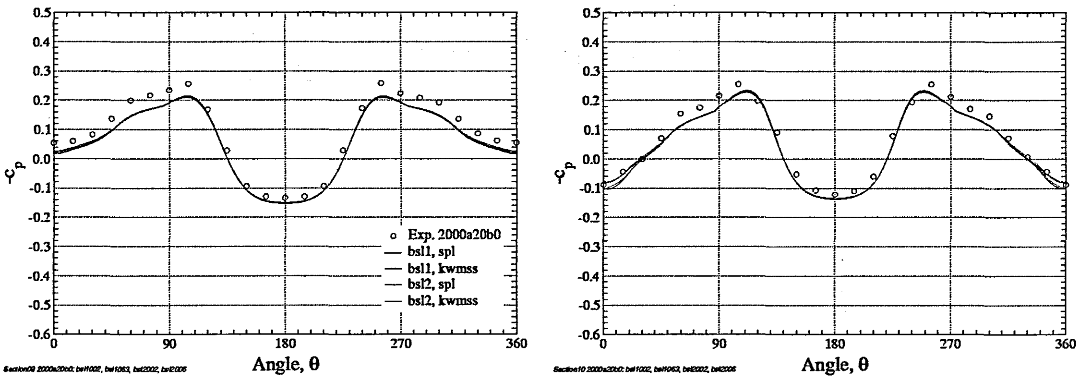

(a) Section 09

(b) Section 10

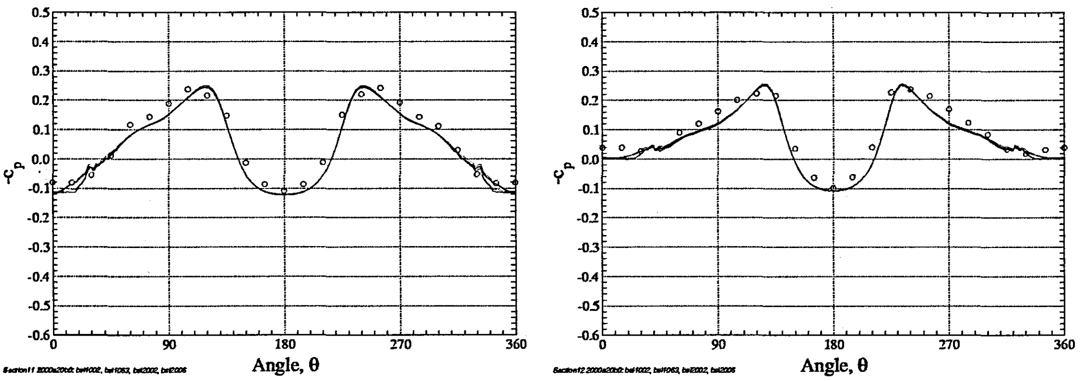

(c) Section 11

(d) Section 12

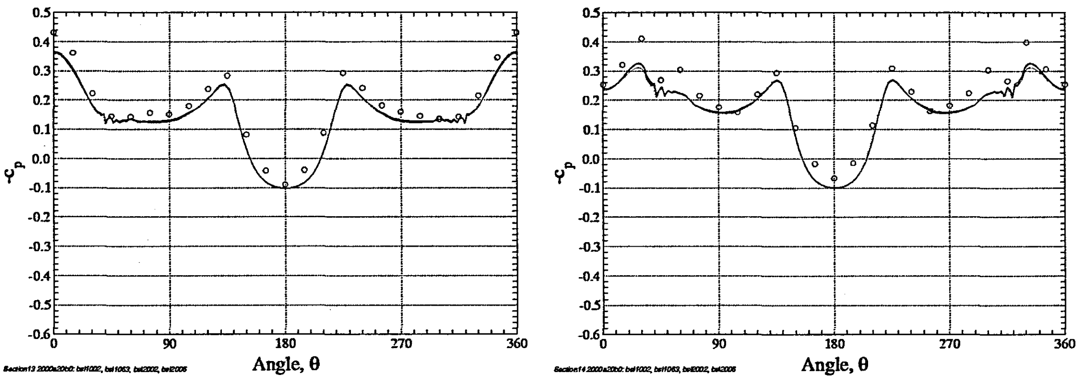

(e) Section 13

(f) Section 14

Figure 4.24: *JAS-39 grids bsl1 & bsl2, M=0.176, Re=4.06×10^6, α=20°. Circumferential c_p distributions, sections 09-14. Comparison of turbulence models and grid effects.*

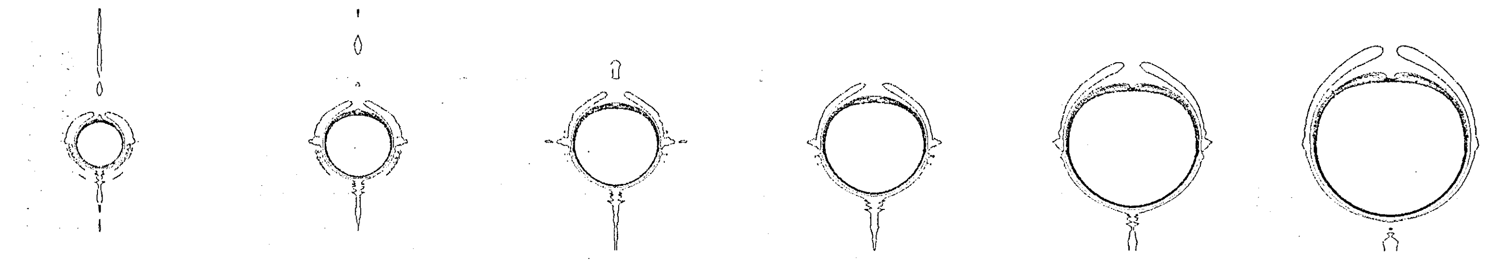

(a) Section 01 (b) Section 02 (c) Section 03 (d) Section 04 (e) Section 06 (f) Section 07

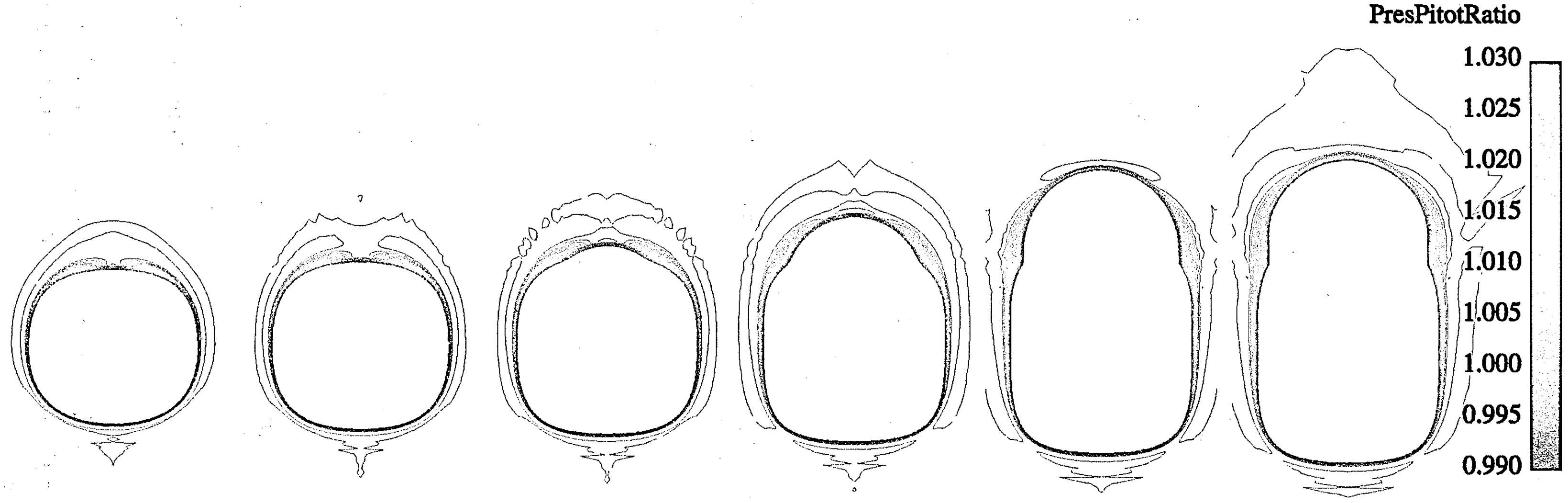

(g) Section 09 (h) Section 10 (i) Section 11 (j) Section 12 (k) Section 13 (l) Section 14

Figure 4.25: *JAS-39 grid bsl2,* M=0.176, $Re=4.06 \times 10^6$, $\alpha=20^o$. *Contours of pitot pressure ratio, Menter k-ω-SST model.*

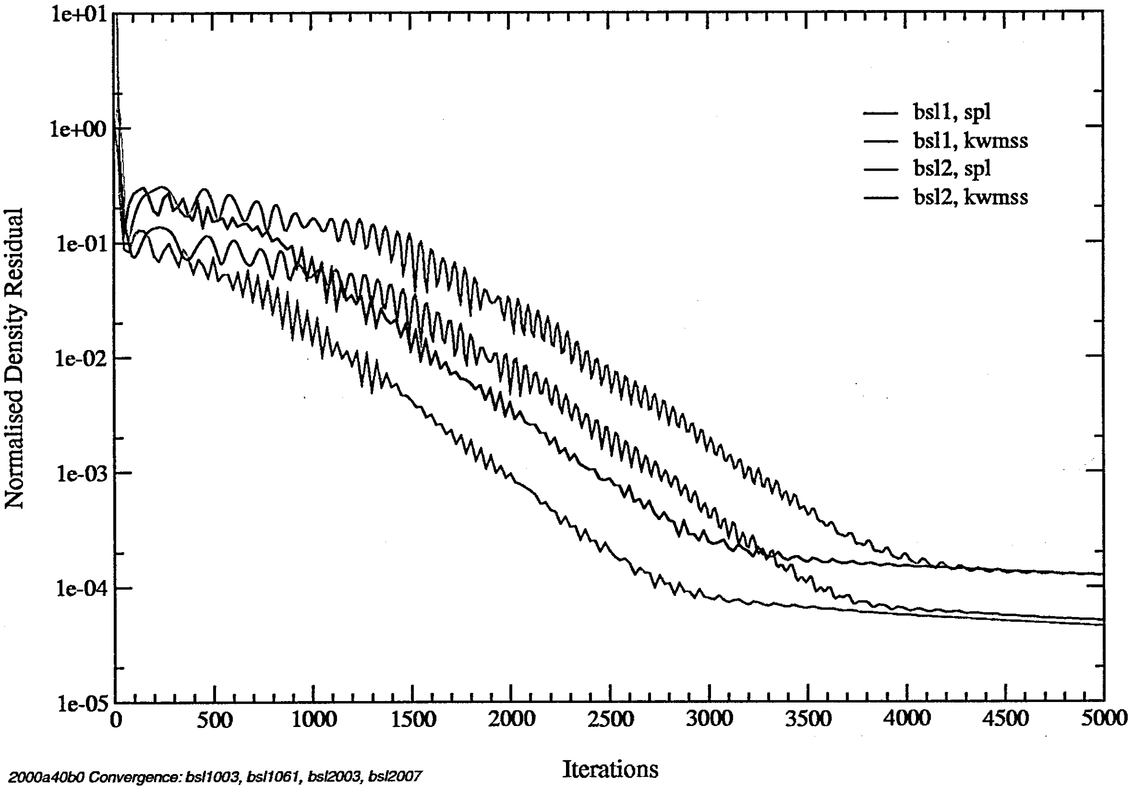

Figure 4.26: JAS-39 grids bsl1 & bsl2, M=0.176, Re=4.06 × 10^6, α=40°. *Comparison of turbulence model density residual convergence history.*

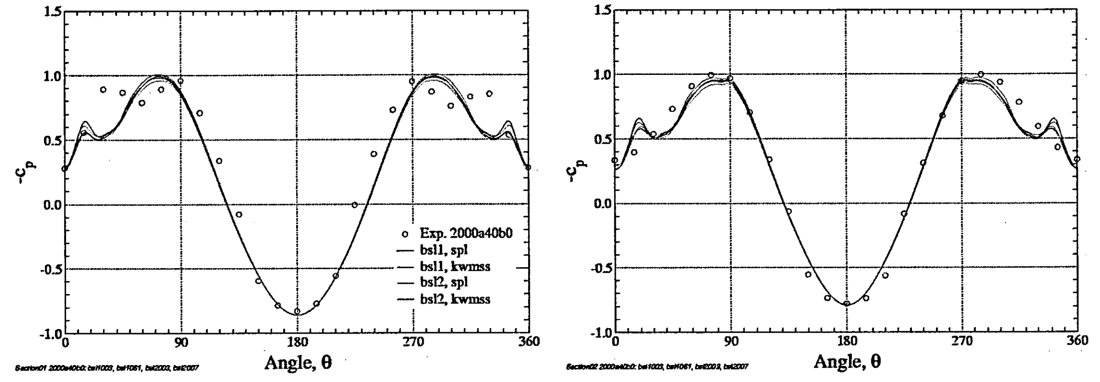

(a) Section 01

(b) Section 02

Figure 4.27: JAS-39 grids bsl1 & bsl2, M=0.176, Re=4.06×10^6, α=40°. *Circumferential* c_p *distributions, sections 01 & 02. Comparison of turbulence models and grid effects.*

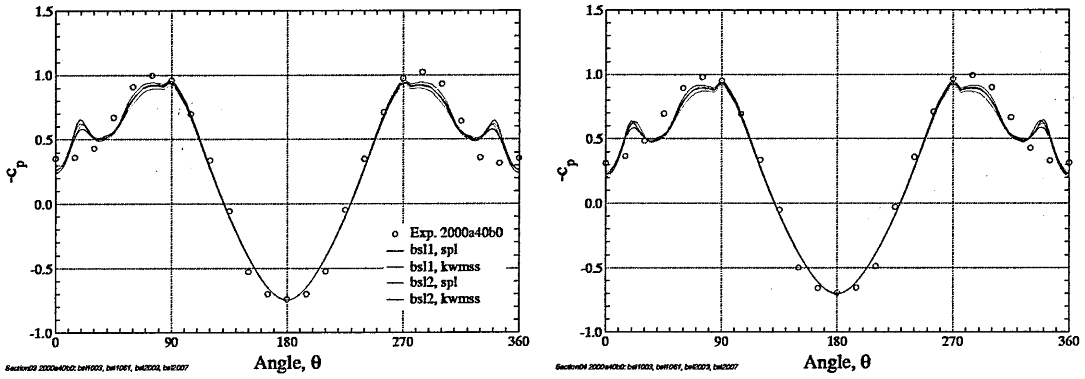

(a) Section 03

(b) Section 04

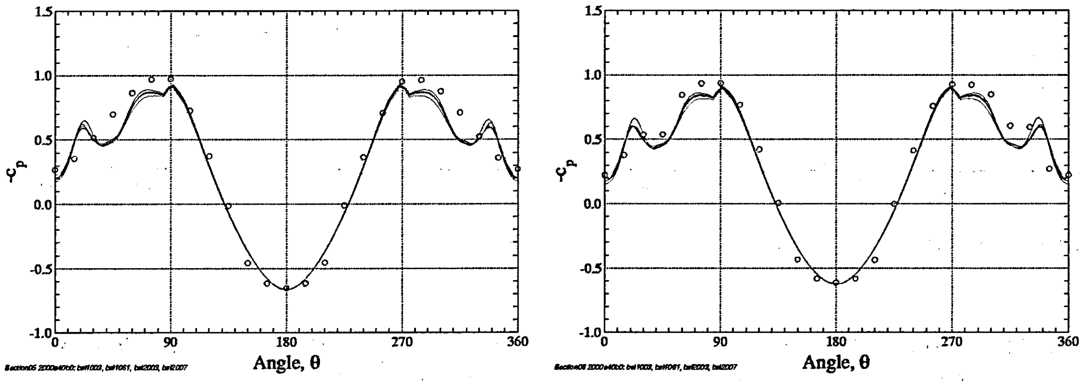

(c) Section 05

(d) Section 06

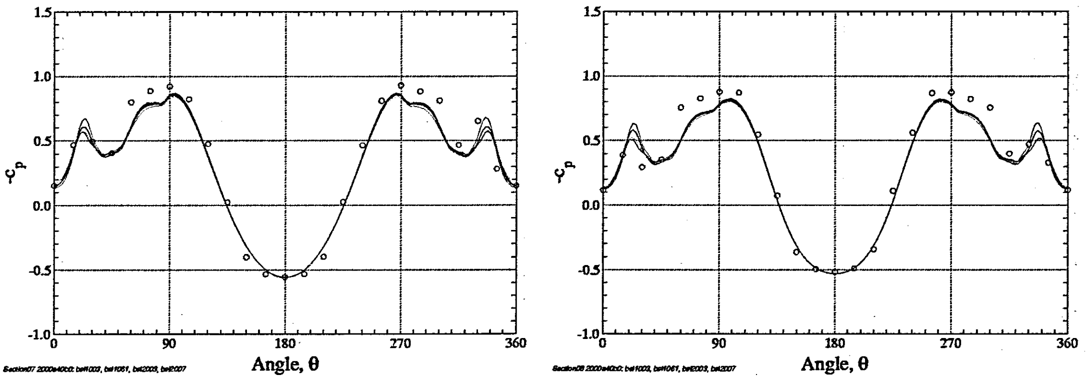

(e) Section 07

(f) Section 08

Figure 4.28: *JAS-39 grids bsl1 & bsl2, M=0.176, Re=4.06×10^6, α=40°. Circumferential c_p distributions, sections 03-08. Comparison of turbulence models and grid effects.*

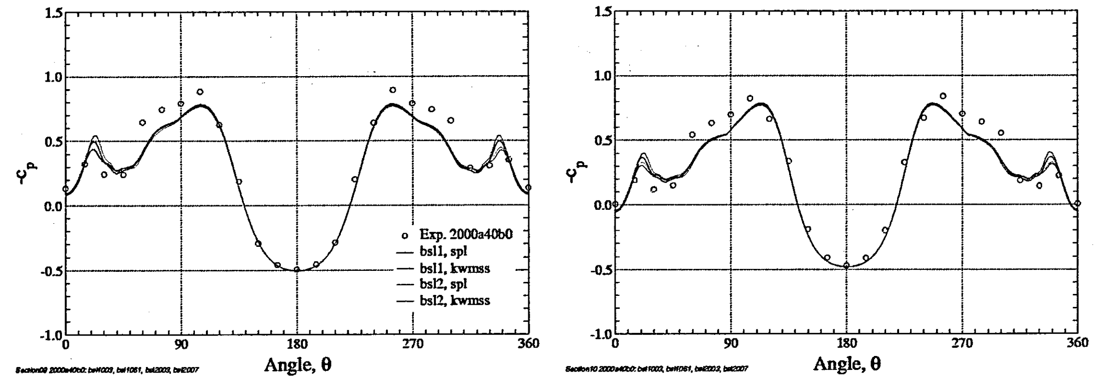

(a) Section 09

(b) Section 10

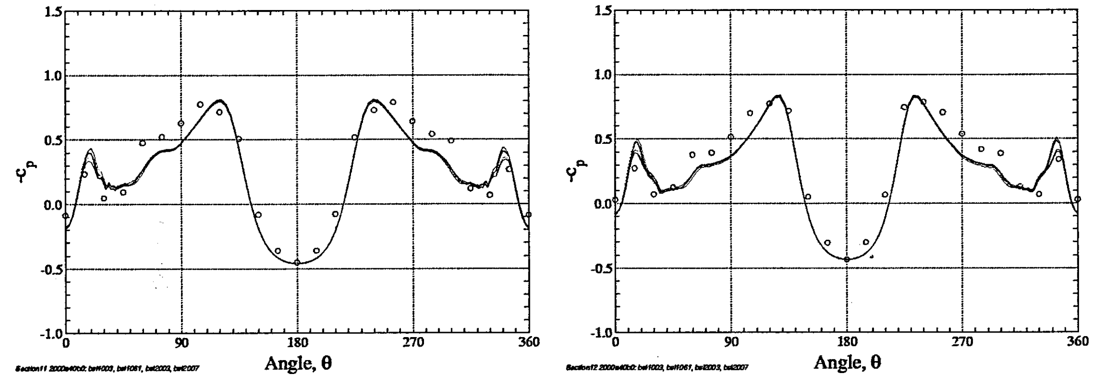

(c) Section 11

(d) Section 12

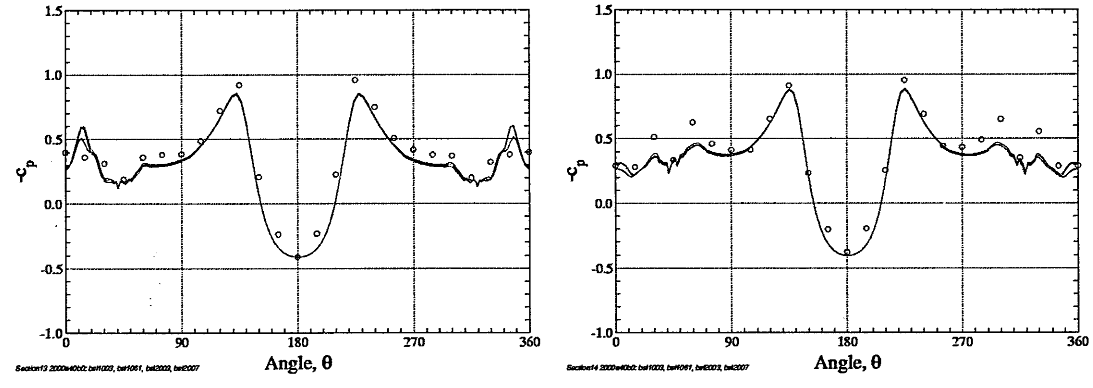

(e) Section 13

(f) Section 14

Figure 4.29: *JAS-39 grids bsl1 & bsl2, M=0.176, Re=4.06×10^6, α=40°. Circumferential c_p distributions, sections 09-14. Comparison of turbulence models and grid effects.*

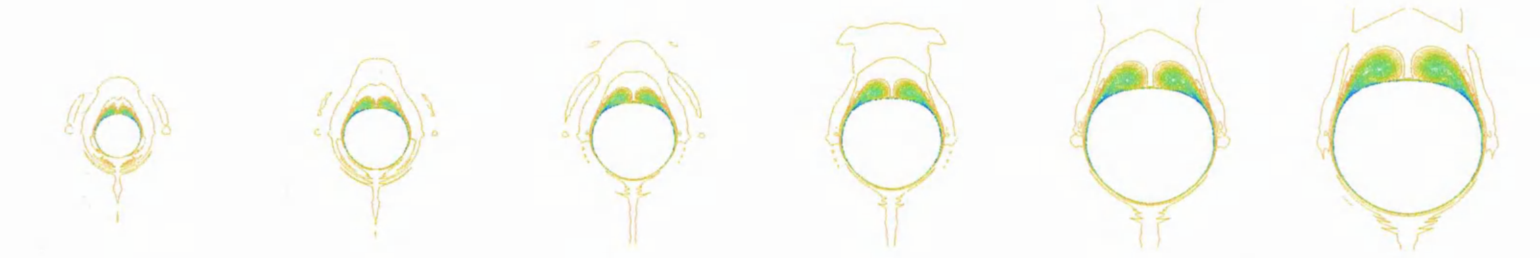

(a) Section 01 (b) Section 02 (c) Section 03 (d) Section 04 (e) Section 06 (f) Section 07

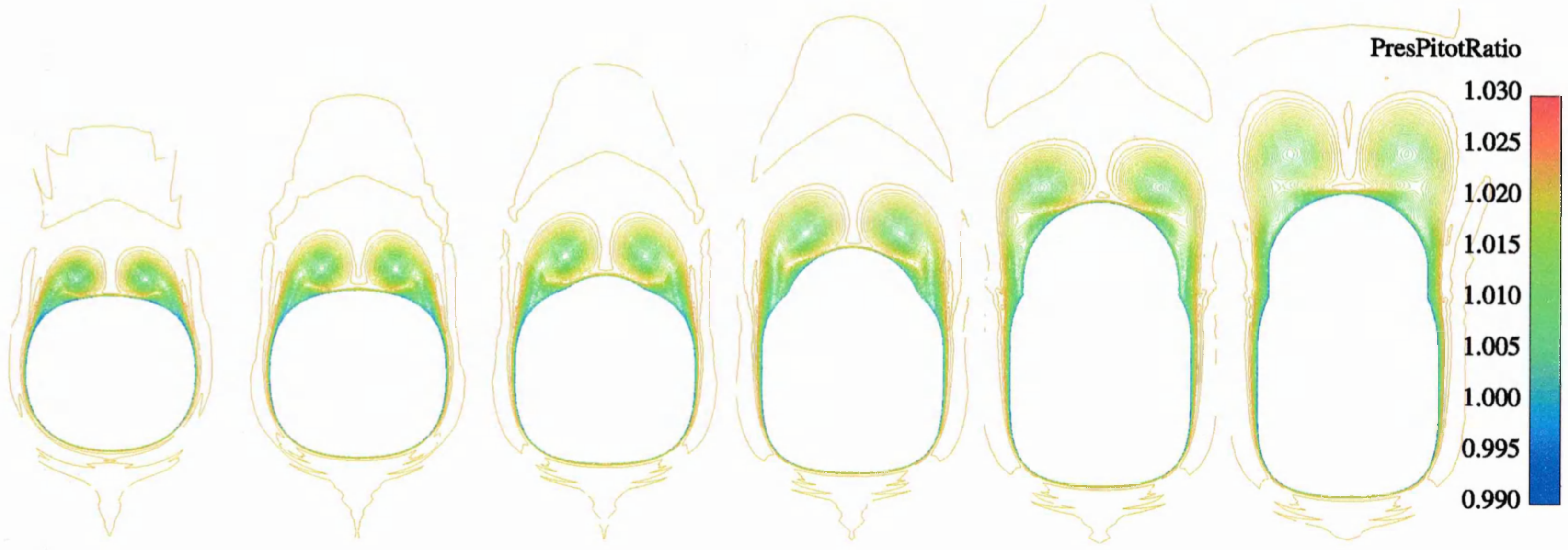

(g) Section 09 (h) Section 10 (i) Section 11 (j) Section 12 (k) Section 13 (l) Section 14

Figure 4.30: *JAS-39 grid bsl2,* M=0.176, Re=4.06 × 10^6, α=40^o. *Contours of pitot pressure ratio, Menter* k-ω-SST *model.*

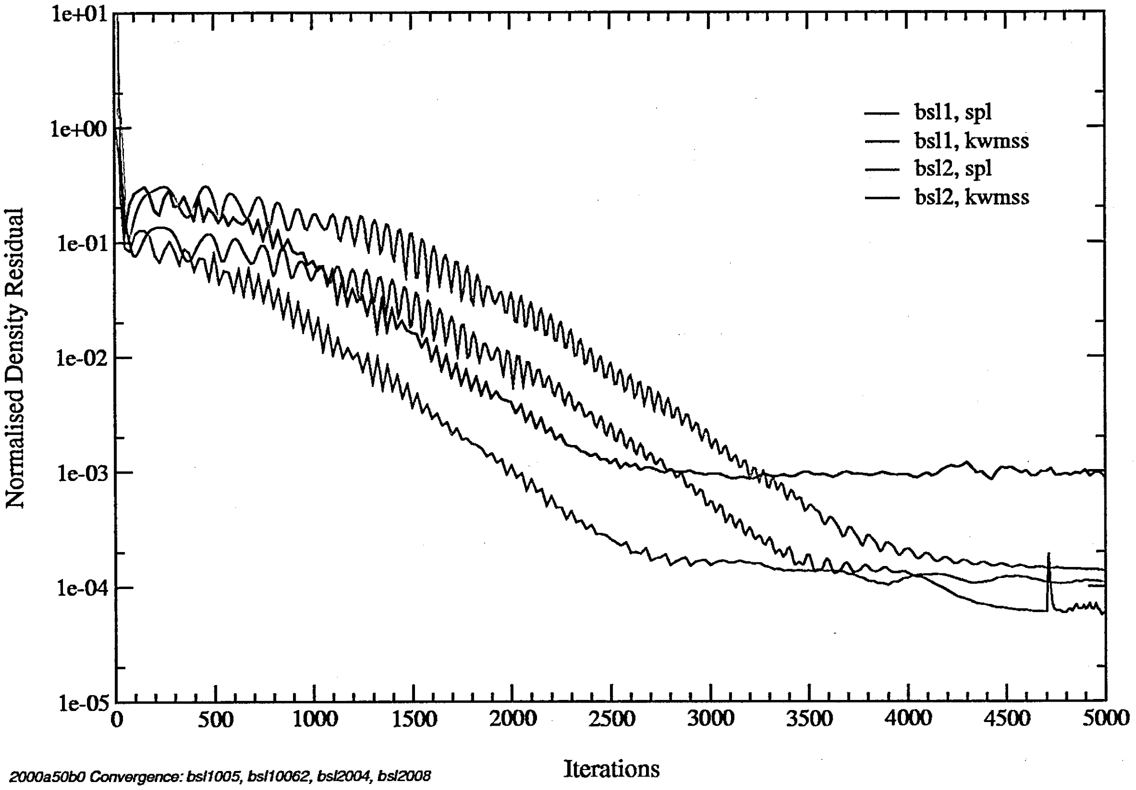

Figure 4.31: *JAS-39 grids bsl1 & bsl2, M=0.176, Re=4.06 × 10^6, α=50°. Comparison of turbulence model density residual convergence history.*

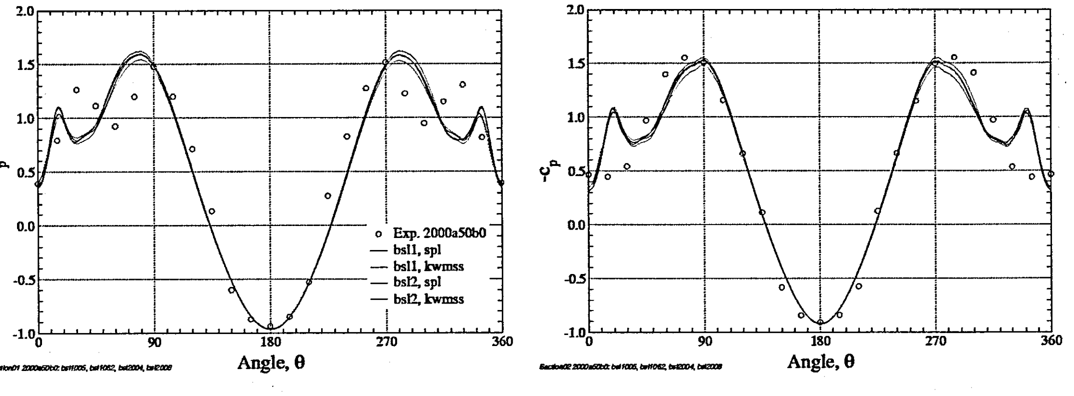

(a) Section 01

(b) Section 02

Figure 4.32: *JAS-39 grids bsl1 & bsl2, M=0.176, Re=4.06×10^6, α=50°. Circumferential c_p distributions, sections 01 & 02. Comparison of turbulence models and grid effects.*

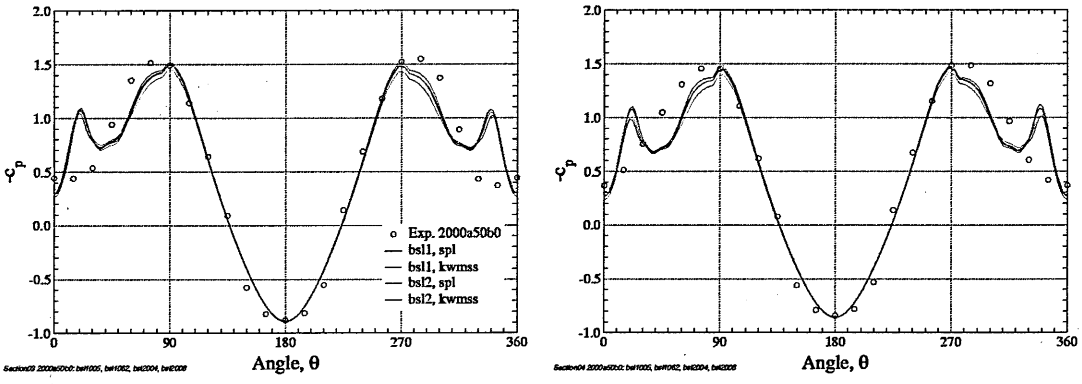

(a) Section 03

(b) Section 04

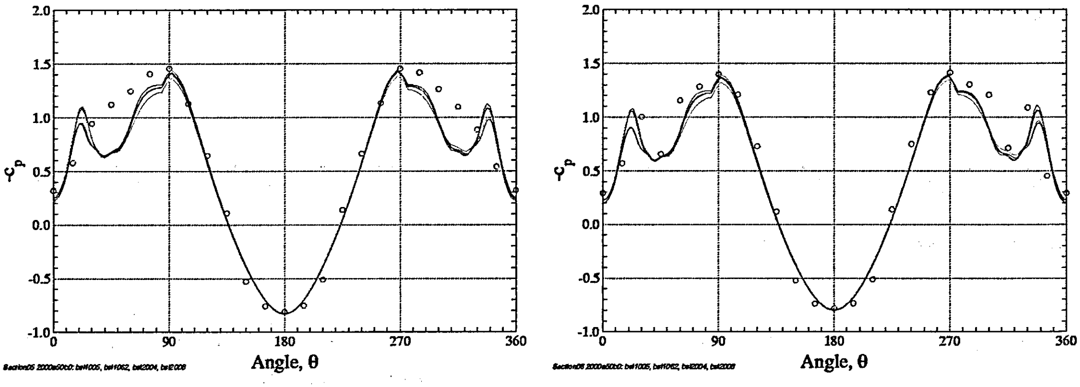

(c) Section 05

(d) Section 06

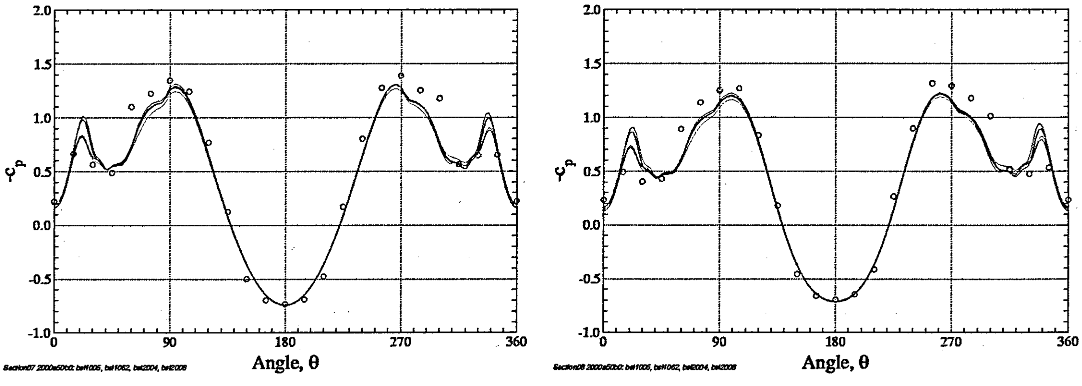

(e) Section 07

(f) Section 08

Figure 4.33: *JAS-39 grids bsl1 & bsl2, M=0.176, Re=4.06×10^6, α=50°. Circumferential c_p distributions, sections 03-08. Comparison of turbulence models and grid effects.*

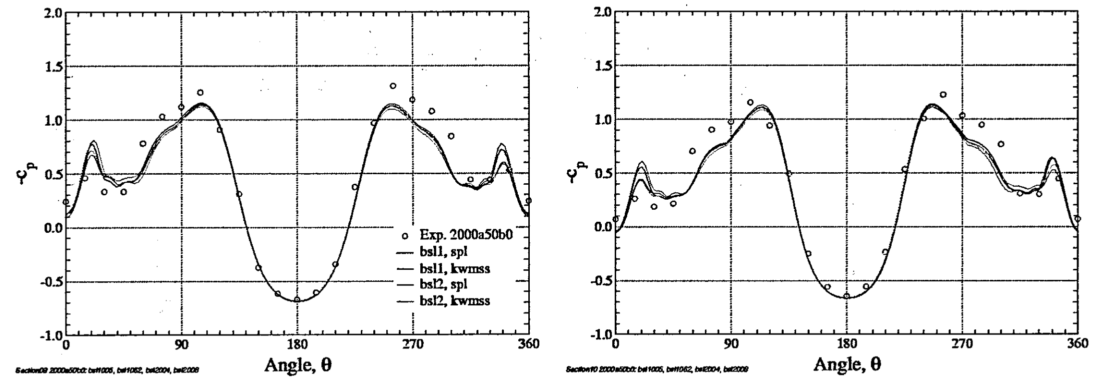

(a) Section 09

(b) Section 10

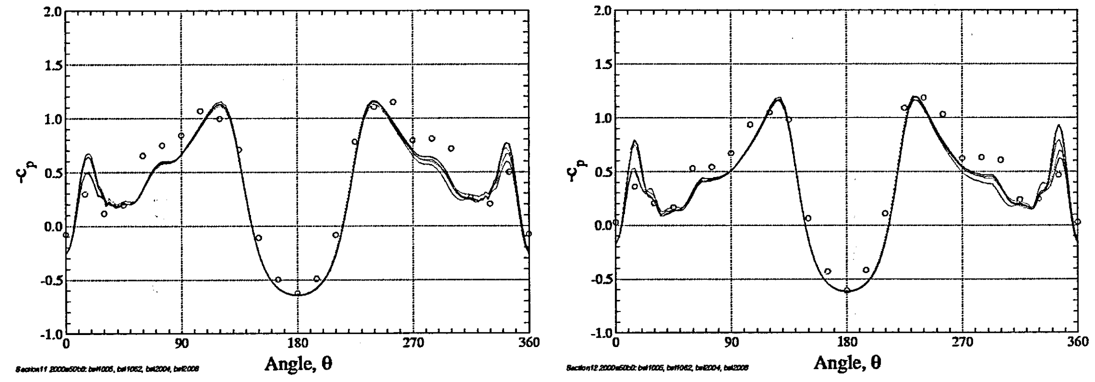

(c) Section 11

(d) Section 12

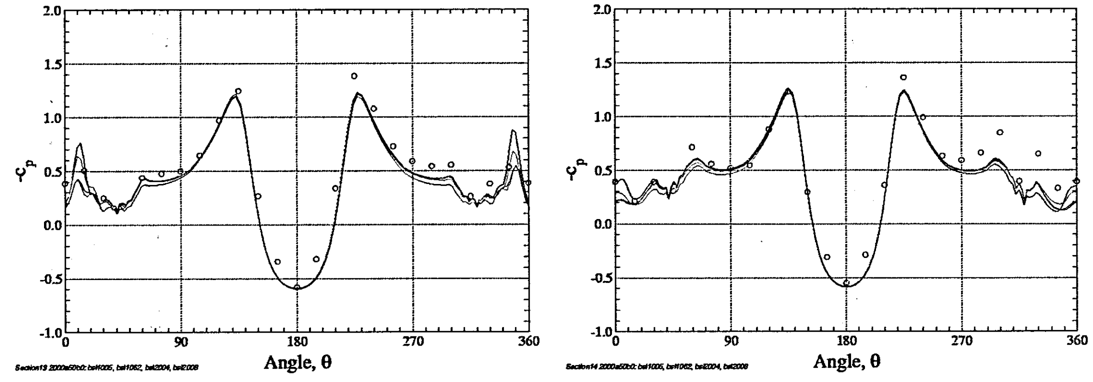

(e) Section 13

(f) Section 14

Figure 4.34: *JAS-39 grids bsl1 & bsl2, M=0.176, Re=4.06×10^6, α=50°. Circumferential c_p distributions, sections 09-14. Comparison of turbulence models and grid effects.*

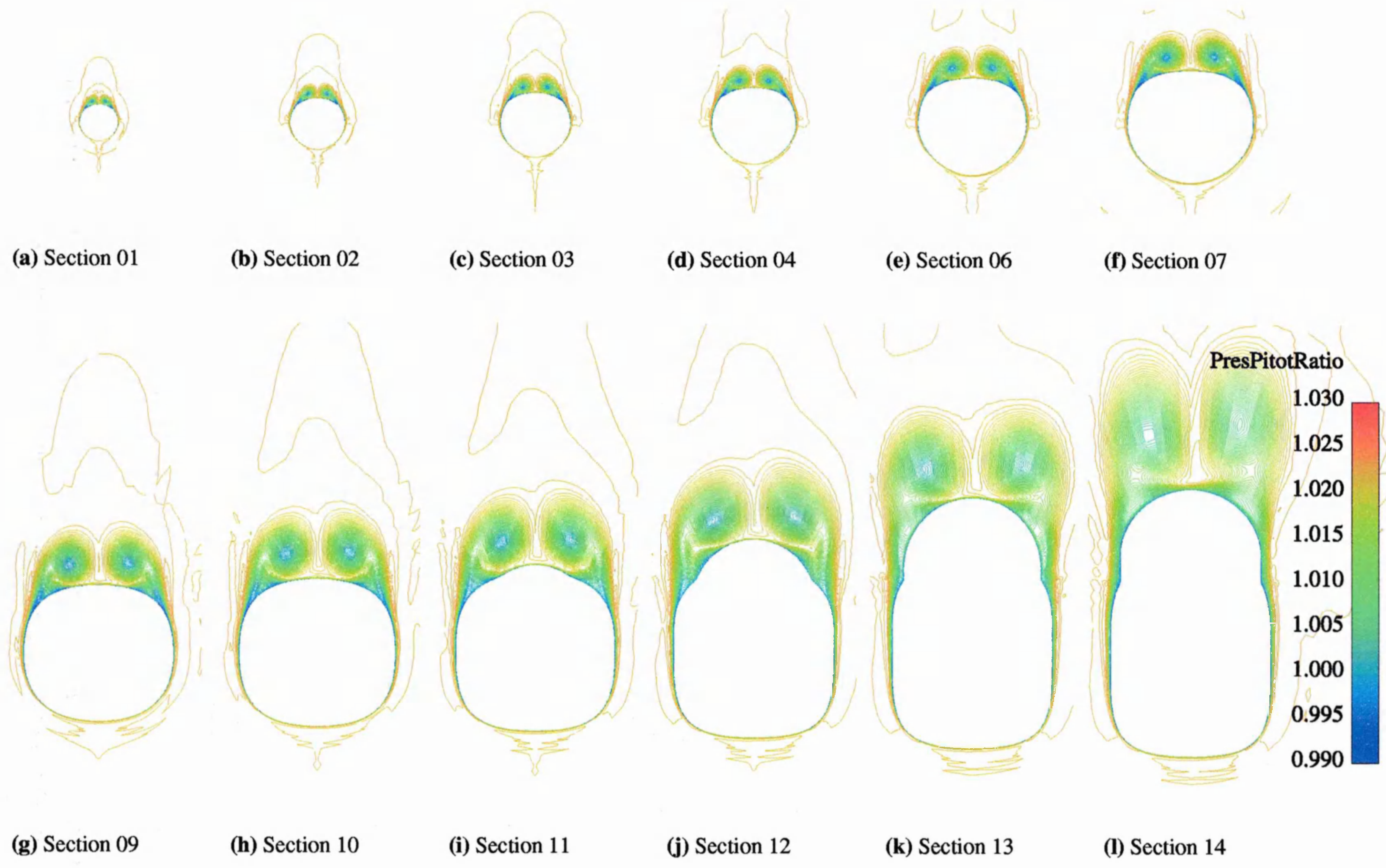

(a) Section 01 **(b)** Section 02 **(c)** Section 03 **(d)** Section 04 **(e)** Section 06 **(f)** Section 07

(g) Section 09 **(h)** Section 10 **(i)** Section 11 **(j)** Section 12 **(k)** Section 13 **(l)** Section 14

Figure 4.35: *JAS-39 grid bsl2, M=0.176, Re=4.06 × 10^6, α=50°. Contours of pitot pressure ratio, Menter k-ω-SST model.*

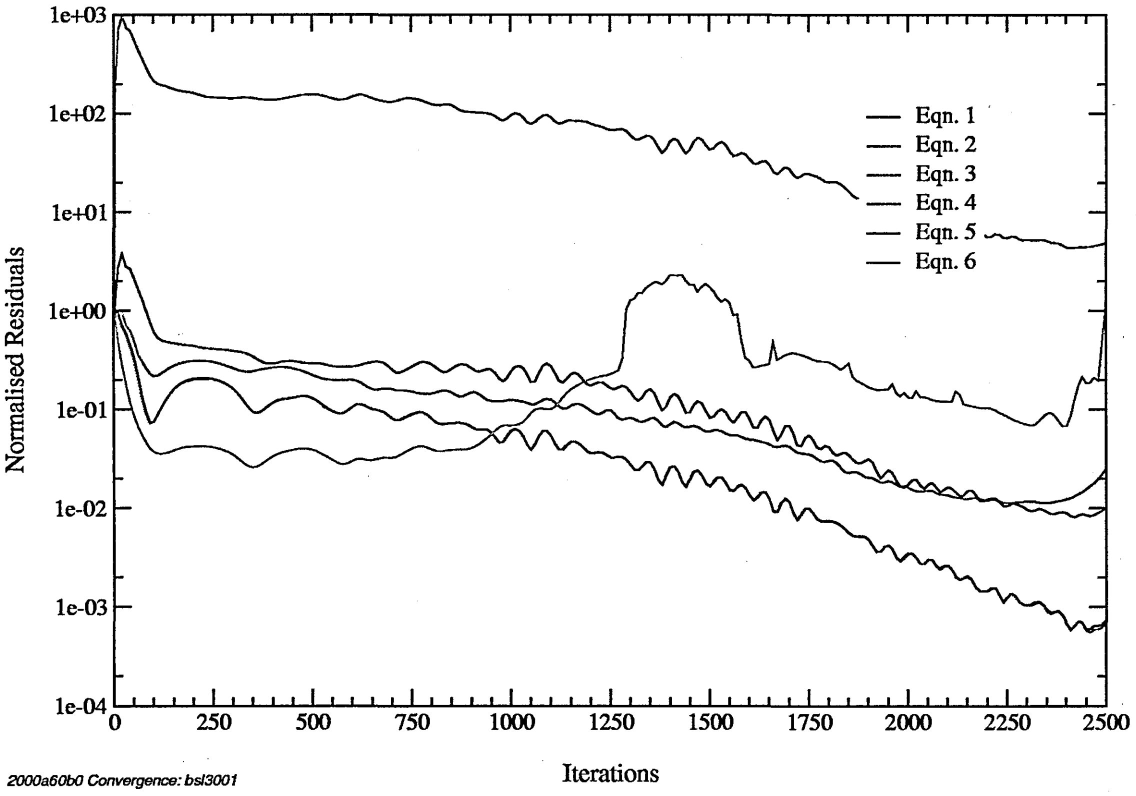

Figure 4.36: *JAS-39 grid bsl3, M=*0.176, *Re=*4.06 × 10^6, *α=*60°. *Normalised residual convergence history, Spalart-Allmaras model.*

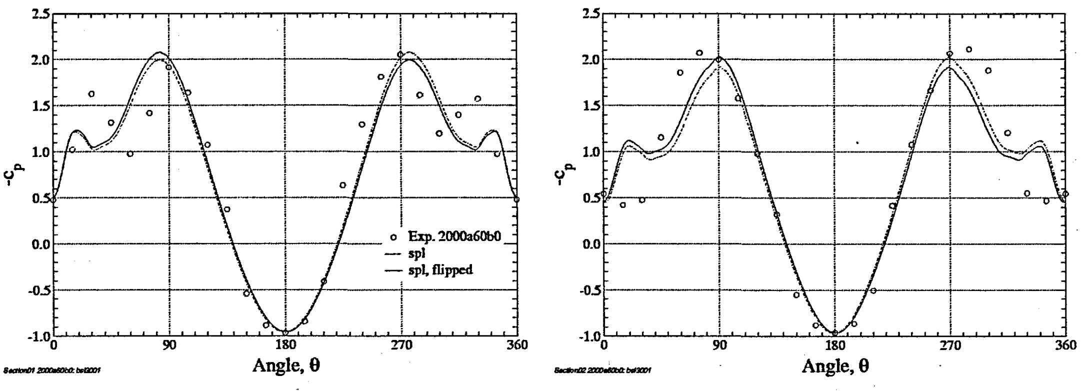

(a) Section 01

(b) Section 02

Figure 4.37: *JAS-39 grid bsl3, M=*0.176, *Re=*4.06 × 10^6, *α=*60°. *Circumferential c_p distributions, sections 01 & 02. Spalart-Allmaras model.*

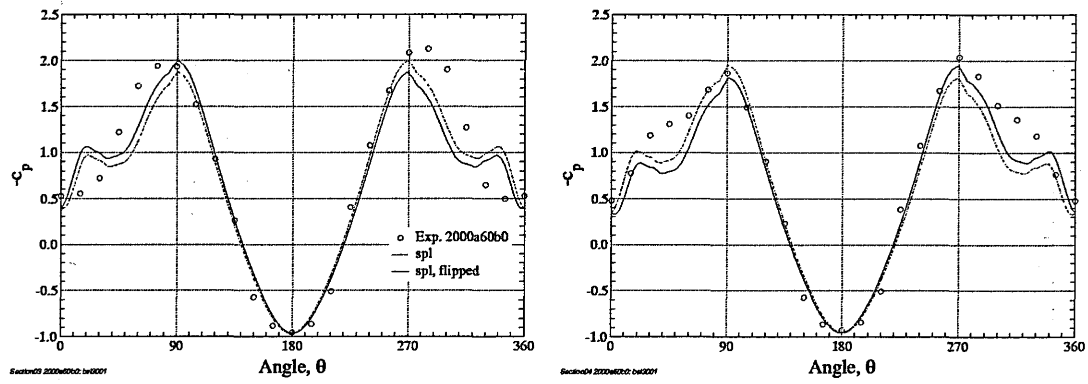

(a) Section 03

(b) Section 04

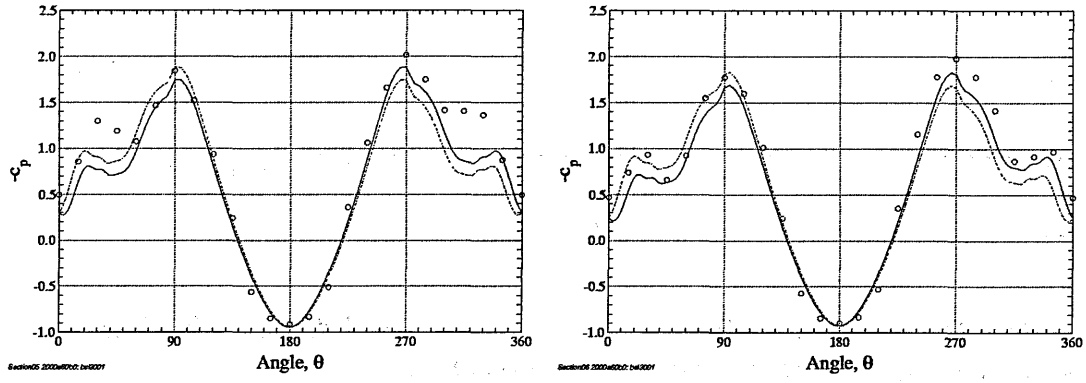

(c) Section 05

(d) Section 06

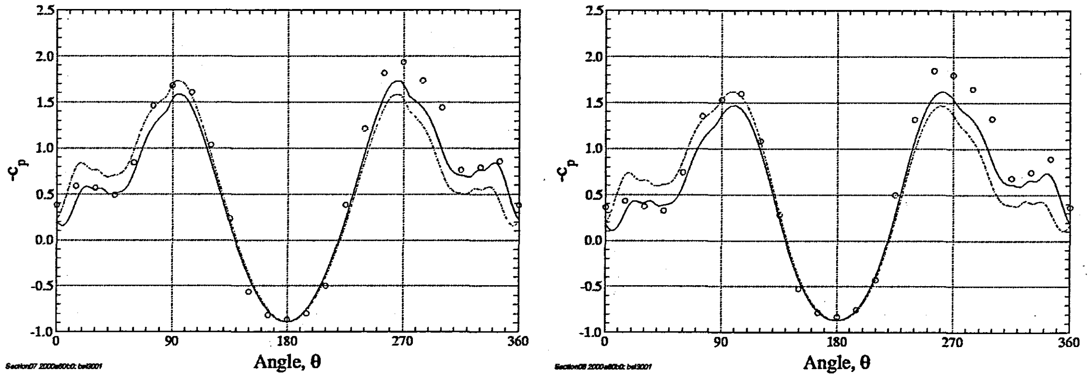

(e) Section 07

(f) Section 08

Figure 4.38: *JAS-39 grid bsl3, M=0.176, Re=4.06 × 10^6, α=60°. Circumferential c_p distributions, sections 03-08. Spalart-Allmaras model.*

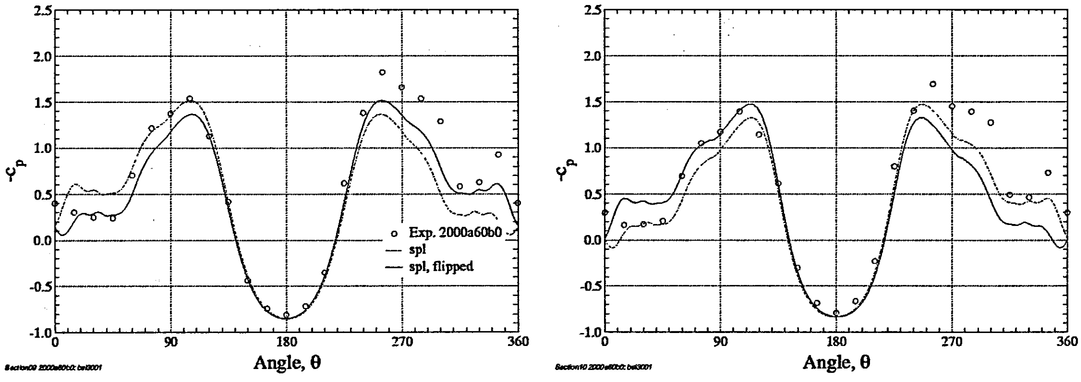

(a) Section 09

(b) Section 10

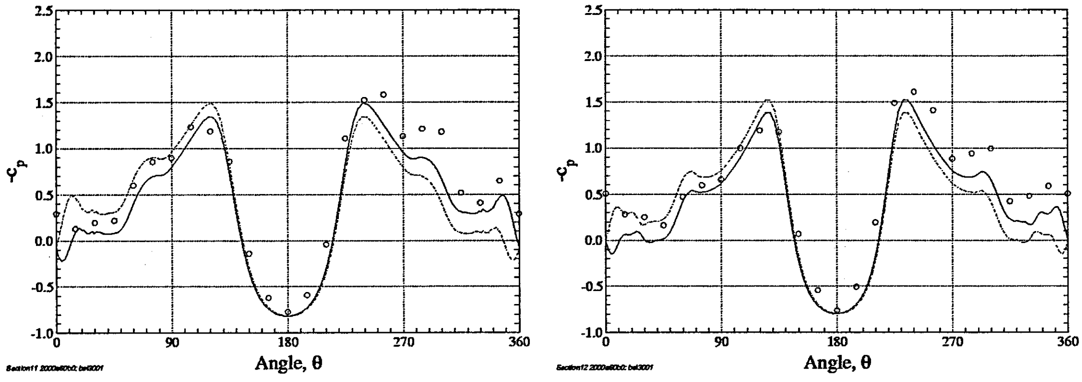

(c) Section 11

(d) Section 12

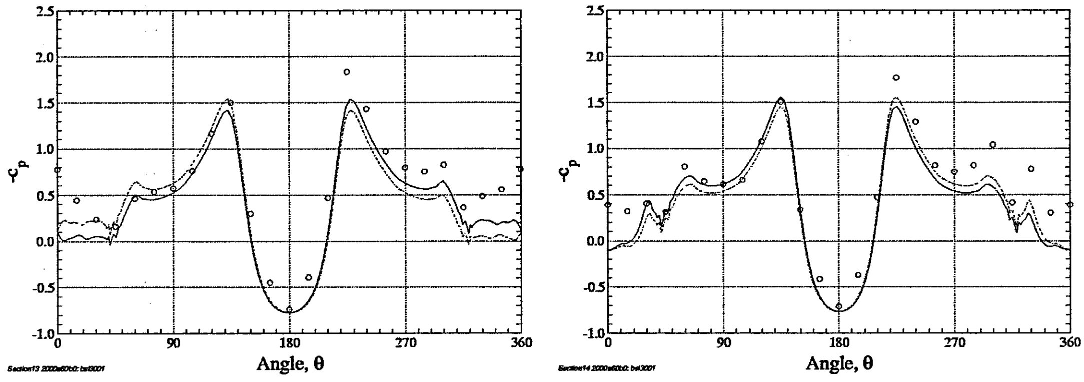

(e) Section 13

(f) Section 14

Figure 4.39: *JAS-39 grid bsl3, M=0.176, Re=4.06 × 10^6, α=60°. Circumferential c_p distributions, sections 09-14. Spalart-Allmaras model.*

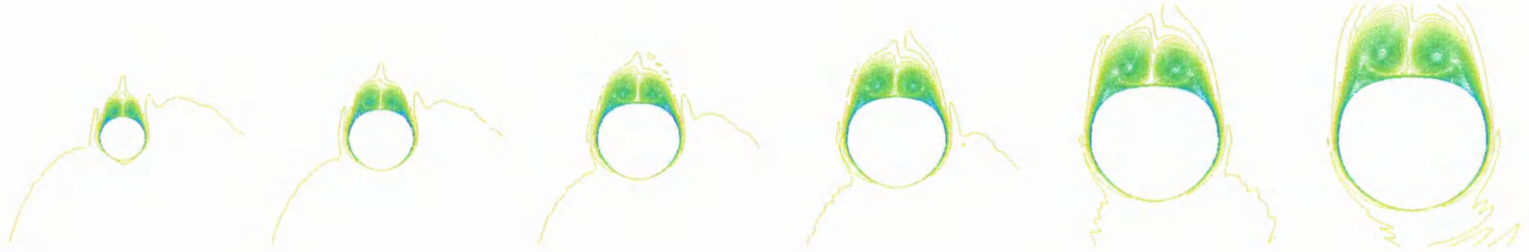

(a) Section 01 (b) Section 02 (c) Section 03 (d) Section 04 (e) Section 06 (f) Section 07

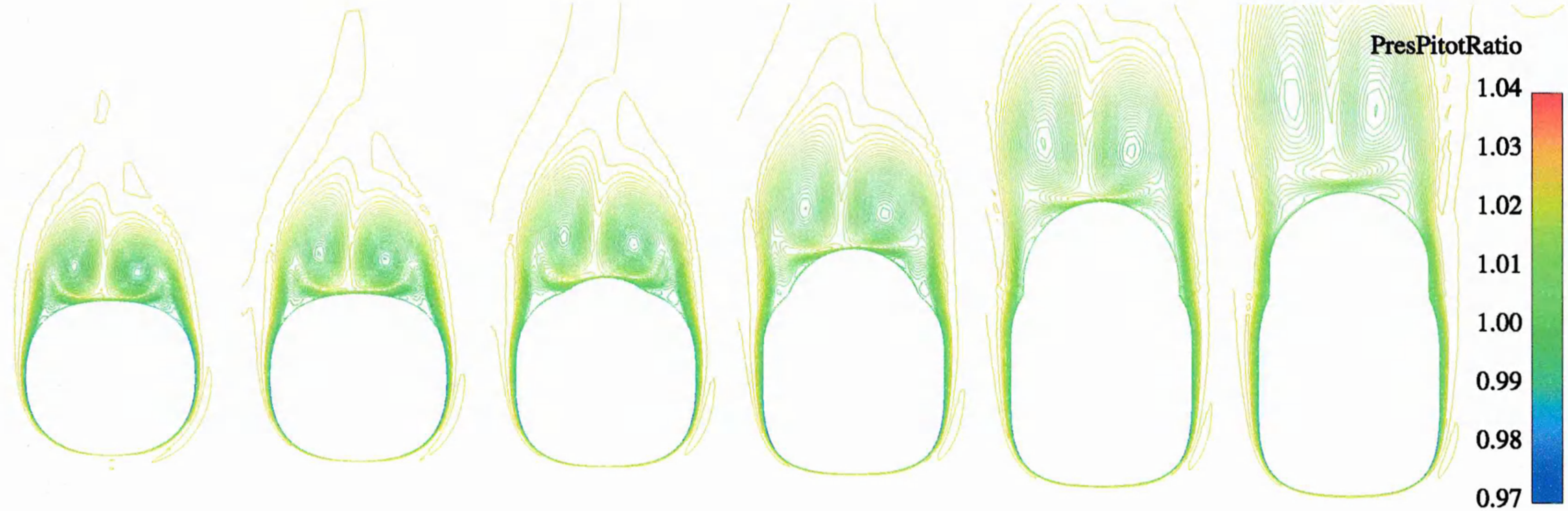

(g) Section 09 (h) Section 10 (i) Section 11 (j) Section 12 (k) Section 13 (l) Section 14

Figure 4.40: *JAS-39 grid bsl3, M=0.176, Re=4.06 × 10^6, α=60°. Contours of pitot pressure ratio, Spalart-Allmaras model.*

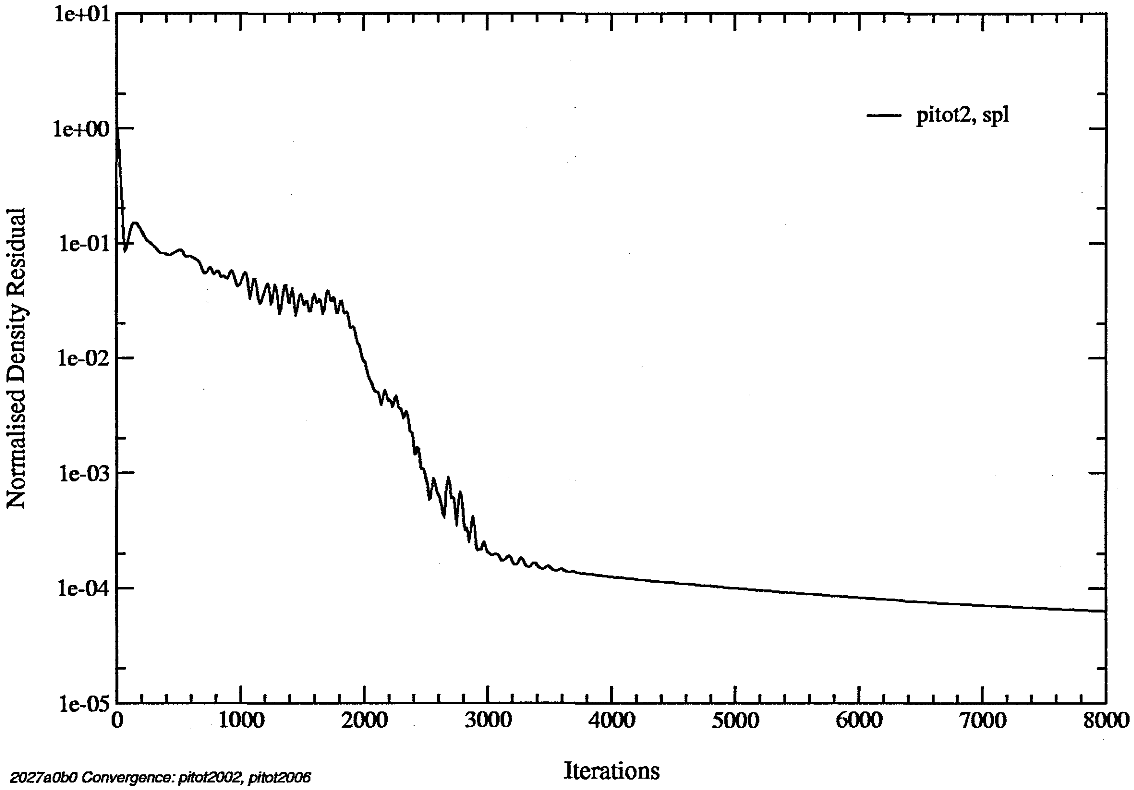

Figure 4.41: *JAS-39 grid pitot2, M=0.176, Re=4.06 × 10^6, α=0°. Normalised density residual convergence history for the Spalart-Allmaras model.*

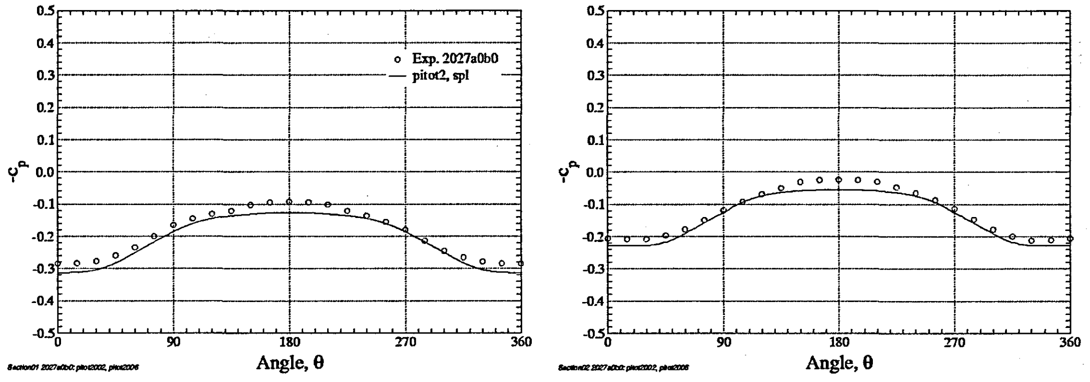

(a) Section 01

(b) Section 02

Figure 4.42: *JAS-39 grid pitot2, M=0.176, Re=4.06 × 10^6, α=0°. Circumferential c_p distributions, sections 01 & 02. Spalart-Allmaras model.*

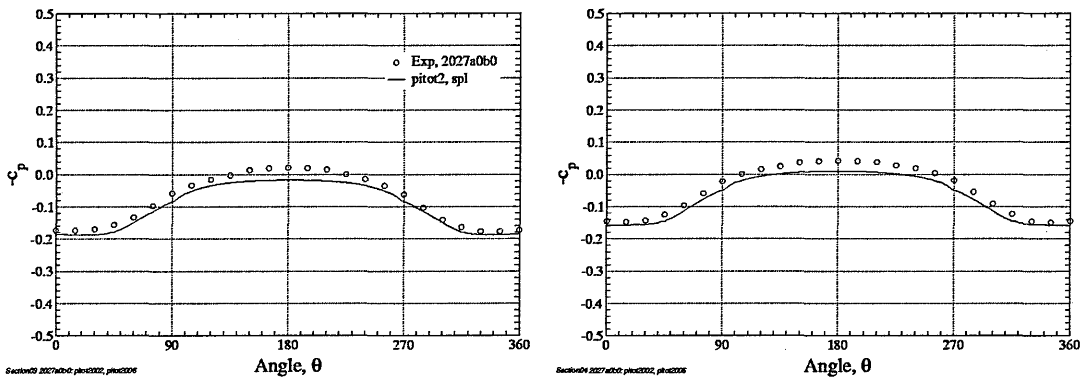

(a) Section 03

(b) Section 04

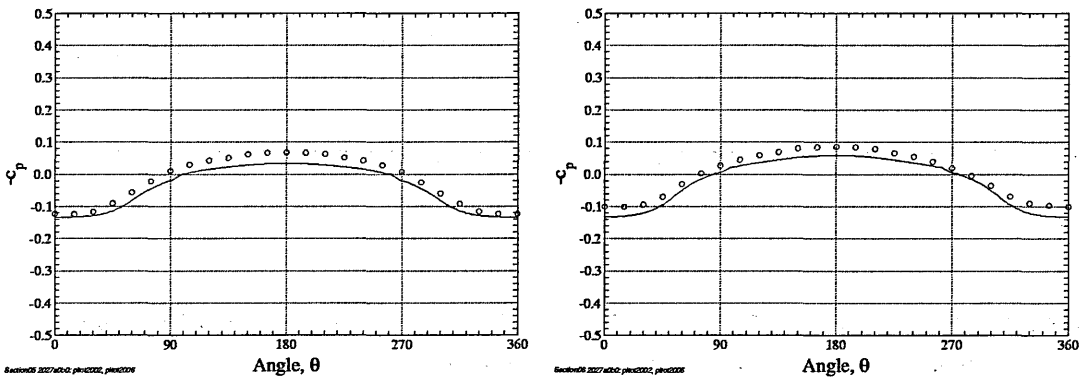

(c) Section 05

(d) Section 06

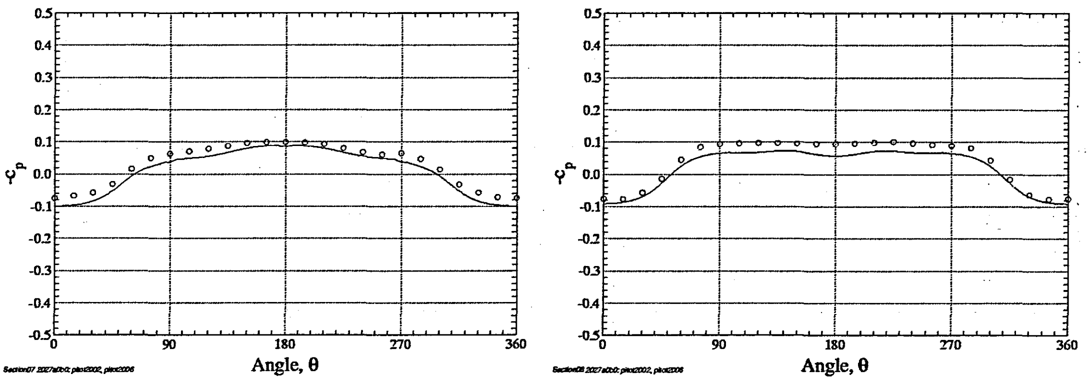

(e) Section 07

(f) Section 08

Figure 4.43: *JAS-39 grid pitot2, M=0.176, Re=4.06 × 10^6, α=0°. Circumferential c_p distributions, sections 03-08. Spalart-Allmaras model.*

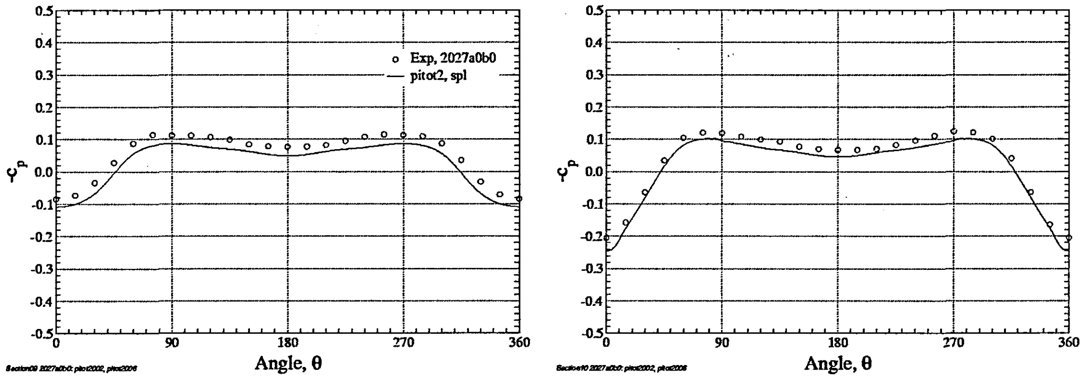

(a) Section 09 (b) Section 10

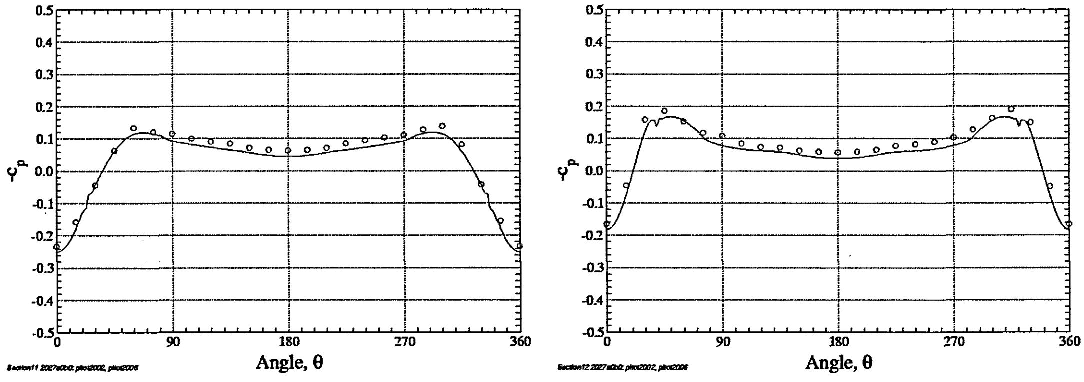

(c) Section 11 (d) Section 12

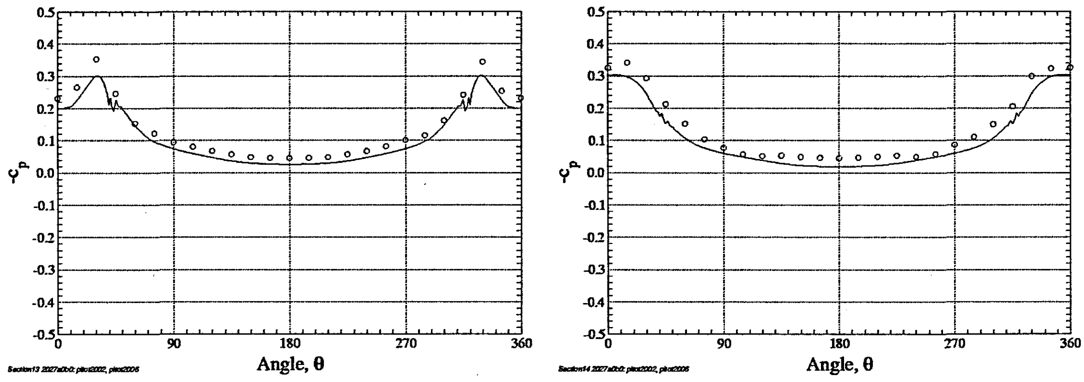

(e) Section 13 (f) Section 14

Figure 4.44: *JAS-39 grid pitot2, M=0.176, Re=4.06 × 10^6, α=0°. Circumferential c_p distributions, sections 09-14. Spalart-Allmaras model.*

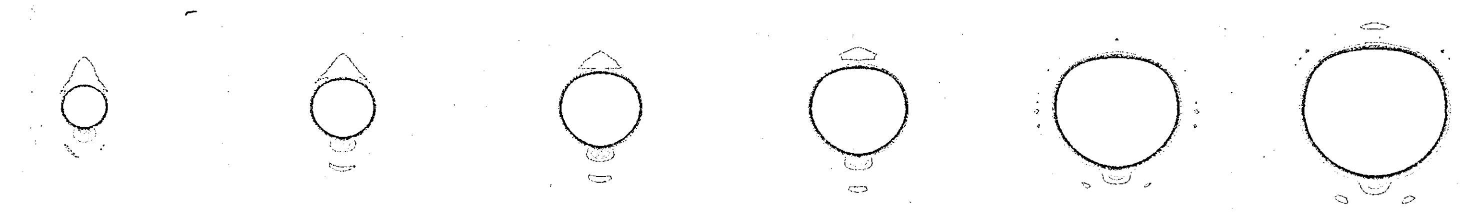

(a) Section 01 (b) Section 02 (c) Section 03 (d) Section 04 (e) Section 06 (f) Section 07

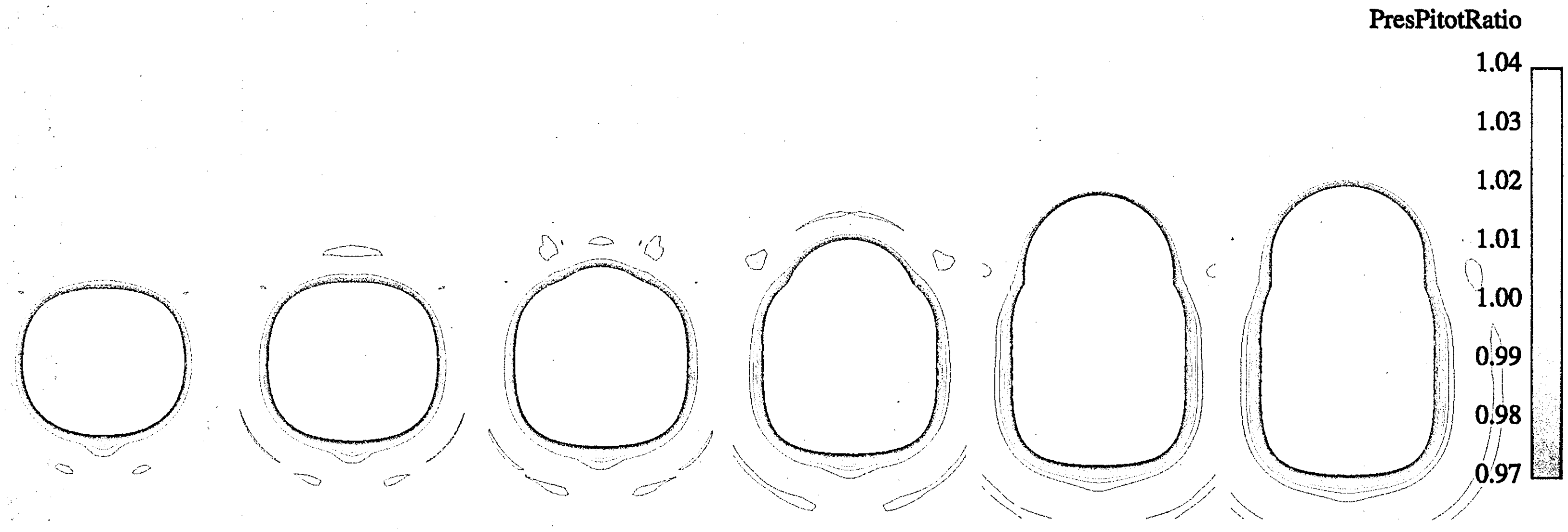

(g) Section 09 (h) Section 10 (i) Section 11 (j) Section 12 (k) Section 13 (l) Section 14

Figure 4.45: *JAS-39 grid pitot2, M=0.176, Re=4.06 × 10^6, α=0°. Contours of pitot pressure ratio, Spalart-Allmaras model.*

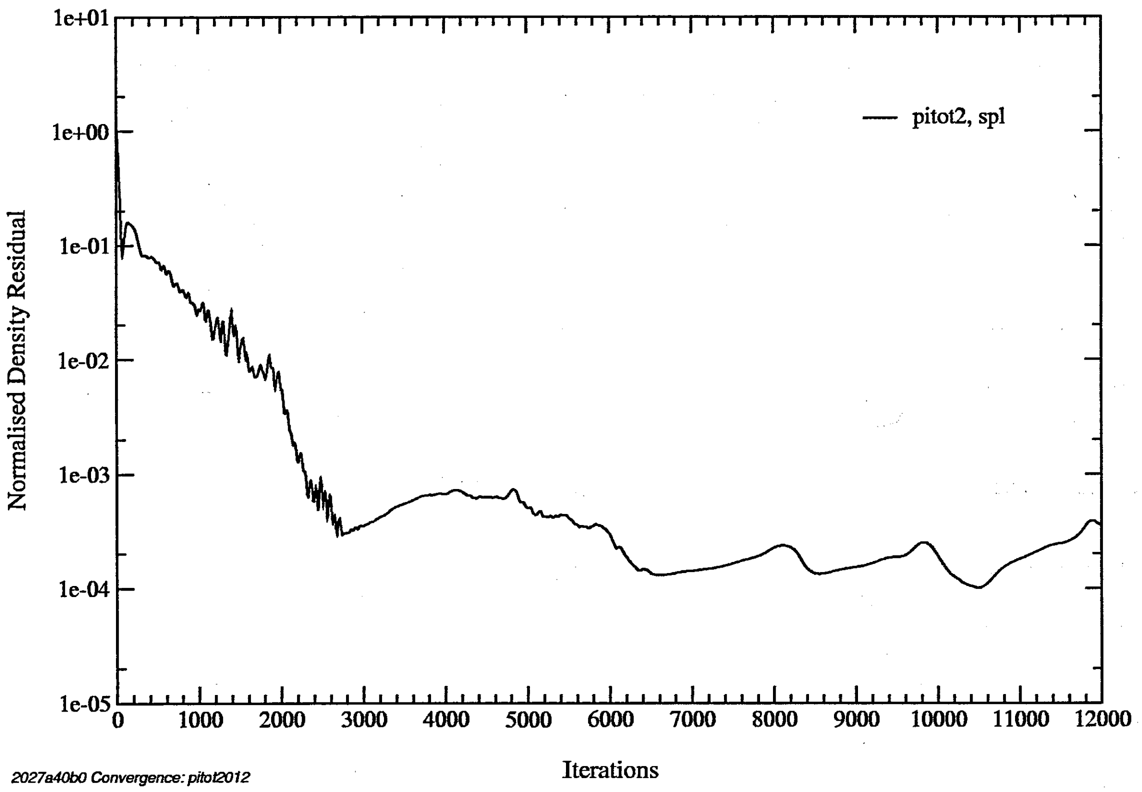

Figure 4.46: JAS-39 grid pitot2, M=0.176, Re=4.06 × 10^6, α=40°. Normalised density residual convergence history for the Spalart-Allmaras model.

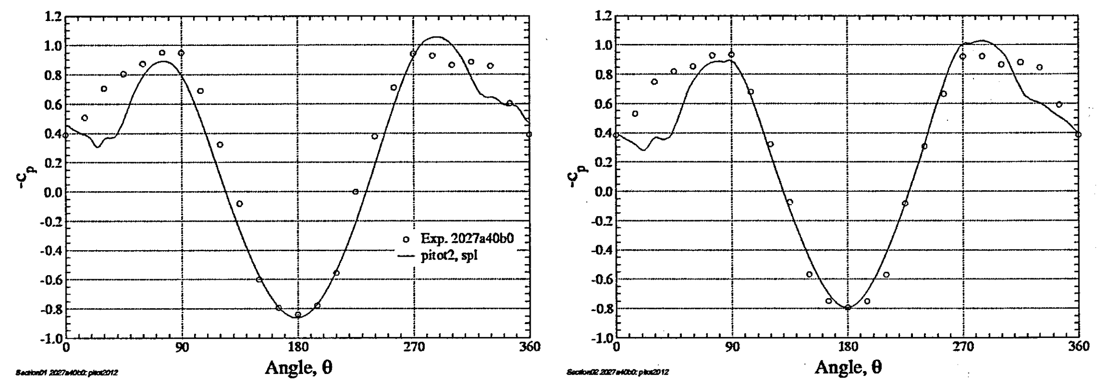

(a) Section 01

(b) Section 02

Figure 4.47: JAS-39 grid pitot2, M=0.176, Re=4.06 × 10^6, α=40°. Circumferential c_p distributions, sections 01 & 02. Spalart-Allmaras model.

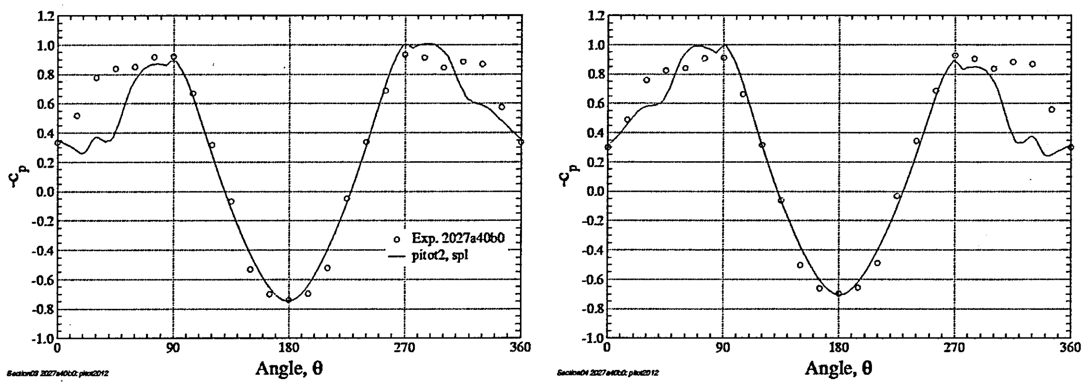

(a) Section 03

(b) Section 04

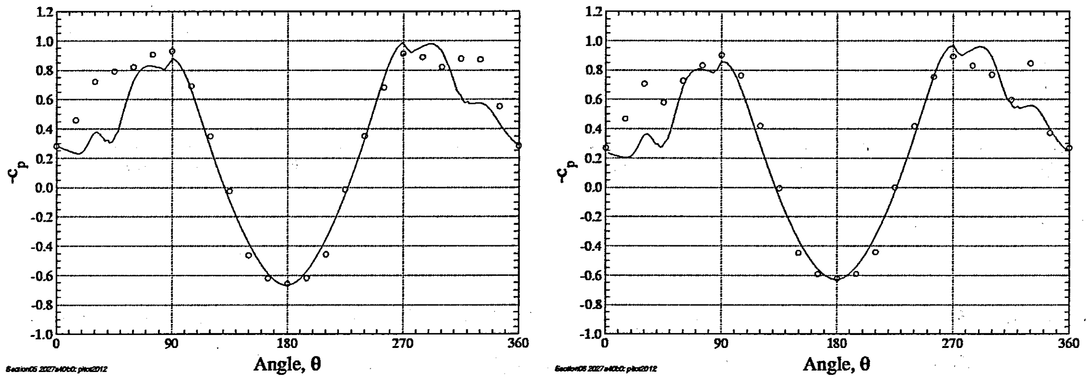

(c) Section 05

(d) Section 06

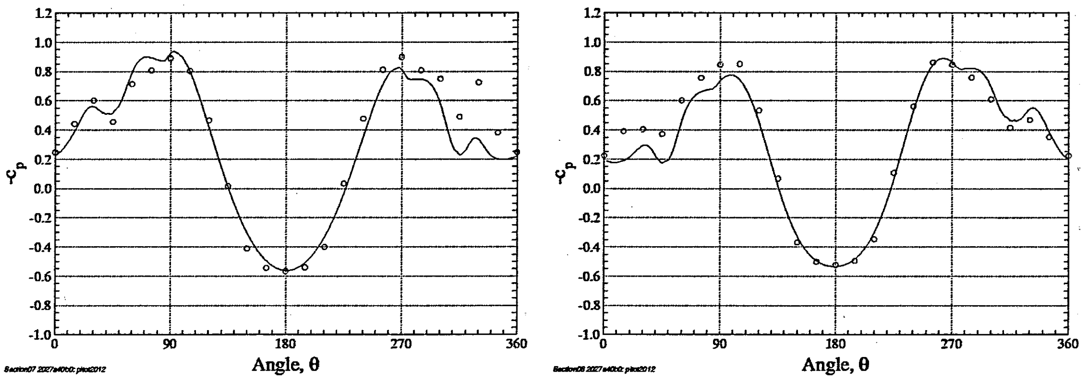

(e) Section 07

(f) Section 08

Figure 4.48: *JAS-39 grid pitot2, M=0.176, Re=4.06 × 10^6, α=40°. Circumferential c_p distributions, sections 03-08. Spalart-Allmaras model.*

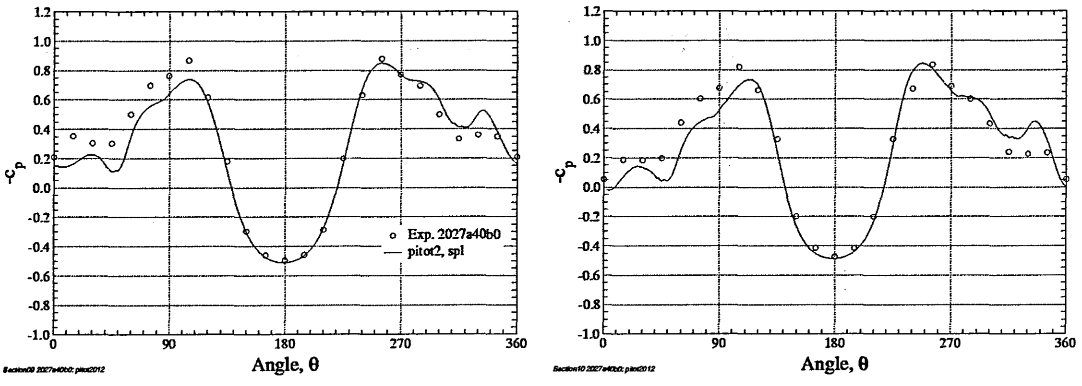

(a) Section 09 (b) Section 10

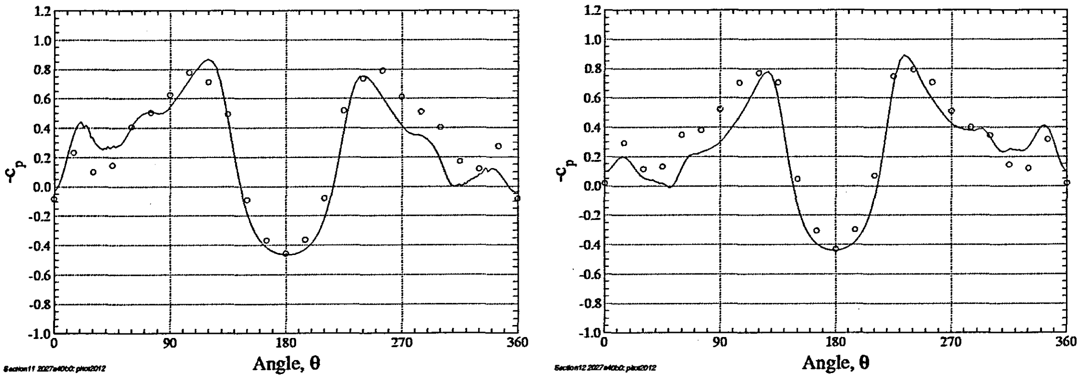

(c) Section 11 (d) Section 12

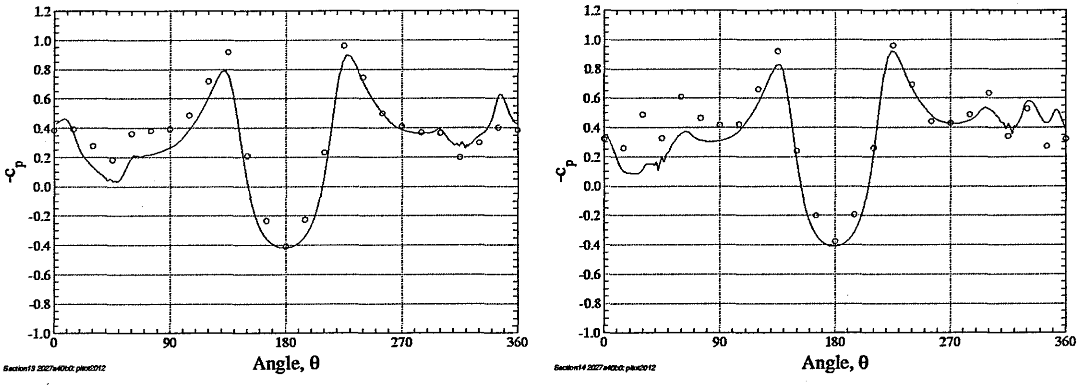

(e) Section 13 (f) Section 14

Figure 4.49: *JAS-39 grid pitot2, M=0.176, Re=4.06 × 10^6, α=40°. Circumferential c_p distributions, sections 09-14. Spalart-Allmaras model.*

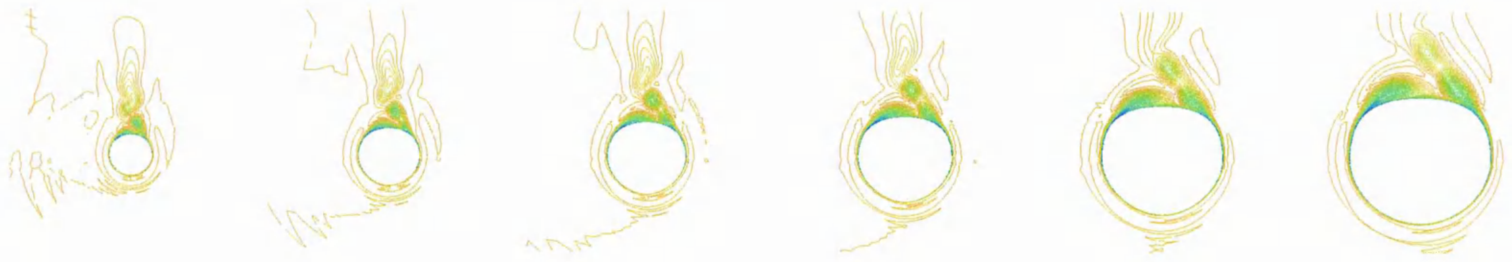

(a) Section 01 **(b)** Section 02 **(c)** Section 03 **(d)** Section 04 **(e)** Section 06 **(f)** Section 07

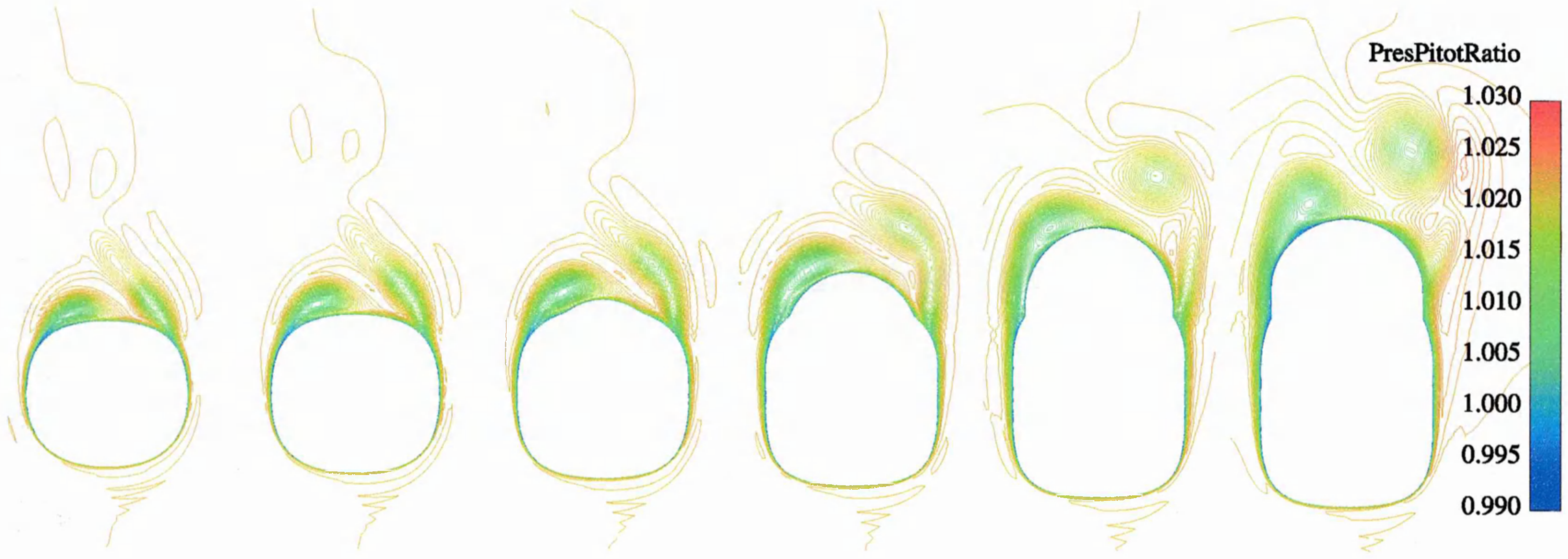

(g) Section 09 **(h)** Section 10 **(i)** Section 11 **(j)** Section 12 **(k)** Section 13 **(l)** Section 14

Figure 4.50: *JAS-39 grid pitot2,* M=0.176, Re=4.06 × 10^6, α=40°. *Contours of pitot pressure ratio, Spalart-Allmaras model.*

4.4 Summary of Results

- Fully turbulent solutions were obtained around the clean JAS-39 geometry at $\alpha = 0^o, 20^o, 40^o, 50^o$ and $\beta = 0^o$ using the non-symmetric implicit LU-SGS algorithm. A partially converged solution was also obtained at $\alpha = 60^o$, $\beta = 0^o$.

- Turbulence was modelled either with the one-equation Spalart-Allmaras model or the blended two-equation k-ω-SST model of Menter. Successful results were achieved with both models for $0^o \leq \alpha \leq 50^o$. No solution could be obtained with $k\omega$-SST at $\alpha = 60^o$.

- Differences due to turbulence model are visible only at very high angles of attack. The k-ω-SST model proved surprisingly robust and gave good resolution of the flowfield. The computed surface pressure coefficient profiles show excellent correlation with experiment, even at the higher angles of attack where solution asymmetries are generated by the LU-SGS algorithm.

- A pitot tube was added to the geometry and solutions obtained at $\alpha = 0^o, 40^o$ and $\beta = 0^o$ with Spalart-Allmaras. At $\alpha = 40^o$, the pitot tube was found to significantly destabilise the calculation and only a partially converged solution could be achieved. The results show a highly asymmetric vortical flowfield with $C_y \approx 27\% C_z$. Despite this, C_z was not seen to increase appreciably above the value recorded for the clean configuration at the same angle of attack. Again, surface C_p profiles agree well with experiment.

5. Forebody Flow Control

It has been shown in previous chapters how serious a problem forebody vortex asymmetry can be for an aircraft attempting extreme manoeuvers. The initial engineering response was, unsurprisingly, to seek a way of minimising the asymmetry in order to stabilise the aircraft at the higher angles of attack required. However, the advent of fly-by-wire and an increasing emphasis on stealth has led to a variety of proposals that utilise the forebody vortices to enhance, or possibly even partially or wholly replace, conventional aerodynamic control surfaces.

5.1 Basic Concepts

The aerodynamic benefits that can be gained by the installation of some form of forebody vortex control/manipulation system in combat aircraft have been shown in both the NASA HARV and X-29 programs along with numerous wind-tunnel tests.

The simplest device aimed at vortex control is the static strake, which works by fixing the position of the two nose vortices, either by imposition of a symmetry plane near the nose apex or by fixing the boundary-layer separation points. Whilst this type of device may be beneficial in improving high angle of attack stability and departure resistance, it cannot be used to harness the vortices and actively improve manoeuverability. Under high alpha flight conditions, the highly energised vortical flowfield enveloping the forebody makes a forebody manipulation and control system an obvious and attractive possibility.

The principle behind any active forebody vortex control system is to introduce small perturbations into the flow which alter the boundary-layer separation points, thereby deflecting the primary vortex system into a favourable disposition. The means by which this is achieved can take the form of either a mechanical or pneumatic device but, since the nature of the flowfield is dominated largely by the tip geometry, the magnitude of the perturbation required to produce a given force increases significantly as the point of application moves further downstream from the nose. Obviously, a limiting positioning factor for the manipulation mechanism in existing combat aircraft is the necessity of the nose radome. In addition, any deployable mechanical device must not degrade pilot vision.

5.2 Body reshaping

In practice, most aircraft forebodies are not perfectly axisymmetric and a certain amount of cross-section reshaping can be done to minimise the effects of any asymmetric vortex pair which may arise. However, care must be taken since data from Northrop, [111], indicates that noses providing stabilising directional stability force components may also give a positive, nose-up, pitching-moment contribution.

Northrop initiated a total redesign of the nose section of the F-5 when a NASA investigation of the F-5A revealed the nose shape to be the major contributor to the directional stability of the aircraft at high α. The result was a *'sharknose'* design, much flatter and broader than the production nose. This modification gave an order of magnitude reduction in yawing moment, shown in Fig.(5.1), due to virtual elimination of zero-sideslip vortex asymmetry. Full details can be found in [24, 109, 111].

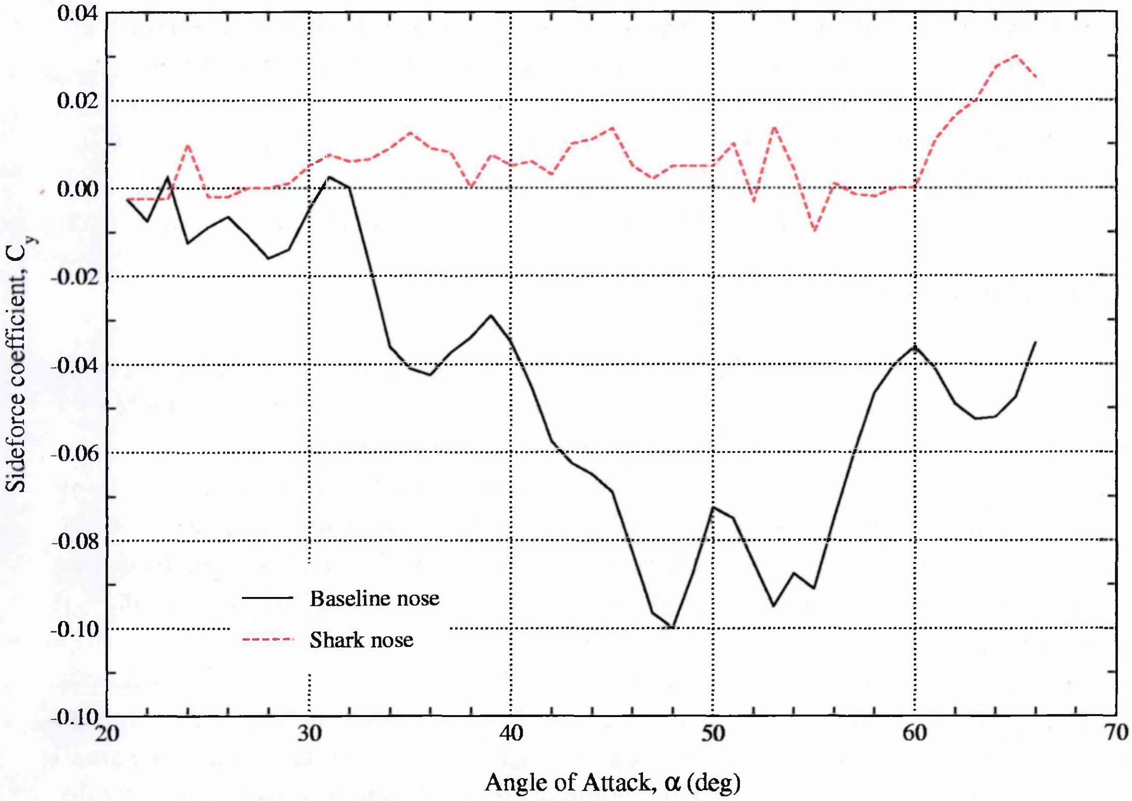

Figure 5.1: *Effect of Sharknose on sideforce coefficient for the Northrop F-5, $\beta = 0^o$, [109].*

5.3 Mechanical Vortex Control

5.3.1 Static strakes

Single static strake

Surprisingly, very little work has been done concerning the effect of adding a small vertical strake near the apex of the forebody along the leeward meridian. The effectiveness of this method of sideforce control relies on reducing the interaction between the two vortices in the critical formative region near the apex. There is no doubt that the apex region is critical in determining the nature of the asymmetry, however, the mechanism by which any asymmetry is being amplified downstream is not wholly clear. Amplification at the saddle point between the two vortices may be the cause but this takes no account of possible mutual entrainment near the tip and the stabilisation effect of the axial flow. Ng, [96], attempted to investigate this by running tests in which a small triangular strake, 8% of the forebody length was added near the apex of a 4.0D model. This would have the effect of reducing the interaction of the vortices in this region.

Without the strake, Ng noted a left-handed asymmetry starting at $\alpha = 30^o$ and becoming stronger at higher angles, as would be expected. This was greatly reduced with the addition of the strake, the positioning of which proved critical: any slight misalignment produced large downstream flow asymmetry. This result can be explained by considering the strongly 3-dimensional nature of the apex flow and the substantial influence of the axial component. Reducing the interaction between the vortices in this region prevents the downstream development of the asymmetry caused by a perturbation at the apex. If this is indeed the case, a single vertical strake may prove to be a simple yet effective method of increasing high alpha stability.

Dual static strakes

Studies performed early in the 1970s demonstrated the ability of strakes placed on either side of the forebody to reduce asymmetric forces, see Coe *et al.*, [10]. Keener *et al.*, [60], employed a slotted model to which one of three flat, sharp-edged plates could be fitted. The model was a 3.5D tangent- ogive of length 53.3cm and the strakes tested had exposed widths of 0.32, 0.64 and 1.27cm. Apart from at the lowest Reynolds number tested, all three sets of strakes virtually eliminated the sideforce.

Smith, Ralston and Mann, [112], performed a thorough review of the YF-16 and F-16 developmental wind-tunnel test program and extracted all data pertinent to the design of forebody and nose strakes. During the test program, General Dynamics had looked into the effects of variation in strake size, strake planform, strake location relative to the nose, and strake span relative to the span of the wing. The investigation included: forebody strakes, extending from the forebody to the leading edge of the wing; nose strakes, extending a short way aft from the apex; canard strakes, placed aft of the nose but not extending to the wing root. Whilst considerable emphasis was placed on the enhancement of available lift for manoeuvering and prevention of low-speed deep stall, the beneficial and negative aspects of addition of nose-strakes were examined in some detail.

For fully subsonic conditions, the improvement in lateral/directional stability of the model due to the nose strake over the baseline model with blended forebody strake was significant for all configurations tested. It was established that the strake width and aft extent are the most critical parameters and, interestingly, a sudden truncation of the strake proved to be more beneficial than fairing in. Actual strake shape was shown to be of little concern. Inclination of the strake with respect to the aircraft *'waterline'* also seemed to have negligible effect.

Smith *et al.* postulate that, without nose strakes, the vortices shed from the forebody evolve from various locations depending on α, β, the exact configuration and so on. The addition of nose strakes, especially truncated nose strakes, helps to hold fixed the separation points of the shear layers which will form the vortices. The resultant vortical structure thus develops in a far more symmetric way. The dependency on the apex region explains why most forebody strakes, positioned as they are further aft, have little stabilising influence by themselves. In addition, any vortices arising from forebody strakes, which generally tend to be wing LEX[1], will be heavily affected by the wing flowfield. In conclusion, Smith *et al.* suggested that whilst forebody strakes could provide enhanced lift for manoeuvering, nose strakes offer significantly improved lateral/directional characteristics with little effect on longitudinal characteristics and, due to the minimal increase in wetted area, negligible increase in drag.

5.3.2 Deployable or actuated strakes

Static nose strakes offer some measure of vortex control which can lead to vastly improved lateral/directional characteristics. However, deployable strakes offer this and the added advantage of being able to force asymmetry when desired in order to produce controlled sideforces and yawing moments and thereby improve manoeuverability. Due to the complexity and high development cost of such systems, most work has been performed under the auspices of the NASA High Alpha Technology Program.

The simplest form of moveable strake is a vertical, pivoting, nose strake, often referred to as a *'rhino horn'*. The rhino horn is a miniature strake mounted on the leeward meridian line of the forebody and pivots about an axis perpendicular to the surface of the forebody, see Fig.(5.2). At zero degree deflection, it acts as a single static strake, stabilising

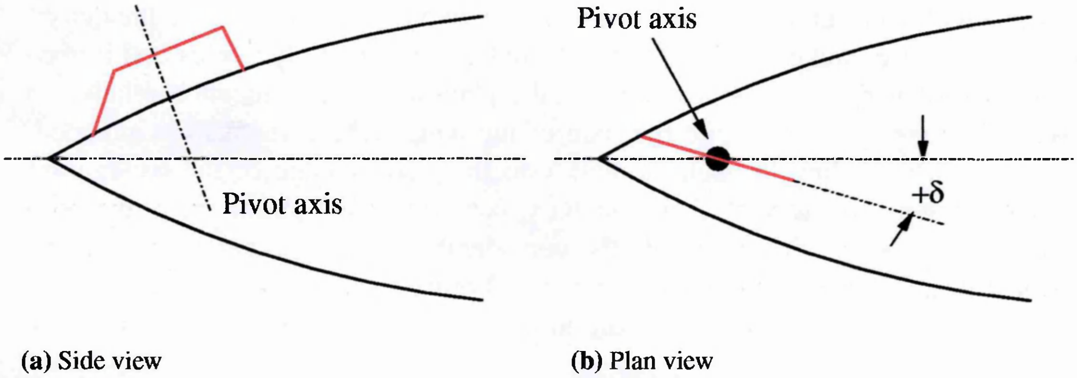

(a) Side view

(b) Plan view

Figure 5.2: *Schematic of rhino horn location on nose.*

---

[1] Leading Edge Extensions

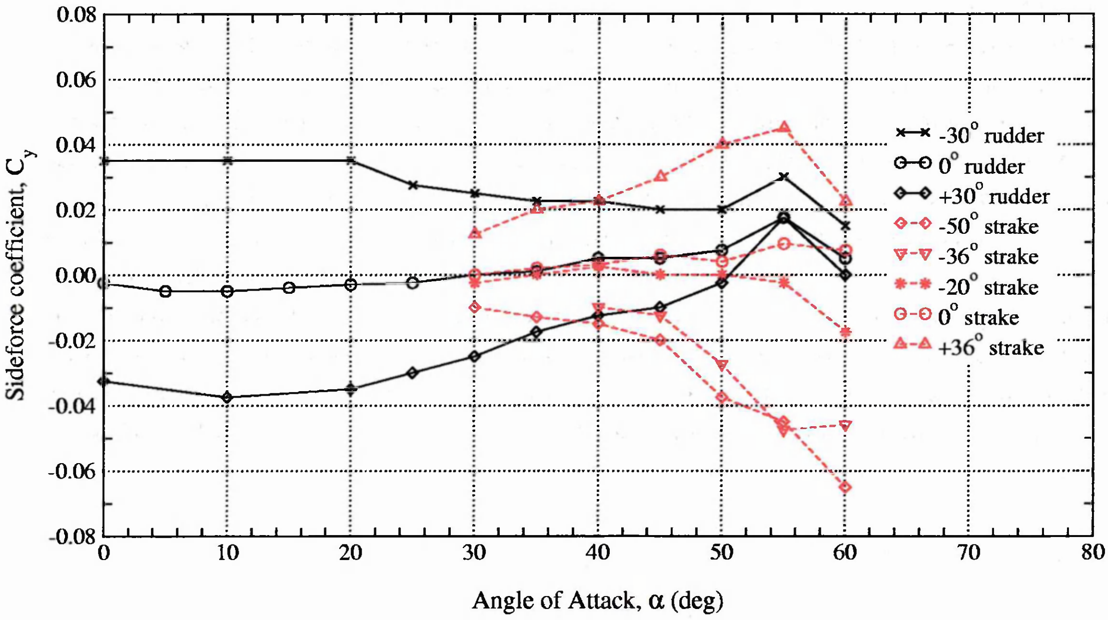

(a) AoA sweep

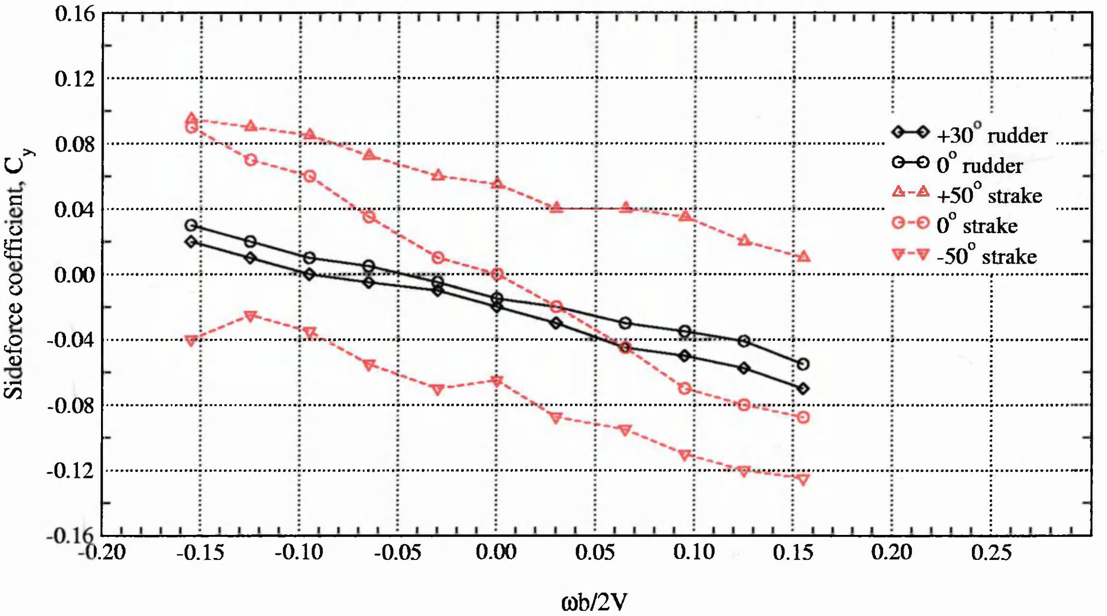

(b) Rotary balance, $\alpha = 51^o$

Figure 5.3: *Comparison of rudder and rhino-horn effectiveness in static and rotary tests. Data from Kramer and Smith, [64].*

the vortices by preventing interaction in the generation region. By deflecting the strake, however, the vortices are forced into an asymmetric state, resulting in a sideforce.

Kramer and Smith, [64], ran a series of tests to evaluate various forebody control techniques on a 6% scale F/A-18. The rhino horn they tested[2] behaved in a similar manner to the single rotating nose tip strake discussed in Subsection 5.3.3, giving well-behaved results up to $\alpha = 60^o$, see Fig.(5.3(a)). A rotary test showed the anti-spin tendency of the aircraft to be increased, see Fig.(5.3(b)). In addition, whilst the device generated no additional positive yawing moment at the maximum negative rotation rate, the moment generated in the undeflected case was double the 0.04 of the unmodified aircraft. Overall, the results suggested that an active control system using the rhino horn could increase the available control power envelope significantly and Kramer and Smith note that the range of available yawing moments was greater with this device than with any of the others tested (these included slot- and jet-blowing).

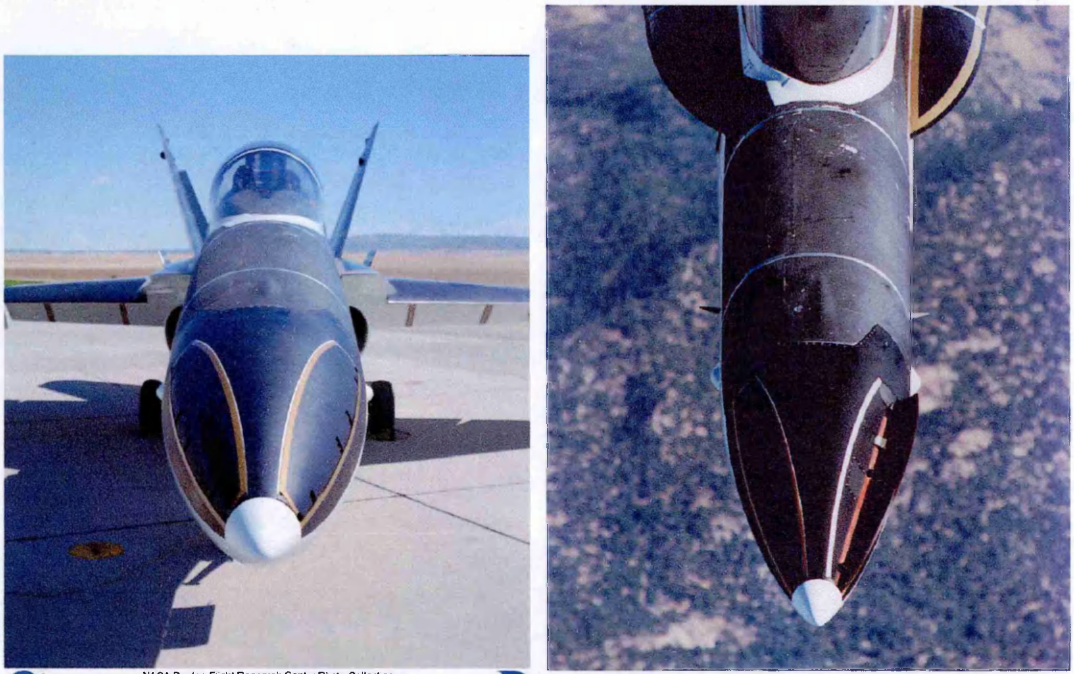

NASA Dryden Flight Research Center Photo Collection
http://www.dfrc.nasa.gov/gallery/photo/index.html
NASA Photo: EC95-43057-8 Date: 1995

F-18 HARV on ramp close-up of actuated nose strakes

Dryden Flight Research Center EC95 43249-14 Photographed 8/95
F-18 HARV: Actuated Nose Strakes for Enhanced Rolling
Hinged strakes produce large side forces for control.

(a) Flush

(b) Port deployment

Figure 5.4: *The F/A-18 HARV ANSER installation. NASA photographs.*

The initial development of the concept of dual actuated forebody strakes was conducted on a generic fighter model at George Washington University by Murri and Rao, [89, 91]. With these wind-tunnel tests confirming the potential benefit of such a device,

---

[2] Equivalent full-scale dimensions: 127mm length, 76.2mm maximum height.

NASA instigated the development of a system suitable for installation on the F-18 HARV, [90]. With the design of the strake finalised, a comprehensive program of ground-based tests started, reviewed in [93], leading to the installation of a conformal[3] actuated forebody strake system in the aircraft, see Fig.(5.4). The subsequent series of flight tests is referred to as the ANSER[4] Flight Experiment.

The ANSER strake development tests showed that maximum strake effectiveness was obtained for 90^o deflection. Using data gained from a 16% model, [93], Fig.(5.5) depicts the effects of maximum deflection on the sideforce characteristic throughout the α-range. It is clear from this how quickly the rudder effectiveness falls off for $\alpha > 20^o$ whilst the strake effectiveness increases. In addition, the natural asymmetric characteristics of the body throughout this range are completely eliminated by strake deflection, being replaced by almost symmetric control effectiveness. The strakes were also seen to provide increased yaw control for $-30^o < \beta < 30^o$, important for high α manoeuvering. Transonic wind-tunnel tests showed the strake effectiveness above $\alpha = 30^o$ to degrade with increasing Mach number. However, for $M \approx 0.8$ and above, the structural g-limit is most likely to be exceeded for $\alpha > 35^o$ and so much of this data is irrelevant.

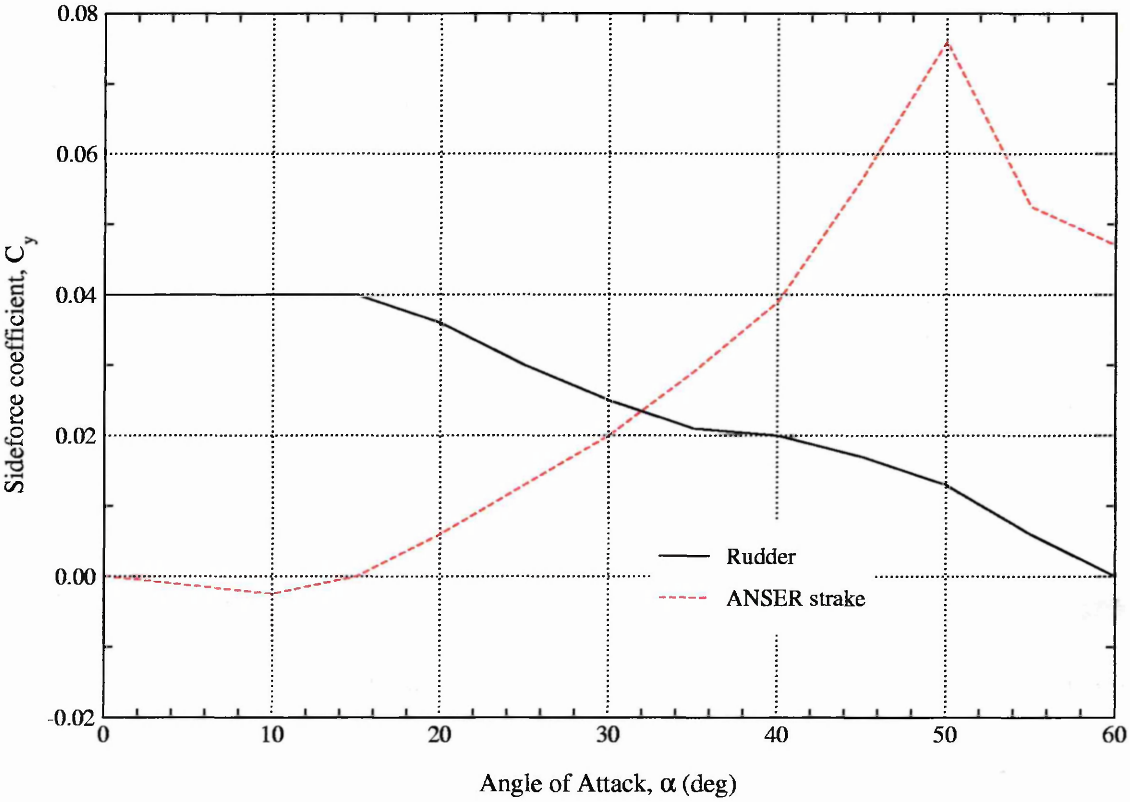

Figure 5.5: Comparison of F/A-18 rudder and ANSER forebody strake yaw control power, 16%-scale model. Data from [92]

---

[3] i.e. when retracted the strakes follow the original radome contour.

[4] Actuated Nose Strakes for Enhanced Rolling.

Flow visualisation was performed on a full-scale F-18 forebody in the Langley 30-by 60-foot tunnel. Deployment of a strake was seen to reduce the suction on the strake-deployed side of the forebody, the suction increasing on the other side. This increased suction is accompanied by a movement of the primary separation line towards the leeward meridian. Hence, Murri *et al.*, [93], postulate that deployment of a strake creates a dominant vortex which delays separation and accelerates the flow on the undeployed side, the opposite occurring on the strake-deployed side of the forebody. The result is a net sideforce in the direction away from the active strake.

Possibly the first current aircraft to benefit from an active forebody vortex control system will be the F-15. With ground- and flight-testing in the HARV and X-29 programs confirming the aerodynamic benefits of forebody vortex control, the McDonnell Douglas Corporation (MDD) initiated the F-15 Forebody Vortex Control (FVC) Program to improve the high angle of attack controllability of the F-15 by developing a production system. Several methods, (including high actuated strakes mounted on the nose barrel aft of the radome), were assessed in the wind-tunnel and control laws developed for a manned simulator evaluation.

5.3.3 Rotating tip devices

A novel method of providing forebody vortex control is the rotatable forebody tip. Moskovitz *et al.*, [87], conducted an exploratory investigation to see how a small rotatable tip device, varying in cross-section from circular at its base to elliptic at the tip, could affect yaw control. The thinking behind this was that previous studies, such as that of Lamont, [68], seemed to indicate that a double cycle sinusoidal variation in sideforce achieved on rotating the model might be due to the tip being slightly elliptic in cross- section. Conventional thinking would be to try and minimise the ellipticity of the cross-section, but Moskovitz *et al.* proposed using a tip of definite elliptic cross-section in order to guarantee the nature of the rotational variation.

Moskovitz *et al.* looked at a 10^o semi-angle cone and a 3.0D tangent-ogive, both mated to a cylindrical afterbody. Two hand-filed tips were made for each model, one with greater ellipticity which stretched further aft than the other. The sideforces obtained on the standard sharp and blunt tips showed irregular variations with roll angle due to the machining imperfections as expected, [86, 88]. However, the exagerrated ellipticity of the modified tips produced a regular, predictable, distribution, moving from a smooth two-cycle sinusoidal pattern at 30^o to a sharp two-cycle square-wave at higher angles. This started to break down at 60^o for the cone but no such problem was encountered for the tangent-ogive. In conclusion, Moskovitz *et al.* ran tests on the ability of the deflected tip to provide a restoring force under sidelipping conditions. This it proved able to do for $\beta < 15^o$ at angles of attack up to 60^o, proving that further research would be valuable.

Working in the Eidetics Water Tunnel, Ng and Malcolm, [98], investigated a system employing rotatable nose-tip strakes, 1/10th the length of the F/A-18 model radome, 1/5th the local forebody diameter and mounted 75^o either side of the windward meridian. Around the baseline configuration, three flow regimes were discerned, [97]: symmetric flow up to $\alpha = 55^o$; asymmetric flow with right vortex high for $55^o \leq \alpha \leq 60^o$; bi-stable asymmetric flow for $60^o \leq \alpha \leq 65^o$. For the second flow regime, the strakes could be used to overcome the baseline asymmetry to promote symmetry or different asymmetric states. For the bi-stable state, the asymmetry could be reduced, increased or flipped but symmetry could not be achieved by holding the strakes in any position. However, by inducing the strakes to rapidly oscillate with a small amplitude about their symmetric position, a quasi-steady state could be forced. Overall, some measure of increased control was attained for $0^o < \beta < 20^o$ and $\alpha > 30^o$ to angles greater than 65^o.

Clearly, the rotating nose-tip strakes function in much the same way as the elliptic tip, creating a purposely asymmetric forebody apex. This can provide a bias to any natural flow asymmetry, adding very little vorticity to the flow. The control characteristics thus depend heavily on the baseline vortical flow. In contrast, since they generate additional sizeable local vorticity, methods of vortex control using large actuated strakes should be able to operate effectively across a greater envelope of flow conditions.

Ng and Malcolm also tested a single rotatable strake but concluded that the presence of a second strake provided a more gradual variation in yawing moment with nose-tip angle. Kramer and Smith, [64], on the other hand, restricted the movement of the single strake they tested to the leeward side of the nose and the device gave well behaved trends for $30^o \leq \alpha \leq 60^o$. When locked in position along the leeward meridian, the strake also provided increased anti-spin damping and, when deflected, it was seen that it could stop or initiate rotary motion throughout the range of rotations examined.

5.4 Pneumatic Vortex Control

5.4.1 Passive porosity

The simplest method of pneumatic forebody vortex control is also the method about which the least information has been published, at least in the public domain. Surface porosity has long been known to be an effective means of passive shock control, see for example [94, 114]. Initially discussed as an option by Modi *et al.*, [84], the first studies into passive porosity as a means for reducing high-alpha forebody asymmetries were conducted by Bauer and Hemsch, [5], and Wood, Banks and Bauer, [125].

Recognising that most aerodynamic fixes to the forebody problem involve the addition of weight and complexity and are of benefit only through a limited range of α, Bauer and Hemsch, [5], postulated that surface porosity might, through an equalisation of pressures around the forebody, reduce or even eliminate any asymmetric forces. With a porous skin and a plenum chamber below the surface, two effects were expected: a reduction in circumferential pressure gradients leading to a reduction in the generation of boundary-layer vorticity and, subsequently, the strength of the wake vortex system; an equalisation of the surface pressures left-to-right thus ensuring symmetric vortex shedding. Working in the 7'×10' High-Speed Wind Tunnel at the NASA Langley Research Center, Bauer and Hemsch compared data obtained for solid and porous 5.0D tangent-ogive/cylinder models. For the porous model, the surface was perforated with 0.020" diameter holes

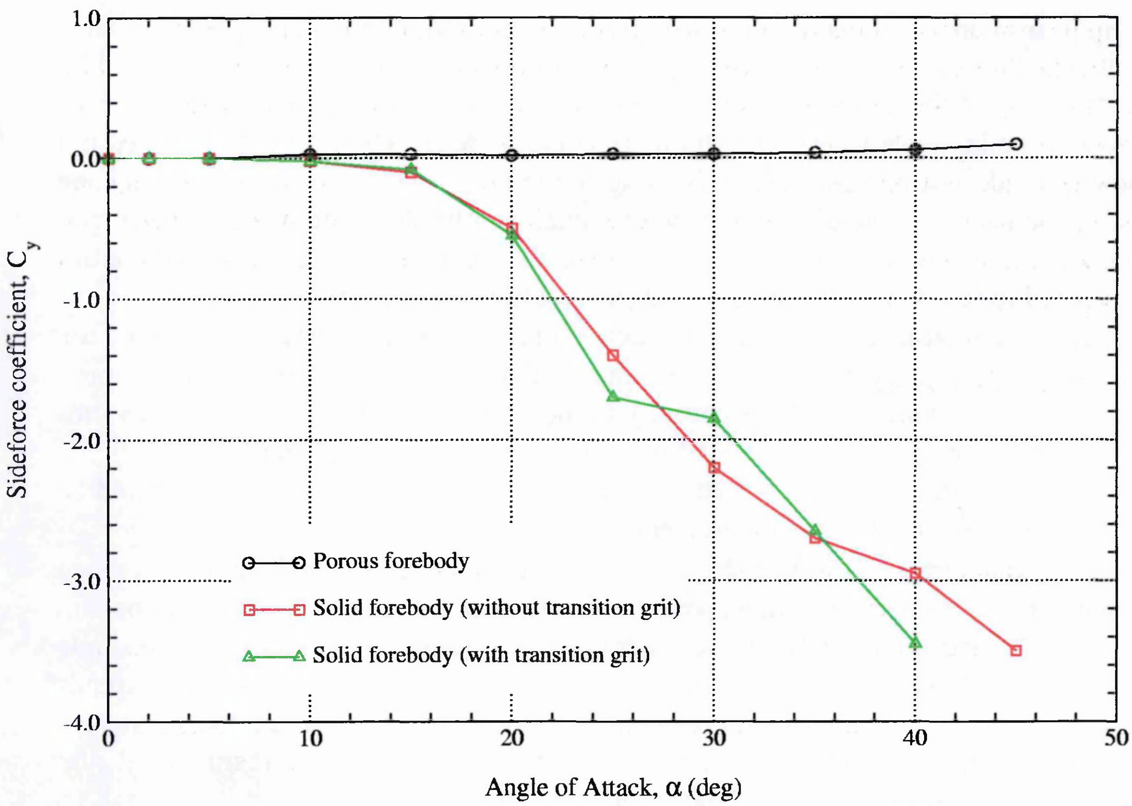

Figure 5.6: *Effect of porosity on sideforce coefficient for a 5.0D tangent-ogive forebody at* $M_\infty = 0.2$. *Data from Bauer and Hemsch, [5].*

0.0534" apart to give a porosity of 20%. This porosity was maintained over the entire length of the tangent-ogive before being linearly reduced over the next 1.25 body diameters. The final 1.25 diameters of the cylindrical afterbody were solid. Assuming that the porous surface would promote early transition, no.80 sand grit was applied over the entire surface of the solid model to facilitate direct comparison of data. The results show the porous forebody to have virtually no Mach number dependence with virtually zero sideforce even at $\alpha = 40^o$. In roll, there are slight variations in C_Z and C_Y but far less than for the solid body. On varying the extent of the porosity aft of the nose, Bauer and Hemsch found that normal force was unaffected but sideforce began to increase as the porous region was reduced to below 3.0 diameters aft. Data taken inside the plenum chamber revealed the plenum pressure to be almost constant and the flow velocity low.

Further work by Wood, Banks and Bauer, [125], aimed to further understanding of the altered flow physics of porous forebodies. Following a series of tests with a porous surface and strakes asymmetrically mounted so as to force asymmetric cross-flow separation and a repeatable, uni-directional sideforce, they conclude that direct pressure equalisation was found to be the dominant mechanism. Limiting the extent of the porosity to the top half of the body only was found to degrade the improvement significantly, as was wholly or partially partitioning the plenum chamber, re-inforcing the importance of direct communication between the high and low pressure regions around the forebody.

Despite the promise of the above work, (or possibly *because* of), subsequent literature is limited to a report by Fears, [29], covering a low-speed wind-tunnel investigation of a porous forebody and nose strakes for the Boeing Multirole Fighter (BMRF) aircraft, a precursor to the Joint Strike Fighter (JSF). With similar results to those discussed above, Fears's conclusions are that, provided *'a way of mechanising the opening and closing of the porous areas can be developed, this ... may be a viable concept for obtaining high-angle-of-attack yaw control on advanced fighters'.*

5.4.2 Blowing and suction

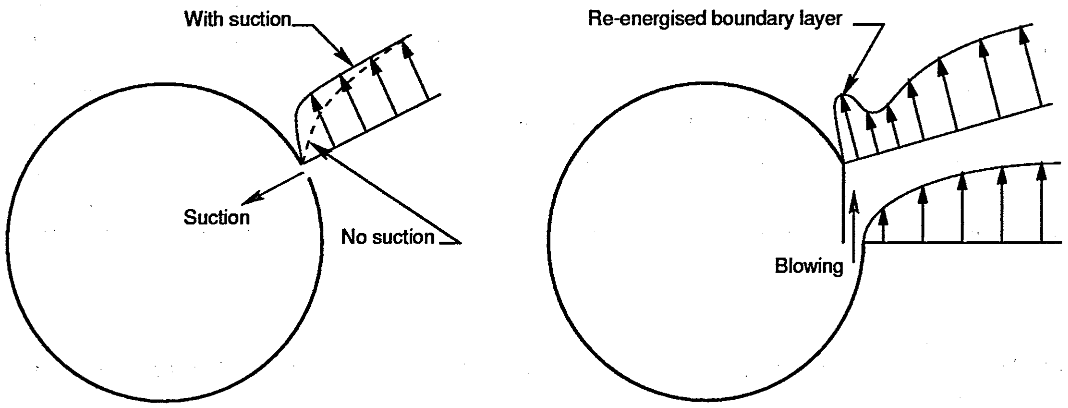

(a) Suction (b) Slot blowing

Figure 5.7: Schematic of influence on boundary-layer of suction and blowing. Figures adapted from Ng and Malcolm, [97].

Forebody blowing methods have been evaluated in some depth since the mid 1980s following some simple tests on an F-5 forebody at Northrop in the 1970s, [110], and on a slender cone at Nasa Ames, [99]. Either ports or slots, as in Fig.(5.7(b)), can be used for blowing but port (jet) blowing was the first pneumatic concept seriously considered for forebody vortex control.

Tests by Eidetics on a generic forebody configuration in the NASA Langley 12-foot low-speed wind tunnel, [75, 76, 77], showed that blowing rates with the momentum blowing coefficient, C_μ, less than 0.0075 could provide yawing moments at incidence equivalent to full rudder and $\alpha = 0^o$. In addition, the directional instability of the baseline geometry, which was already equipped with small nose strakes to minimise high-alpha asymmetries, could be overcome even at $\alpha = 60^o$.

Later, experiments by the USAF and Eidetics on a 1/15th-scale F-16 forebody model equipped with nozzles at two locations aft of the nose showed that, as for a mechanical device, jets near the nose apex were most effective at producing a yawing moment, [71].

Higher blowing rates produced larger yawing moments, with the yawing moment directed away from the side on which the jet was active, the opposite effect to that noted with during tests on the generic forebody. The forward nozzles were permanently set to blow aft whilst the rearmost nozzles were canted outboard. These results indicate that either the boundary-layer was being induced to separate prematurely on the side of the active jet or the vortex was being displaced from the surface, either of these resulting in a net increase in sideforce away from the active side.

However, results using a 1/8th-scale X-29 model, reported by Guyton and Maerki, [36], and Cornelius *et al.*, [13], agree with the trends seen on the generic forebody. Blowing on the left-hand side generated a negative yawing moment and *vice-versa*, the effect amplified by canting the jets in towards the body. Whilst the jet in the F-16 study displaced the vortex from the body on the side of operation, the arrangement on the X-29, with the ports blowing tangentially to the surface, resulted in the jet delaying separation on the active side. Canting the jets inboard would have the additional effect of displacing the opposite vortex hence increasing the net difference in pressure between the two sides. The optimal configuration was found to be an inboard cant of 60^o. Further investigations were carried out in-flight using the X-29a aircraft with its nose appropriately modified. Bottles of compressed nitrogen gave about 15 seconds of blowing time with $\dot{m}$ and C_μ being varied by changing the nozzle size. Results showed the obtained yawing moments to be at least as great as those predicted experimentally, whilst there was little impact on the aircraft rolling moment or delay between initiation of the system and aircraft response.

Concurrent with the above work, Eidetics water-tunnel tested a 6%-scale F/A-18 forebody model to evaluate the potential of various FVC methods, [97]. A left-hand nozzle blowing aft was seen to generate a negative yawing moment whilst a positive yawing moment resulted from blowing forward. Since yawing moment was seen to vary with C_μ, a control system based on the concept might be viable and the study was extended into the NASA Ames 7'×10' wind tunnel using a 6%-scale fibreglass model, [65]. Blowing straight aft produced low yawing moments opposite in direction to the side of blowing, as for the F-16, and the optimal configuration was once again found to be with the nozzles canted 60^o inboard.

More recently, a study by Eidson and Mosbarger, [23], sought to expand on previous tests by evaluating the performance of a nozzle-blowing system at lower angles of attack but at increased Mach number, more realistic operating conditions for a manoeuvering combat aircraft. Although the trends relating to nozzle position, cant angle and C_μ were seen to be similar to existing data, a horizontally-slotted, hence tangentially blowing, nozzle proved more suitable for generating large yawing moments at lower angles of attack than a vertical-slotted nozzle. In addition, pulsing the air rather than blowing continuously allowed the mean mass-flow rate to be reduced by some 21% without reducing the mean sideforce.

Slot blowing works in much the same way as tangential port blowing, with the injected air serving to re-energise the boundary layer and delay separation on the active side. Evaluation of the technique on a full-scale F/A-18 showed there to be a complex relationship between the location and length of the slot, the mass-flow rate and the effectiveness of the system, [70]. Low blowing rates were also seen to produce yawing moments in the opposite direction since the velocity of the expelled air was not high enough to accelerate the boundary layer but rather disturbed it and promoted early separation. Similarly, a maximum effective blowing rate appeared to be reached and rates above this were shown to have little additional benefit or even to be detrimental. This was also found in slot-blowing tests with the previously mentioned 1/15th-scale F-16 model, see [71].

When slot suction is employed, the low energy air in the boundary layer is removed and separation delayed, suction therefore being generated, see Fig.(5.7(a)). Little has been published in this area aside from brief notes by Ng and Malcolm, [97], regarding a 6% scale F/A-18 forebody water-tunnel model equipped with a slot at 135° from the windward meridian. Optimisation of the slot geometry was not attempted, but control could be effected even with the shortest slot tested. It was found that large degrees of asymmetry could be generated with relatively low suction rates but, as with both slot and port blowing, the nature of the baseline flow can have a strong bearing on the characteristics and effectiveness of the system.

5.5 Transition Control Methods

Boundary-layer trips can provide a simple method of guaranteeing symmetric separation. Letko, [72], tried promoting separation by fitting a ring made from $\frac{1}{16}$ inch diameter wire around the sharp-nosed body of revolution he was testing. He found that the addition of the ring had little effect on the yawing moment until angles greater than about 15°. After this point, the yawing moment was reversed in sign and the absolute value reduced compared with the plain fuselage case. By looking at the lateral force coeffcients, Letko found that this was due to both a reduction in the overall sideforce and a shift in the centre of pressure for the sideforce. In other words, the sideforce distribution along the body had been altered by the presence of the ring. Tuft-probe examination revealed that the disposition of the asymmetric vortices had been changed but Letko could not explain why this might happen. He did note, however, that increasing the distance of the ring from the nose reduced the effectiveness. A further method of yawing-moment reduction tested by Letko was the addition of carborundum grains over the nose, thus increasing roughness. This apparently had a similar effect to the ring.

Twenty years later, Keener *et al.*, [60], tested the effect of adding boundary-layer transition strips and surface roughness to their 3.5D tangent-ogive forebody model.Taking $\theta = 0^o$ as the windward meridian, for a Mach number of 0.25 the addition of longitudinal strips at $\theta = \pm 15^o$ or $\theta = \pm 30^o$ gave a reduction in sideforce of 50% or more. Lowering the length of these transition strips to $1/3$ of the forebody length reduced the sideforce even further, this emphasising the importance of the nose region. Positioning the transition strips at $\theta = \pm 60^o$ or $\theta = 0^o$ made little impact on the magnitude of the sideforce. Keener *et al.* also discovered that a ring of roughness elements around the body was effective in reducing sideforce. Of the various lengthwise positions tested, the furthest forward, at $x/l = 0.05$, and the furthest aft, at $x/l = 0.286$, gave the least reduction.

Erickson and Lorincz, [25], shed some light on the mechanism by which boundary-layer trips reduce the sideforce. The model tested was a Northrop F-5 aircraft with helical trips positioned on the nose. The trips were seen to encourage symmetry of the separation points, thus delaying the onset of asymmetric vortices until higher angles of attack than would otherwise be the case. However, the flow-visualisation pictures of the model with and without the trips show that this is achieved because the trips disrupt the feeding of vorticity from the attached boundary-layer on the rear section of the forebody into the separated vortical shear layer. Thus the primary vortices are significantly weakened and therefore more stable, remaining in their symmetric state.

More recently, longitudinal boundary-layer transition strips have been evaluated under flight conditions at NASA Dryden Flight Research Center as part of their ongoing high-alpha program, [33]. The transition strips were installed on the F-18 HARV forebody, a preproduction F/A-18 radome with a known problem at $\alpha \approx 50^o$ and the two X-31 aircraft. Results were mixed. Whereas the yaw asymmetry was reduced for the HARV, no appreciable improvements could be made with the pre-production nose. Research into the yawing moment asymmetries of the two X-31 aircraft is documented fully by Cobleigh, [9]. The two test aircraft both exhibited asymmetries, though of differing magnitudes, above $\alpha = 40^o$, with the problem being exascerbated by the underslung nose boom. It was found that application of transition strips to the nose both amplified the asymmetric yawing moments and widened the α-range where they occurred, although the random switching of the wake appeared to be reduced. Transition grit along the length of the nose boom was also seen to be of benefit, acting to guarantee turbulent separation and hence reduce the width of the vortex wake.

6. JAS-39 Forebody with Rhino horn

The previous chapter reviews some of the techniques and devices that may be utilised to alleviate the forebody aerodynamics problems that can arise at high angles of attack. Having successfully computed a clean Gripen forebody complete with nose pitot, the final stage of this research comprised adding one of these devices, a single vertical nose strake or 'rhino horn', and assessing the potential aerodynamic benefits. The following chapter presents results from those computations.

The results achieved on the baseline JAS-39 forebody showed NSMB to be capable of predicting surface pressures reasonably accurately for high angle-of-attack flows. Whilst the newly implemented k-ω-SST model produced excellent results, the one-equation Spalart-Allmaras model demonstrated far superior robustness for the more complex problems and near equivalent capability in terms of feature resolution. The difficulties encountered with code stability resulted in a decision being made to continue with fully turbulent Spalart-Allmaras calculations for the remainder of the research rather than attempting to improve the physical realism of the simulations by including the effects of transition. Although the importance of transition with regards to this type of problem cannot be over-emphasised, it was felt that correlation between the experimental and fully turbulent computed pressure coefficients was good enough to allow this simplification to remain. With the inclusion of a flow control device to the forebody/pitot model as the final stage in the research, this would provide code stability and hopefully ensure that solutions could be obtained.

6.1 Experimental Reference

Saab evaluated several forebody devices during development work on the JAS-39 Gripen. Whilst the production aircraft is equipped with two small nose strakes mounted at $\theta = 90^o, 270^o$ at the base of the pitot, a single vertical strake, commonly referred to as a 'rhino horn' was also tested. As documented in Chapter 5, a device of this type can either be left in a central position to act as a stabilising device by preventing the interaction of the two primary vortices in their critical formation region near the nose, or deflected to generate a controlled asymmetry which can provide additional control power. Schematics of two of the devices investigated by Saab are shown in Fig.(6.1). The strakes were installed on the same 1:6.5 scale pre-production forebody model as documented in Section 4.1 and tested over a complete incidence and sideslip range at a variety of deflections. Unfortunately, much of the surface pressure coefficient data that was gathered has not been reduced to a readily accessible form and so all computed results are compared to data taken on the forebody with pitot tube and strake 51, the smaller of the two devices, at zero deflection.

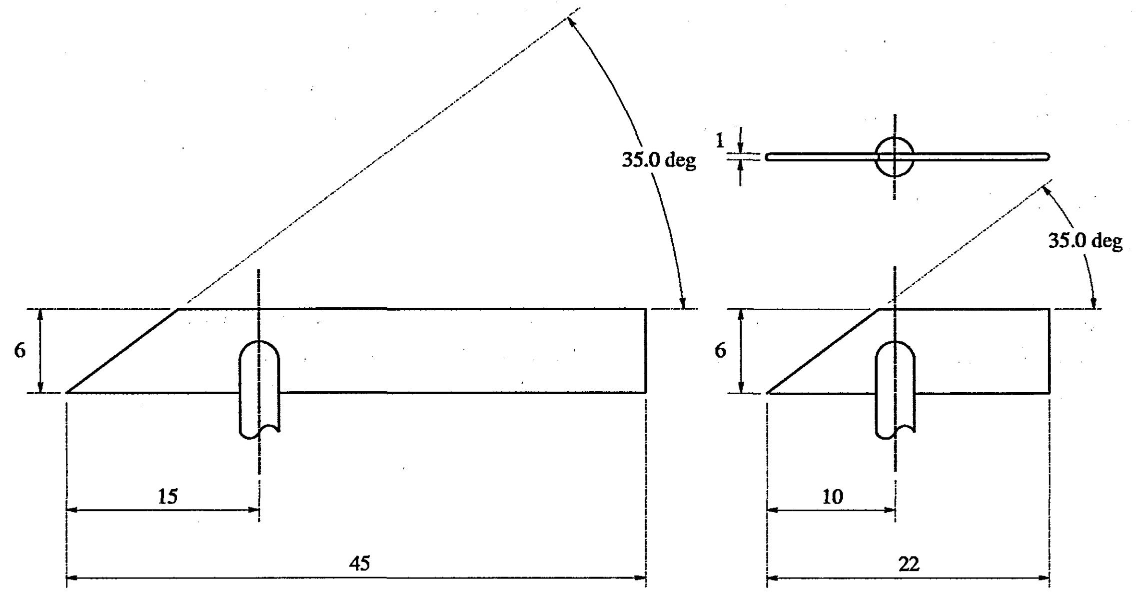

(a) Strake 46 (b) Strake 51

Figure 6.1: Rhino-horn geometry definition. All dimensions in mm modelscale.

6.2 Computational Details

6.2.1 Grid generation

The pitot2 grid for the forebody and pitot only was generated with approximately 3.1 million cells, see Subsection 4.2.1. Unforunately, this number of cells, in combination with use of an implicit algorithm, meant that only the 256Mb nodes on the T3E could be used. Additionally, the queueing system on the T3E places a limit of 32 256Mb nodes as the maximum which can be used by any one job. Therefore, although the addition of the rhino horn to the model necessitated a further increase in the number of grid cells, there was an upper limit of about 4.2 million beyond which the job would have to be submitted as a special request and, as a result, have the lowest priority in the queue[1].

Keeping the above in mind, the first grid generated, hereafter referred to as horn1, was for the clean JAS-39 forebody fitted with the larger of the two strakes, strake 46, in a central position, i.e. $\delta_{horn} = 0^o$. Rather than mirroring a half-body grid, an 18 block full-body grid was generated with 3,972,960 cells in total. This was decomposed and load-balanced to 42 blocks using MB-Split. A view of the surface mesh topology in the

---

[1] The memory limitation also removed the option of using full matrix implicit LU-SGS.

region of the nose and rhino horn is shown in Fig.(6.2). Although the mesh topology proved simple to set up, major problems were encountered owing to the proximity of the front of the horn to the conical nose and the high cell densities necessary for adequate feature resolution. The resulting highly skewed cells could not be avoided.

The second grid generated, phorn1, was for the forebody and pitot with the smaller strake, strake 51, fitted in a central position, $\delta_{horn} = 0^o$. The reduced length of the strake and the addition of the pitot tube, and therefore elimination of the conical nose, resulted in far fewer problems being encountered with grid quality. A surface view of the model showing the horn *in situ* is shown in Fig.(6.3(a)). Grid size was kept down to a manageable 4,193,920 cells.

The second pitot+horn grid, phorn2, was generated using the undeflected grid as a starting point. The rhino horn was rotated 5^o to port about its pivot axis in ICEM DDN, the blocks reattached to the moved surfaces and the block boundaries and cells smoothed to minimise skewness. A head-on view of the resulting grid, of identical size to phorn1, is shown in Fig.(6.3(a)). The various surface faces have been colour-coded for the sake of clarity.

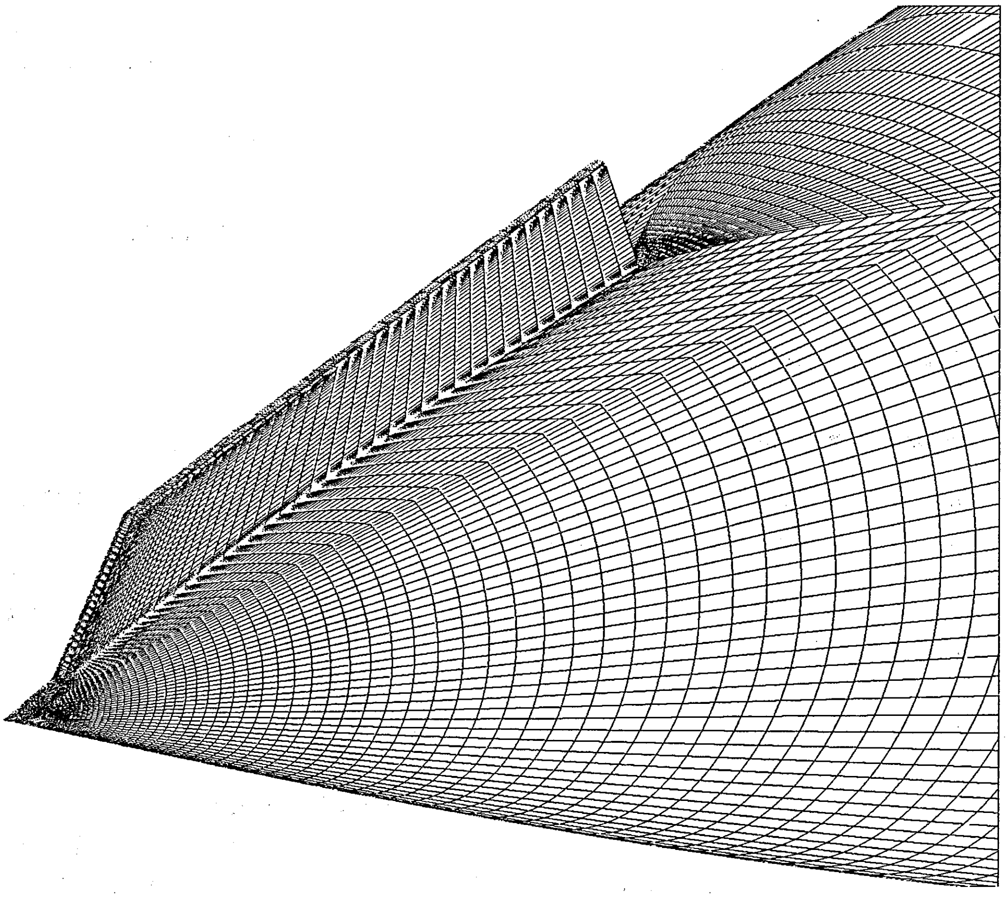

Figure 6.2: *Grid horn1, surface mesh near the nose showing the location of strake 46.*

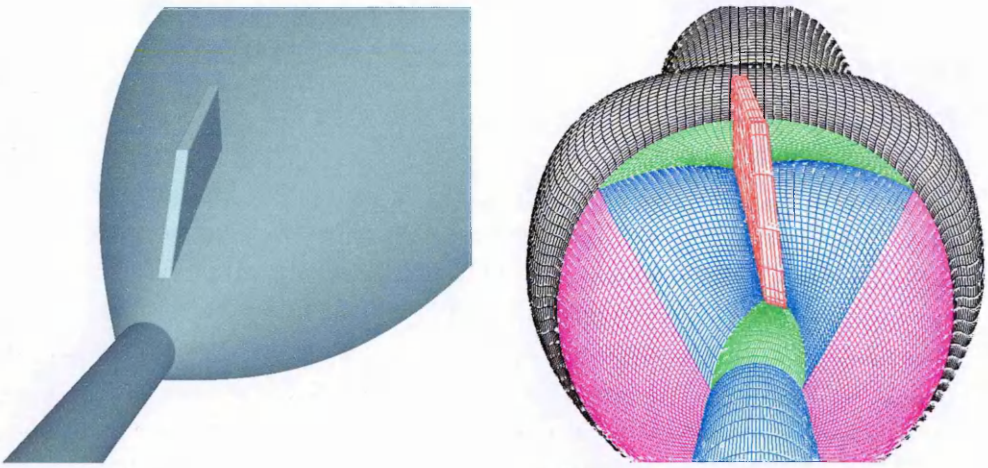

(a) phorn1, $\delta_{horn} = 0^o$

(b) phorn2, $\delta_{horn} = -5^o$

Figure 6.3: *Grids phorn1 and phorn2, forebody with pitot and strake 51. Surface close-up of undeflected device and surface mesh topology for* $\delta_{horn} = -5^o$. *n.b. some cell boundaries have been removed on the rhino horn surface for the purpose of clarity.*

6.2.2 Boundary conditions

Boundary conditions remained unchanged from the first stage of the JAS-39 calculations. The outer domain was maintained far enough away from the body to allow freestream values to be applied and the exit condition stayed a simple linear extrapolation.

6.2.3 Flow conditions

Flow conditions match those used for the baseline geometry as documented in Chapter 4 but are included here as Table (6.1) for completeness.

Re/m	4,058,823
$Mach\ No.$	0.176
$\rho_\infty\ (kg/m^3)$	1.225
$P_\infty\ (Pa)$	101325
$T_\infty\ (K)$	288.2
$a_\infty\ (m/s^2)$	340.3
$U_\infty\ (m/s)$	59.89

Table 6.1: *Flow conditions, computations on JAS-39 Gripen with forebody vortex control device.*

6.2.4 Solver setup

No changes were made to the solver setup on moving to the new geometries. The configuration was felt to be an optimum and, as before, variations between runs were restricted to CFL numbers and turbulence modelling parameters. As a result, no sample input file specific to this final stage of work is included.

6.3 Results

Users of the machines at NSC are allotted a monthly quota of CPU time. Once this has been used up, any further jobs which are submitted before the end of the calendar month are transferred to a bonus queue. When the machines are running below a certain capacity, the highest priority job on the bonus queue is moved to the main queuing system, thus ensuring that CPU time is not wasted. In this final stage of the research, allocated CPU time amounted to 3000 CPU hours per month, equating to just under 94 hours use of 32 processors. Referring back to Table (3.4), it can easily be calculated that only 15,000 iterations on a ca. 4 million cell mesh would be possible each month before falling into the bonus queue. With CPU time at such a premium, relatively few computations would be possible on these final three meshes. After several unsuccessful attempts with the k-ω-SST model, fully turbulent Spalart-Allmaras computations were run at $\alpha = 0^o, 40^o$ for each of the three configurations. No laminar computations were made.

As for the baseline geometry, the following sections cover solution convergence and flow structure with additional comparisons being made between the differing configurations.

For each case the following graphical information is shown: the normalised density-residual convergence history; comparison of computed and experimental surface C_p at 14 cross-sections; pitot pressure ratio contours at 12 selected cross-sections. To re-iterate, the experimental surface pressure data was taken on the forebody configured with pitot and strake 51, $\delta_{horn} = 0^o$.

6.3.1 Convergence

Normal and side force coefficient convergence histories for the three configurations at $\alpha = 0^o, 40^o$ are shown in Fig.(6.4). As expected, both sets of forces converged well at $\alpha = 0^o$. Of more interest are the results at $\alpha = 40^o$. Since no convergence problems were encountered with the baseline grid bsl2 at this angle, addition of the rhino horn unsurprisingly made little difference. However, for the two grids with both horn and pitot, the addition of the rhino horn gives a noticeable improvement in convergence behaviour over the pitot-only configuration, see Fig.(4.9). With $\delta_{horn} = 0^o$, the oscillations are almost eliminated and the sideforce appears to be settling towards a steady value. For the case of $\delta_{horn} = -5^o$, the flowfield is evidently settling into a stable asymmetric disposition. The density residuals shown in Fig.(6.14) confirm the stability of the solutions, c.f. Fig.(4.46). Unfortunately, CPU constraints meant that it was impossible to continue these calculations any further.

Force coefficients for the rhino horn cases are tabulated against earlier data for the clean forebody and the forebody with pitot[2] in Table (6.2). The five cases show good agreement for all force components at $\alpha = 0^o$, although C_z appears to be reduced by the introduction of the horn. C_x and C_z values at $\alpha = 40^o$ show good agreement whilst the effect of the deflected rhino horn on sideforce, C_y, is again readily apparent. Only 5^o deflection generates a stable sideforce equal in magnitude to 50% of lift.

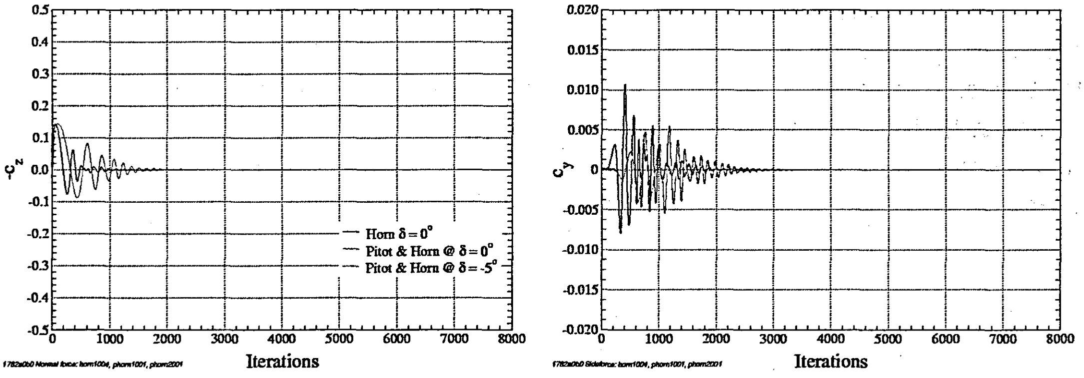

(a) Normal force, $\alpha = 0^o$

(b) Side force, $\alpha = 0^o$

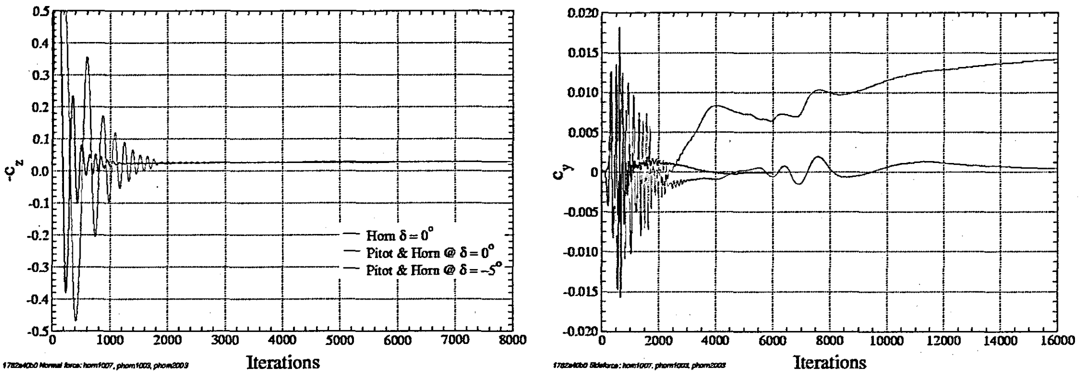

(c) Normal force, $\alpha = 40^o$

(d) Side force, $\alpha = 40^o$

Figure 6.4: *JAS-39 grids horn1, phorn1 & phorn2, M=0.176, Re=4.06 × 10⁶, $\alpha = 0^o$ & $\alpha = 40^o$. Comparison of normal and side-force coefficients for the forebody with horn only at $\delta_{horn} = 0^o$ & horn and pitot with $\delta_{horn} = 0^o$ & $\delta_{horn} = -5^o$.*

---

[2] n.b. the pitot-only calculation at $\alpha = 40^o$ is <u>not</u> converged.

Configuration	Grid	α (^{o})	δ_{horn} (^{o})	Run	C_x	C_y	C_z
Clean	bsl2	0	-	001	0.00260	0.00000	-0.00060
Pitot only	pitot2		-	002	0.00187	0.00000	-0.00079
Horn only	horn1		0	004	0.00226	-0.00001	-0.00029
Pitot & horn (undeflected)	phorn1		0	001	0.00193	-0.00002	-0.00035
Pitot & horn (deflected)	phorn2		-5	001	0.00193	-0.00002	-0.00035
Clean	bsl2	40	-	003	0.01340	-0.00010	-0.02750
Pitot only	pitot2		-	004	0.01356	-0.00789	-0.02893
Horn only	horn1		0	007	0.01263	-0.00007	-0.02707
Pitot & horn (undeflected)	phorn1		0	003	0.01233	0.00037	-0.02716
Pitot & horn (deflected)	phorn2		-5	003	0.01335	0.01423	-0.02828

Table 6.2: *JAS-39 forebody forces. The effect of horn installation and deflection. All results are for the Spalart-Allmaras model, comprise pressure and viscous components and are with relation to wind axes. Hence,* $C_L \equiv -C_z$ *and* $C_D \equiv C_x$.

6.3.2 Flow structure

$\alpha = 0^o$, **Figs.(6.7) - (6.13)** Surface pressure coefficients show excellent agreement with experimental values for all three configurations. A slight underprediction in the strength of the suction peaks at sections 13 and 14, see Figs.(6.10(e)) - (6.10(f)), may be attributed to inadequate numbers of cells in the streamwise direction over the top of the canopy, an area where considerable flow acceleration would be expected. As has been noted for solutions on earlier grids, a slight oscillation is also visible at $\theta \approx 45^o, 315^o$, corresponding to the canopy/body junction. Little can be remarked about the contours of pitot pressure ratio aside from the disturbance visible on the underside on the body when the pitot tube is present. This is, of course, a result of the pitot being mounted along the x_{nos} axis at -5.4^o relative to the waterline of the aircraft.

$\alpha = 40^o$, **Figs.(6.14) - (6.20)** All three sets of pressure coefficient profiles show poor correlation with experiment for the first two sections, see Figs.(6.15(a)) & (6.15(b)), with peak suctions massively overpredicted. The particularly bad agreement at the first section is understandable for the horn1 case since the longer strake extends aft beyond section 01. However, the poor correlation of the other two solutions might indicate a problem with the experimental figures. Also noticeable on the section 01 profiles are slight oscillations in C_p at $\theta \approx 55^o, 305^o$ which correspond to grid discontinuities at the boundaries of the blocks surrounding the horn. These are slightly surprising given the relatively converged nature of the solutions but possibly an unavoidable result of the block topology.

Moving aft to sections 03-08, Fig.(6.16), the horn1 and phorn1 profiles show improving agreement for $45^o \leq \theta \leq 315^o$. However, as has been remarked before, the density of the experimental data points for the 90^o quadrant straddling the leeward meridian is almost certainly too low to be able to adequately resolve the flow features. Towards the rear of the body, the match between computed and experimental profiles improves further. It should be noted that, at this point, very little differentiation can be made between the experimental profiles with and without rhino horn, compare Figs.(4.49(f)) & (6.17(f)), but that the computed solutions have benefitted significantly from the flowfield stability brought by the device. Another interesting point to be made is the overall similarity between the horn1 and phorn1 profiles at all sections. Slight differences appear for $\theta \approx \pm 60^o$ but the horn masks the presence of the pitot almost completely. Pitot pressure ratio contours for the two sets of data are shown in Figs.(6.18) & (6.19).

(a) Pitot & undeflected horn

(b) Pitot only

Figure 6.5: JAS-39 grids pitot2 & phorn1, M=0.176, Re=4.06 × 10^6, α=40^o. *Effect of addition of rhino-horn at* $\delta_{horn} = 0^o$ *on surface pressure coefficient.*

With the horn deflected 5^o to port, both C_p profiles and pitot pressure ratio contours, Fig.(6.20), show the starboard boundary layer to have separated early and the primary vortex to have moved outboard. On the port side, separation has been delayed and the primary vortex shifted inboard. The effect convects the length of the body and does not appear to be significantly damped.

Figs.(6.5) & (6.6) allow comparison between contours of surface pressure coefficient for the pitot-only and pitot with horn configurations. In marked contrast to the pitot-only configuration, with $\delta_{horn} = 0^o$, the contours can be seen to be almost completely symmetric both over the forebody and, more surprisingly, the pitot tube. Symmetry is maintained over the pitot when the horn is deflected.

Clearly visible again in Fig.(6.6) are the non-physical flow disturbances near the rhino horn caused by grid discontinuity at the block boundaries.

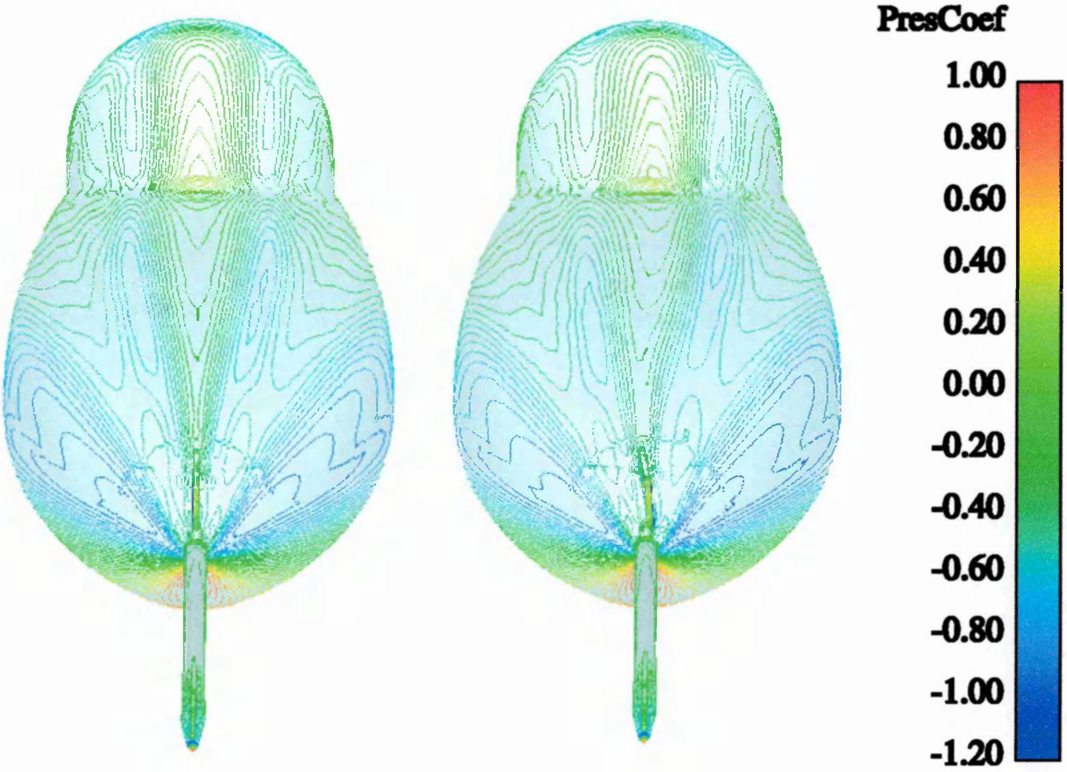

(a) Pitot & undeflected horn (b) Pitot & deflected horn, $\delta_{horn} = -5^o$

Figure 6.6: *JAS-39 grids phorn1 & phorn2,* M=0.176, Re=4.06 × 10^6, α=40^o. *Effect of horn deflection on surface pressure coefficient.*

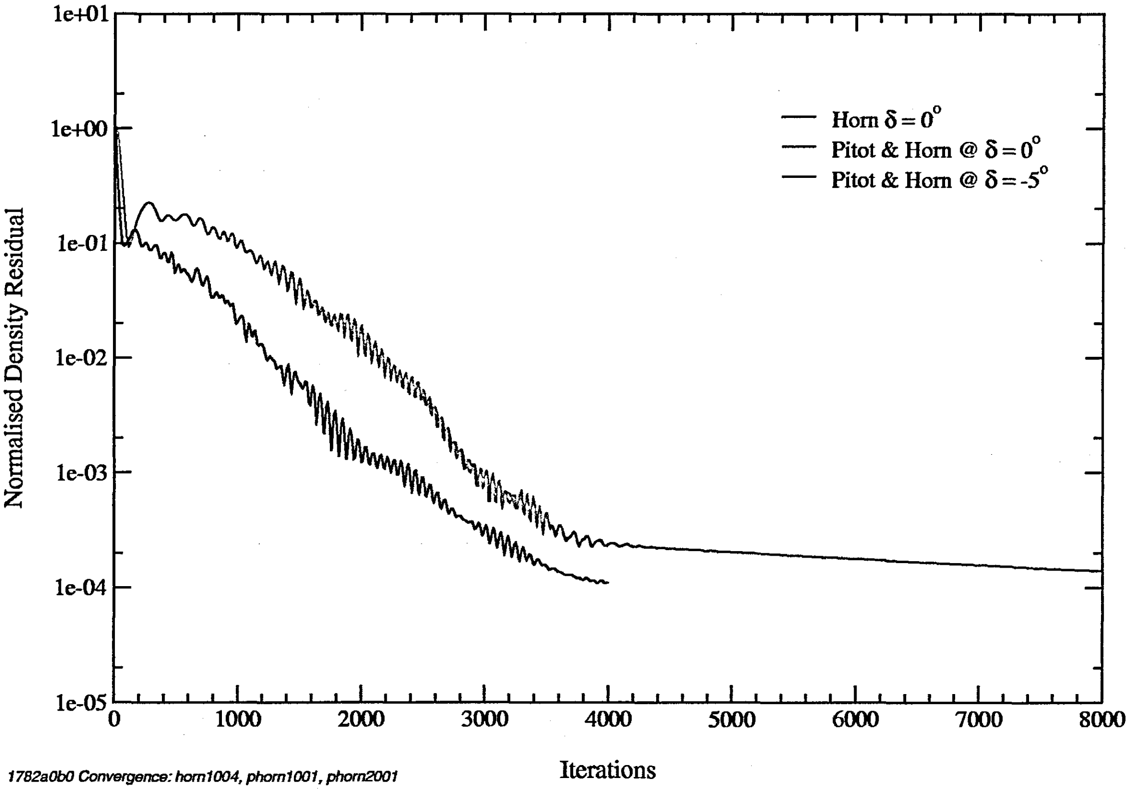

Figure 6.7: JAS-39 grids horn1, phorn1 & phorn2, M=0.176, Re=4.06 × 10^6, α=0°. Comparison of density residual convergence history for forebody with horn only at $\delta_{horn} = 0^o$ & horn and pitot with $\delta_{horn} = 0^o$ & $\delta_{horn} = -5^o$.

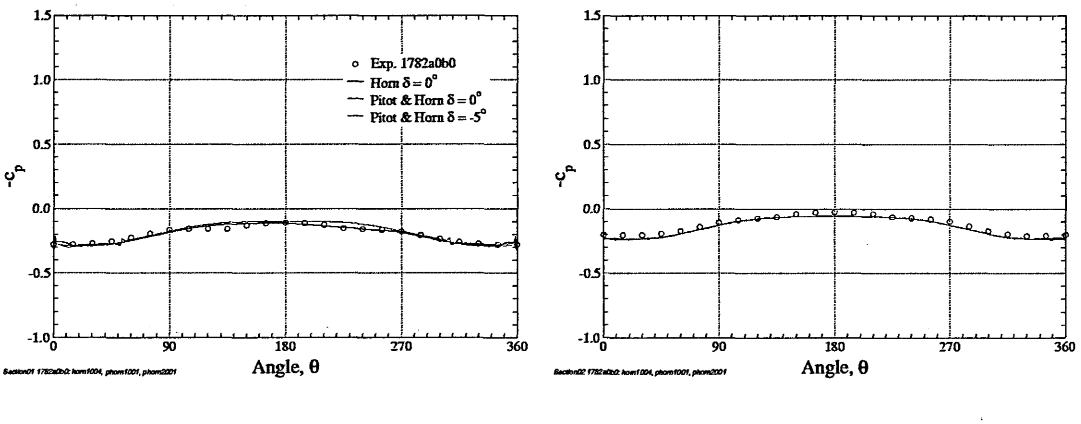

(a) Section 01

(b) Section 02

Figure 6.8: JAS-39 grids horn1, phorn1 & phorn2, M=0.176, Re=4.06 × 10^6, α=0°. Circumferential c_p distributions, sections 01 & 02. Comparison of horn only at $\delta_{horn} = 0^o$ & horn and pitot with $\delta_{horn} = 0^o$ & $\delta_{horn} = -5^o$.

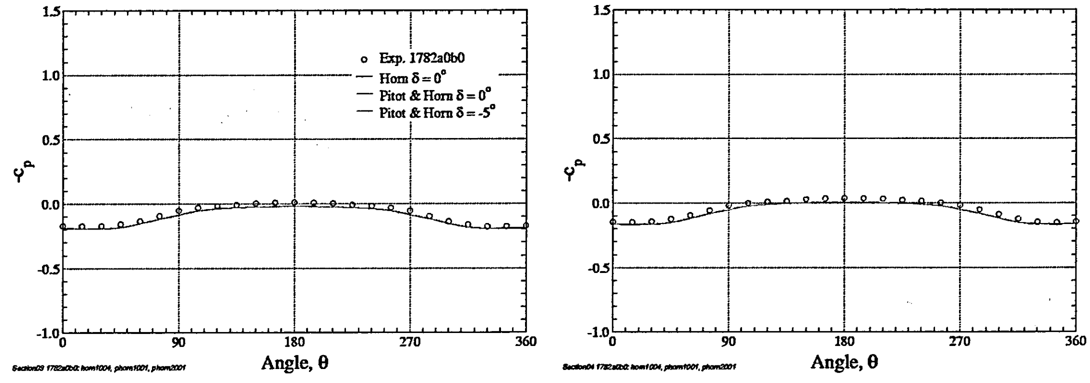

(a) Section 03

(b) Section 04

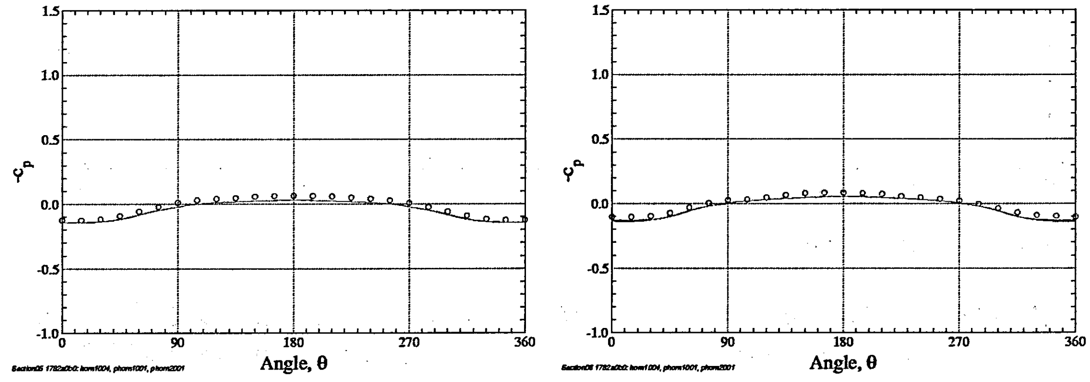

(c) Section 05

(d) Section 06

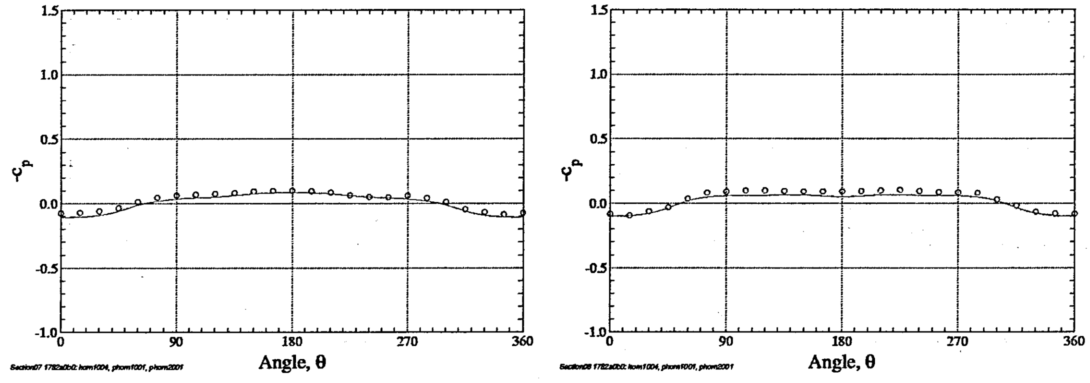

(e) Section 07

(f) Section 08

Figure 6.9: *JAS-39 grids horn1, phorn1 & phorn2,* M=0.176, Re=4.06 × 10^6, α=0°. *Circumferential* c_p *distributions, sections 03-08. Comparison of horn only at* $\delta_{horn} = 0^o$ *& horn and pitot with* $\delta_{horn} = 0^o$ *&* $\delta_{horn} = -5^o$.

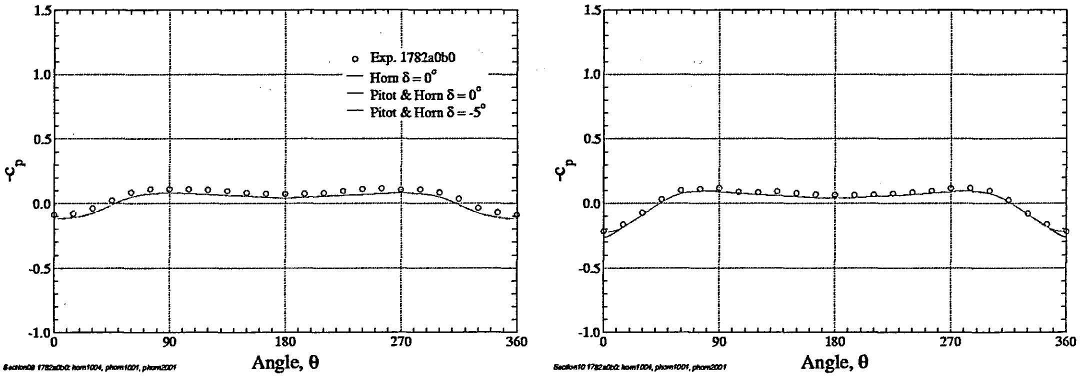

(a) Section 09

(b) Section 10

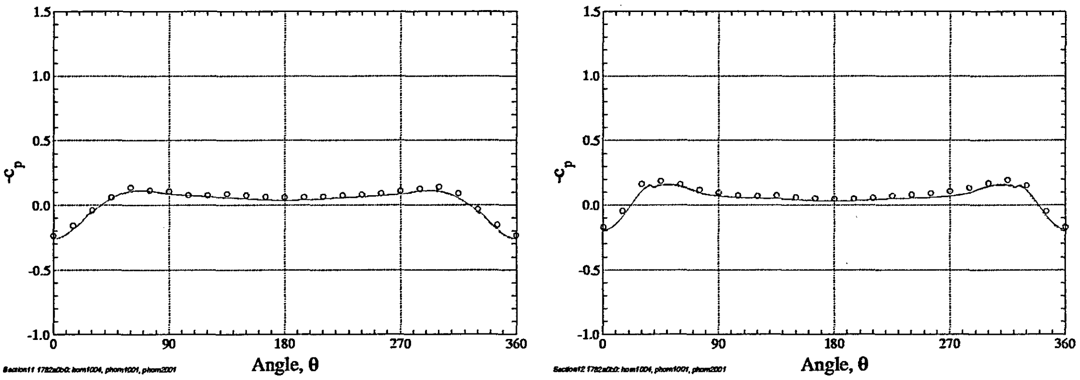

(c) Section 11

(d) Section 12

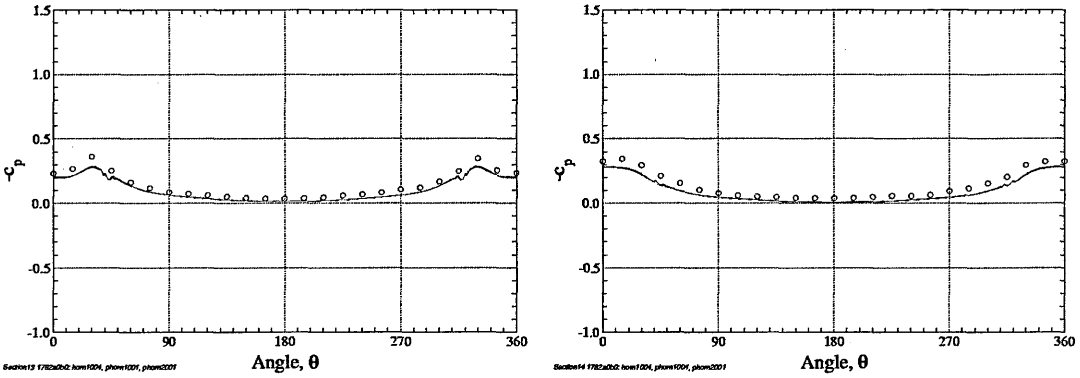

(e) Section 13

(f) Section 14

Figure 6.10: *JAS-39 grids horn, phorn1 & phorn2, M=0.176, Re=4.06 × 10^6, α=0°. Circumferential c_p distributions, sections 09-14. Comparison of horn only at $\delta_{horn} = 0^o$ & horn and pitot with $\delta_{horn} = 0^o$ & $\delta_{horn} = -5^o$.*

(a) Section 01 (b) Section 02 (c) Section 03 (d) Section 04 (e) Section 06 (f) Section 07

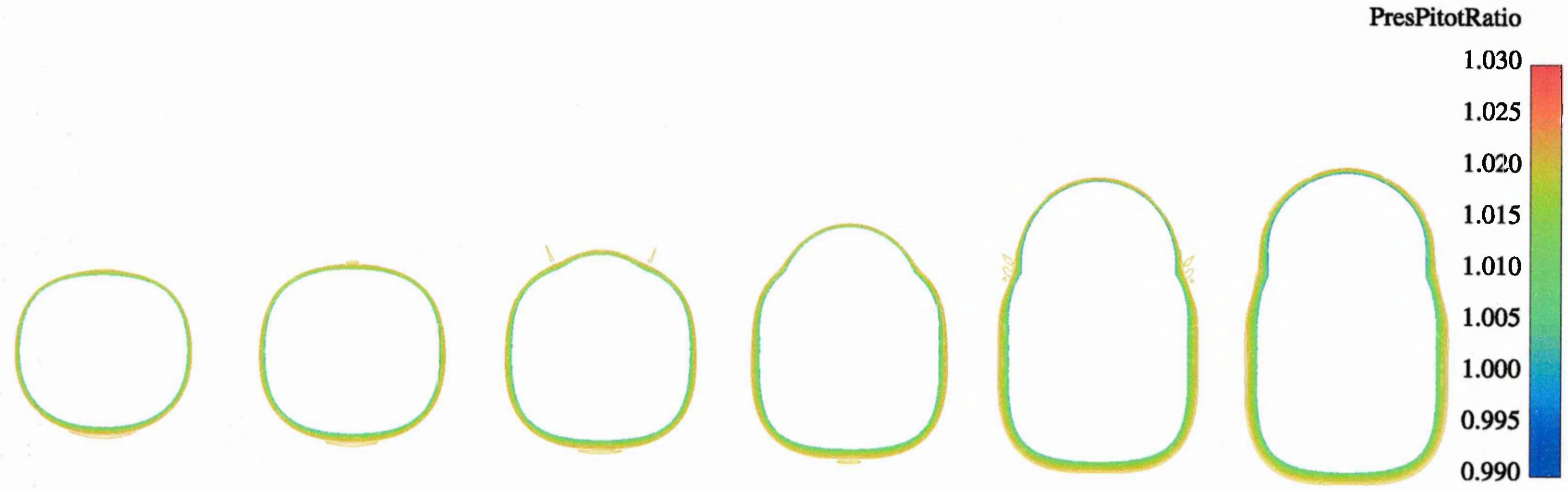

(g) Section 09 (h) Section 10 (i) Section 11 (j) Section 12 (k) Section 13 (l) Section 14

Figure 6.11: *JAS-39 grid horn1,* M=0.176, Re=4.06 × 10^6, α=0^o, $\delta_{horn} = 0^o$. *Contours of pitot pressure ratio, Spalart-Allmaras model.*

(a) Section 01 (b) Section 02 (c) Section 03 (d) Section 04 (e) Section 06 (f) Section 07

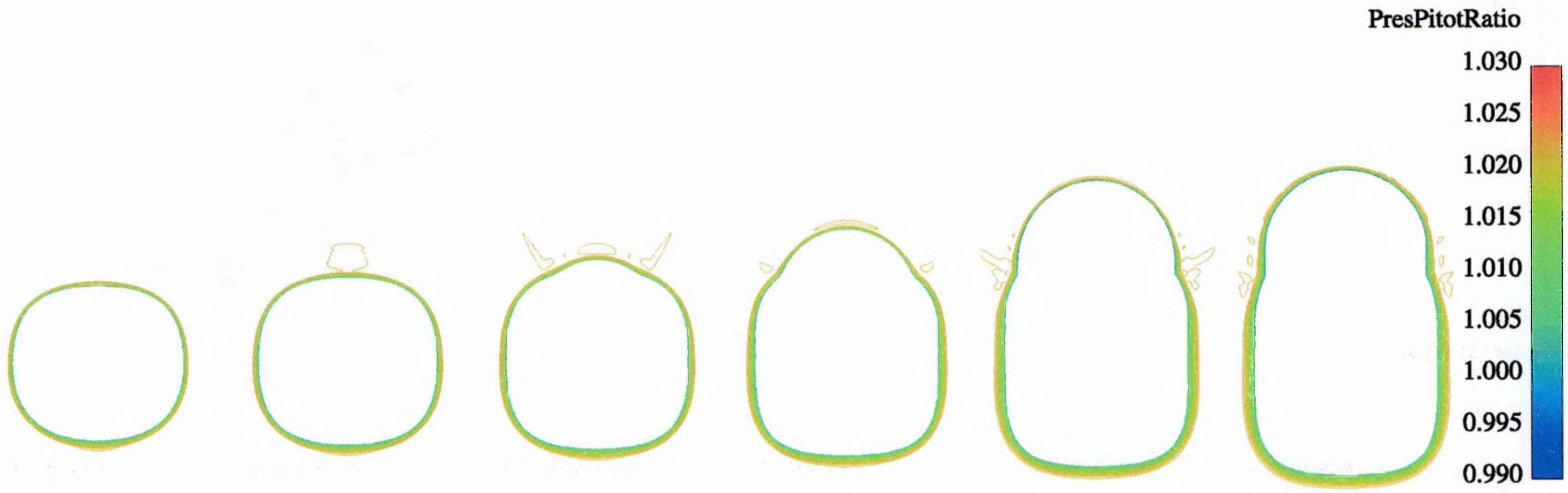

(g) Section 09 (h) Section 10 (i) Section 11 (j) Section 12 (k) Section 13 (l) Section 14

Figure 6.12: *JAS-39 grid phorn1, M*=0.176, *Re*=4.06×10^6, α=0^o, $\delta_{horn} = 0^o$. *Contours of pitot pressure ratio, Spalart-Allmaras model.*

(a) Section 01 (b) Section 02 (c) Section 03 (d) Section 04 (e) Section 06 (f) Section 07

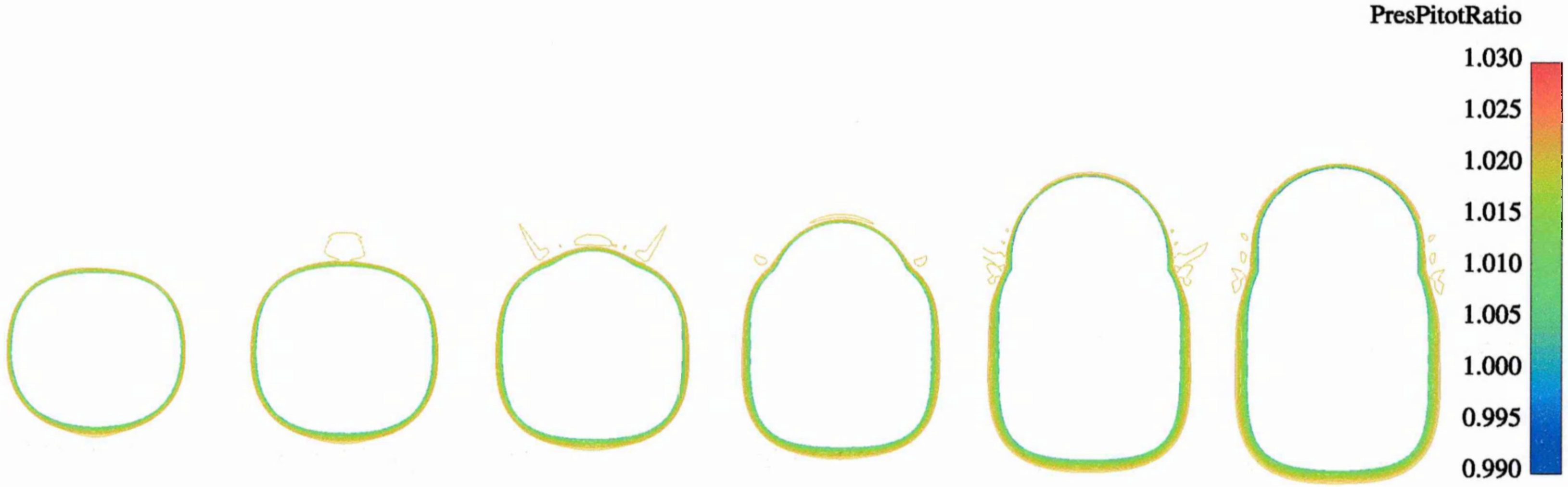

(g) Section 09 (h) Section 10 (i) Section 11 (j) Section 12 (k) Section 13 (l) Section 14

Figure 6.13: *JAS-39 grid phorn2, M*=0.176, *Re*=4.06×10^6, α=0^o, $\delta_{horn} = -5^o$. *Contours of pitot pressure ratio, Spalart-Allmaras model.*

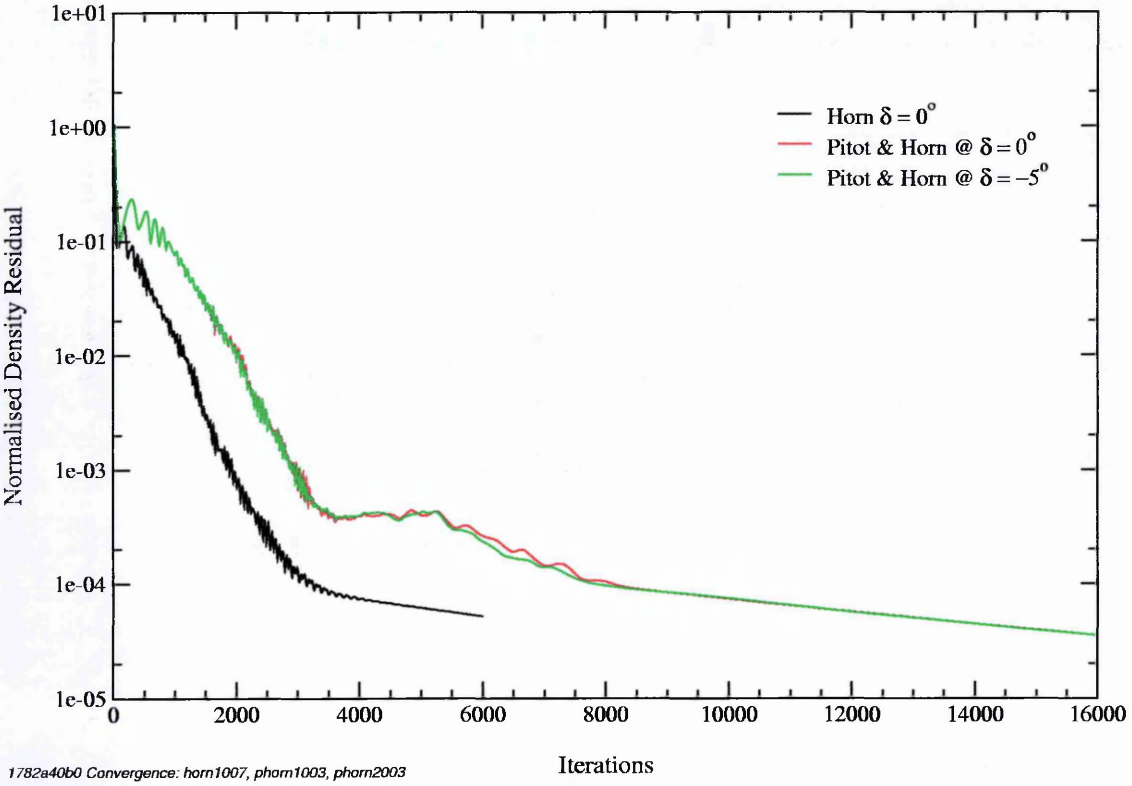

1782a40b0 Convergence: horn1007, phorn1003, phorn2003

Figure 6.14: *JAS-39 grids horn1, phorn1 & phorn2, M=0.176, Re=4.06 × 10^6, α=40°. Comparison of density residual convergence history for forebody with rhino horn only at $\delta_{horn} = 0^o$ & horn and pitot with $\delta_{horn} = 0^o$ & $\delta_{horn} = -5^o$.*

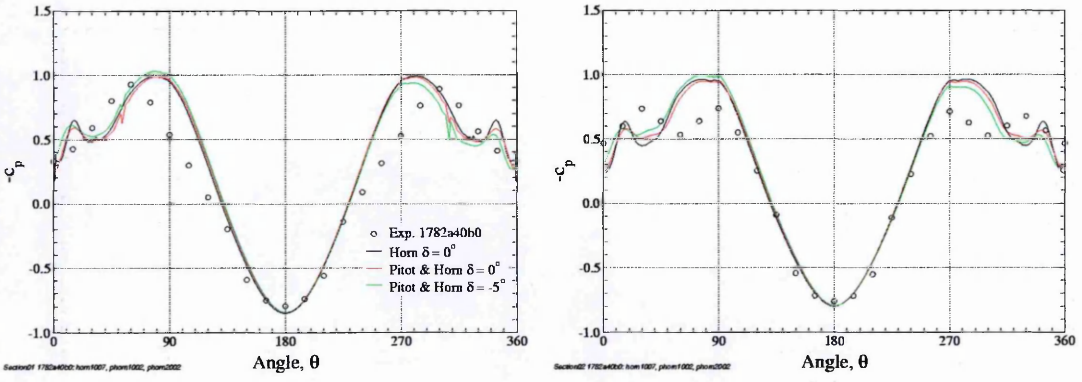

(a) Section 01

(b) Section 02

Figure 6.15: *JAS-39 grids horn1, phorn1 & phorn2, M=0.176, Re=4.06 × 10^6, α=40°. Circumferential c_p distributions, sections 01 & 02. Comparison of horn only at $\delta_{horn} = 0^o$ & horn and pitot with $\delta_{horn} = 0^o$ & $\delta_{horn} = -5^o$.*

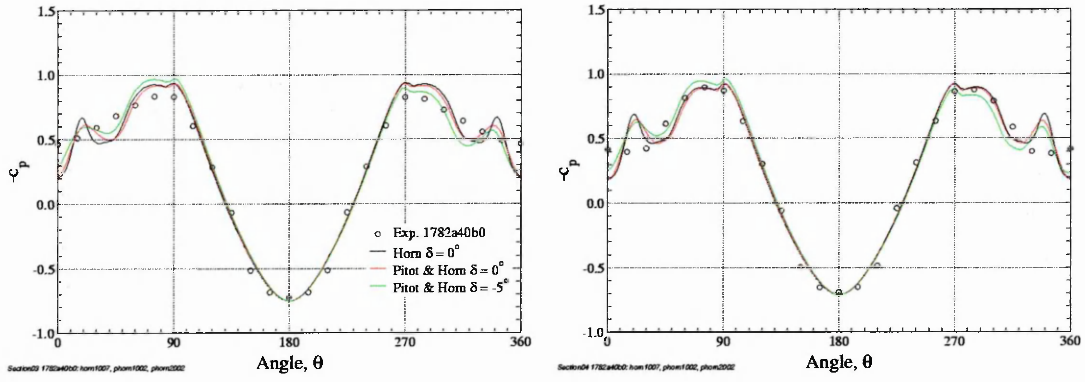

(a) Section 03

(b) Section 04

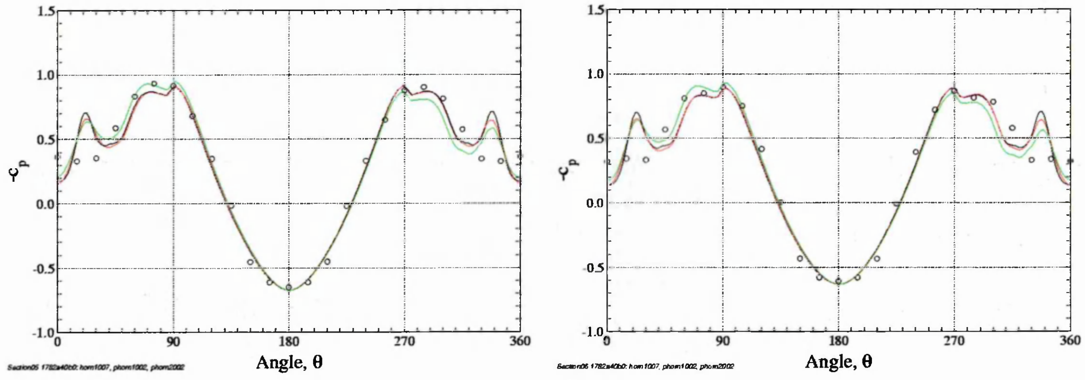

(c) Section 05

(d) Section 06

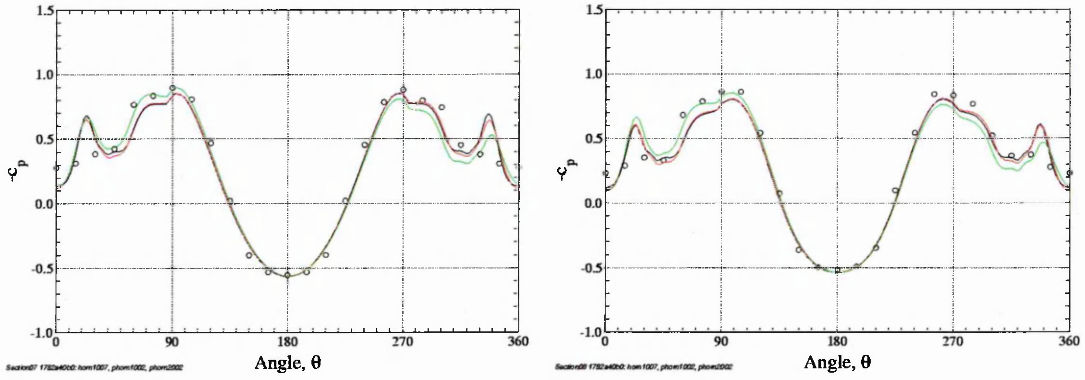

(e) Section 07

(f) Section 08

Figure 6.16: *JAS-39 grids horn1, phorn1 & phorn2,* M=0.176, Re=4.06 × 10^6, α=40°. *Circumferential* c_p *distributions, sections 03-08. Comparison of horn only at* $\delta_{horn} = 0^o$ *& horn and pitot with* $\delta_{horn} = 0^o$ *&* $\delta_{horn} = -5^o$.

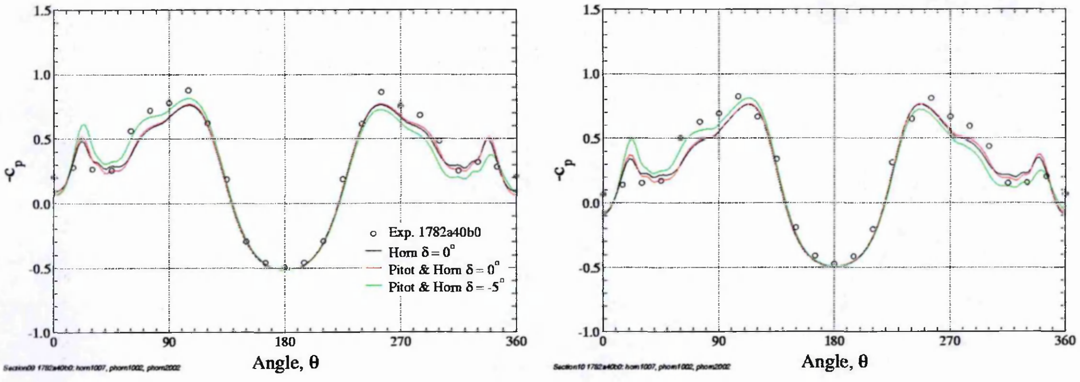

(a) Section 09

(b) Section 10

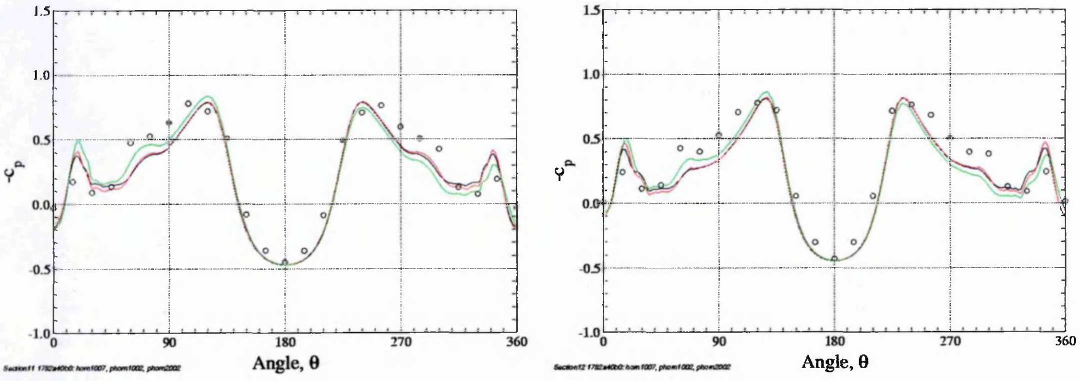

(c) Section 11

(d) Section 12

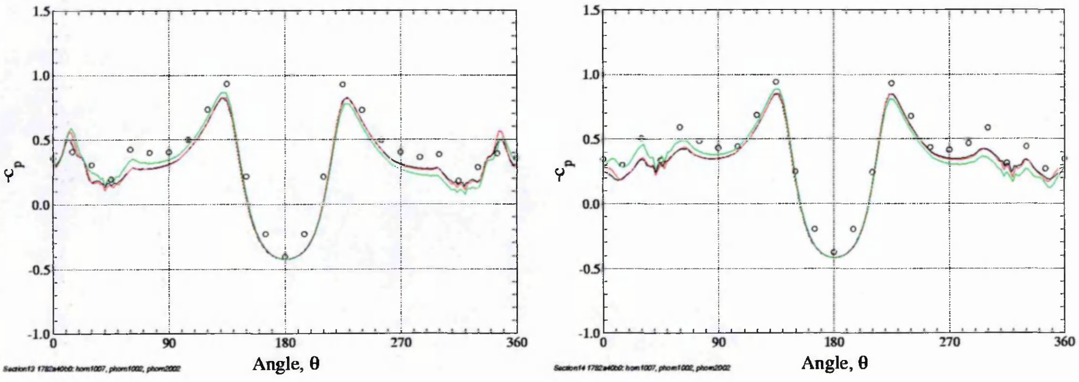

(e) Section 13

(f) Section 14

Figure 6.17: *JAS-39 grids horn, phorn1 & phorn2,* M=0.176, Re=4.06 × 10^6, α=40°. *Circumferential* c_p *distributions, sections 09-14. Comparison of horn only at* $\delta_{horn} = 0^o$ *& horn and pitot with* $\delta_{horn} = 0^o$ *&* $\delta_{horn} = -5^o$.

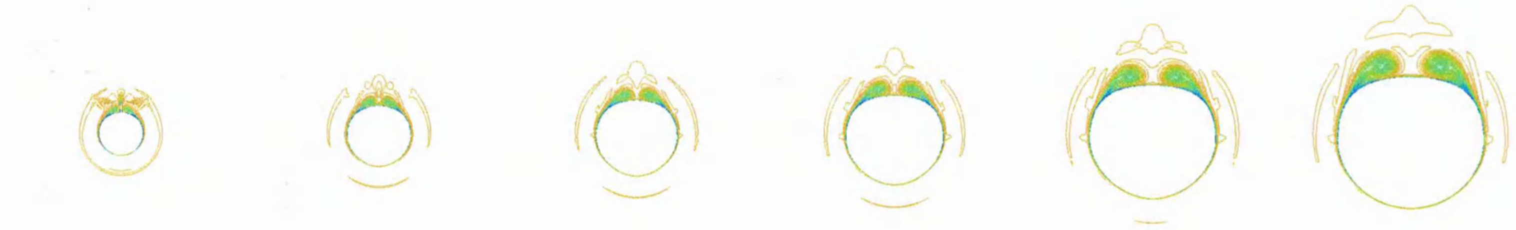

(a) Section 01 (b) Section 02 (c) Section 03 (d) Section 04 (e) Section 06 (f) Section 07

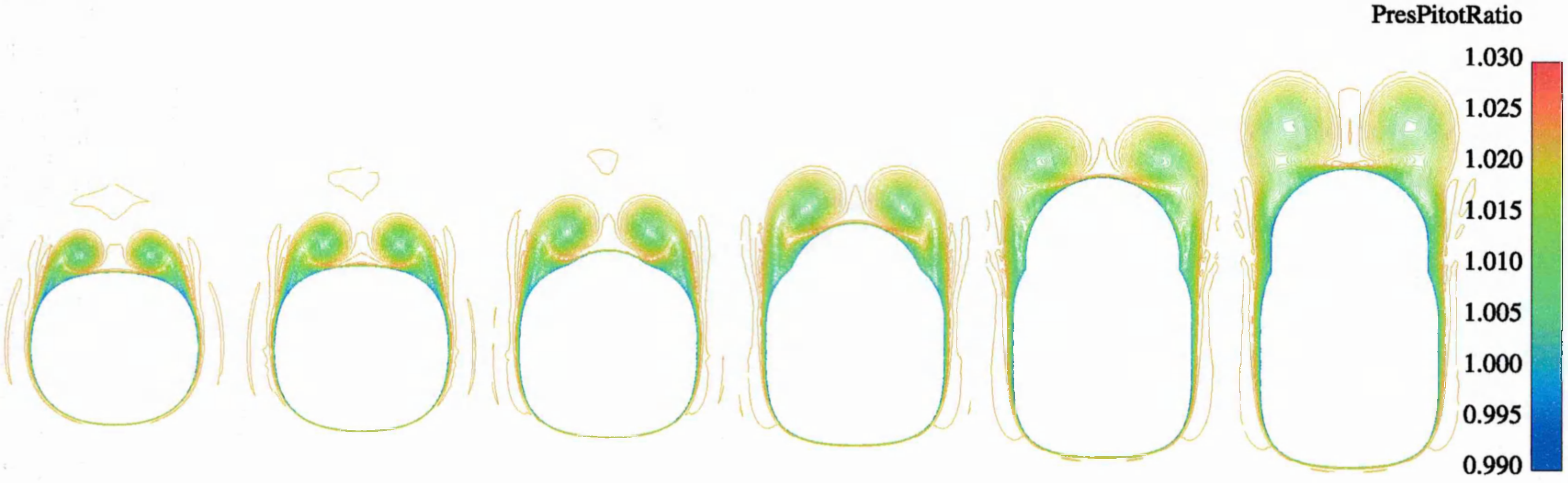

(g) Section 09 (h) Section 10 (i) Section 11 (j) Section 12 (k) Section 13 (l) Section 14

Figure 6.18: *JAS-39 grid horn1, M*=0.176, *Re*=4.06 × 10^6, α=40^o, $\delta_{horn} = 0^o$. *Contours of pitot pressure ratio, Spalart-Allmaras model.*

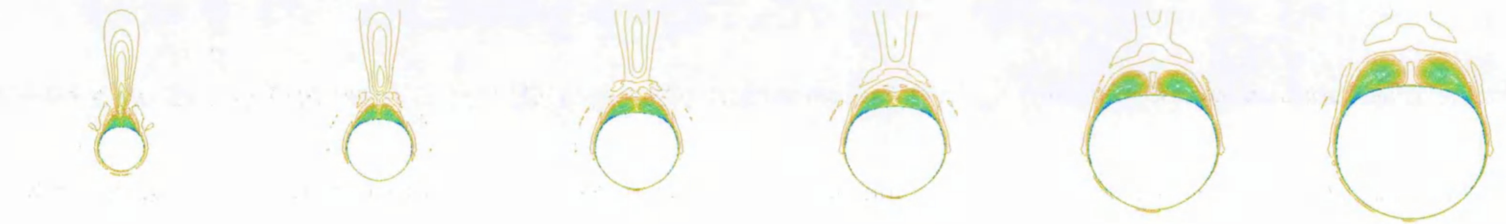

(a) Section 01 (b) Section 02 (c) Section 03 (d) Section 04 (e) Section 06 (f) Section 07

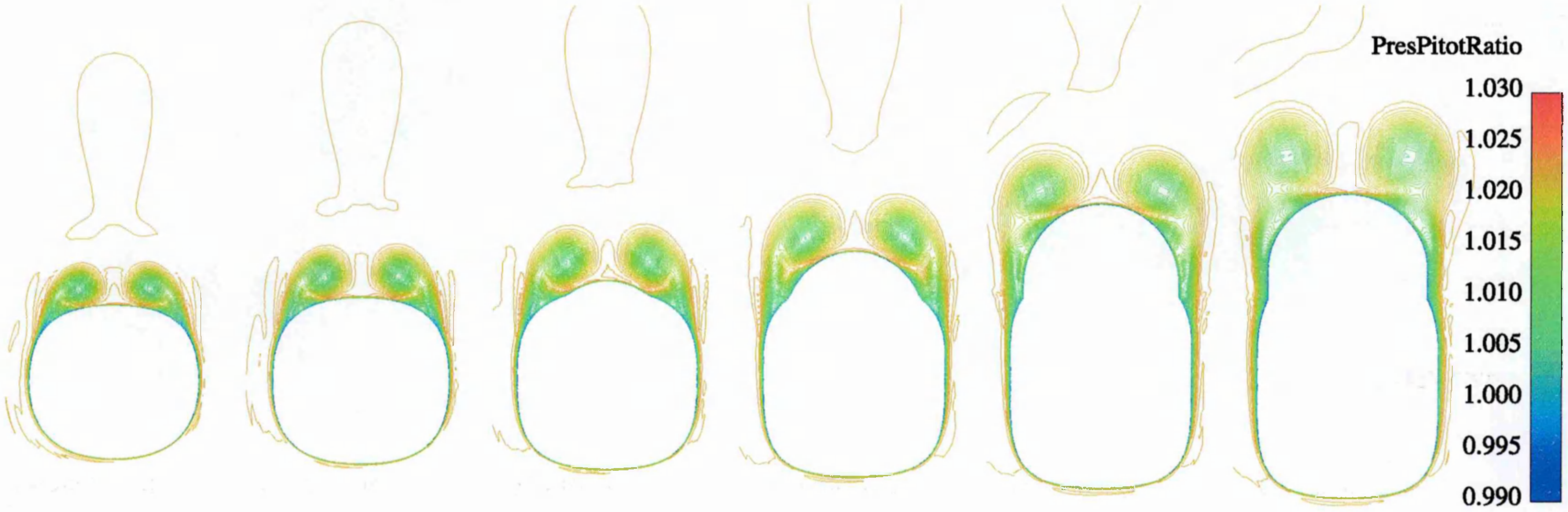

(g) Section 09 (h) Section 10 (i) Section 11 (j) Section 12 (k) Section 13 (l) Section 14

Figure 6.19: *JAS-39 grid phorn1,* M=0.176, Re=4.06 $\times$ 10^6, α=40^o, δ_{horn} = 0^o. *Contours of pitot pressure ratio, Spalart-Allmaras model.*

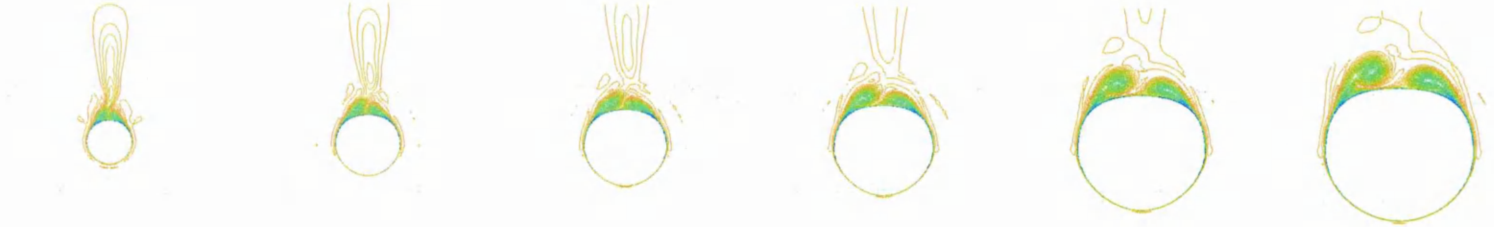

(a) Section 01 (b) Section 02 (c) Section 03 (d) Section 04 (e) Section 06 (f) Section 07

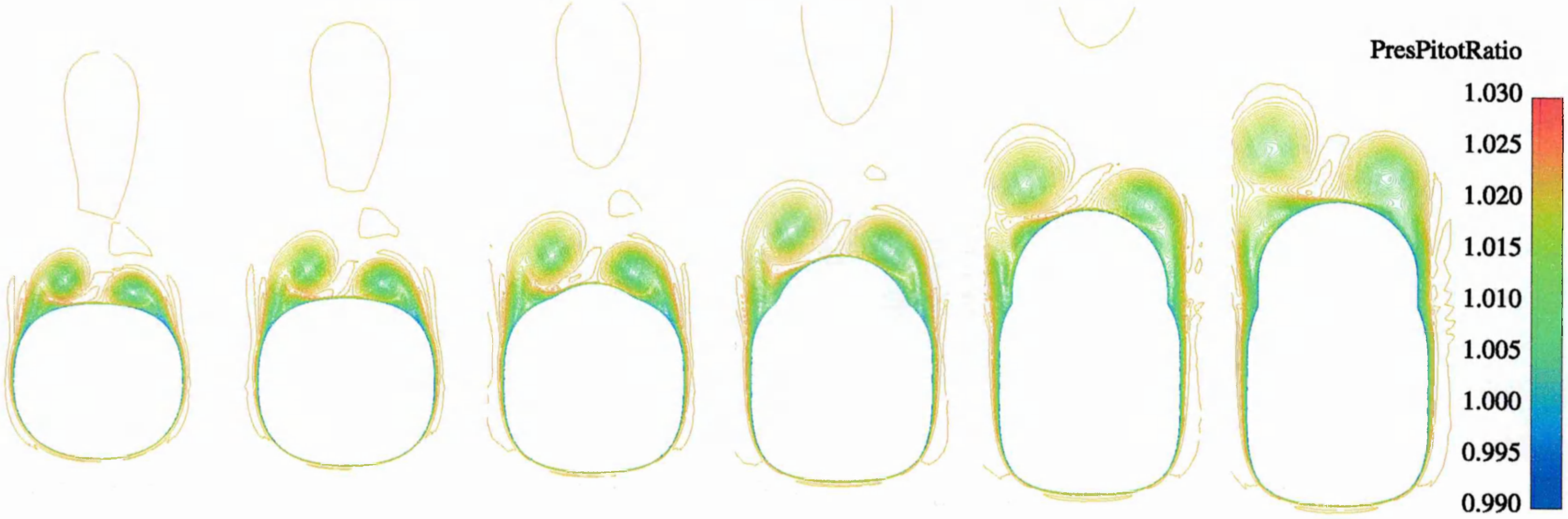

(g) Section 09 (h) Section 10 (i) Section 11 (j) Section 12 (k) Section 13 (l) Section 14

Figure 6.20: *JAS-39 grid phorn2,* M=0.176, Re=4.06 × 10^6, α=40^o, δ_{horn} = -5^o. *Contours of pitot pressure ratio, Spalart-Allmaras model.*

6.4 Summary of Results

- Fully turbulent flow around a JAS-39 forebody modified with a single strake or *rhino horn* to act as a flow control device has been successfully computed for $\alpha = 0^o, 40^o$ using the non-symmetric implicit LU-SGS algorithm and the Spalart-Allmaras model.

- Three configurations were tested: clean forebody with a long strake mounted undeflected; forebody with nose-mounted pitot tube and short strake mounted undeflected; forebody with nose-mounted pitot tube and short strake deflected by 5^o, nose to port.

- Agreement of computed surface C_p with experimental data is excellent for $\alpha = 0^o$, although there is slight underprediction of the suction peaks over the canopy.

- The addition of the undeflected rhino horn was seen to stabilise the flowfield at $\alpha = 40^o$ and eliminate the large-scale fluctutations in side force that appeared on addition of the pitot to the clean forebody. Both configurations with the device undeflected converged to virtually symmetric solutions with near zero side force. Flow over the pitot, forward of the device, was also symmetric for each case.

- Agreement with experimental surface C_p at $\alpha = 40^o$ for the two undeflected configurations is poor at sections near the nose but excellent further aft although, as for $\alpha = 0^o$, suction over the canopy is slightly underpredicted.

- Pivoting the horn by 5^o at $\alpha = 40^o$ produced a stable asymmetric solution and a side force equal to approximately 50% of the lift acting in the direction of the deflection. No convergence problems were encountered.

7. Fighter Procurement

As the world changes, so do the roles and requirements of the armed forces. In the West, the collapse of the Soviet Union and the growing number of NATO and UN peacekeeping operations has led to widespread re-assessment of fighter procurement needs in the face of shrinking defence budgets. Additionally, many former Warsaw Pact countries have been left with ageing airforces in dire need of modernisation but little capital. The following chapter looks at how airforce requirements are changing and some of the various procurement options that are currently available.

7.1 A New World Order

With the collapse of the Soviet Union in the late 1980's, the Cold War ended and the East vs. West total warfare scenario that dominated military thinking since the end of World War Two receded as a threat. However, the break-up of the USSR has precipitated numerous regional conflicts breaking out as the indigenous populations of satellite states try to reassert their own national identities and emerge from Russian control, for example in Chechnya or Georgia. Unfortunately, the pattern of regional warfare is repeated around the world:

- UN peacekeepers remain in the former Yugoslav republics after ten years of warfare.

- Tension in the Middle East has continued following the invasion of Kuwait by Iraq in 1990 and the subsequent liberation in Operation Desert Storm in 1991. Despite the ground offensive being over ten years ago, Allied aircraft are still enforcing no-fly zones in nothern and southern Iraq.

- India and Pakistan tested each others nerve by detonating nuclear devices within days of each other back in 1998 and since then have continued the ongoing dispute over Kashmir.

- China remains adamant in its territorial claims on Taiwan, seeing the island as a breakaway region that should be part of the P.R.C.. The threat of conflict in the region in the immediate future may have lessened with the awarding of the 2008 Olympics to Beijing, but a diplomatic solution in the near future does not look likely.

With the Cold War threat removed but regional conflict proliferating, many countries are now re-assessing the *raison d'être* of their armed forces in the post-Cold War world. Many countries are now restructuring their military machines to be smaller, leaner and more capable of rapid response, with the flexibility of airpower at the heart.

7.1.1 Changing committments

Traditional allegiances and procurement priorities are changing to reflect the shape of the post-Cold War world. In Europe, many of the former Warsaw Pact countries are starting to think about rebuilding their airforces as they gradually modernise and reform to the western model. While under Soviet control, all arms purchasing and tactical decision making was made in Moscow, with each Pact member assigned a specific military task should there be a European conflict. The legacy now being dealt with is that the equipment left behind following Soviet withdrawal is tactically inflexible and, more often than not, obsolescent. In order to help countries such as Hungary and the Czech Republic restructure militarily, NATO initiated the Partnership for Peace (PFP) program. The aim of this program is to aid participants in:

- managing defence reforms
- establish and maintain a democratically controlled military
- defence planning
- resource allocation
- budget decision making

A major stumbling block for many of the countries participating in the PFP program is that, although they wish to take on a role in the NATO organisation, they may not have the necessary capital to do so. Understandably, defence spending is low on the list of government spending priorities with economic and social reform often a more pressing need. Table (7.1) shows trends in total military spending for selected countries around the world. Most sets of figures reveal there to have been continuous reduction in government defence spending for the majority of the 1990's, but this trend now appears to be reversing. As regards NATO members, this is mainly due to the NATO Defence Capabilities Initiative, which is intended to improve NATO capability for power projection, mobility and inter-operability. This sea change follows experiences in the Gulf and Bosnia and indicates that NATO is now prepared to engage in out-of-area operations when the interests of member nations are at stake. It should be noted that although the 1949 Washington Treaty specifically excludes NATO out-of-area operation, there is considerable provision made for expansion of the organisation. By bringing in countries on the periphery of the current member states, NATO will be able to extend power and stability into Southern and Eastern Europe as well as North Africa. Thus, countries such as Hungary, Poland and the Czech Republic are left with the problem of upgrading their ageing airforces with equipment that is preferably NATO inter-operable and at minimum cost. An option being taken by some is to ignore the problem, continue buying Soviet-designed equipment, remembering that not all Soviet-bloc aircraft manufacturers were based in what is now Russia, and maintaining links with the old allies.

Country	1991	1992	1993	1994	1995	1996	1997	1998	1999	2000
USA	335436	354293	335582	316763	298228	282047	280599	274278	275014	280620
	4.7	4.8	4.5	4.1	3.8	3.5	3.3	3.1	3.0	-
Russia	-	80400	70900	68600	43400	39500	42200	30600	37900	43900
	-	5.5	5.3	5.9	4.1	3.8	4.2	3.2	3.8	-
UK	49270	44537	43544	42110	38818	39463	37032	37232	36780	36262
	4.2	3.8	3.6	3.3	3.0	3.0	2.7	2.7	2.5	-
France	45906	44436	43954	44177	42009	40978	41152	40042	40386	40442
	3.6	3.4	3.4	3.3	3.1	3.0	2.9	2.8	2.7	-
Germany	44646	42452	38185	35615	34980	34286	33065	33146	33816	33025
	2.3	2.1	2.0	1.8	1.7	1.6	1.6	1.5	1.5	-
Hungary	954	889	800	678	598	541	515	618	707	733
	2.2	2.1	1.9	1.6	1.4	1.3	1.1	1.3	1.4	-
Poland	2754	2717	3011	2905	2923	3075	3239	3363	3343	3332
	2.3	2.3	2.6	2.3	2.1	2.1	2.1	2.1	2.0	-
Czech R.	-	-	1148	1075	1014	997	946	1040	1123	1141
	-	-	2.4	2.1	1.8	1.7	1.7	1.9	2.0	-
China	12700	15400	14200	13600	13900	15300	16600	19000	21100	23000
	2.5	2.7	2.1	1.9	1.8	1.8	1.9	2.0	2.1	-
Taiwan	8039	8189	9411	9428	9352	8507	8765	9030	7896	7222
	4.6	4.4	4.2	4.5	4.2	3.6	3.5	3.4	2.8	-
Iran	3811	3637	4568	6197	4588	5189	5821	5737	5432	7144
	2.5	2.2	2.4	3.1	2.5	2.8	3.1	3.1	2.7	-
Israel	7636	7811	7298	7349	7478	8013	8119	8489	8453	8912
	11.0	10.5	9.4	8.8	8.4	8.5	8.4	8.4	8.1	-
India	7532	7211	8139	8112	8341	8569	9309	9390	10731	12315
	2.6	2.5	2.4	2.3	2.2	2.1	2.2	2.2	2.4	-
Pakistan	3079	3293	3288	3204	3257	3253	3117	3111	3064	3097
	5.8	6.1	5.7	5.2	5.2	5.0	4.8	4.6	4.4	-
Chile	1706	1763	1817	2059	2091	2216	2244	2564	2259	1747
	3.4	3.3	3.2	3.4	3.1	3.2	3.1	3.5	3.1	-
S.Africa	3565	3138	2858	3023	2691	2337	2151	1921	1833	2127
	3.2	2.9	2.5	2.6	2.2	1.8	1.6	1.4	1.3	-

Table 7.1: Military expenditure by country in (upper) millionUSD at constant 1998 prices and exchange rates and (lower) percentage GDP. Data from the SIPRI Military Expenditure Database, Stockholm International Peace Research Institute, http://www.sipri.se.

Western nations, however, have a different set of problems. The ending of the Cold War brought a shift in the focus of operation from all-out continental warfare towards peacekeeping operations in localised conflicts, for example in the Balkans, and humanitarian missions, such as maintaining the no-fly zones protecting the Iraqi Kurds. The changing focus has brought with it a re-write of Western airpower doctrine and altered fighter aircraft requirements. For example, the Lockheed-Martin F-22 and Eurofighter Typhoon were initially designed as short-range air-dominance fighters with a Soviet enemy in mind. Whilst it is true that Soviet-designed aircraft such as the MiG-29 and Su-27 are taking their place in the airforces of many countries around the world, the circumstances and theatre of operations in which they might now be encountered will most likely be substantially different from the NATO vs. USSR scenario. Of interest now are mission-flexible aircraft that are capable of long distance force projection and round-the-clock operation. With fighter projects taking ever longer to mature and new-build equipment ever more expensive, it is critical that the correct procurement decisions are made and take into account possible technological developments or changes in role over the lifetime of the aircraft.

7.2 New Technologies

The majority of fighters in service in Western airforces today can be classed as 3rd generation aircraft with their roots in designs from as far back as the late 1960's. Continuous upgrades over the years enable improvements in capability to be made, but certain technological developments are difficult to integrate into platforms not designed for them from the outset. Some of these technologies offer the potential for significantly enhanced lethality, survivability and therefore far greater combat effectiveness than was previously attainable.

7.2.1 Stealth

Possibly the greatest revolution in fighter design since the advent of the jet engine, few combat aircraft are now designed without some aspect of stealthiness being incorporated. The angular, faceted design of the Lockheed F-117 Nighthawk is entirely down to the limited computer power that was available to generate a low-RCS[1] body in the mid 1970s and modern designs may be almost as invisble to radar whilst being considerably more conventional in their appearance. Subtle shaping of surfaces and junctions can help to minimise RCS, as can radar absorbent coatings and the internal carriage of stores. Other stealth features focus on the reduction of total elimination of emissions, whether electronic - the F-117 is not equipped with an active radar - or physical - designing engine nozzles for cold exhaust and minimal plume.

Since it is so dependent on shape, stealth is something that is hard to retro-fit to aircraft, and it is hard to envisage a non-stealthy fighter being able to survive against an aircraft where it is a designed-in attribute.

7.2.2 Data management

Continuing advances in microprocessor technology mean that onboard computers and data management systems are now immensely capable. The Saab JAS-39 Gripen was designed from the outset with a high capacity datalink which enables pilots to communicate real-time targetting information with other units and ground control centres whilst remaining undetected by the opponent. Loosely grouped formations of aircraft can thus patrol large expanses of territory but react immediately in concert when a threat emerges.

---

[1] Radar Cross Section

The datalink is combined with a beyond visual range (BVR) radar which can also be used as a fire-control and guidance system for the engagement of multiple targets.

A data management system with capabilities as described above can potentially be retro-fitted to current aircraft. The US House Defense Appropriations Subcommittee recently proposed such an upgrade to the US F-15 fleet at the expense of new-build F-22 aircraft. They acknowledged that installation of a datalink system would be achieveable for approximately $200,000 per aircraft yet offer a five-fold increase in air-to-air kill ratio, see [63].

7.2.3 Weapons systems

Advances in weapons systems have centred around improvements in air-to-air missile targetting technology. Fighter aircraft of 1950s and 1960s vintage will have extremely short-range radars with a limited field of vision. Thus, the pilot will usually have to be flying towards the bogey in order to lock-on and acquire the target. Such systems are typical of the majority of aircraft in service in China and what the US refers to as 'rogue' states - Iran, Iraq and North Korea. Modern targetting systems now offer look-down/shoot-down capability for visual-range combat with helmet-mounted sights allowing the pilot to designate a target simply by visual selection. As mentioned in the section above, powerful BVR radars also allow pilots to engage opponents before visual acquisition is possible.

Integration of new weapons systems is a common way of upgrading capability and is usually possible so long as there is space in the airframe for the electronics and suitable hardpoints on the aircraft for mounting the necessary sensor-pods or weaponry.

7.2.4 Super-manoeuverability

The benefit, or not, of super-manoeuverability has been a contentious topic since the Su-27 Flanker first demonstrated the Cobra manoeuver to an astounded airshow audience. In a traditional dog-fight situation, a manoeuverability advantage over an opponent allows a pilot to control the encounter and, more than likely, bring guns to bear first. The Cobra was devised as a method of suddenly changing the aircraft attitude to open up a missile launch opportunity but this option would seem to be of reduced importance given the improved targetting offered by helmet-mounted sights. The Herbst manoeuver, however, allows a pilot to initiate a rapid heading change, out-turn an opponent and get into a firing position. This assumes that no BVR engagement occurred and that visual-range combat has been initiated, but this is entirely possible if the aircraft were initially operating at low-level or both stealthy to some degree.

Much of the high angle-of-attack capability of the Su-27 and MiG-29 is due to their innovative blended aerodynamic form and was achieved without any additional devices. Western super-manoeuverability studies, however, have involved engine thrust-vectoring nozzles (TVC) and forebody vortex control (FVC) methods, both of which may be retro-fitted to current airframes. Kramer and Smith, [64], report that an FVC-equipped F-16 gained a significant combat advantage over a standard F/A-18:

- Envelope opened to hi-AOA: The configurations were stable, controllable and had predictable responses. The increased angle-of-attack envelope resulted in a large turn rate and turn radius advantage.
- Increased control of manoeuver plane: FVC gave velocity vector roll control allowing the manoeuver plane to be changed without unloading from high angle of attack.
- Different flying technique, easier: This resulted in a smoother, more continuous approach to the target. Adjustments to the plane of the primary manoeuver could be made during the approach to capture.
- More manoeuver options: A larger variety of defensive and offensive manoeuvers are available for the pilot to choose from allowing more shot opportunities.

Similar benefits have been seen with TVC equipped aircraft such as the X-31 or F-18 HARV, and it is likely that retro-fits of FVC or TVC equipment will become a common MLU[2] for current aircraft in order to maintain their competitiveness.

7.3 Procurement Options

In an ideal world, the priority in any procurement process would be to obtain the maximum capability for the outlay. In reality, procurement decisions are often heavily biased by political considerations and the best solution will not be an acceptable one. Politics have long been a factor in the policy of many Arab governments not to buy American. Similarly, whilst Hungary wishes NATO involvement, its ageing airforce will more than likely be upgraded by newer MiG or Sukhoi aircraft due to political pressure from Moscow. However, the following sections briefly cover a few of the current options available in the fighter market.

7.3.1 New build

The first thing to note is that new build does not necessarily mean new technology - China's CAIC continues to offer a heavily upgraded version of the MiG-21 with a BAe Super Skyranger multimode radar and Western avionics. More modern Soviet-designed aircraft are available such as the MiG-29 and Su-27/35, both highly effective fighters which, in the hands of a competent pilot, are a match for current Western equipment. Versions currently being offered include compatibility with Western avionics/weaponry and improved air-ground capability. However, many RSK MiG and Sukhoi customers have had problems with parts supply and the durability of Russian-designed engines is still questionable.

Previous generation western aircraft still on offer include the European Dassault Mirage 2000, and BAe Hawk and American F-15, F-16 and F-18E/F. These are still very

---

[2] Mid-Life Upgrade

much current aircraft and it is expected that many will continue in service for another 20-30 years.

Only four fourth-generation aircraft are in, or approaching, production status: the Dassault Rafale, Saab/BAe Gripen, Lockheed-Martin F-22 and Eurofighter Typhoon. Of these, the F-22 is almost without doubt the most capable, but if and when export versions become available the expected pricetag is in the region of $120m-$150m and it is unlikely to find many overseas customers. Rafale has received little interest abroad and orders from the French Government have been slow in coming. Eurofighter has received expressions of interest from several European governments and has sold to Greece, but is likely to be too costly to operate for many potential buyers. Saab has received a firm order from South Africa and it appears likely to sell to Chile and the Czech Republic as well. The aircraft is a modern, highly capable, NATO inter-operable design which remains maintainable by conscripts and is the best placed aircraft to take market share away from the F-16.

7.3.2 Previously enjoyed

Second-hand aircraft are the preferred choice of many airforces due to budgetary constraints. Surplus US Air National Guard aircraft are commonly available and many airforces will buy secondhand with the intention of immediately upgrading avionics and weapons systems. Cheap, modern aircraft have also been offered from parts of the former USSR.

In addition, it is possible to lease surplus aircraft from an existing operator and this is often done whilst waiting for budget to become available for new build.

7.3.3 Maintain & upgrade

The rising cost of new aircraft has resulted in the upgrade market booming. Popular choices for modernisation include the Northrop F-5 (1,234 in service), Lockheed-Martin F-16 (3,347 in service, of which 1,887 are outside the US), McDonnell Douglas F-4 (892 in service), MiG-17 & variants (1,730 in service), MiG-19 & variants (3,361 in service) and MiG-21 & variants (2,147 in service). For example, Belgium, Denmark, the Netherlands and Norway commenced the upgrade of 343 F-16A/Bs in 1996, the package including the Block 50 cockpit and a radar capable of guiding the AIM-120 BVR AAM.

In addition to OEM-fitted upgrades, third-party manufacturers such as IAI are beginning to offer tailored packages to take advantage of this market. As an example, RSK have cooperated with India to produce an upgrade for 125 Indian Airforce MiG-21s, the refitting of which will be done by HAL using Russian-supplied kits.

7.3.4 Disband

Disbanding the combat arm of an airforce is a fairly radical step and it is unlikely that many countries would be willing to make such a decision. However, when faced the option of replacing or upgrading their small force of A-4 Skyhawks, that is exactly what the New Zealand Government decided to do. The decision is likely to be fought strongly for as long as a reprieve seems possible and there are questions about how the country can respect its defence committments in the Pacific.

7.4 Conclusions

The rapidly spiralling cost of new aircraft inevitably means that cheaper options will be sought by the many airforces looking to upgrade or modernise their fleets. It is likely that the upgrade market will continue to expand with the range and extent of modifications on offer growing as well to include more aerodynamic, performance and stealth-related enhancements. For many of the smaller airforces seeking replacement aircraft with NATO inter-operability, the logical choice is still the F-16 or possibly the more modern Gripen. It remains to be seen how many of the fourth generation offerings will succeed in the export markets and whether or not new-build procurement decisions will be deferred until JSF becomes a realistic option.

8. Concluding Remarks

"If we knew what it was we were doing, it would not be called research, would it?"

- Albert Einstein

An investigation has been made into methods for computationally modelling the complex three-dimensional vortical flowfields that develop around the slender forebodies of combat aircraft at high angles of attack.

Initial computations centred around evaluation of the capability of an existing Navier-Stokes solver and methods of capturing the asymmetric flow that is a characteristic of the problem. A simplified tangent-ogive/cylinder geometry was used as a testcase.

It was confirmed that use of a symmetric solution scheme on a symmetric grid would require the use of a time- and space-fixed geometric perturbation near the apex of the nose in order to provoke asymmetric flow. This cannot be regarded as a viable option for simulation of this type of flowfield since the size and location of the surface excrescence dictates the character of the flowfield. Correctly sizing and positioning the excrescence requires prior knowledge of the flowfield, rendering the method of little use for the evaluation of unknown geometries. Additionally, the large size of the required excrescence in comparison to the local body diameter indicates the method to be an un-physical modelling approach - in the past, both models and full-size test aircraft have been machined to fine tolerances but nevertheless exhibited asymmetric flow.

Asymmetric flow can be computationally captured on a symmetric grid through the use of an asymmetric solution algorithm such as the LU-SGS method of Yoon and Jameson. This approach provided symmetric solutions at low angles of attack but asymmetric solutions as α was increased. However, solution stability severely degraded and it proved impossible to produce a converged result. Whilst this is a negative aspect in that it might prove impossible to obtain a side-force prediction, non-convergence can still be used as a means of estimating when a flow is likely to be highly asymmetric. Since it is desirable to design a forebody which does not exhibit asymmetric characteristics, this may be all that is required.

During these initial computations, it was quickly established that high-alpha forebody flow is a demanding problem both in terms of modelling methods and computer resources. In terms of meshing, full body models are necessary. The farfield must be positioned as far away from the model as possible with high cell densities required both in the boundary layer and away from the surface of the forebody in order to give sufficient resolution of the vortex wake. Additionally, the treatment of the rear of the model has been shown to be a problem with domain truncation the only acceptable option.

The highly separated nature of the flowfield requires that relatively sophisticated turbulence modelling be employed and, ideally, some way of modelling the laminar regions near the nose. If transition cannot be included, as for this research, correlation with experiment has been shown to remain acceptable when the flow is modelled as being fully turbulent. The blended k-ω-SST model of Menter has not previously been tested on this problem and it was found to give excellent agreement with experiment for the baseline geometry. However, stability problems were encountered for the more complex cases and the Spalart-Allmaras model was shown to perform equally well whilst being significantly more robust.

Fully turbulent Spalart-Allmaras solutions over the clean JAS-39 forebody were seen to correlate well with experiment but stable results could not be obtained above $\alpha = 50^o$ due to increased interaction between the primary vortex pair as they detached from the surface of the body. The addition of the pitot tube destabilised the flowfield considerably and a stable solution could not be generated even at $\alpha = 40^o$. The inclusion of a pitot would therefore seem to be essential to any computational forebody simulation if one is present on the real aircraft.

Addition of the rhino horn device stabilised the flow and eliminated the asymmetric vortex shedding from the pitot tube. At zero deflection, the device acted as a splitter plate to prevent interaction of the port and starboard vortex systems in the crucial nose region. With 5^o deflection, a stable asymmetric solution was generated with a steady side force, equal in magnitude to 50% of body lift. These results make clear that, in the absence of the flow instabilities which are present in real life, the small numerical errors in the asymmetric algorithm can be used to provide the potential for solution asymmetry in a computational environment. Aerodynamic fixes such as the rhino-horn can then be evaluated by means of their ability to stabilise or control the base flow.

In conclusion, it has been shown that current solver technology does not allow physically realistic simulation of steady-state high-α forebody flowfields. However, fully turbulent calculations on a structured mesh with an asymmetric solution scheme can give good experimental correlation for angles at which the flow should be symmetric and provide an indication of probable flow asymmetry by virtue of solution instability. In an engineering environment, this may also provide a useful means of producing a repeatable unstable baseline solution for the evaluation of corrective aerodynamic devices such as the rhino horn, which has been demonstrated to be a simple and effective method of providing forebody vortex control.

Recommendations for further computational work in this area include: moving from steady-state to time-dependent calculations; the inclusion of a transition trigger based on boundary-layer momentum thickness; the application of LES, large-eddy simulation; a systematic study of mechanical forebody devices to assess size and positioning requirements and relative effectiveness; the modelling of a porous nose and internal plenum chamber; modelling tangential slot and port blowing.

Bibliography

[1] MEM-COM An Integrated Memory and Data Management System, User Reference Manual 6.2. SMR Corporation, P.O. Box 41, CH-2500 Bienne, 1994.

[2] H.J. Allen and E.W. Perkins. Characteristics of Flow Over Inclined Bodies of Revolution. Technical Report RM-A50L07, NACA, 1951.

[3] J.D. Anderson. *Fundamentals of Aerodynamics*. McGraw-Hill, 1991. ISBN 0071007679.

[4] B.S. Baldwin and H. Lomax. Thin Layer Approximation and Algebraic Model for Separated Turbulent Flows. AIAA Paper 78-0257, January 1978.

[5] S.X.S. Bauer and M.J. Hemsch. Alleviation of Sideforce on Tangent-Ogive Forebodies Using Passive Porosity. AIAA Paper 92-2711, 1992.

[6] J. Boussinesq. Théorie des ecoulements tourillonaires. CRAS T23, 1877.

[7] D. Canter. X-31 Post-Stall Envelope Expansion and Tactical Utility Testing. In *NASA Fourth High Angle of Attack Conference, Dryden Flight Research Center, Edwards, CA, July 12-14*, volume 2, 1994.

[8] N.Q. Chen, Z.Y. Wang, and Z. Huang. Asymmetric Vortices and Alleviation on the Slender Bodies with and without Wings. AIAA Paper 97-0748, 1997.

[9] B.R. Cobleigh. High Angle-of-Attack Yawing Moment Asymmetry of the X-31 Aircraft from Flight Test. Contractor Report CR-186030, NASA, 1994.

[10] P.L. Coe, J.R. Chambers, and W. Letko. Asymmetric Lateral Directional Characteristics of Pointed Bodies of Revolution at High Angles of Attack. Technical Report TN D-7095, NASA, 1973.

[11] D.E. Coles and E.A. Hirst. Computation of turbulent boundary-layers. In *1968 AFOSR-IFP-Stanford Conference*, volume 2, Palo Alto, CA, 1969. Stanford University.

[12] P.H. Cook, M.A. McDonald, and M.C.P. Firmin. Aerofoil RAE 2822 - Pressure Distributions, and Boundary Layer and Wake Measurements. In *AGARD AR-138*. 1979.

[13] K.C. Cornelius, N. Pandit, R.F. Osborn, and R.W. Guyton. An Experimental Study of Pneumatic Vortex Control on High Angle of Attack Forebody Model. AIAA Paper 92-0018, 1992.

[14] D. Degani. Numerical Investigation of the Origin of Vortex Asymmetry. AIAA Paper 90-0593, 1990.

[15] D. Degani and Y. Levy. Asymmetric Turbulent Vortical Flows over Slender Bodies. *AIAA Journal*, 30(9):2267–2273, September 1992.

[16] D. Degani and L.B. Schiff. Computation of Turbulent Supersonic Flows Around Pointed Bodies Having Crossflow Separation. *Journal of Computational Physics*, 66:173–196, 1986.

[17] D. Degani and L.B. Schiff. Numerical Simulation of Asymmetric Vortex Flows Occurring on Bodies of Revolution at Large Incidence. AIAA Paper 87-2628, 1987.

[18] D. Degani and L.B. Schiff. Numerical Simulation of the Effect of Spatial Disturbances on Vortex Asymmetry. AIAA Paper 89-0340, 1989.

[19] D. Degani and M. Tobak. Effect of Upstream Disturbance on Flow Asymmetry. AIAA Paper 92-0408, 1992.

[20] P.C. Dexter and B.L. Hunt. The Effects of Roll Angle on the Flow over a Slender Body of Revolution at High Angles of Attack. AIAA Paper 81-0358, 1981.

[21] N. Duquesne. Implementation of two-equation eddy-viscosity turbulence models, non-linear eddy-viscosity models and explicit algebraic reynolds-stress models into the NSMB flow solver. Swedish NFFP Project 2.246 Final Report, Dept. of Aeronautics, KTH, Stockholm, 1999.

[22] D.E. Dyer, S.P. Fiddes, and J.H.B. Smith. Asymmetric Vortex Formation From Cones at Incidence - A Simple Inviscid Model. RAE Tech Report TR81130, 1981.

[23] R.C. Eidson and N.A. Mosbarger. Forebody Pneumatic Devices at Low Angles of Attack and Transonic Speed. AIAA Paper 97-0042, 1997.

[24] G.E. Erickson. Water Tunnel Flow Visualisation: Insight into Complex Three-Dimensional Flowfields. AIAA Paper 79-1530, 1979.

[25] G.E. Erickson and D.J. Lorincz. Water Tunnel and Wind Tunnel Studies of Asymmetric Load Alleviation on a Fighter Aircraft at High Angles of Attack. AIAA Paper 80-1618, 1980.

[26] L.E. Ericsson and J.P. Reding. Steady and Unsteady Vortex-Induced Asymetric Loads on Slender Vehicles. *Journal of Spacecraft and Rockets*, 18(2):155–162, 1977.

[27] L.E. Ericsson and J.P. Reding. Vortex Induced Asymmetric Loads in 2-D and 3-D Flows. AIAA Paper 80-0181, 1980.

[28] A. Favre. Equations des gaz turbulents compressibles. *Journal de Méchanique*, (4):361–421, 1965.

[29] S.P. Fears. Low-Speed Wind-Tunnel Investigation of a Porous Forebody and Nose Strakes for Yaw Control of a Multirole Fighter Aircraft. Contractor Report 4685, NASA, August 1995.

[30] S.P. Fiddes. A Theory of the Separated Flow Past a Slender Elliptic Cone at Incidence. RAE Tech Memo TM1858, 1980.

[31] S.P. Fiddes. Separated Flow about Cones at Incidence - Theory and Experiment. RAE Tech Memo AERO TM2055, 1985.

[32] S.P. Fiddes. Separated Flow About Cones at Incidence - Theory and Experiment. In *Procedings of the Symposium on Studies of Vortex Dominated Flow*. NASA/LRC, 1985.

[33] D.F. Fisher and B.R. Cobleigh. Controlling Forebody Asymmetries in Flight - Experience with Boundary Layer Transition Strips. AIAA Paper 94-1826, 1994.

[34] D.F. Fisher, J.H. Del Frate, and D.M. Richwine. In-Flight Flow Visualization Characteristics of the NASA F-18 High-Alpha Research Vehicle at High Angles of Attack. TM 4193, NASA, May 1990.

[35] J.H. Fisher, D.F. Del Frate and F.A. Zuniga. Summary of In-Flight Flow Visualization Obtained from the NASA High Alpha Research Vehicle. TM 101734, NASA, January 1991.

[36] R.W. Guyton and G. Maerki. X-29 Forebody Jet Blowing. AIAA Paper 92-0017, 1992.

[37] W. Haase, F. Brandsma, E. Elsholz, M. Leschziner, and D. Schwamborn. *EUROVAL: A European Initiative on Validation of CFD Codes.* Number 42 in Notes on Numerical Fluid Mechanics. Vriedr. Vieweg & Sohn Verlagsgesellschaft mbH., 1993.

[38] W. Haase, E. Chaput, E. Elsholz, M.A. Leschiner, and Müller U.R. *ECARP - European Computational Aerodynamics Research Project: Validation of CFD Codes and Assessment of Turbulence Models*, volume 58 of *Notes on Numerical Fluid Mechanics*. Vriedr. Vieweg & Sohn Verlagsgesellschaft mbH., 1997. ISBN 3-528-06958-9.

[39] R.M. Hall. Forebody and Missile Sideforces and the Time Analogy. AIAA Paper 87-0327, 1987.

[40] R.M. Hall, G.E. Erickson, W.A. Straka, S.E. Peters, B.H. Maines, M.C. Fox, J.E. Hames, and S.P. LeMay. Impact of Nose-Probe Chines on the Vortex Flows about the F-16C. AIAA Paper 90-0386, 1990.

[41] P. Hartwich and R. Hall. Navier-Stokes Solutions for Vortical Flows Over a Tangent-Ogive Cylinder. AIAA Paper 89-0337, 1989.

[42] P. Hartwich, R. Hall, and M. Hemsch. Navier-Stokes Computations of Vortex Asymmetries Controlled by Small Surface Imperfections. AIAA Paper 90-0385, 1990.

[43] A. Hellsten. On the solid-wall boundary condition of ω in the k-ω-type turbulence models. Technical Report B-50, Laboratory of Aerodynamics, Helsinki University of Technology, 1998. Series B.

[44] A. Hellsten. Some improvements in Menter's k-ω-sst turbulence model. AIAA Paper 98-2554, 1998.

[45] Hellström, T. Reynolds stress model transonic flow computations around the rae2822 profile. Technical report, Chalmers University of Technology, 1993. Diploma Thesis, Report 93-3.

[46] C. Hirsch. *Numerical Computation of Internal and External Flows*, volume 1. John Wiley and Sons Ltd., 1989.

[47] C. Hirsch. *Numerical Computation of Internal and External Flows*, volume 2. John Wiley and Sons Ltd., 1989.

[48] R. Howard, M. Rabang, M. Lung, and J. Pinaire. Effects of Freestream Turbulence on Asymmetric Vortex Formation Over a Tangent-Ogive Forebody. AIAA Paper 91-0290, 1991.

[49] B.L. Hunt. Asymmetric Vortex Forces and Wakes on Slender Bodies (Invited Paper). AIAA Paper 82-1336, 1982.

[50] B.L. Hunt and P.C. Dexter. Paper 17: Pressures on a Slender Body at High Angle of Attack in a Very Low Turbulence Level Airstream. In *AGARD CP247*, 1978.

[51] S. Hwang and O. Rho. Numerical Simulation of Asymmetric Vortical Flows on a Slender Body at High Incidence. AIAA Paper 95-1799, 1995.

[52] A. Jameson and S. Yoon. Multigrid Solution of the Euler Equations Using Implicit Schemes. *AIAA Journal*, 24(11):1737–1743, November 1986.

[53] A. Jameson and S. Yoon. Lower-Upper Implicit Schemes with Multiple Grids for the Euler Equations. *AIAA Journal*, 25(7):929–935, July 1987.

[54] T. Jongen. *Simulation and Modelling of Turbulent Incompressible Fluid Flows.* PhD thesis, IMHEF/EPFL, Lausanne, Switzerland, 1997.

[55] O.A. Kandil, T.C. Wong, and C.H. Liu. Navier-Stokes Computations of Symmetric and Asymmetric Vortex Shedding Around Slender Bodies. AIAA Paper 89-3397, 1989.

[56] P. Kaurinkoski and A. Hellsten. FINFLO: the parallel multi-block flow solver. Technical Report A-17, Laboratory of Aerodynamics, Helsinki University of Technology, Otaniemi, Finland, 1998.

[57] E.R. Keener. Flow Separation on Symmetric Forebodies. TM 86016, NASA, 1986.

[58] E.R. Keener and G.T. Chapman. Onset of Aerodynamic Side Forces at Zero Sideslip on Symmetric Forebodies at High Angles of Attack. AIAA Paper 74-0770, 1974.

[59] E.R. Keener and G.T. Chapman. Similarity in Vortex Asymmetries Over Slender Bodies and Wings. *AIAA Journal*, 15(9):1370–1372, September 1977.

[60] E.R. Keener, G.T. Chapman, L. Cohen, and J. Talaghani. Side Forces on a Tangent-Ogive Forebody with a Fineness Ratio of 3.5 at High Angles of Attack and Mach Numbers from 0.1 to 0.7. Technical Report TM X-3437, NASA, 1977.

[61] E.R. Keener, G.T. Chapman, and R.L. Kruse. Effects of Mach Number and Afterbody Length on Onset of Asymmetric Forces on Bodies at Zero Sideslip and High Angles of Attack. AIAA Paper 76-0066, 1976.

[62] A.N. Kolmogorov. Equations of turbulent motion of an incompressible fluid. *Izvestia Academy of Sciences, USSR; Physics*, 6(1 and 2):56–58, 1942.

[63] S.M. Kosiak. US Fighter Modernization: An Alternative Approach. *Issues in Science and Technology*, Spring 2000.

[64] B. Kramer and B. Smith. F/A-18 and F-16 Forebody Vortex Control, Static and Rotary-Balance Results. In *NASA Fourth High Angle of Attack Conference, Dryden Flight Research Center, Edwards, CA, July 12-14*, volume 3, 1994.

[65] B.R. Kramer, C.J. Suarez, and G.N. Malcolm. Forebody Vortex Control with Jet and Slot Blowing on an F/A-18. AIAA Paper 93-3449, 1993.

[66] R.L. Kruse, E.R. Keener, and G.T. Chapman. Investigation of the Asymmetric Aerodynamic Characteristics of Bodies of Revolution With Variations in Nose Geometry and Rotational Orientation at Angles of Attack to 58^o and Mach Numbers to 2. TM 78533, NASA, 1979.

[67] P.J. Lamont. Pressures Around an Inclined Ogive Cylinder with Laminar, Transitional or Turbulent Separation. AIAA Paper 80-1556, 1980.

[68] P.J. Lamont. Pressure Around an Inclined Cylinder with Laminar, Transitional, or Turbulent Separation. *AIAA Journal*, 20(11):1492–1499, November 1982.

[69] P.J. Lamont. The Complex Asymmetric Flow over a 3.5d Ogive Nose and Cylindrical Afterbody at High Angles of Attack. AIAA Paper 82-0053, 1982.

[70] W.R. Lanser and L.A. Meyn. Forebody Flow Control on a Full-Scale F/A-18 Aircraft. AIAA Paper 92-2674, 1992.

[71] S.P. LeMay, W.G. Sewall, and J.F. Henderson. Forebody Vortex Control on the F-16C Using Tangential Slot and Jet Nozzle Blowing. AIAA Paper 92-0019, 1992.

[72] W. Letko. A Low-Speed Experimental Study of the Directional Characteristics of a Sharp-Nosed Fuselage Through a Large Angle-of-Attack Range at Zero Angle of Sideslip. Technical Report TN 2911, NACA, 1953.

[73] Y. Levy, L. Hesselink, and D. Degani. Anomalous Asymmetries in Flows Generated by Algorithms that Fail to Conserve Symmetry. *AIAA Journal*, 33(6):999–1007, June 1995.

[74] R.W. MacCormack and A.J. Paullay. Computational Efficiency Achieved by Time Splitting of Finite Difference Operators. AIAA Paper, 1972.

[75] G.N. Malcolm and T.T. Ng. Paper 15: Aerodynamic Control of Fighter Aircraft by Manipulation of Forebody Vortices. In *AGARD CP497*, 1991.

[76] G.N. Malcolm, T.T Ng, L.C. Lewis, and D.G. Murri. Development of Non-Conventional Control Methods for High Angle of Attack Flight Using Vortex Manipulation. AIAA Paper 89-2192, 1989.

[77] G.N. Malcolm, T.T. Ng, L.C. Lewis, and D.G. Murri. Paper 11: Development of Non-Conventional Control Methods for High Angle of Attack Flight Using Vortex Manipulation. In *AGARD CP465*, 1990.

[78] F. Marconi. Asymmetric Separated Flows about Sharp Cones in a Supersonic Stream. In *Procedings of the 11th International Conference on Numerical Methods in Fluid Dynamics*, Williamsburg, VA, 1988.

[79] L. Martinelli. *Calculation of Viscous Flows with a Multigrid Method.* PhD thesis, Princeton, 1987.

[80] P.W. McDonald. The Computation of Transonic Flow through Two-Dimensional Gas Turbine Cascades. ASME Paper, 1971.

[81] F.R. Menter. Influence of freestream values on k-ω turbulence model predictions. *AIAA Journal*, 30(6):1657–1659, June 1992.

[82] F.R. Menter. Zonal two equation k-ω turbulence models for aerodynamic flows. AIAA Paper 93-2906, 1993.

[83] F.R. Menter. Two-equation eddy-viscosity turbulence models for engineering applications. *AIAA Journal*, 32(8):1598–1605, August 1994.

[84] V.J. Modi, C.W. Cheng, A. Mak, and T. Yokomizo. Reduction of the Sideforce on Pointed Forebodies Through Add-on Tip Devices. AIAA Paper 90-3005, 1990.

[85] I.R.M. Moir. An Experimental Investigation of the Effect of Fineness Ratio on Lateral Force on a Pointed Slender Body of Revolution. RAE Tech Memo AERO TM2225, 1991.

[86] C.A. Moskovitz, R.M. Hall, and F.R. DeJarnette. Effects of Surface Perturbations on the Asymmetric Vortex Flow Over a Slender Body. AIAA Paper 88-0483, 1988.

[87] C.A. Moskovitz, R.M. Hall, and F.R. DeJarnette. Experimental Investigation of a New Device to Control the Asymmetric Flowfield on Forebodies at Large Angles of Attack. AIAA Paper 90-0069, 1990.

[88] C.A. Moskowitz, R.M. Hall, and F.R. DeJarnette. Effects of Nose Bluntness, Roughness and Surface Perturbations on the Asymmetric Flow Past Slender Bodies at Large Angles of Attack. AIAA Paper 89-2236, 1989.

[89] D.G. Murri. Wind-Tunnel Investigation of Actuated Forebody Strakes for Yaw Control at High Angles of Attack. Master's thesis, George Washington University, 1987.

[90] D.G. Murri, R.T. Biedron, G.E. Erickson, F.L. Jordan, and K.D. Hoffler. Development of Actuated Forebody Strake Controls for the F-18 High Alpha Research Vehicle. Technical Report CP-3149, NASA, 1990.

[91] D.G. Murri and D.M. Rao. Exploratory Studies of Actuated Forebody Strakes for Yaw Control at High Angles of Attack. AIAA Paper 87-2557, 1987.

[92] D.G. Murri, G.H. Shah, and D.J. DiCarlo. Preparations for Flight Research to Evaluate Actuated Forebody Strakes on the F-18 High-Alpha Research Vehicle. In *NASA Fourth High Angle of Attack Conference, Dryden Flight Research Center, Edwards, CA, July 12-14*, volume 3, 1994.

[93] D.G. Murri, G.H. Shah, D.J. DiCarlo, and T.W. Trilling. Actuated Forebody Strake Controls for the F-18 High-Alpha Research Vehicle. AIAA Paper 93-3675, 1993.

[94] H.T. Nagamatsu and R.D. Orozco. Porosity Effect on Supercritical Airfoil Drag Reduction by Shock Wave/Boundary Layer Control. AIAA Paper 84-1682, June 1984.

[95] R.C Nelson and E.L. Fleeman. High Angle of Attack Aerodynamics on a Slender Body with a Jet Plume. *Journal of Spacecraft and Rockets*, 12(1):12–16, 1975.

[96] T.T. Ng. Effect of a Single Strake on the Forebody Vortex Asymmetry. *Journal of Aircraft*, 27(9):844–846, 1990.

[97] T.T. Ng and G.N. Malcolm. Aerodynamic Control Using Forebody Blowing and Suction. AIAA Paper 91-0619, 1991.

[98] T.T. Ng and G.N. Malcolm. Aerodynamic Control Using Forebody Strakes. AIAA Paper 91-0618, 1991.

[99] D.J. Peake and F.K. Owen. Control of Forebody Three-dimensional Flow Separation. In *AGARD CP262*, 1979.

[100] D.J. Peake, F.K. Owen, and D.A. Johnson. Control of Forebody Vortex Orientation to Alleviate Side Forces. AIAA Paper 80-0183, 1980.

[101] D.J.. Peake and M. Tobak. On Issues Concerning Flow Separation and Vortical Flows in Three Dimensions. TM 84374, NASA, 1983.

[102] G.S. Pick. Investigation of Side Forces on Ogive-Cylinder Bodies at High Angles of Attack in the $M = 0.5$ to 1.1 Range. AIAA Paper 71-0570, 1971.

[103] D.I.A. Poll. Transition in the Infinite Swept Attachment-Line Boundary Layer. *The Aeronautical Quarterly*, XXX:607–628, 1979.

[104] D.I.A. Poll. On the effects of boundary-layer transition on a cylindrical afterbody at incidence in low-speed flow. *The Aeronautical Journal of The Royal Aeronautical Society*, pages 315–327, October 1985.

[105] D.I.A. Poll. Some Observations of the Transition Process on the Windward Face of a Long Yawed Cylinder. *Journal of Fluid Mechanics*, 150:329–356, January 1985.

[106] O. Reynolds. On the Dynamical Theory of Incompressible Viscous Fluids and the Determination of the Criterion. In *Philosophical Transactions of the Royal Society of London, Series A*, volume 186, page 123, 1895.

[107] A.W. Rizzi and M. Inouye. Time Split Finite Volume Method for Three-Dimensional Blunt Body Flows. *AIAA Journal*, 11:1478–1485, 1973.

[108] M.J. Siclari and F. Marconi. The Computation of Navier-Stokes Solutions Exhibiting Asymmetric Vortices. AIAA Paper 89-1817, 1989.

[109] A.M. Skow and G.E. Erickson. Modern Fighter Aircraft Design for High Angle of Attack. In *AGARD Lecture Series No.121: High-Angle-of-Attack Aerodynamics*. 1982.

[110] A.M. Skow, W.A. Moore, and D.J. Lorincz. Forebody Vortex Blowing - A Novel Concept to Enhance the Departure/Spin Recovery Characteristics of Fighter Aircraft. In *AGARD CP262*, 1979.

[111] A.M. Skow, A. Titiriga, and W.A. Moore. Paper 6: Forebody/Wing Vortex Interactions and their Influence on Departure and Spin Resistance. In *AGARD CP247*, 1978.

[112] C.W. Smith, J.N. Ralston, and H.W. Mann. Aerodynamic Characteristics of Forebody and Nose Strakes Based on F-16 Wind-Tunnel Test Experience, Volume 1: Summary and Analysis. Contractor Report 3053, NASA, 1979.

[113] P.R. Spalart and S.R. Allmaras. A one-equation turbulence model for aerodynamic flows. AIAA Paper 92-0439, 1992.

[114] P. Thiede, P. Krogmann, and E. Stanewsky. Active and Passive Shock/Boundary Layer Interaction Control on Supercritical Airfoils. In *AGARD CP365*, 1984.

[115] J.L. Thomas. Reynolds Number Effects on Supersonic Asymmetric Flow Over a Cone. *Journal of Aircraft*, 30(4):488–495, 1993.

[116] M. Tobak and D.J. Peake. Topology of Two-Dimensional and Three-Dimensional Separated Flows. AIAA Paper 79-1480, 1979.

[117] K.J. Vanden. Thin-Layer Navier-Stokes Solutions of the Asymmetric Vortical Flow on a Tangent-Ogive Body. Master's thesis, University of Florida, 1989.

[118] K.J. Vanden and D.M. Belk. Numerical Investigation of Subsonic and Supersonic Asymmetric Vortical Flow. AIAA Paper 91-2869-CP, 1991.

[119] J.B. Vos *et al.* NSMB 5.0 handbook. Technical Report: LMF-DGM-EPFL, CERFACS, Dept. Aeronautics KTH, Aerospatiale Matra Airbus, SAAB AB, 2000.

[120] A.B. Wardlaw and A.M. Morrison. Induced Sideforces at High Angles of Attack. *Journal of Spacecraft and Rockets*, 13(10):589–593, 1976.

[121] A.B. Wardlaw and W.J. Yanta. Multistable vortex patterns on slender, circular bodies at high incidence. *AIAA Journal*, 20(4):509–515, April 1982.

[122] D.C. Wilcox. Reassessment of the scale-determining equation for advanced turbulence models. *AIAA Journal*, 26(11):1299–1310, November 1988.

[123] D.C Wilcox. Comparison of two-equation turbulence models for boundary layers with pressure gradient. *AIAA Journal*, 31(8):1414–1421, August 1993.

[124] D.C. Wilcox. *Turbulence Modelling for CFD*. DCW Industries Inc., 1993. ISBN 0963605100.

[125] R.M. Wood, D.W. Banks, and S.X.S. Bauer. Assessment of Passive Porosity with Free and Fixed Separation on a Tangent Ogive Forebody. AIAA Paper 92-4494-CP, 1992.

[126] S. Yoon and A. Jameson. An LU-SSOR Scheme for the Euler and Navier-Stokes Equations. AIAA Paper 87-0600, 1987.

[127] A. Ytterström. MB-Split: A structured mesh partitioning tool for load-balancing on mimd computers. in *Proceedings of the Second ECCOMAS Conference on Numerical Methods in Engineering, Paris, France*, 1996.

[128] G. Zilliac, D. Degani, and M. Tobak. Asymmetric Vortices on a Slender Body of Revolution. AIAA Paper 90-0388, 1990.

[129] G.G. Zilliac. Computational/Experimental Study of the Flowfield on a Body of Revolution at Incidence. *AIAA Journal*, 27(8):1008–1016, August 1989.

[130] G.G. Zilliac, D. Degani, and M. Tobak. Asymmetric Vortices on a Slender Body of Revolution. *AIAA Journal*, 29(5):667–675, May 1991.

A. Turbulence Model Validation

Three validation cases were used to assess the implementation of each of the turbulence models in the k-ω family. These test-cases cover a range of physical conditions and were also used by Duquesne, [21], in the previous phase of turbulence model implementation. Where possible, solver parameters have been kept consistent with these earlier calculations. The results produced by the six k-ω models are presented and compared with those generated using three existing eddy-viscosity models: the one-equation model of Spalart and Allmaras and the low Reynolds-number, two-equation models of Chien and Hoffman.

A.1 Flat Plate Turbulent Boundary Layer

A.1.1 Grid & boundary conditions

The grid for the flat plate boundary layer comprised a single block of 40 × 80 × 2 cells in the i, j and k directions respectively. The cells were evenly spaced in the streamwise direction but geometrically clustered normal to the wall to give approximately 40 cells in the fully developed boundary layer. Plate length was 1.0m. Details of the freestream and boundary conditions are given in Tables (A.2) & (A.1) below.

Face	Location	b.c.	Type	i	j	k
1	entry	130	freestream	1	1 to 80	1
2	exit	220	linear extrapolation	40	1 to 80	1
3	plate	300	solid adiabatic wall	1 to 40	1	1
4	top	130	freestream	1 to 40	80	1
5	left	413	mirror w-velocity	1 to 40	1 to 80	1
6	right	413	mirror w-velocity	1 to 40	1 to 80	2

Table A.1: *Boundary conditions for the flat plate.*

Mach no.	0.4
Re/m	5.0×10^6
Flow state	fully turbulent

Table A.2: *Freestream conditions for the flat plate.*

A.1.2 Computational details

All computations were run on a single 195MHz R10000 processor on an SGI Octane workstation equipped with 1Gb RAM. Initial test calculations utilising the explicit solver were run before the scalar and full matrix implicit LU-SGS implementations were tried. All results shown below were generated using the matrix LU-SGS algorithm. The standard central spatial discretisation was selected for all calculations and all other numerical parameters were held constant so as to purely assess the effect of varying the turbulence model. CFL number was initially set at 0.5 with an increase factor each time-step of 1.02 up to a maximum of 1×10^9.

A sample NSMB input file for the flat plate validation case is included below for completeness, the turbulence model in this case being the original Menter k-w-SST.

```
# database, I/O
#
database      : plate-10.db
init flag     : 0
output flag   : 1
print flag    : 1
solution in   : 0
solution out  : 4
title         : Plate 2eq-kwmss benchmark
comment       : Implicit central kwmss
#
# physical problem description
#
unsteady  : 0
gas model : 1
flow model: 2eq-kwmss
#
# flow parameters
#
mach                 : 0.4
rho infinity         : 1.
pressure infinity    : 1.
gamma                : 1.4
gas constant         : 1.
alpha                : 0.
beta                 : 0.
Reynolds             : 5.0E6
prandtl              : 0.72
viscosity model      : constant
#
# general turbulence parameters
#
prte               : 0.9
cf0                : 0.005
myt/my max         : 500.
#wall distance flag: 1
pointwise implicit: implicit
```

```
transition flag   : 0
#
# temporal/spatial schemes
#
time scheme            : implicit
space scheme           : central
implicit approximation: matrix
cfl                    : 0.5
cfl increase factor    : 1.02
cfl end                : 1.e9
#
# artificial dissipation (central spatial discretisation)
#
dissipation model      : standard
dis2I                  : 0.00
dis2J                  : 0.00
dis2K                  : 0.00
dis4                   : 0.01
damping model          : 0
damping order          : 0
#
# steady-state/inner time-stepping loop
#
nsteps                  : 100000
db resultinterval       : 200000
residual interval inner: 10
tolerance               : 1.e-6
```

A.1.3 Results

As can be seen from the sample input file, the problem was assumed to have converged once the normalised density residual $< 1.0 \times 10^{-6}$. Fig.(A.1) shows the convergence to be similar for all models with the exception of the Hoffman k-ε model. On inspection of the velocity and μ_t profiles in Figs.(A.2) & (A.3), it becomes clear that the model is behaving strangely and so further benchmarking against it was curtailed. The remaining models show similar boundary-layer characteristics aside from the low Reynolds number version of the Menter k-ω-SST model, which appears to underpredict U^+ in the log layer, see Fig.(A.4(d)).

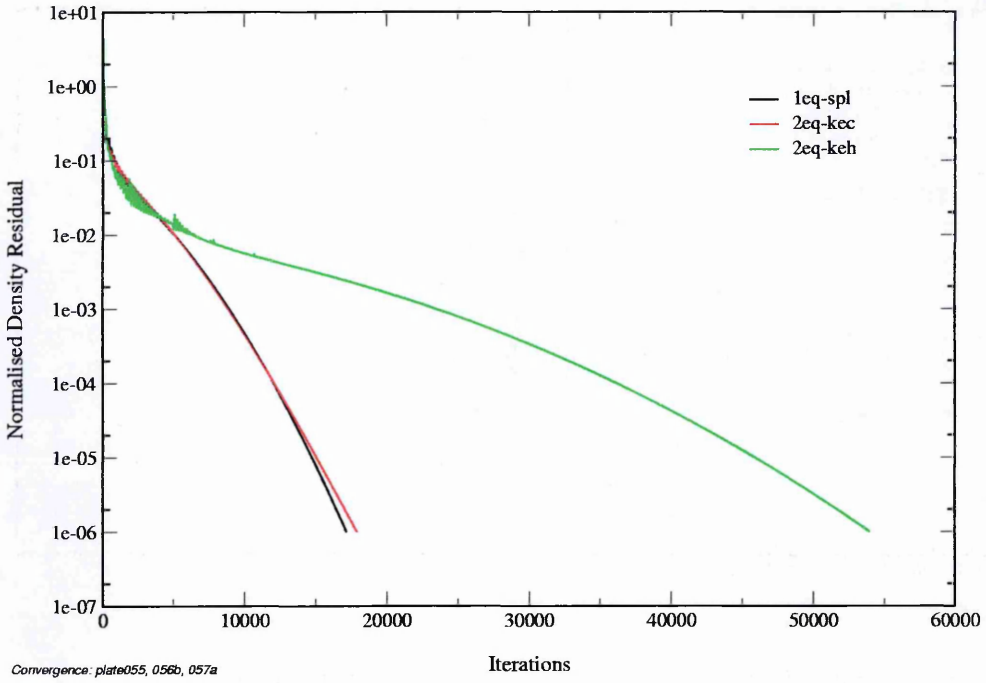

(a) Existing NSMB turbulence models.

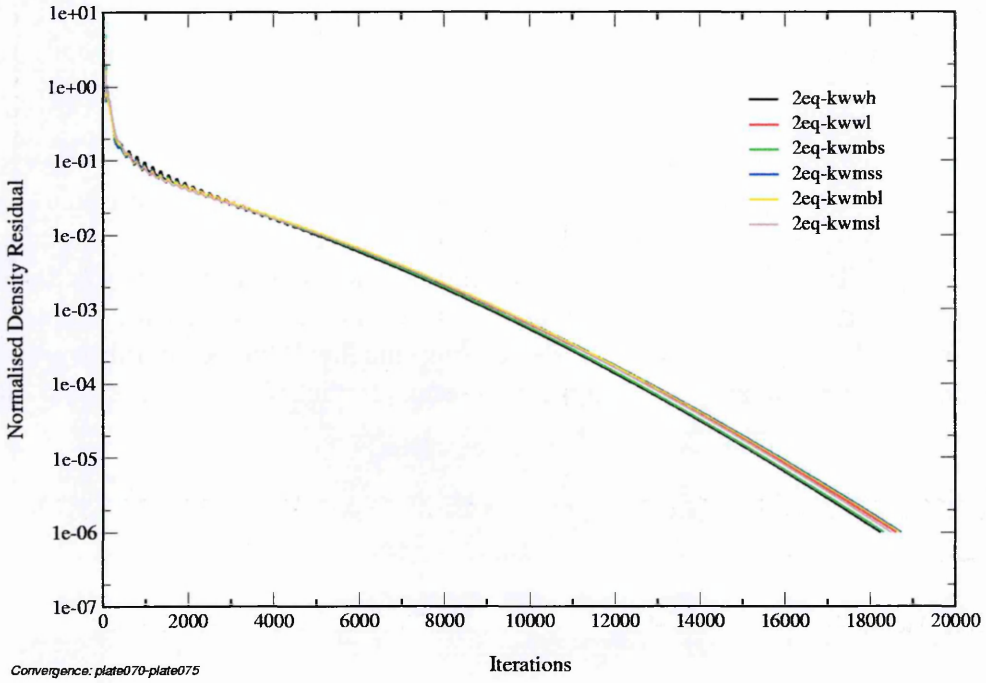

(b) k-ω -family turbulence models.

Figure A.1: *Convergence histories for flat plate validation case.*

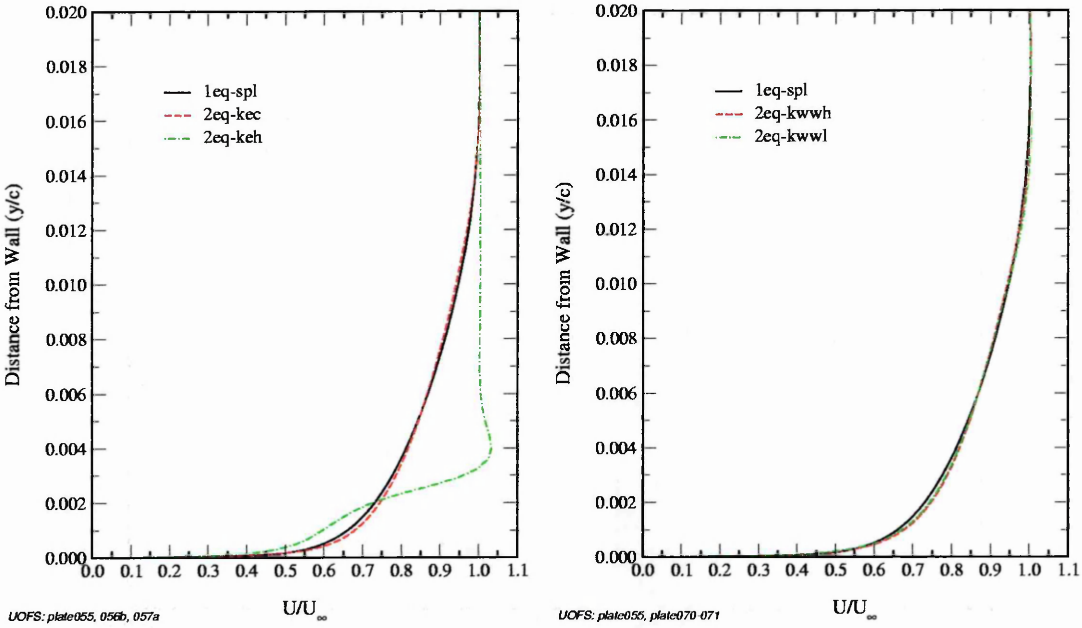

(a) Existing NSMB turbulence models.

(b) Wilcox *k*-ω & LRN *k*-ω .

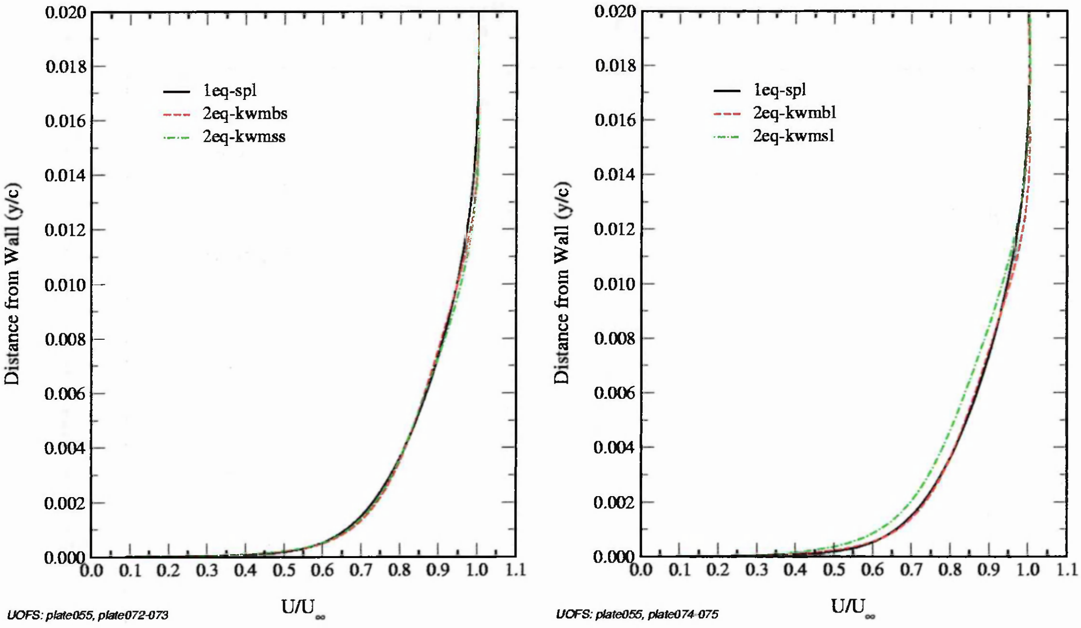

(c) Original Menter *k*-ω-BSL & *k*-ω-SST .

(d) LRN Menter *k*-ω-BSL & *k*-ω-SST .

Figure A.2: *Flat plate boundary-layer velocity profiles at x/c=0.9. The one-equation Spalart-Allmaras model is included on all the above plots for the purpose of comparison.*

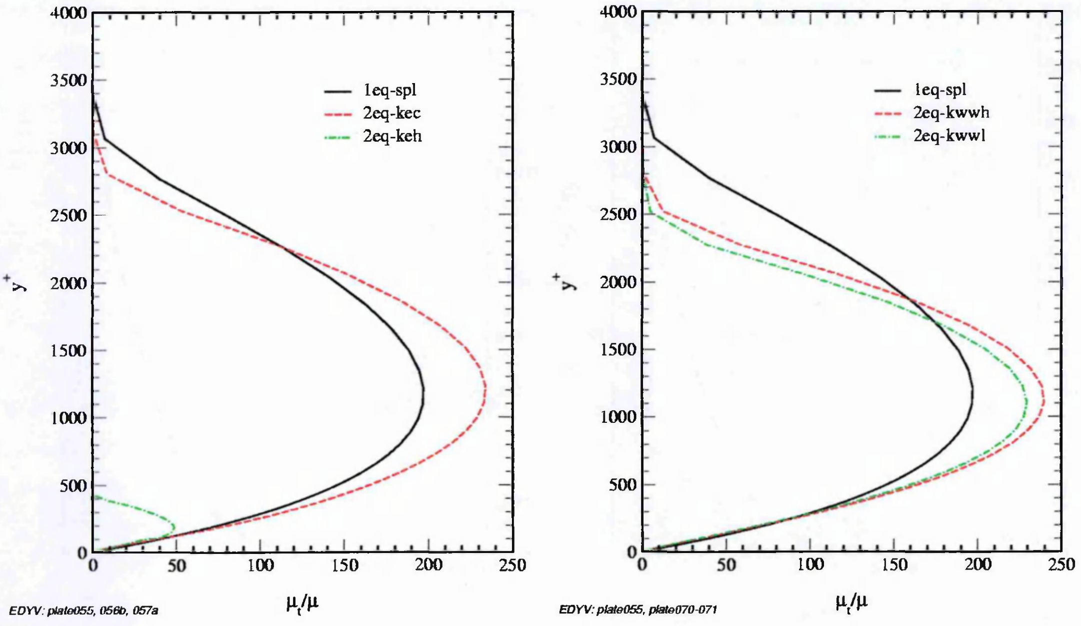

EDYV: plate055, 056b, 057a

EDYV: plate055, plate070-071

(a) Existing NSMB turbulence models.

(b) Wilcox k-ω & LRN k-ω .

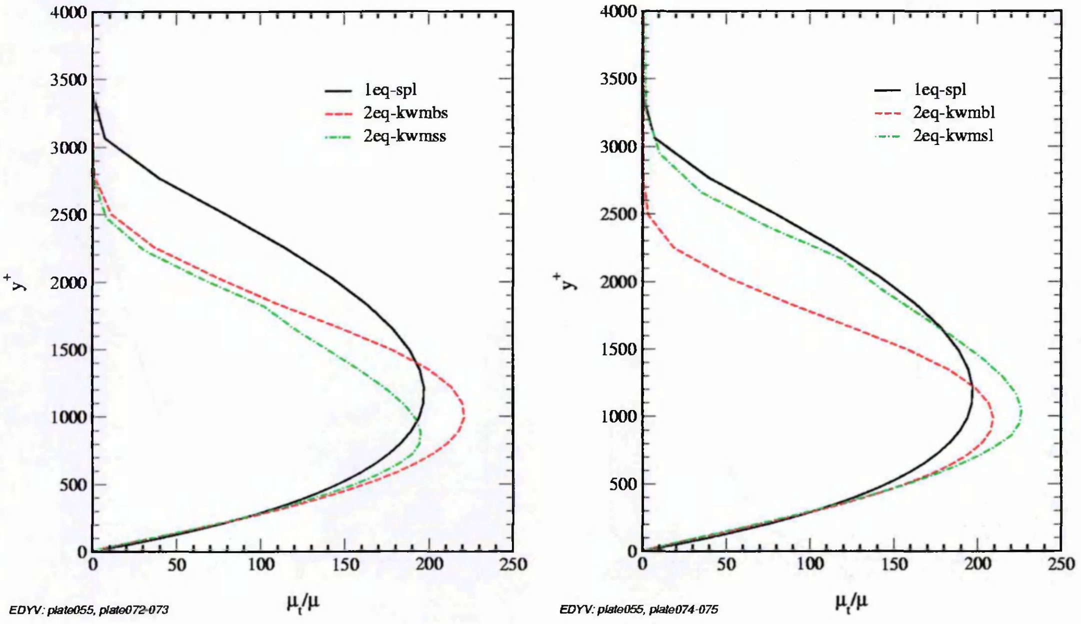

EDYV: plate055, plate072-073

EDYV: plate055, plate074-075

(c) Original Menter k-ω-BSL & k-ω-SST .

(d) LRN Menter k-ω-BSL & k-ω-SST .

Figure A.3: *Flat plate boundary-layer eddy-viscosity profiles at x/c=0.9. The one-equation Spalart-Allmaras model is included on all the above plots for the purpose of comparison.*

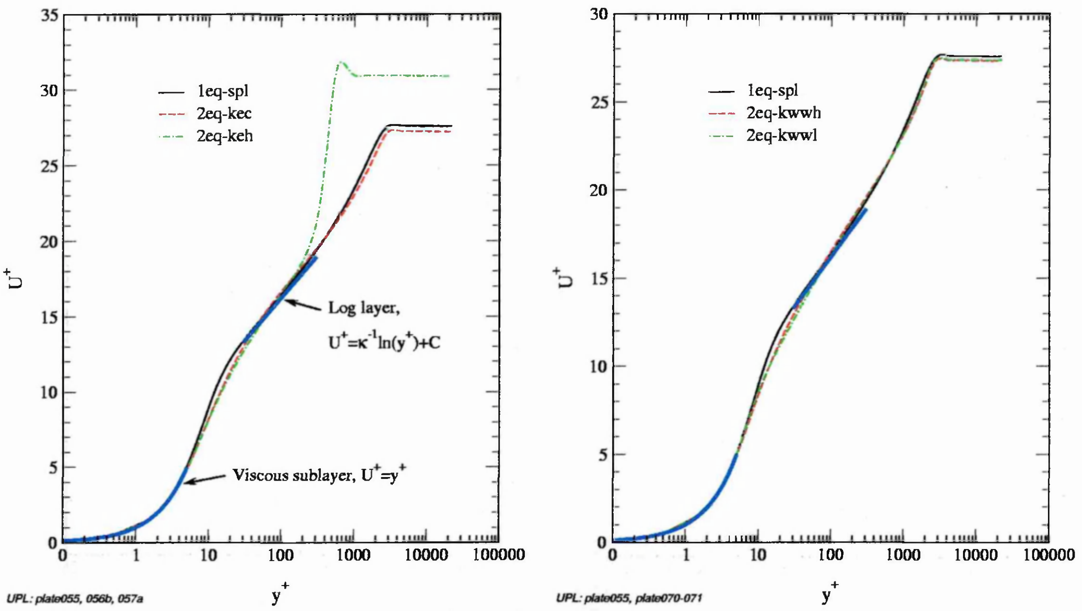

(a) Existing NSMB turbulence models.

(b) Wilcox k-ω & LRN k-ω .

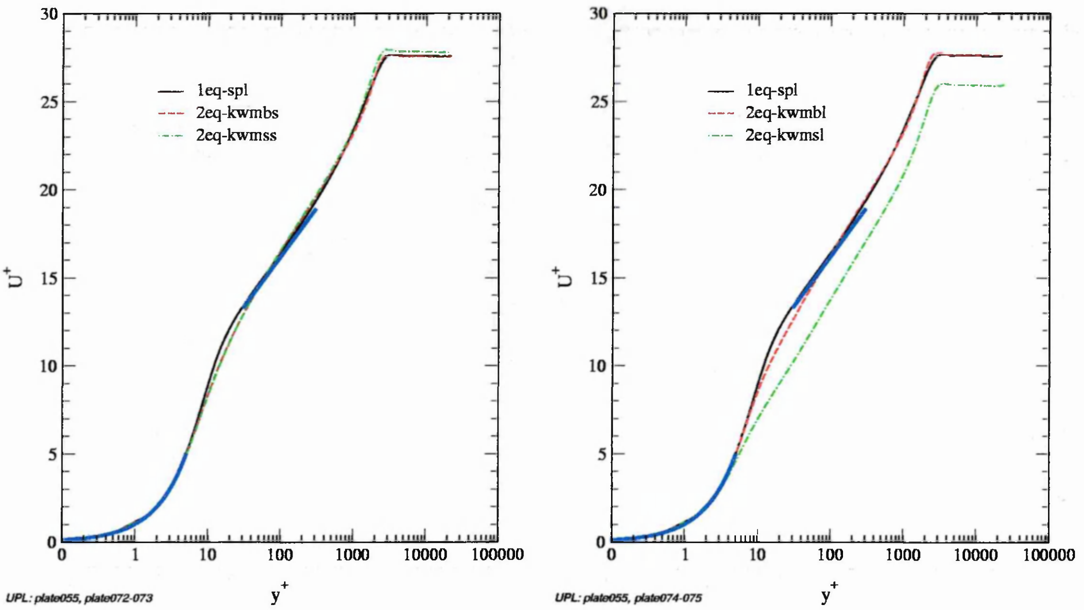

(c) Original Menter k-ω-BSL & k-ω-SST .

(d) LRN Menter k-ω-BSL & k-ω-SST .

Figure A.4: *Flat plate boundary-layer velocity in wall units. Profiles taken at x/c=0.9. The one-equation Spalart-Allmaras model is included on all the above plots for the purpose of comparison as are the theoretical profiles for the viscous sublayer and log layer.*

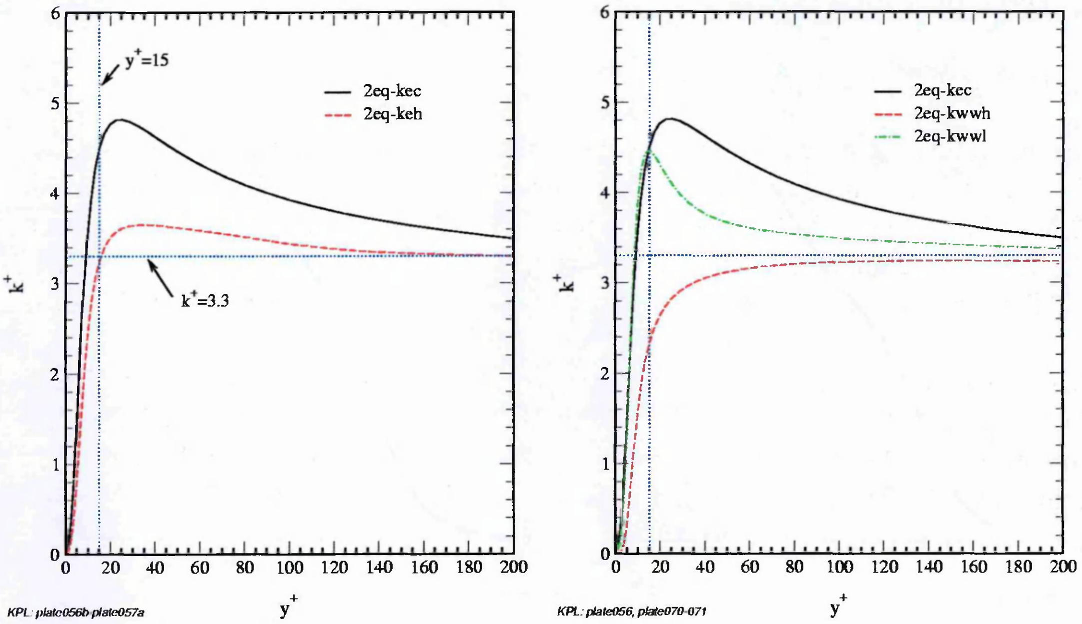

(a) Existing NSMB turbulence models.

(b) Wilcox k-ω & LRN k-ω .

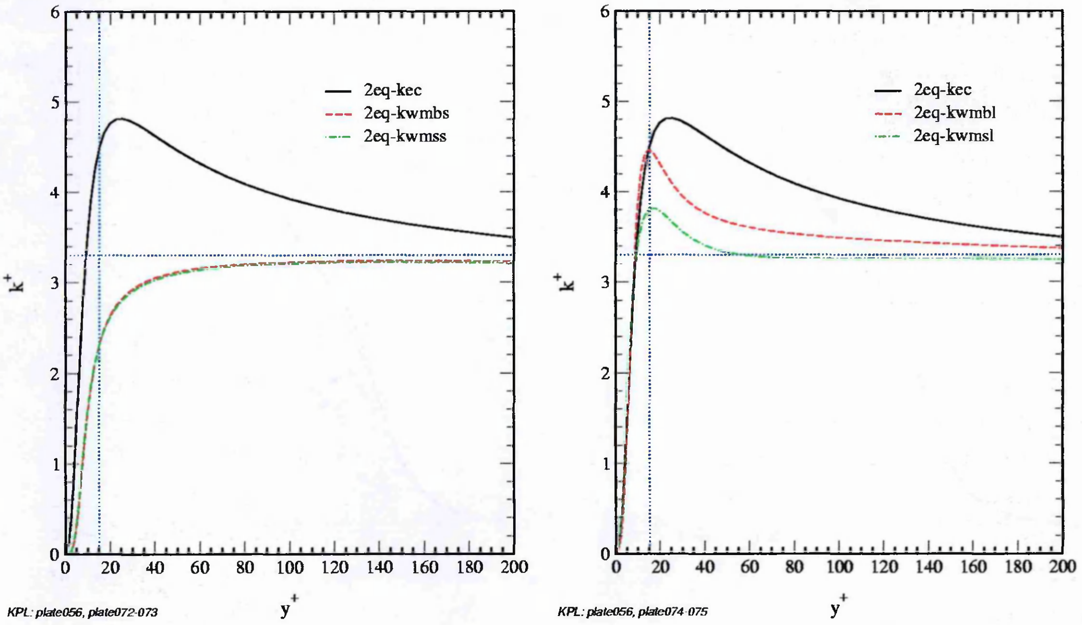

(c) Original Menter k-ω-BSL & k-ω-SST .

(d) LRN Menter k-ω-BSL & k-ω-SST .

Figure A.5: *Flat plate boundary-layer turbulent kinetic energy in wall units. Profiles taken at x/c=0.9. The two-equation k-ε model of Chien is included on all the above plots for the purpose of comparison.*

A.2 Aerospatiale A-aerofoil

A.2.1 Grid & boundary conditions

The second validation case chosen involves the Aerospatiale A-aerofoil. Two sets of experimental data are available for this configuration, the first taken in the ONERA F1 1.5×3.5m wind tunnel in 1987 and the second in the ONERA F2 1.4×1.8m tunnel a year later. Owing to the comprehensive experimental database, this was a standard testcase for the ECARP[1] Project - Validation of CFD Codes and Assessment of Turbulence Models, [38].

Two C-type grids of varying fineness were tested, the aerofoil2 grid of $128 \times 32 \times 2$ cells in the i, j and k directions respectively and the finer aerofoil3 grid of $256 \times 64 \times 2$ cells, the mandatory ECARP mesh. All data presented here were calculated using the finer grid, shown in Fig.(A.6). The freestream and boundary conditions are given in Tables (A.3) & (A.4).

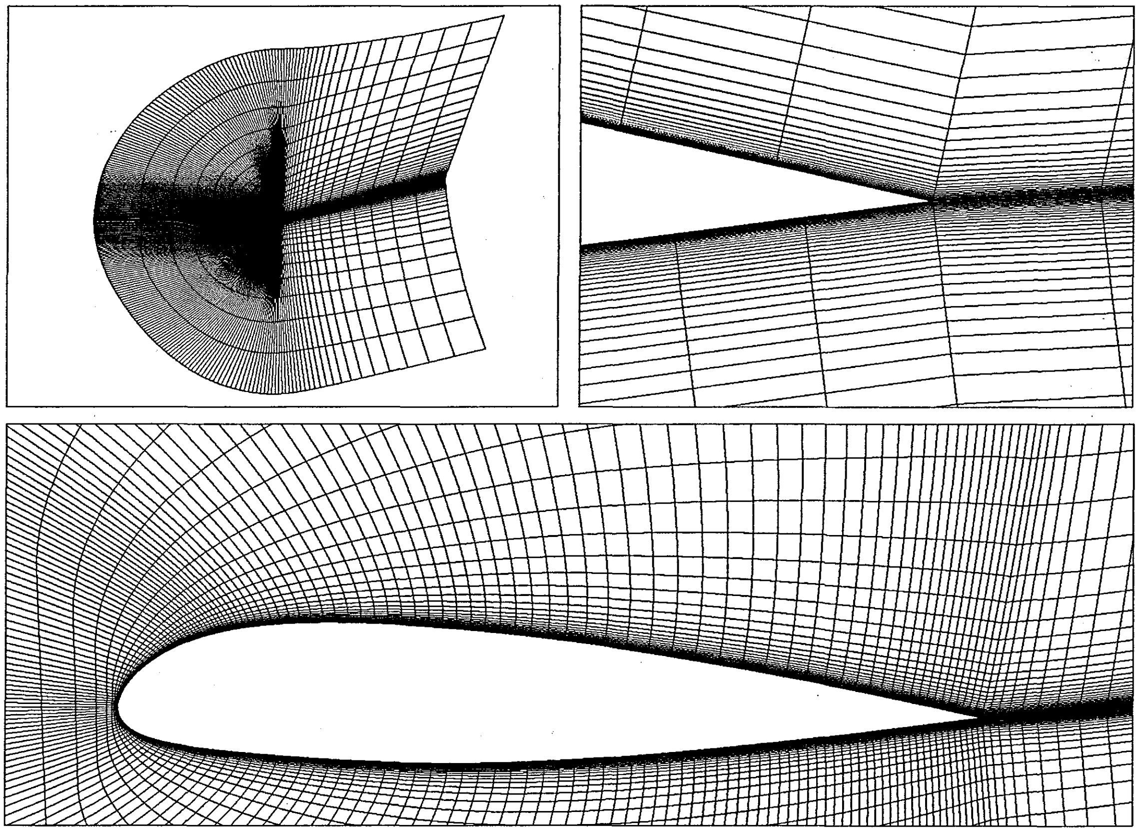

Figure A.6: *A-aerofoil grid no.3,* $256 \times 64 \times 2$ *cells. The grid is optimised for* $\alpha = 13.3^o$.

---

[1] European Computational Aerodynamics Research Project

Mach no.	0.15	0.15
Re/m	2.07×10^6	2.0×10^6
α	12.1^o	13.3^o
Wind-Tunnel	F1	F2

Table A.3: Freestream conditions for the A-aerofoil.

Face	Location	b.c.	Type	i	j	k
1	exit (bottom)	131	characteristic variables	1	1 to 64	1
2	exit (top)	131	characteristic variables	256	1 to 64	1
3	wake (bottom)	502	wake replaced by a block	1 to 32	1	1
	aerofoil	300	solid adiabatic wall	33 to 224	1	1
	wake (top)	502	wake replaced by a block	225 to 256	1	1
4	farfield	131	characteristic variables	1 to 256	64	1
5	right side	430	periodic	1 to 256	1 to 64	1
6	left side	430	periodic	1 to 256	1 to 64	2

Table A.4: Boundary conditions for the A-aerofoil.

A.2.2 Computational details

The experimental database for the A-aerofoil is quite considerable, arising as it does from two fairly comprehensive wind-tunnel studies. However, in his Application-Oriented Synthesis of the ECARP turbulence model validation exercise, see [38] pp.327-346, Chaput notes that, owing to greater flow two-dimensionality, the data taken in the larger cross-section F1 tunnel are more appropriate for referencing the global lift and drag coefficients, pressure and skin-friction distributions, whilst any boundary-layer profile comparisons should be made with the F2 data. The two sets of flow conditions used in this study were chosen with this in mind, α=12.1^o, Re=2.07×10^6 being suitable for comparison with F1 global data and α=13.3^o, Re=2.0×10^6 for F2 boundary-layer measurements.

As for the flat plate testcase, all computations were run on a single 195MHz R10000 processor on an SGI Octane workstation equipped with 1Gb RAM. All results shown below were generated using the matrix LU-SGS algorithm. The standard central spatial discretisation was selected for all calculations and all other numerical parameters were held constant. The only exceptions to this were additional k-ε (Chien) calculations run with the adtbeq1 parameter set to -1. The Hoffman k-ε model was not considered following the poor results obtained on the flat plate. CFL number was initially set at 0.5 with an increase factor each time-step of 1.02 up to a maximum of 1×10^9.

Transition in the F1 experiments was prescribed at 30%$\bar{c}$ on the lower surface and left free on the upper surface. Oil-flow data taken during the F2 studies showed there to be a laminar separation bubble terminated by transitional/turbulent reattachment at the higher angles of attack being considered in this study - flow reattachment was recorded at 15%$\bar{c}$ at α=12^o and 12%$\bar{c}$ at α=13.3^o. After initial fully turbulent calculations, transition was prescribed first at 30%$\bar{c}$ (lower) & 12%$\bar{c}$ (upper) with a 5%$\bar{c}$ blending region, before being moved slightly forward to 23%$\bar{c}$ (lower) & 5%$\bar{c}$ (upper), with a 7%$\bar{c}$ blending region.

A sample NSMB input file for the A-aerofoil validation case is included below.

```
# database, I/O
#
database      : aaerofoil3-19.db
init flag     : 0
output flag   : 1
print flag    : 1
solution in   : 0
solution out  : 4
title         : A-Aerofoil 12.1deg
comment       : Matrix-implicit central 2eq-kwmss, itrans=3
#
# physical problem description
#
unsteady  : 0
gas model : 1
flow model: 2eq-kwmss
#
# flow parameters
#
mach                 : 0.15
rho infinity         : 1.
pressure infinity    : 1.
gamma                : 1.4
gas constant         : 1.
alpha                : 12.1
beta                 : 0.
Reynolds             : 2.07E6
prandtl              : 0.72
viscosity model      : constant
#
# general turbulence parameters
#
prte               : 0.9
cf0                : 0.005
myt/my max         : 2000.
wall distance flag: 1
pointwise implicit: implicit
transition flag    : 3
#
# temporal/spatial schemes
#
time scheme             : implicit
space scheme            : central
implicit approximation: matrix
cfl                     : 0.5
cfl increase factor     : 1.02
cfl end                 : 1.e9
#
# artificial dissipation (central spatial discretisation)
```

```
#
dissipation model     : standard
dis2I                 : 0.0
dis2J                 : 0.0
dis2K                 : 0.0
dis4                  : 0.01
damping model         : 0
damping order         : 0
#
# steady-state/inner time-stepping loop
#
nsteps                 : 30000
db resultinterval      : 200000
residual interval inner: 10
tolerance              : 1.e-6
```

A.2.3 Results

As before, convergence was assumed to have occurred when the normalised density residual $< 1.0 \times 10^{-6}$ but this was not always achieved. Convergence information and system performance timings are included in Tables (A.5) & (A.7) whilst Figs.(A.9) - (A.20) depict convergence histories, surface c_p and boundary-layer velocity profiles for the test-runs. Some c_p distributions and boundary-layer results are included for the F2 case using the k-ω-SST-LRN model, however, these should largely be discounted given the basic problems highlighted by the flat plate boundary-layer profiles.

Run no.	Convergence	Iterations	CPUsecs./It.	Turbulence model
Fully turbulent				
107	1.0×10^{-6}	13200	2.139	Spalart-Allmaras
108	8.7×10^{-5}	25000	2.271	Chien k-ε
102	1.0×10^{-6}	13060	2.161	Standard Wilcox k-ω
103	1.0×10^{-6}	13340	2.238	Wilcox k-ω-LRN
104	1.0×10^{-6}	13670	2.422	Menter k-ω-BSL
105	1.0×10^{-6}	38220	2.508	Menter k-ω-SST
106	1.0×10^{-6}	13870	2.470	Menter k-ω-BSL-LRN
Transition at 23%$\bar{c}$ (lower), 5%$\bar{c}$ (upper), 7%$\bar{c}$ blend				
109	1.0×10^{-6}	13800	2.130	Spalart-Allmaras
110	6.2×10^{-3}	25000	2,256	Chien k-ε
083	1.0×10^{-6}	14600	2.278	Standard Wilcox k-ω
084	1.0×10^{-6}	14930	2.328	Wilcox k-ω-LRN
085	1.0×10^{-6}	14100	2.500	Menter k-ω-BSL
086	1.0×10^{-6}	18130	2.565	Menter k-ω-SST
087	1.0×10^{-6}	14330	2.533	Menter k-ω-BSL-LRN
Transition at 30%$\bar{c}$ (lower), 12%$\bar{c}$ (upper), 5%$\bar{c}$ blend				
111	1.0×10^{-6}	16480	1.955	Spalart-Allmaras
112	9.8×10^{-4}	25000	2.167	Chien k-ε
088	1.0×10^{-6}	17250	2.275	Standard Wilcox k-ω
089	1.0×10^{-6}	17160	2.318	Wilcox k-ω-LRN
090	1.0×10^{-6}	16480	2.497	Menter k-ω-BSL
091	1.0×10^{-6}	18420	2.567	Menter k-ω-SST
092	1.0×10^{-6}	16620	2.504	Menter k-ω-BSL-LRN

Table A.5: *A-aerofoil,* M=0.15, Re=2.07×10^{6}, α=12.1°. *System performance summary.*

Run no.	Turbulence model	c_l	c_d
Fully turbulent			
107	Spalart-Allmaras	1.384	0.02470
108	Chien k-ε (default)	1.443	0.02519
102	Standard Wilcox k-ω	1.332	0.02470
103	Wilcox k-ω-LRN	1.332	0.02455
104	Menter k-ω-BSL	1.318	0.02504
105	Menter k-ω-SST	1.208	0.02617
106	Menter k-ω-BSL-LRN	1.305	0.02494
Transition at 23%$\bar{c}$ (lower), 5%$\bar{c}$ (upper), 7%$\bar{c}$ blend			
109	Spalart-Allmaras	1.451	0.02081
110	Chien k-ε (default)	1.584	0.02994
083	Standard Wilcox k-ω	1.441	0.02052
084	Wilcox k-ω-LRN	1.437	0.02019
085	Menter k-ω-BSL	1.432	0.02094
086	Menter k-ω-SST	1.379	0.02050
087	Menter k-ω-BSL-LRN	1.428	0.02061
Transition at 30%$\bar{c}$ (lower), 12%$\bar{c}$ (upper), 5%$\bar{c}$ blend			
111	Spalart-Allmaras	1.505	0.01798
112	Chien k-ε (default)	1.671	0.01989
088	Standard Wilcox k-ω	1.503	0.01795
089	Wilcox k-ω-LRN	1.497	0.01779
090	Menter k-ω-BSL	1.497	0.01824
091	Menter k-ω-SST	1.460	0.01789
092	Menter k-ω-BSL-LRN	1.491	0.01804
	Experiment, F1 data	1.481	0.01860

Table A.6: *A-aerofoil, $M=0.15$, $Re=2.07\times10^{6}$, $\alpha=12.1^{\circ}$. Comparison of calculated lift- and drag coefficients.*

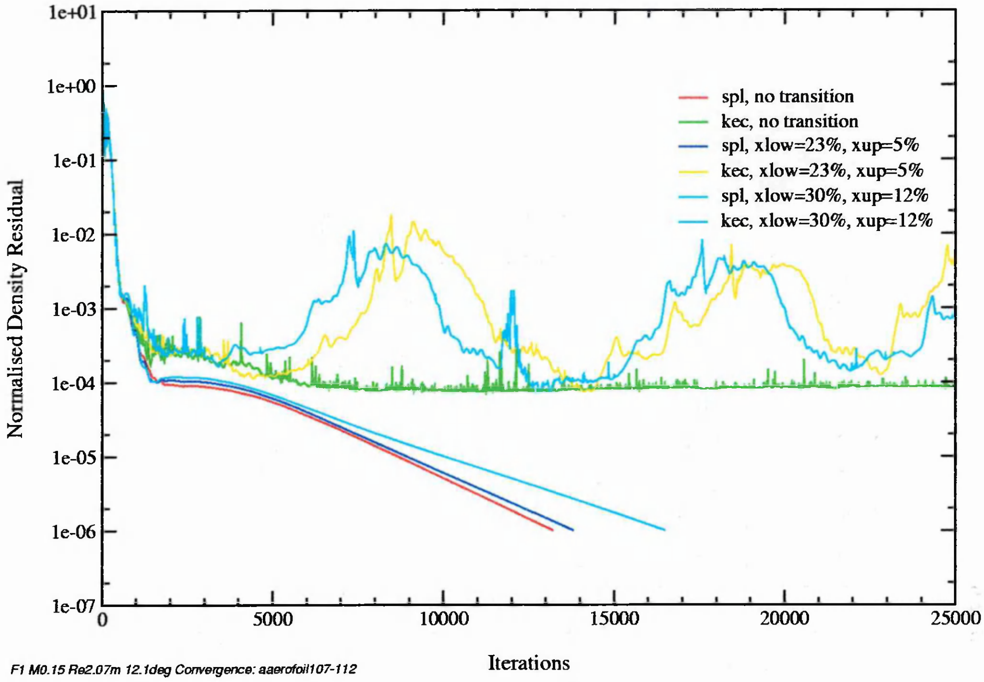

F1 M0.15 Re2.07m 12.1deg Convergence: aaerofoil107-112

(a) Convergence.

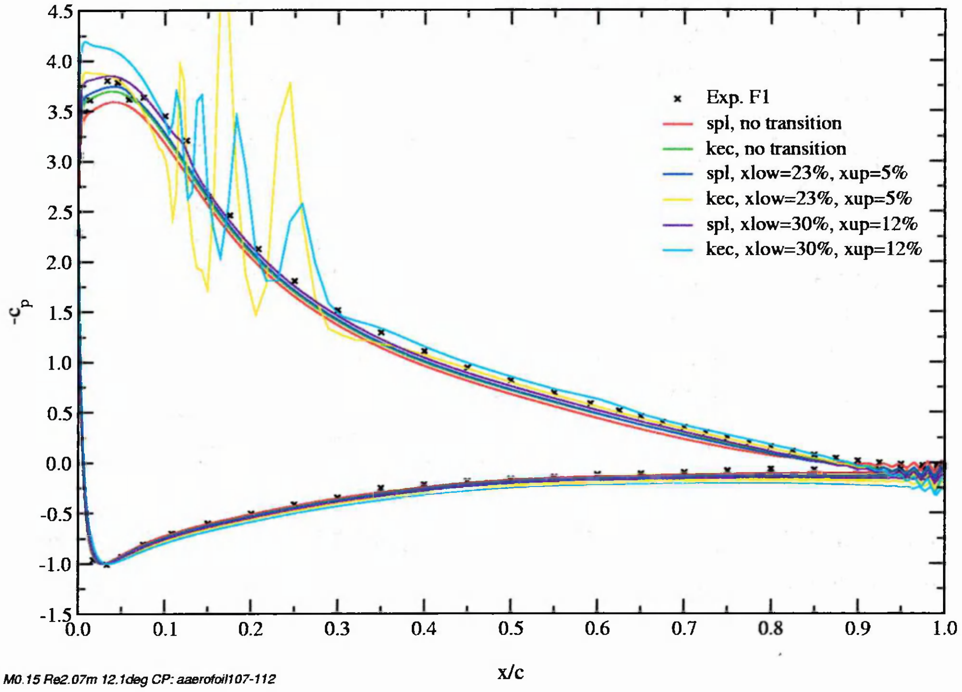

F1 M0.15 Re2.07m 12.1deg CP: aaerofoil107-112

(b) Surface c_p.

Figure A.7: *A-aerofoil, M*=0.15, *Re*=2.07×10^6, $\alpha = 12.1^o$, *Existing turbulence models. Fully turbulent calculations and with transition prescribed. Convergence and comparison of surface* c_p *with experiment.*

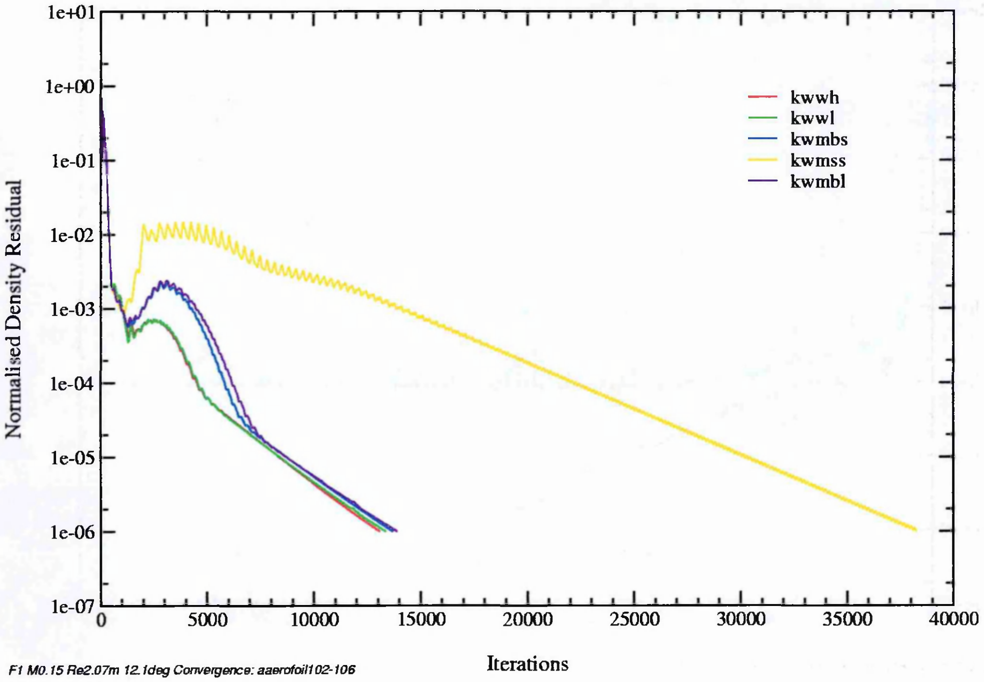

(a) Convergence.

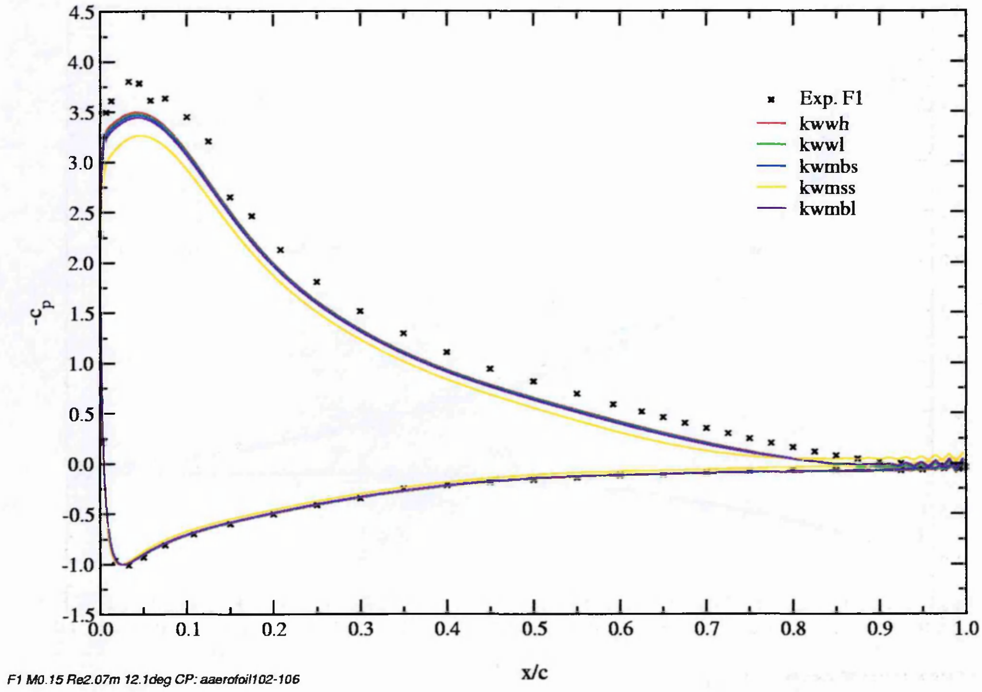

(b) Surface c_p.

Figure A.8: *A-aerofoil, M=0.15, Re=2.07 × 10^6, $\alpha = 12.1^o$, k-ω family of models. Fully turbulent calculations. Convergence and comparison of surface c_p with experiment.*

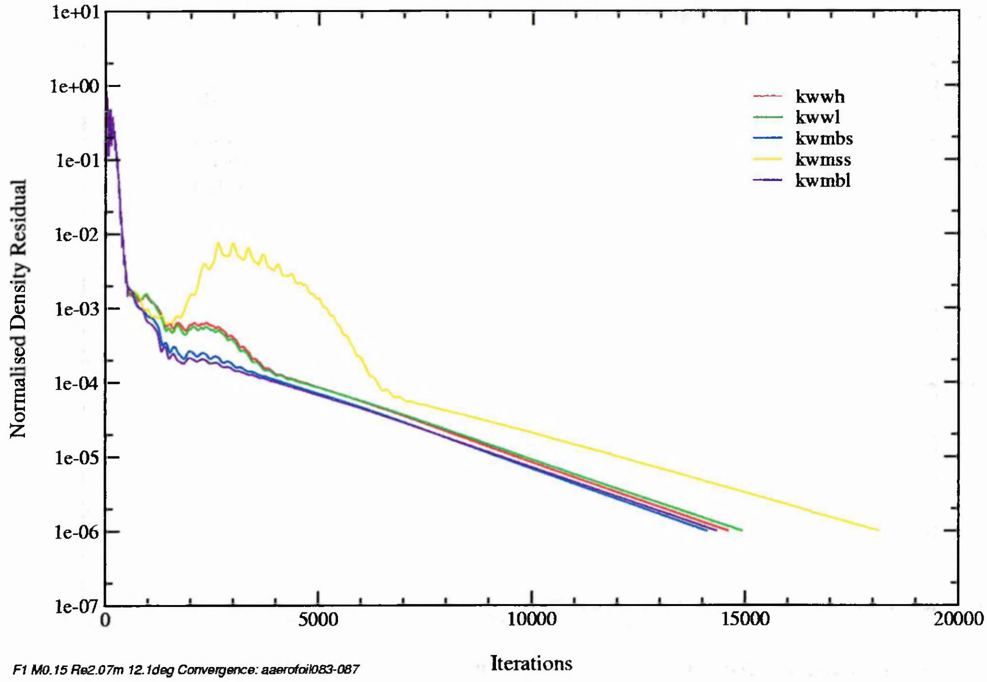

F1 M0.15 Re2.07m 12.1deg Convergence: aaerofoil083-087

(a) Convergence.

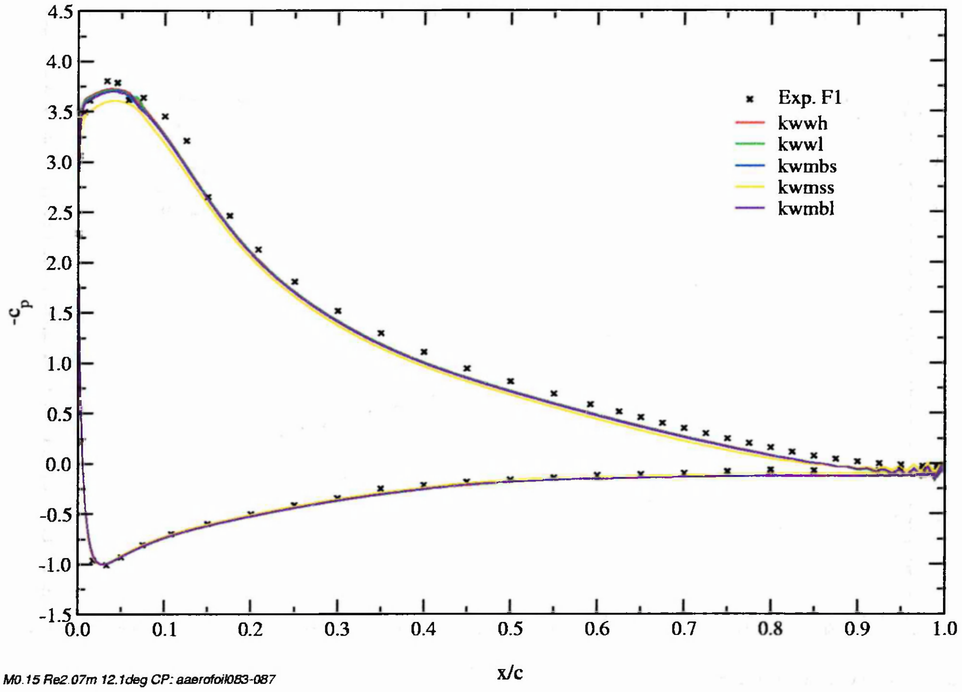

F1 M0.15 Re2.07m 12.1deg CP: aaerofoil083-087

(b) Surface c_p.

Figure A.9: *A-aerofoil, M=0.15, Re=2.07 × 10^6, $\alpha = 12.1^o$, k-ω family of models. Transition prescribed at 23%$\bar{c}$ (lower) and 5%$\bar{c}$ (upper) with a blend of 7%$\bar{c}$. Convergence and comparison of surface c_p with experiment.*

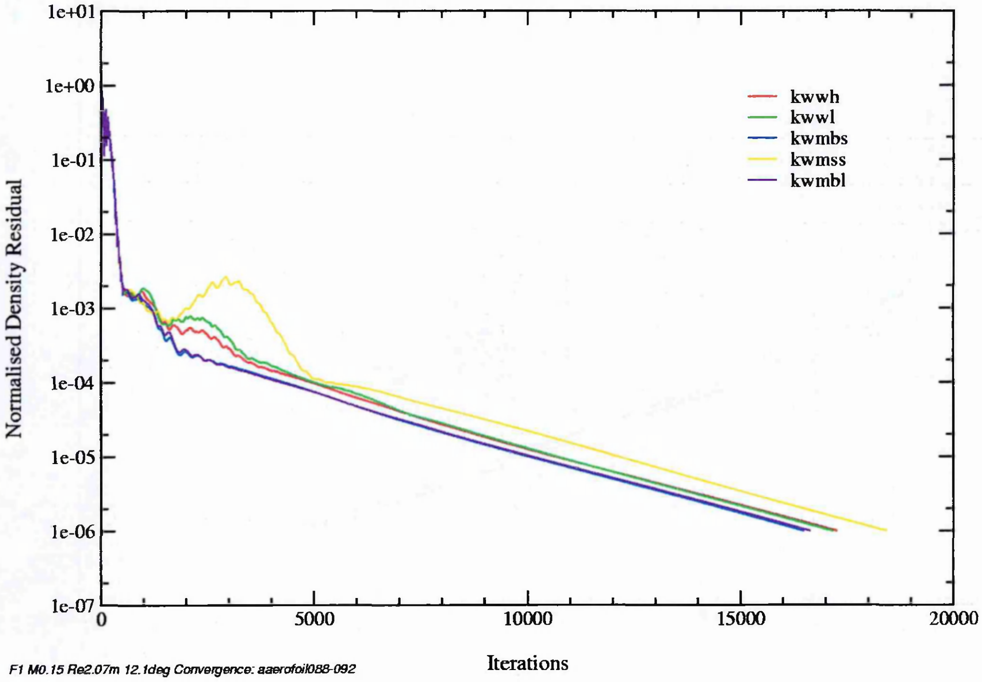

(a) Convergence.

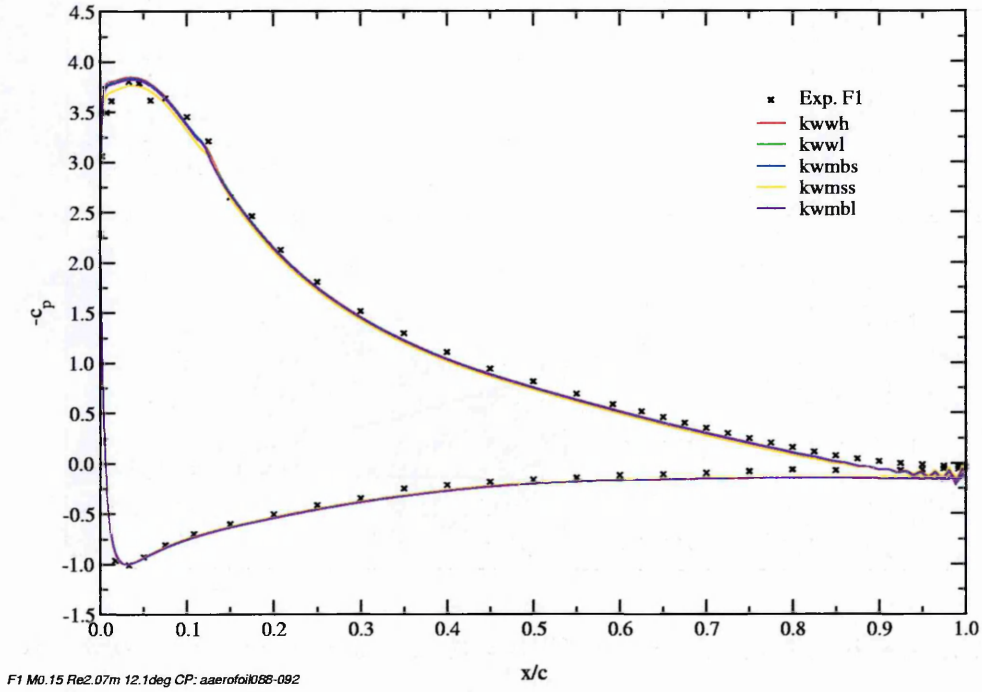

(b) Surface c_p.

Figure A.10: *A-aerofoil, M=0.15, Re=2.07×10^6, $\alpha = 12.1^o$, k-ω family of models. Transition prescribed at 30%$\bar{c}$ (lower) and 12%$\bar{c}$ (upper) with a blend of 5%$\bar{c}$. Convergence and comparison of surface c_p with experiment.*

Run no.	Convergence	Iterations	CPUsecs./It.	Turbulence model
Fully turbulent				
093	1.0×10^{-6}	15820	2.165	Spalart-Allmaras
094	1.1×10^{-3}	25000	2.332	Chien k-ε (iamortfd=-1)
099	1.9×10^{-4}	25000	2.015	Chien k-ε (default)
065	1.0×10^{-6}	14340	2.316	Standard Wilcox k-ω
066	1.0×10^{-6}	14560	2.341	Wilcox k-ω-LRN
067	1.0×10^{-6}	14920	2.518	Menter k-ω-BSL
068	7.4×10^{-3}	20000	2.551	Menter k-ω-SST
069	1.0×10^{-6}	15810	2.473	Menter k-ω-BSL-LRN
070	2.9×10^{-2}	15000	2.622	Menter k-ω-SST-LRN
Transition at 30%$\bar{c}$ (lower), 12%$\bar{c}$ (upper), 5%$\bar{c}$ blend				
095	1.0×10^{-6}	14880	2.155	Spalart-Allmaras
096	3.4×10^{-4}	25000	2.236	Chien k-ε (iamortfd=-1)
100	4.5×10^{-4}	25000	2.030	Chien k-ε (default)
071	1.0×10^{-6}	18830	2.198	Standard Wilcox k-ω
072	1.0×10^{-6}	18880	2.077	Wilcox k-ω-LRN
073	1.0×10^{-6}	17760	2.438	Menter k-ω-BSL
074	1.0×10^{-6}	20960	2.240	Menter k-ω-SST
075	1.0×10^{-6}	17930	2.221	Menter k-ω-BSL-LRN
076	1.0×10^{-6}	21060	2.277	Menter k-ω-SST-LRN
Transition at 23%$\bar{c}$ (lower), 5%$\bar{c}$ (upper), 7%$\bar{c}$ blend				
097	1.0×10^{-6}	17630	1.885	Spalart-Allmaras
098	1.9×10^{-3}	25000	2.012	Chien k-ε (iamortfd=-1)
101	3.2×10^{-3}	25000	2.011	Chien k-ε (default)
077	1.0×10^{-6}	16120	2.250	Standard Wilcox k-ω
078	1.0×10^{-6}	16470	2.284	Wilcox k-ω-LRN
079	1.0×10^{-6}	15520	2.193	Menter k-ω-BSL
080	1.0×10^{-6}	21210	2.515	Menter k-ω-SST
081	1.0×10^{-6}	15690	2.502	Menter k-ω-BSL-LRN
082	4.8×10^{-3}	20000	2.455	Menter k-ω-SST-LRN

Table A.7: *A-aerofoil, M=0.15, Re=2×10^6, α=13.3°. System performance summary.*

Run no.	Turbulence model	c_l	c_d
Fully turbulent			
093	Spalart-Allmaras	1.453	0.02888
094	Chien k-ε (iamortfd=-1)	1.695	0.02086
099	Chien k-ε (default)	1.536	0.02899
065	Standard Wilcox k-ω	1.370	0.02823
066	Wilcox k-ω-LRN	1.362	0.02801
067	Menter k-ω-BSL	1.483	0.03137
068	Menter k-ω-SST	1.316	0.05424
069	Menter k-ω-BSL-LRN	1.470	0.03129
070	Menter k-ω-SST-LRN	0.810	0.01989
Transition at 30%$\bar{c}$ (lower), 12%$\bar{c}$ (upper), 5%$\bar{c}$ blend			
095	Spalart-Allmaras	1.546	0.02321
096	Chien k-ε (iamortfd=-1)	1.475	0.02598
100	Chien k-ε (default)	1.746	0.01830
071	Standard Wilcox k-ω	1.602	0.01965
072	Wilcox k-ω-LRN	1.594	0.01950
073	Menter k-ω-BSL	1.597	0.01998
074	Menter k-ω-SST	1.540	0.01991
075	Menter k-ω-BSL-LRN	1.589	0.01982
076	Menter k-ω-SST-LRN	1.444	0.02287
Transition at 23%$\bar{c}$ (lower), 5%$\bar{c}$ (upper), 7%$\bar{c}$ blend			
097	Spalart-Allmaras	1.612	0.01976
098	Chien k-ε (iamortfd=-1)	1.534	0.04212
101	Chien k-ε (default)	1.290	0.03692
077	Standard Wilcox k-ω	1.515	0.02261
078	Wilcox k-ω-LRN	1.504	0.02241
079	Menter k-ω-BSL	1.505	0.02324
080	Menter k-ω-SST	1.430	0.02331
081	Menter k-ω-BSL-LRN	1.496	0.02303
082	Menter k-ω-SST-LRN	1.240	0.00097
	Experiment, F2 data	1.515	0.03078
	Experiment, F1 data (interpolated)	1.55-1.575	0.0208-0.0212

Table A.8: *A-aerofoil, M=0.15, Re=2×10^6, α=13.3^o. Comparison of calculated lift- and drag coefficients.*

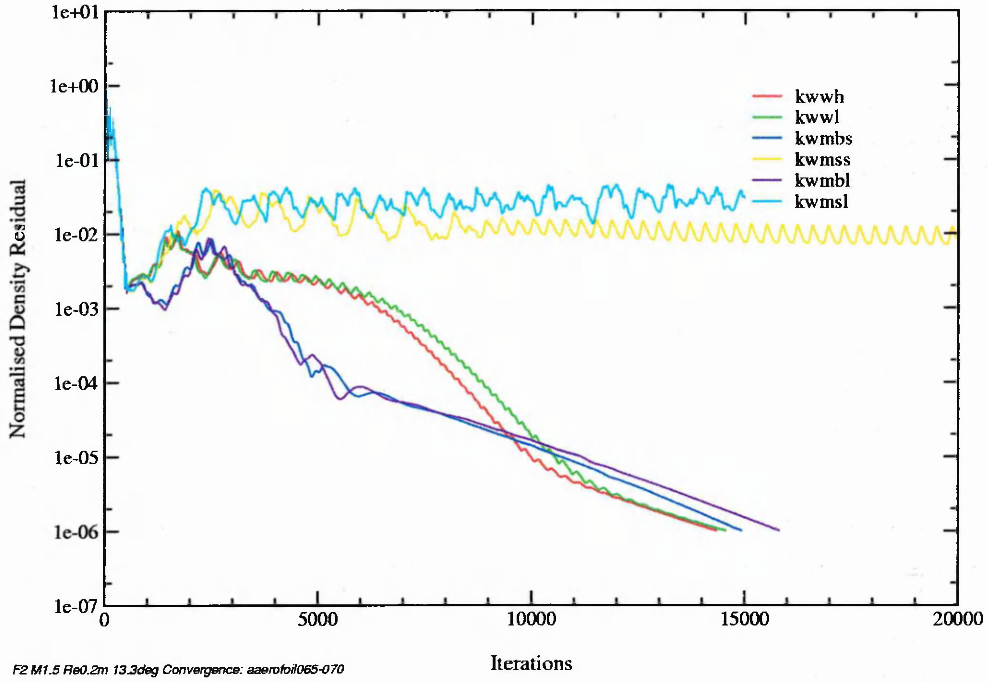

F2 M1.5 Re0.2m 13.3deg Convergence: aaerofoil065-070

(a) Convergence.

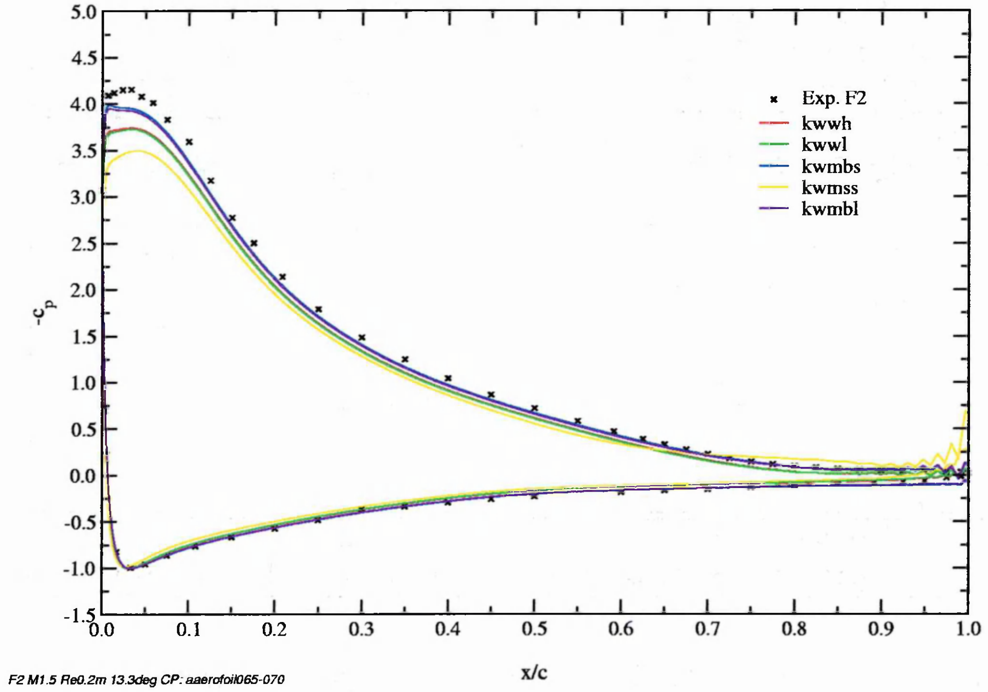

F2 M1.5 Re0.2m 13.3deg CP: aaerofoil065-070

(b) Surface c_p.

Figure A.11: *A-aerofoil, M=0.15, Re=2 × 10^6, $\alpha = 13.3^o$. Fully turbulent calculation. Convergence and comparison of surface c_p with experiment.*

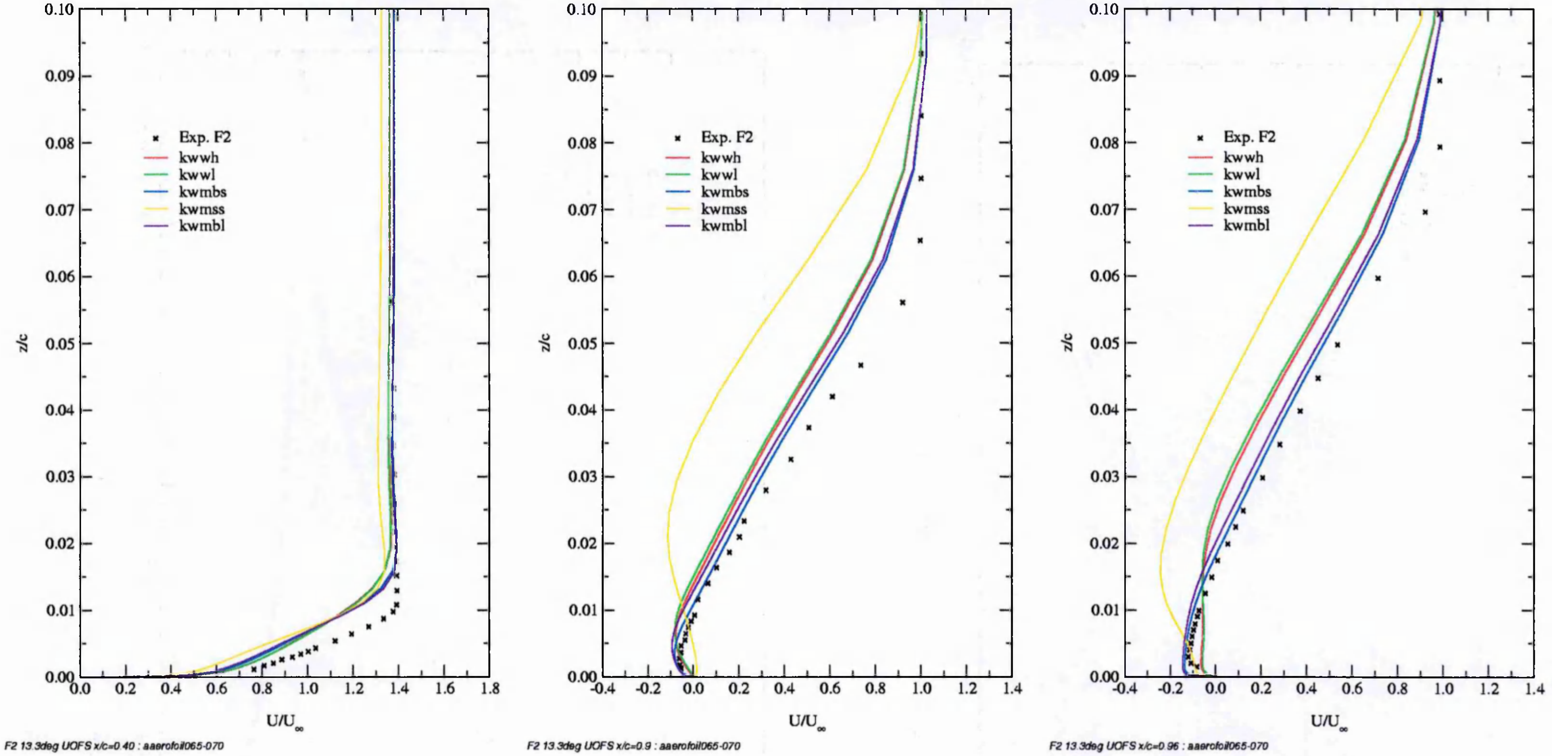

(a) x/c=0.40 **(b)** x/c=0.90 **(c)** x/c=0.96

Figure A.12: *A-aerofoil, M=0.15, Re=2 × 10^6, $\alpha = 13.3^o$. Fully turbulent calculation. Comparison of boundary-layer velocity profiles with experiment.*

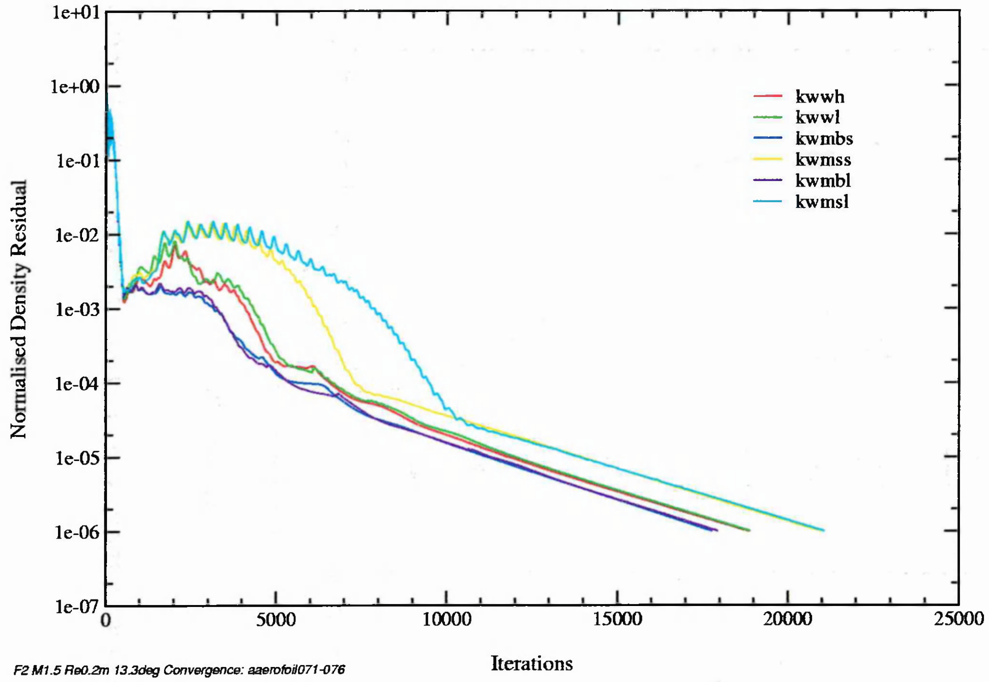

(a) Convergence.

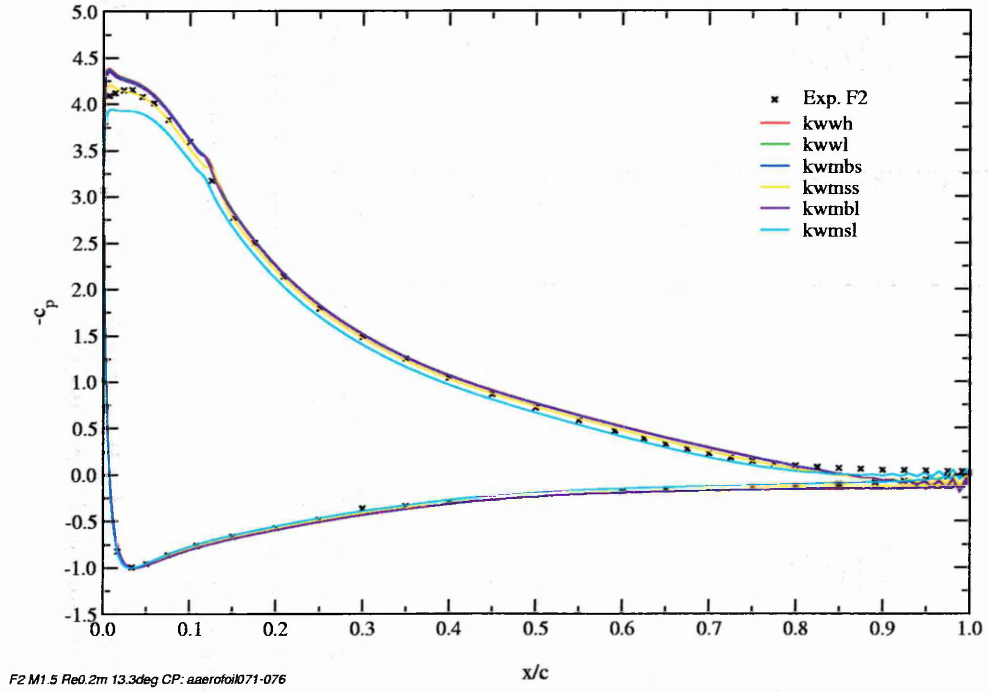

(b) Surface c_p.

Figure A.13: *A-aerofoil, M=0.15, Re=2×10^6, $\alpha = 13.3^o$. Transition prescribed at 30%$\bar{c}$ (lower) and 12%$\bar{c}$ (upper) with a blending region of 5%$\bar{c}$. Convergence and comparison of surface c_p with experiment.*

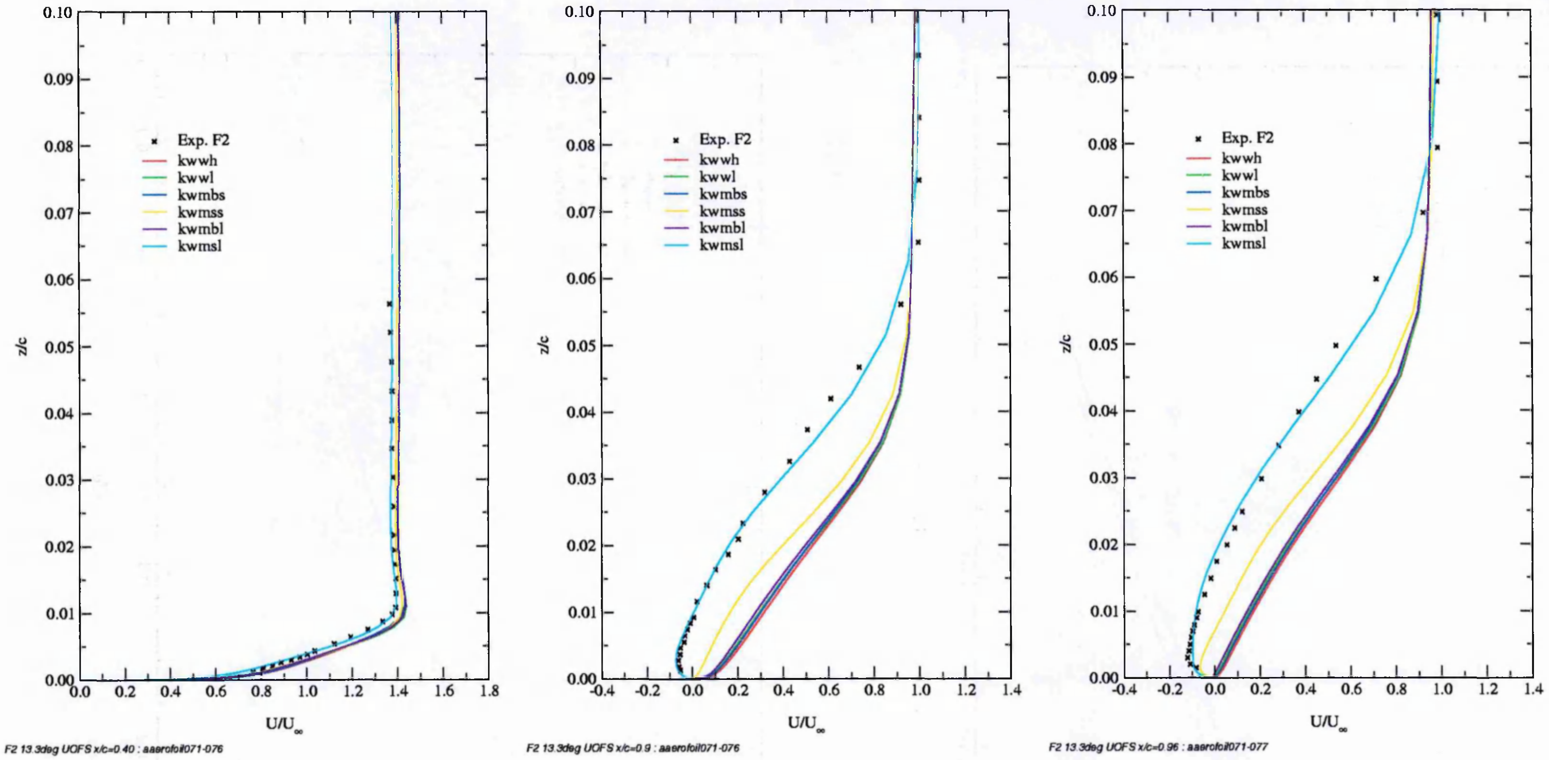

(a) x/c=0.40

(b) x/c=0.90

(c) x/c=0.96

Figure A.14: *A-aerofoil,* M*=*0.15*,* Re*=*2×10^6*,* $\alpha = 13.3^o$*. Transition prescribed at 30%*$\bar{c}$ *(lower) and 12%*$\bar{c}$ *(upper) with a blending region of 5%*$\bar{c}$*. Comparison of boundary-layer velocity profiles with experiment.*

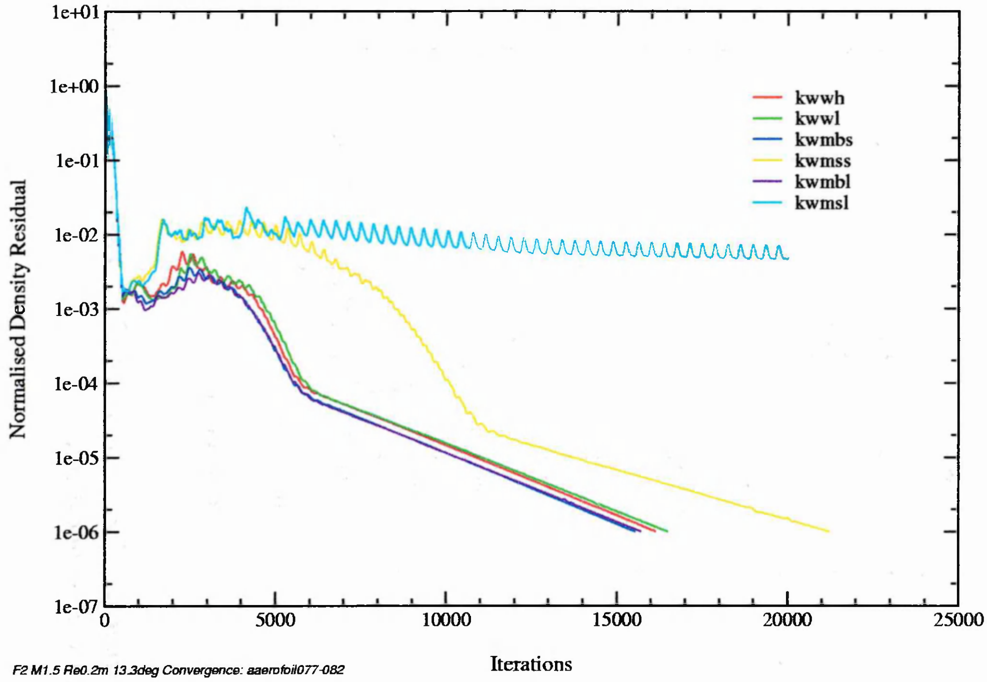

F2 M1.5 Re0.2m 13.3deg Convergence: aaerofoil077-082

(a) Convergence.

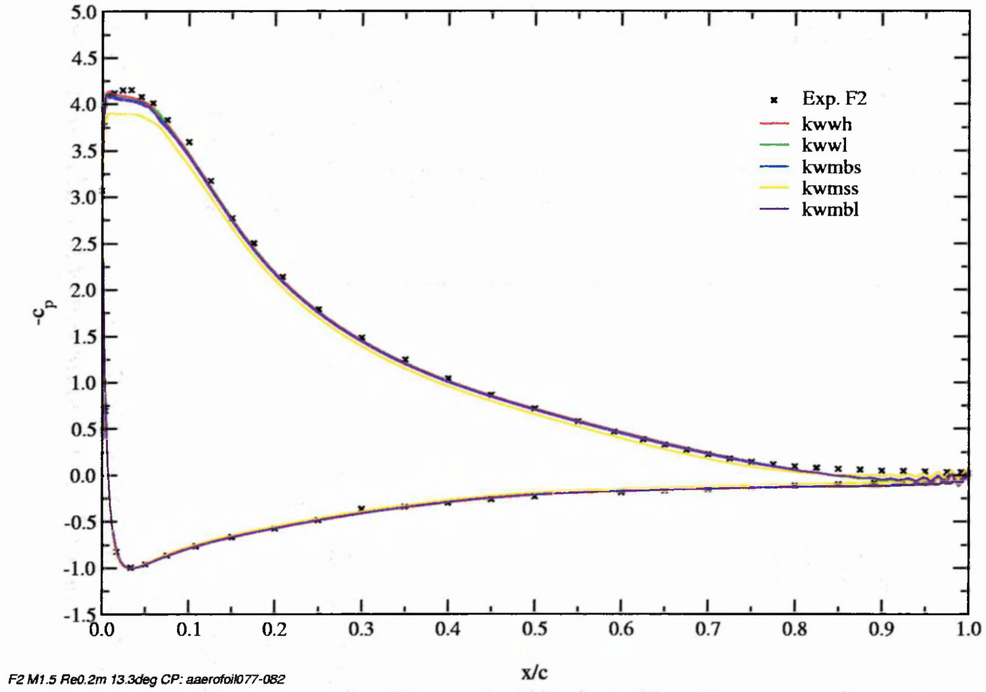

F2 M1.5 Re0.2m 13.3deg CP: aaerofoil077-082

(b) Surface c_p.

Figure A.15: *A-aerofoil, M=0.15, Re=2 × 10^6, $\alpha = 13.3^o$. Transition prescribed at 23%$\bar{c}$ (lower) and 5%$\bar{c}$ (upper) with a blending region of 7%$\bar{c}$. Convergence and comparison of surface c_p with experiment.*

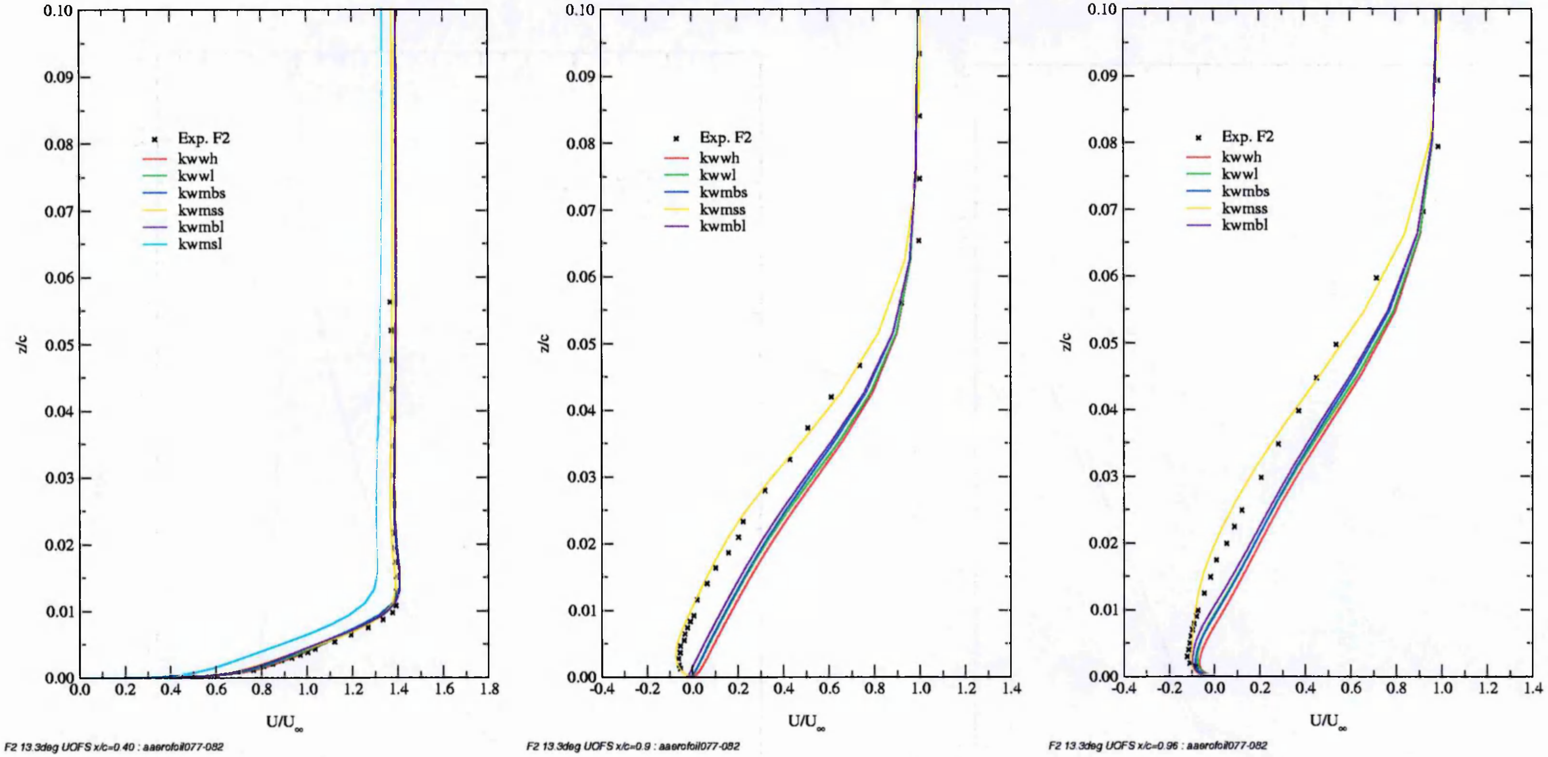

(a) x/c=0.40 (b) x/c=0.90 (c) x/c=0.96

Figure A.16: *A-aerofoil, M=0.15, Re=2×10^6, $\alpha = 13.3^o$. Transition prescribed at 23%$\bar{c}$ (lower) and 5%$\bar{c}$ (upper) with a blending region of 7%$\bar{c}$. Comparison of boundary-layer velocity profiles with experiment.*

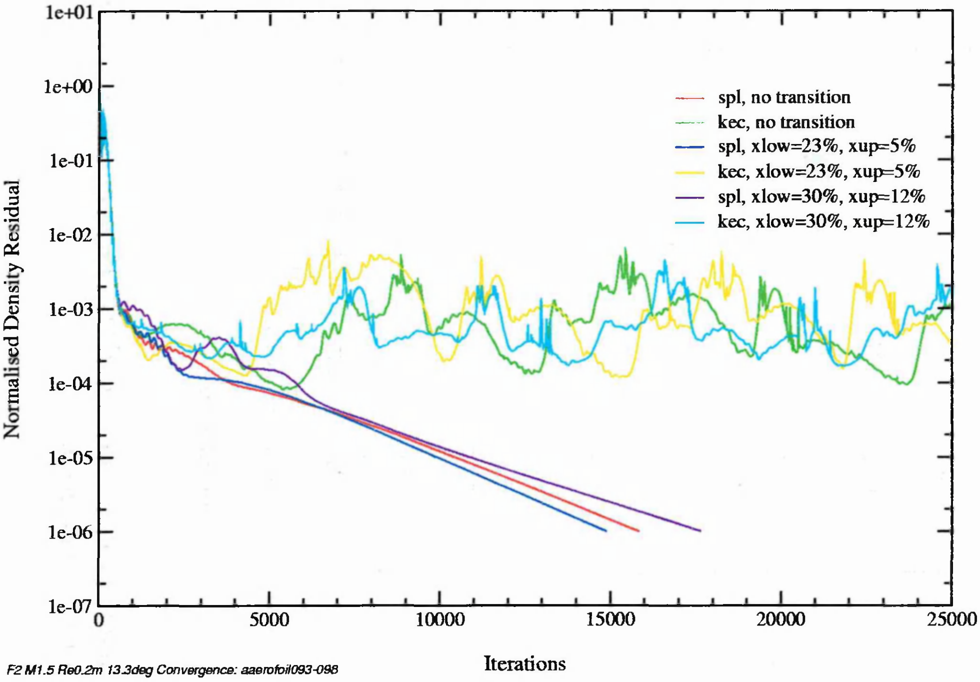

F2 M1.5 Re0.2m 13.3deg Convergence: aaerofoil093-098

(a) Convergence.

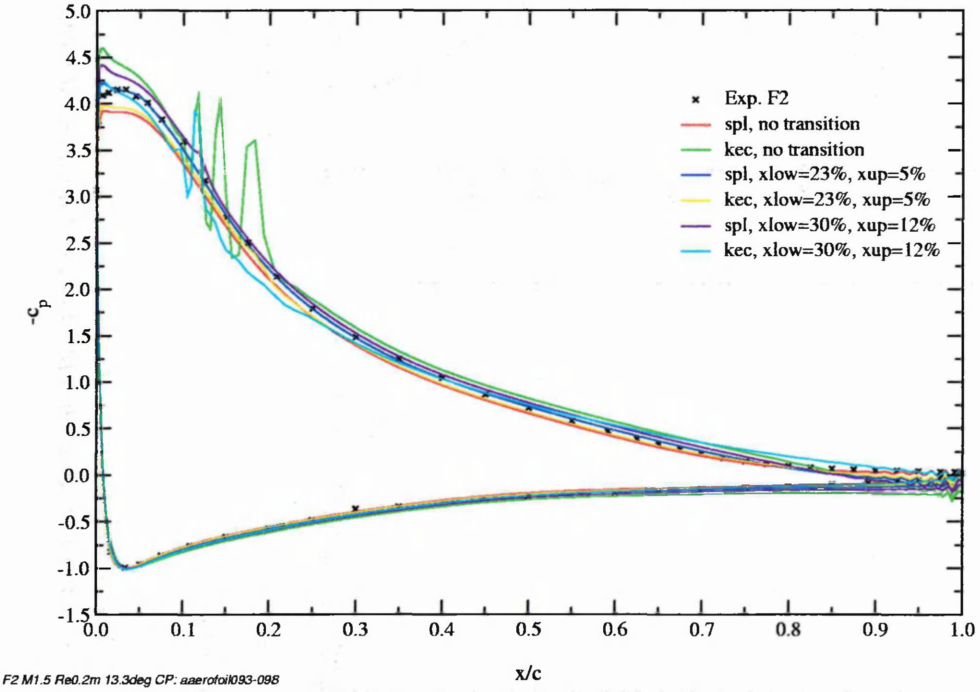

F2 M1.5 Re0.2m 13.3deg CP: aaerofoil093-098

(b) Surface c_p.

Figure A.17: *A-aerofoil, M=0.15, Re=2 × 10^6, $\alpha = 13.3^o$. Existing turbulence models, convergence and comparison of surface c_p with experiment.*

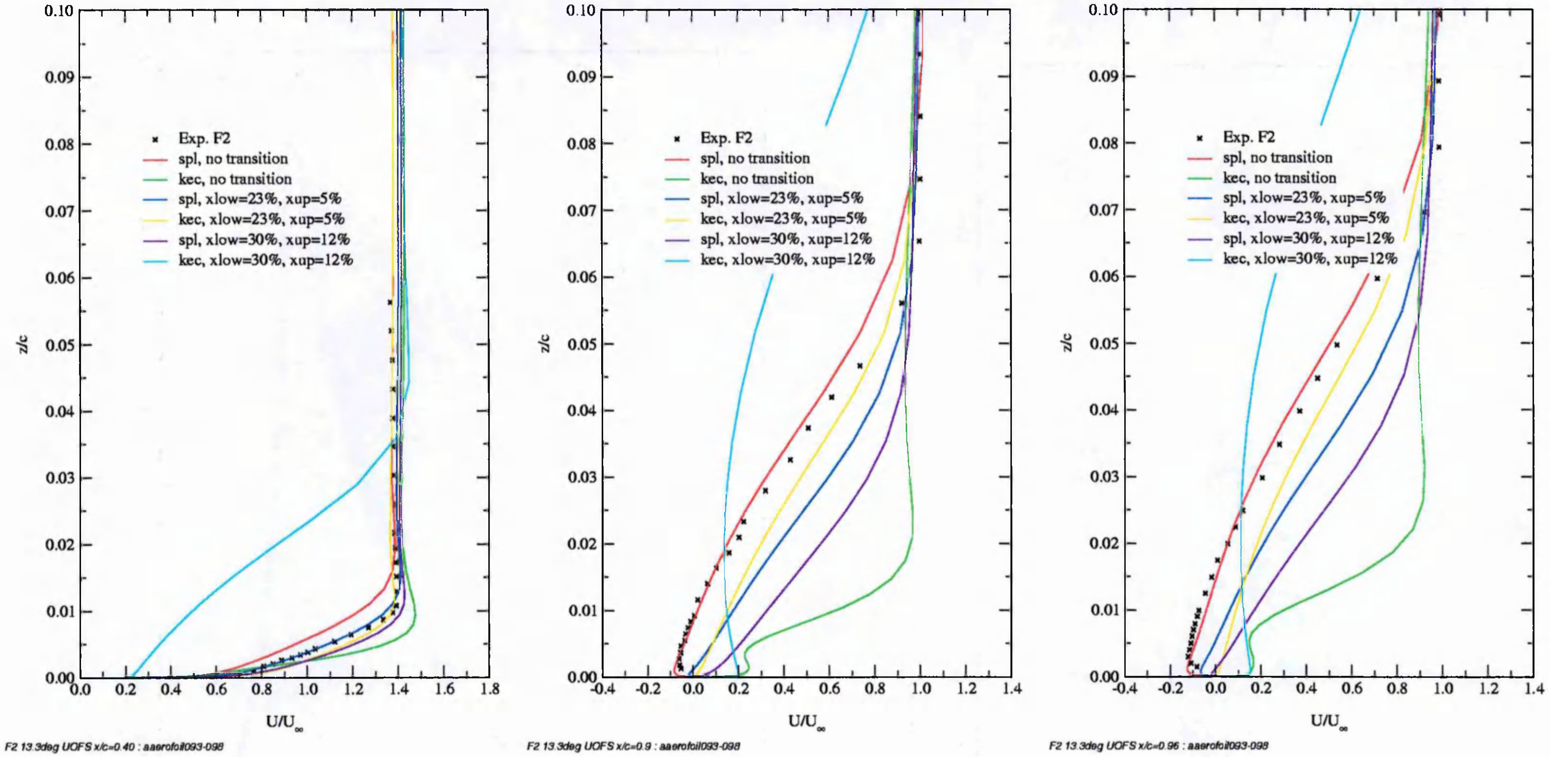

(a) x/c=0.40 **(b)** x/c=0.90 **(c)** x/c=0.96

Figure A.18: *A-aerofoil, M=0.15, Re=2 × 10^6, α = 13.3°. Existing turbulence models, comparison of boundary-layer velocity profiles with experiment. k-ε calculations run with adtbeq1=-1 (no pressure sensor).*

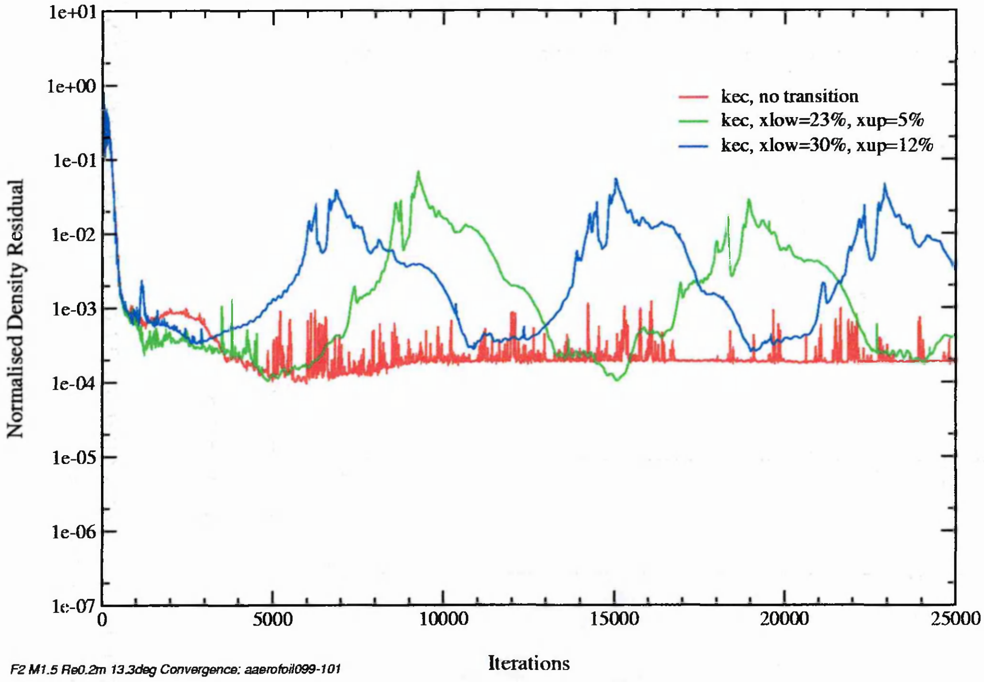

F2 M1.5 Re0.2m 13.3deg Convergence: aaerofoil099-101

(a) Convergence.

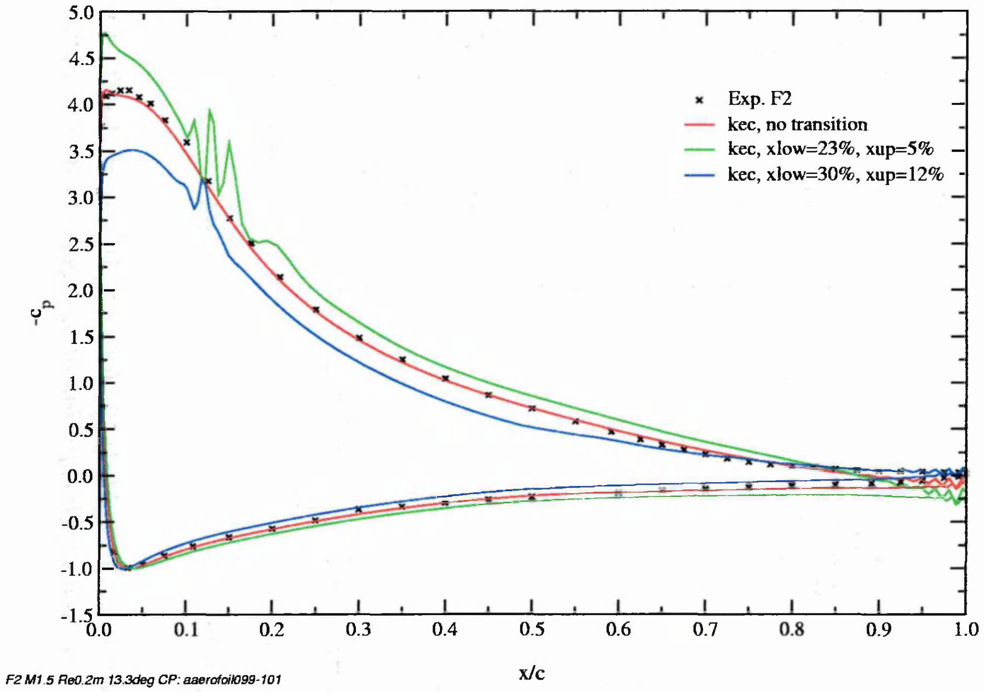

F2 M1.5 Re0.2m 13.3deg CP: aaerofoil099-101

(b) Surface c_p.

Figure A.19: *A-aerofoil, M*=0.15, *Re*=2×10^6, $\alpha = 13.3^o$. *Existing turbulence models, convergence and comparison of surface* c_p *with experiment.*

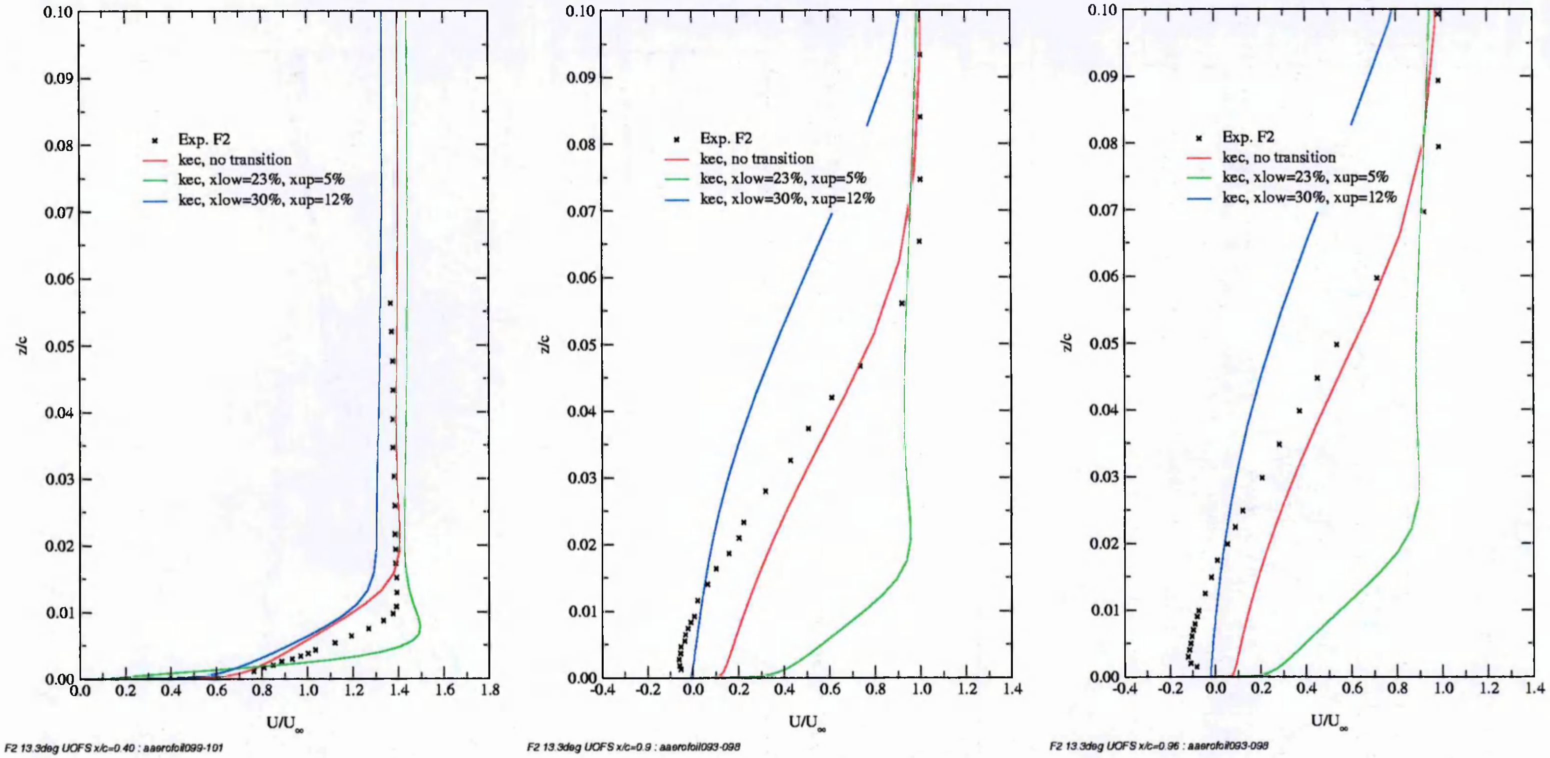

(a) x/c=0.40

(b) x/c=0.90

(c) x/c=0.96

Figure A.20: *A-aerofoil, M=0.15, Re=2 $\times$ 10^6, α = 13.3°. Existing turbulence models, comparison of boundary-layer velocity profiles with experiment. k-ε model run with default parameters.*

A.3 RAE2822 Aerofoil

A.3.1 Grid & boundary conditions

The RAE2822 aerofoil provides a suitable transonic aerofoil testcase. An extensive experimental database is available, [12], covering a range of flow conditions and incidences, with *case 9* being chosen for validation purposes. Freestream and boundary conditions are shown in Tables (A.9) & (A.10) with the 256 × 64 × 2 cell, C-type aerofoil mesh shown as Fig.(A.21). This mesh has previously been used successfully for turbulence model validation by Haase [37], in the Euroval program, and Duquesne [21]. Note that the corrected case 9 flow conditions as recommended for the Euroval project have been slightly altered as suggested by Hellström, [45].

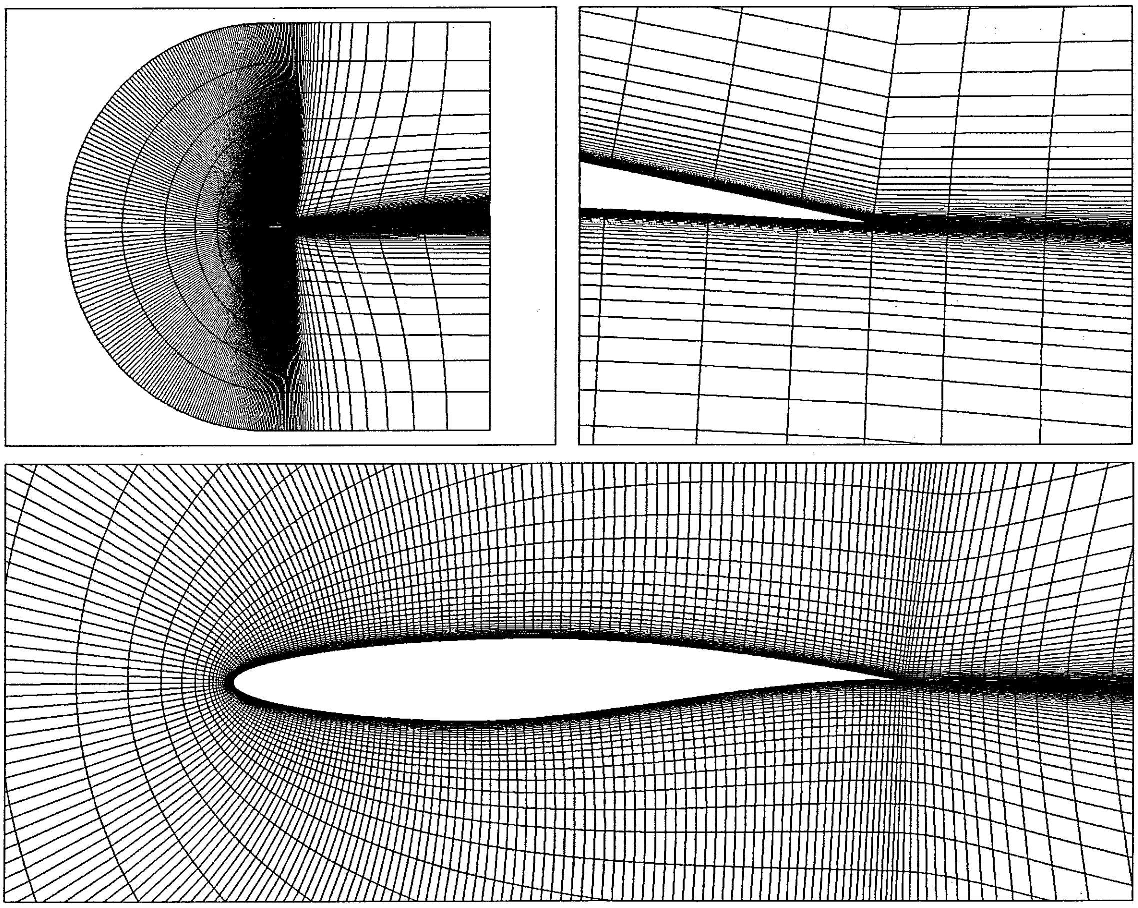

Figure A.21: *RAE2822 aerofoil grid,* 256 × 64 × 2 *cells.*

	Experiment	Euroval	Hellström
Mach no.	0.730	0.734	0.734
Re/m	6.5×10^6	6.5×10^6	6.5×10^6
α	3.19°	2.54°	2.79°

***Table A.9:** RAE2822 aerofoil, case 9, freestream conditions.*

Face	Location	b.c.	Type	i	j	k
1	exit (bottom)	131	characteristic variables	1	1 to 64	1
2	exit (top)	131	characteristic variables	256	1 to 64	1
3	wake (bottom)	500	block connectivity	1 to 24	1	1
	aerofoil	300	solid adiabatic wall	25 to 232	1	1
	wake (top)	500	block connectivity	233 to 256	1	1
4	farfield	131	characteristic variables	1 to 256	64	1
5	right side	413	mirror w-velocity	1 to 256	1 to 64	1
6	left side	413	mirror w-velocity	1 to 256	1 to 64	2

***Table A.10:** Boundary conditions for the RAE2822 aerofoil.*

A.3.2 Computational details

As before, all computations were run on a single 195MHz R10000 processor on an SGI Octane workstation equipped with 1Gb RAM. All results shown below were generated using the matrix LU-SGS algorithm. The standard central spatial discretisation was selected for all calculations and all other numerical parameters were held constant. The Hoffman k-ε model was not used. CFL number was initially set at 0.3 with an increase factor each time-step of 1.02 up to a maximum of 1×10^9. Transition was specified at $0.3\%\bar{c}$ on both upper and lower surfaces of the aerofoil using the NSMB trans.dat file.

A sample NSMB input file for the RAE2822 validation case is included below.

```
# database, I/O
#
database       : rae2822-5.db
init flag      : 0
output flag    : 1
print flag     : 1
solution in    : 0
solution out   : 3
title          : RAE2822 Case 9
comment        : Matrix-implicit central 2eq-kwmbs, indiv. klim & wlim updating
#
# physical problem description
#
unsteady  : 0
gas model : 1
flow model: 2eq-kwmbs
```

```
#
# flow parameters
#
mach                 : 0.734
rho infinity         : 1.
pressure infinity    : 1.
#temperature infinity: 288.2
gamma                : 1.4
gas constant         : 1.
alpha                : 0.
beta                 : 2.79
Reynolds             : 6.5E6
prandtl              : 0.72
viscosity model      : sutherl
#
# general turbulence parameters
#
prte               : 0.9
cf0                : 0.005
myt/my max         : 5000.
wall distance flag: 1
pointwise implicit: implicit
transition flag    : 1
#
# temporal/spatial schemes
#
time scheme            : implicit
space scheme           : central
implicit approximation: matrix
cfl                    : 0.3
cfl increase factor    : 1.02
cfl end                : 1.e9
#
# artificial dissipation (central spatial discretisation)
#
dissipation model      : standard
dis2I                  : 0.5
dis2J                  : 0.5
dis2K                  : 0.5
dis4                   : 0.015
damping model          : 0
damping order          : 0
#
# steady-state/inner time-stepping loop
#
nsteps                  : 10000
db resultinterval       : 200000
residual interval inner: 10
tolerance               : 1.e-6
```

A.3.3 Results

Run no.	Turbulence model	c_l	c_d
001	Spalart-Allmaras	0.799	0.0217
002	Chien k-ε	0.799	0.0230
020	Standard Wilcox k-ω	0.800	0.0241
021	LRN Wilcox k-ω	0.801	0.0241
022	Menter k-ω-BSL	0.760	0.0216
023	Menter k-ω-SST	0.719	0.0196
024	LRN Menter k-ω-BSL	0.760	0.0214
025	LRN Menter k-ω-SST	NaN	NaN
	Experiment	0.794	0.0166

Table A.11: *RAE2822 aerofoil case 9. Calculated lift- and drag coefficients.*

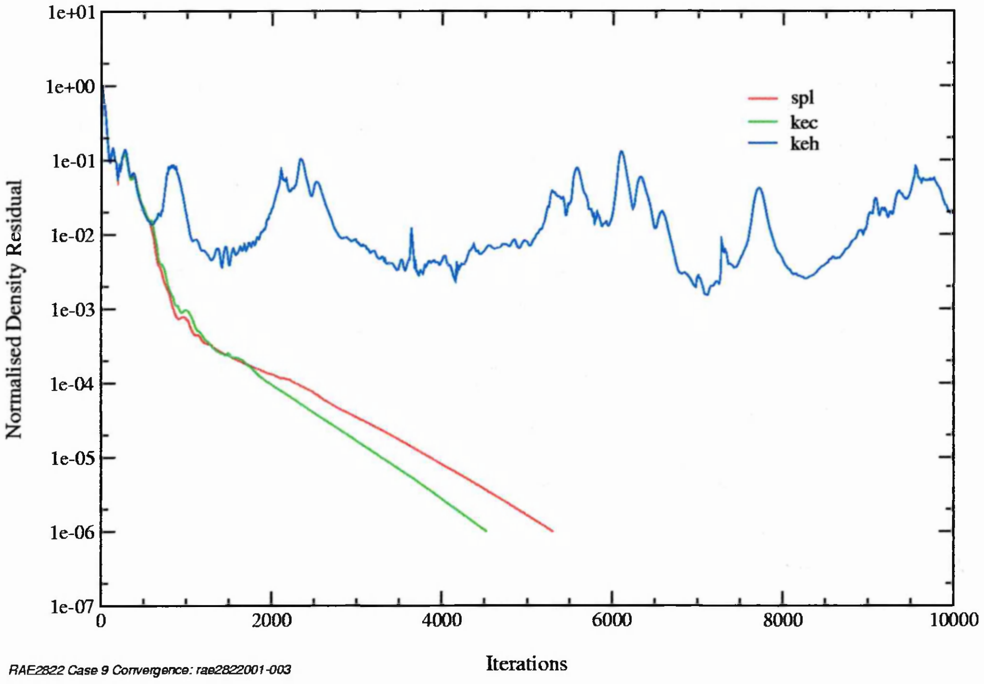

(a) Convergence.

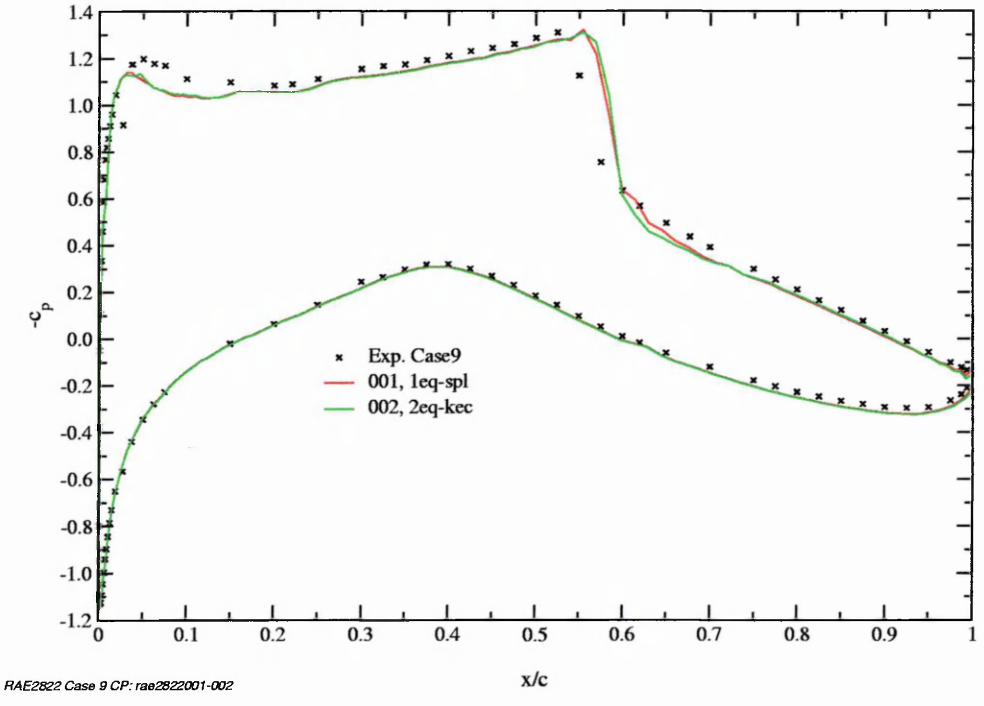

(b) Surface c_p.

Figure A.22: *RAE2822 aerofoil Case 9,* M=0.734, Re=6.5 $\times$ 10^6, $\alpha = 2.79^o$. *Existing turbulence models, convergence and comparison of surface* c_p *with experiment.*

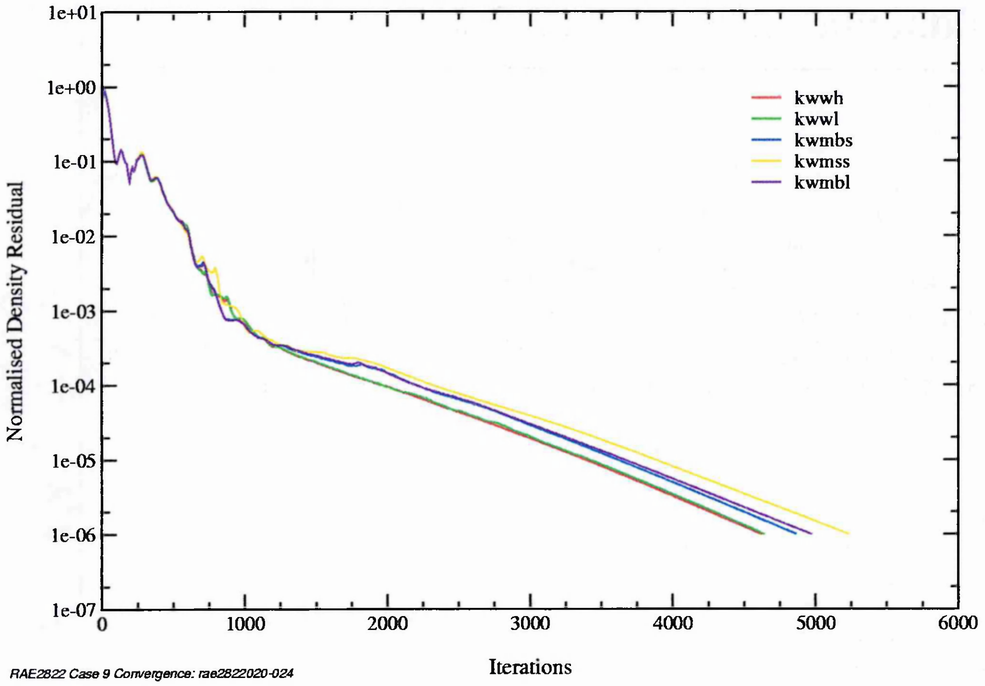

RAE2822 Case 9 Convergence: rae2822020-024

(**a**) Convergence.

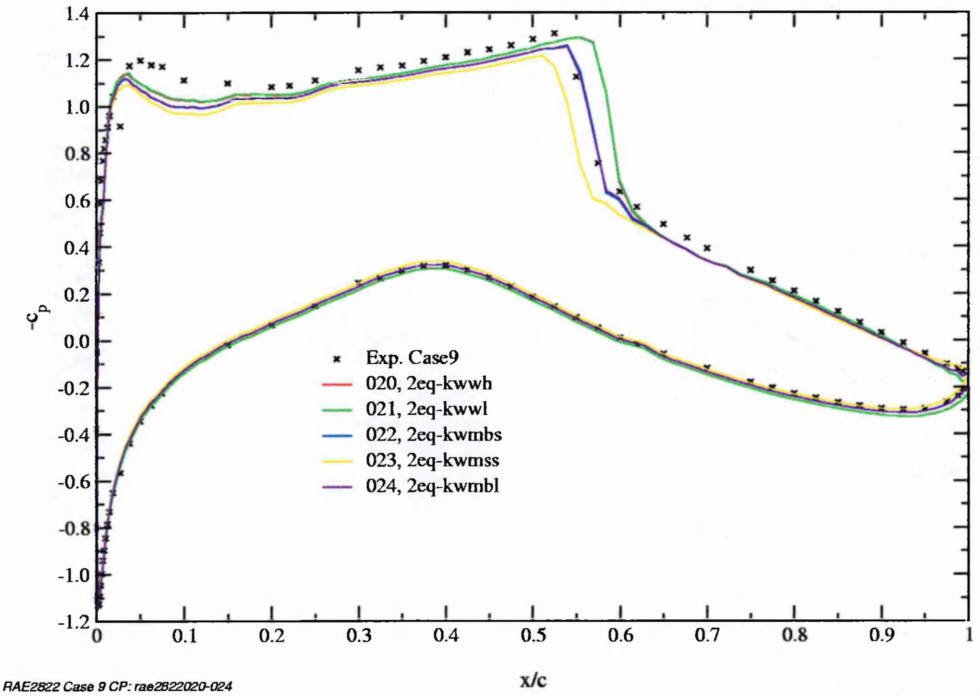

RAE2822 Case 9 CP: rae2822020-024

(**b**) Surface c_p.

Figure A.23: *RAE2822 aerofoil Case 9,* M=0.734, Re=6.5 × 10^6, $\alpha = 2.79^o$. *k-ω family of turbulence models, convergence and comparison of surface c_p with experiment.*

B. Additional Clean JAS-39 Data

This appendix contains additional information pertaining to computations made on the clean JAS-39 forebody, without the rhino-horn device. Following a sample input file, convergence history and circumferential C_p comparisons are included for the Spalart-Allmaras model and four variants of the k-ω models at $\alpha = 0^o$ and $\alpha = 40^o$.

```
# database, I/O
database      : jas39-pitot2-3.db
init flag     : 0
output flag   : 1
print flag    : 1
solution in   : 0
solution out  : 1
#loadbalancing: file
title         : Jas39 pitot2
comment       : Implicit central kwmss, no preconditioning
#
# physical problem description
#
unsteady   : 0
gas model  : 1
flow model: 2eq-kwmss
#
# flow parameters
#
mach                    : 0.176
rho infinity            : 1.225
pressure infinity       : 101325
temperature infinity: 288.2
gamma                   : 1.4
gas constant            : 287.0
alpha                   : 0.0
beta                    : 0.0
Reynolds                : 4058823
prandtl                 : 0.72
viscosity model         : sutherl
#
# general turbulence parameters
#
prte                 : 0.9
cf0                  : 0.005
myt/my max           : 5000.
```

```
#wall distance flag: 1
pointwise implicit: implicit
transition flag   : 0
#
# preconditioning
#
preconditioner flag : 0
#
# temporal/spatial schemes
#
time scheme            : implicit
space scheme           : central
implicit approximation: scalar
cfl                    : 0.5
cfl increase factor    : 1.002
cfl end                : 1.e3
#
# artificial dissipation (central spatial discretisation)
#
dissipation model      : standard
dis2I                  : 0.00
dis2J                  : 0.00
dis2K                  : 0.00
dis4                   : 0.03
damping model          : 0
damping order          : 0
#
# steady-state/inner time-stepping loop
#
nsteps                  : 4000
db resultinterval       : 100000
residual interval inner: 10
tolerance               : 1.e-6
```

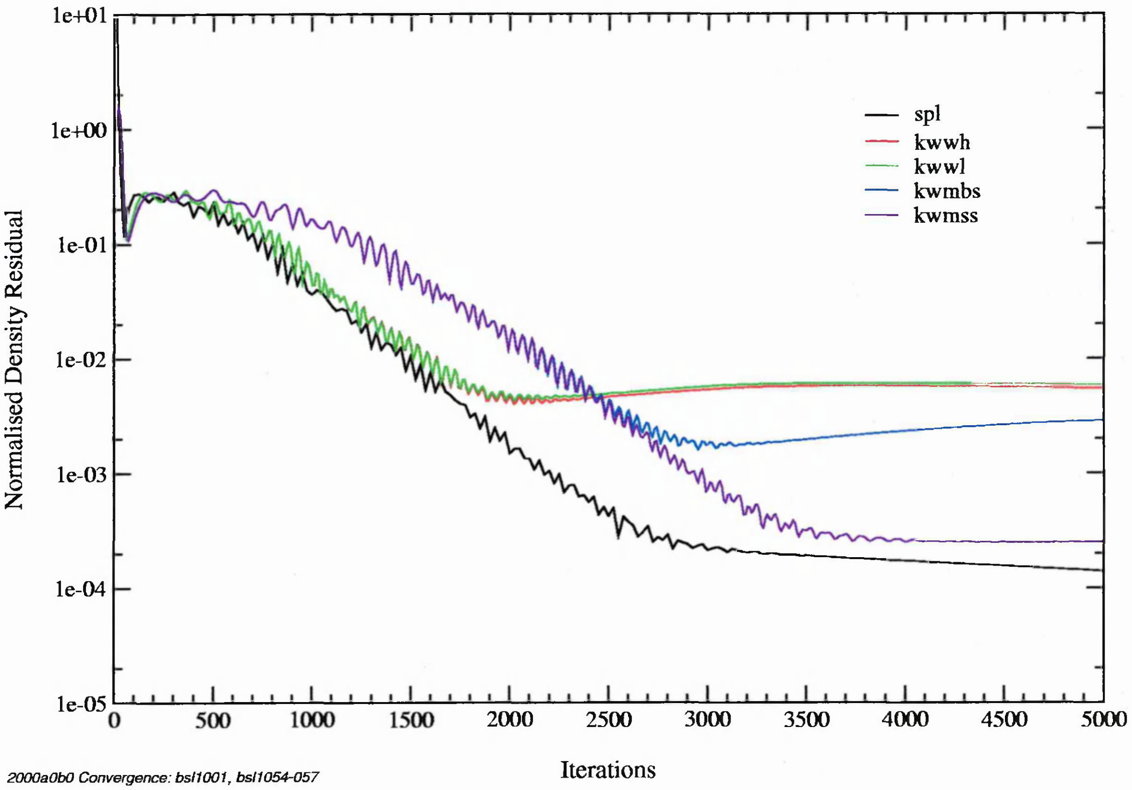

2000a0b0 Convergence: bsl1001, bsl1054-057

Figure B.1: *JAS-39 grid bsl1, M=0.176, Re=4.06$\times 10^6$, α=0°. Comparison of turbulence model density residual convergence history.*

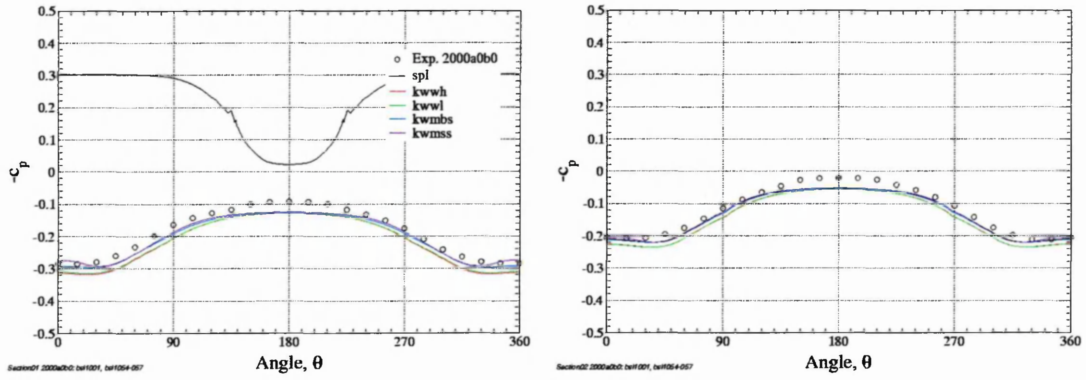

(a) Section 01

(b) Section 02

Figure B.2: *JAS-39 grid bsl1, M=0.176, Re=4.06 × 10^6, α=0°. Circumferential c_p distributions, sections 01 & 02. Comparison of turbulence models.*

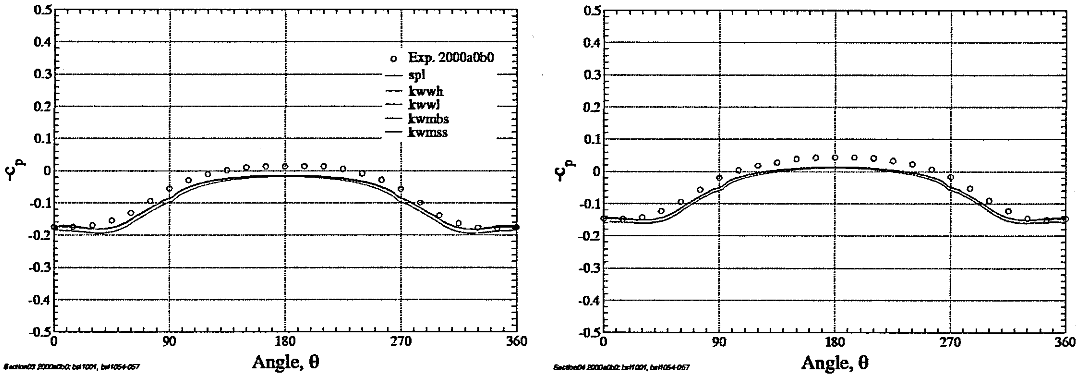

(a) Section 03

(b) Section 04

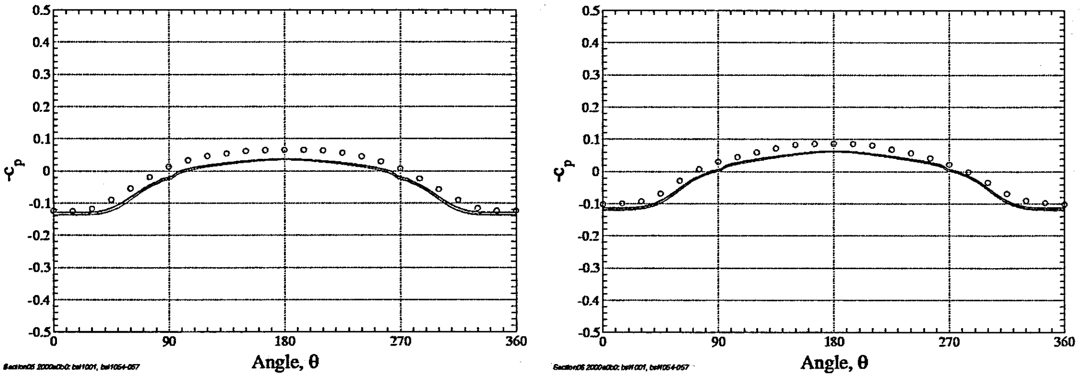

(c) Section 05

(d) Section 06

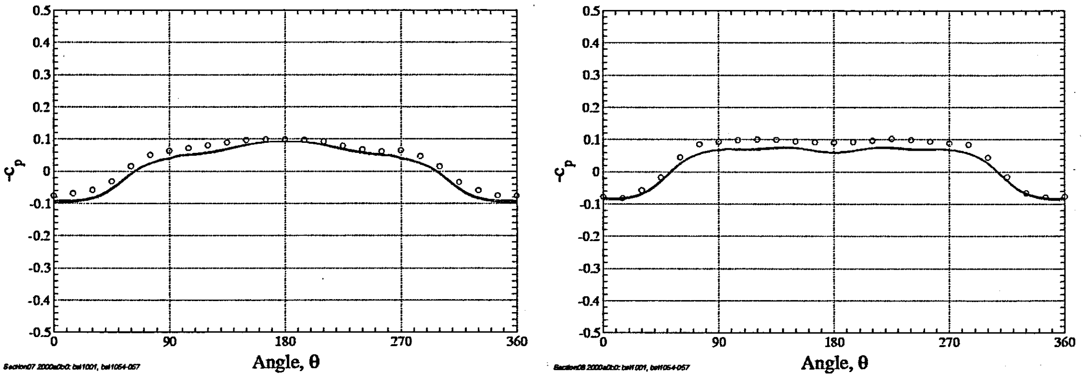

(e) Section 07

(f) Section 08

Figure B.3: *JAS-39 grid bsl1, M=0.176, Re=4.06 × 10^6, α=0°. Circumferential c_p distributions, sections 03-08. Comparison of turbulence models.*

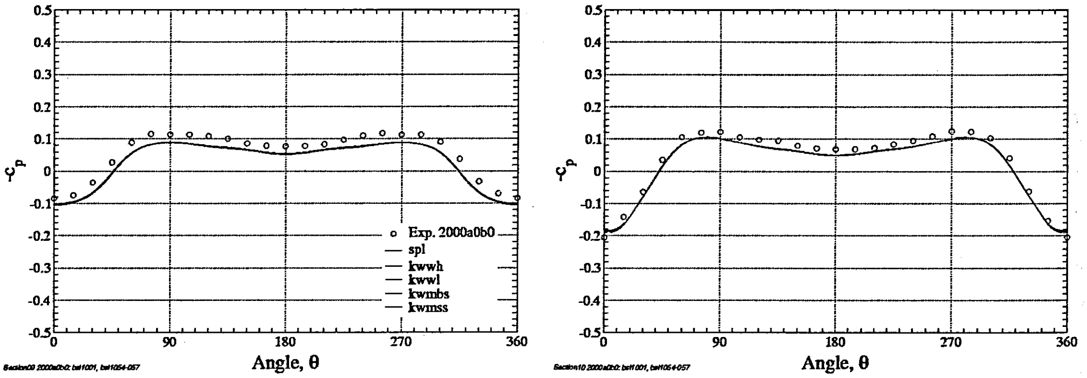

(a) Section 09 (b) Section 10

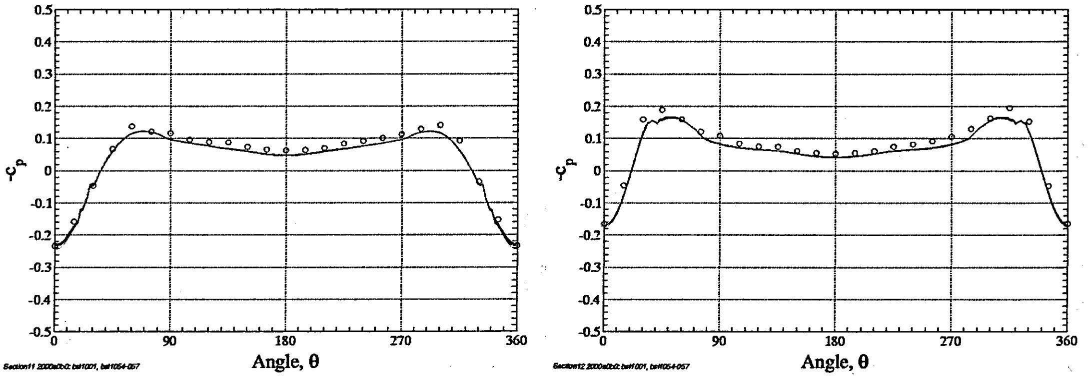

(c) Section 11 (d) Section 12

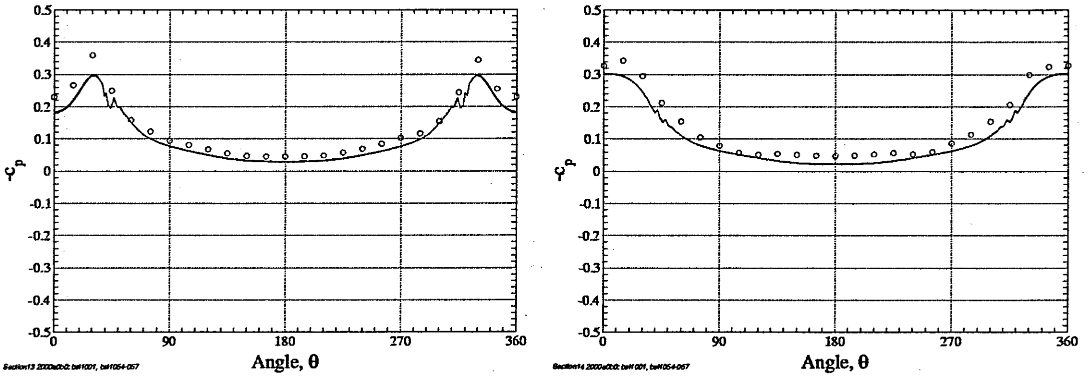

(e) Section 13 (f) Section 14

Figure B.4: *JAS-39 grid bsll, M=0.176, Re=4.06 × 10^6, α=0°. Circumferential c_p distributions, sections 09-14. Comparison of turbulence models.*

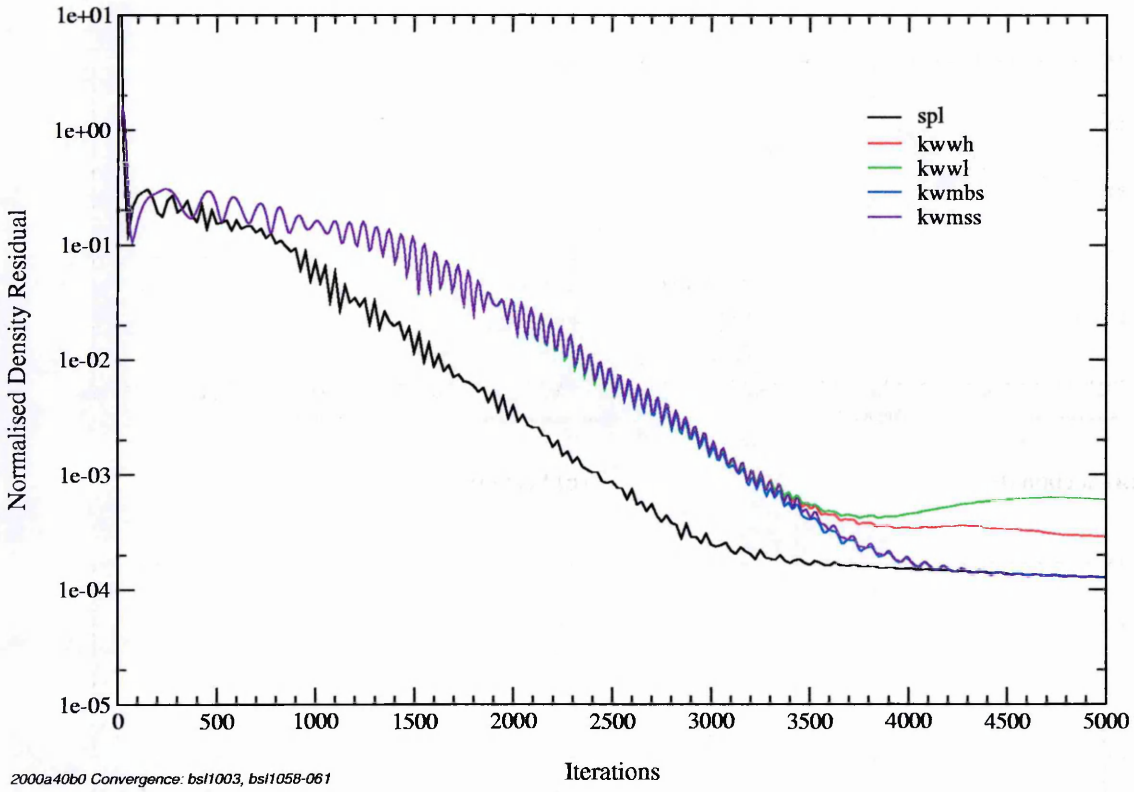

2000a40b0 Convergence: bsl1003, bsl1058-061

Figure B.5: *JAS-39 grid bsl1, M=0.176, Re=4.06 × 10^6, α=40°. Comparison of turbulence model density residual convergence history.*

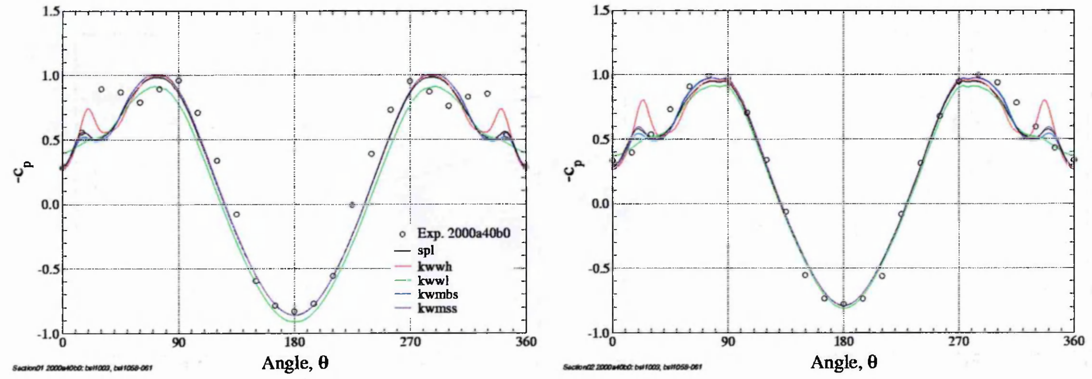

Section01 2000a40b0: bsl1003, bsl1058-061

Section02 2000a40b0: bsl1003, bsl1058-061

(a) Section 01

(b) Section 02

Figure B.6: *JAS-39 grid bsl1, M=0.176, Re=4.06 × 10^6, α=40°. Circumferential c_p distributions, sections 01 & 02. Comparison of turbulence models.*

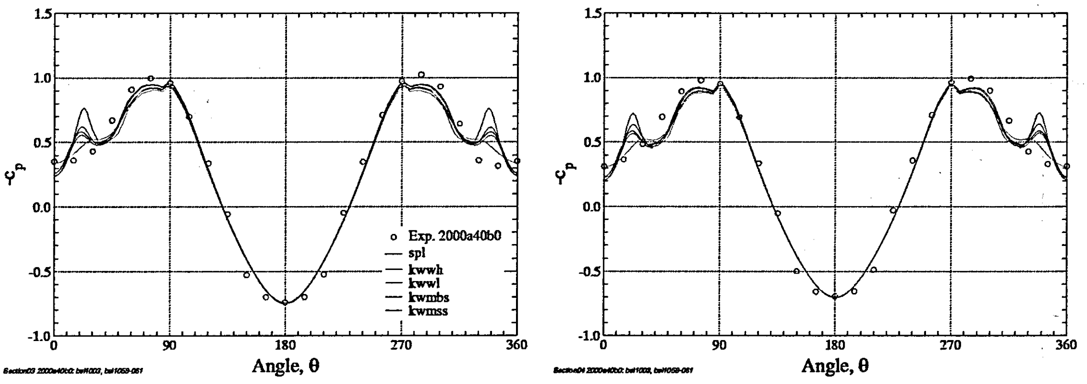

(a) Section 03 (b) Section 04

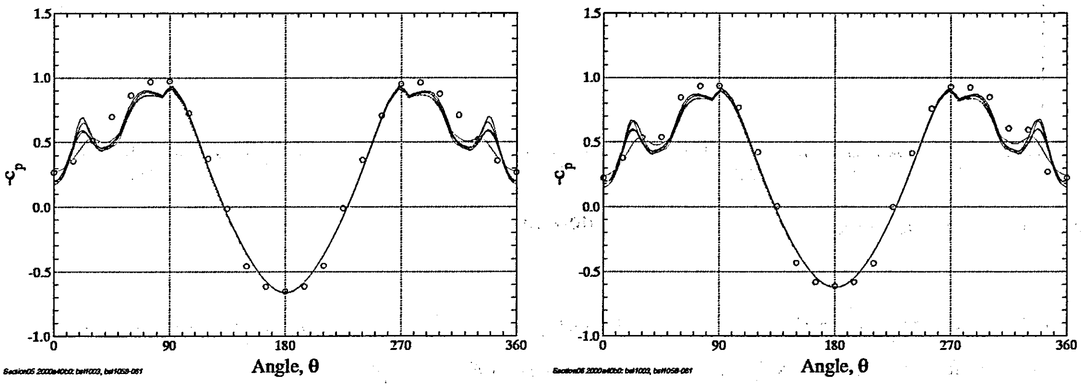

(c) Section 05 (d) Section 06

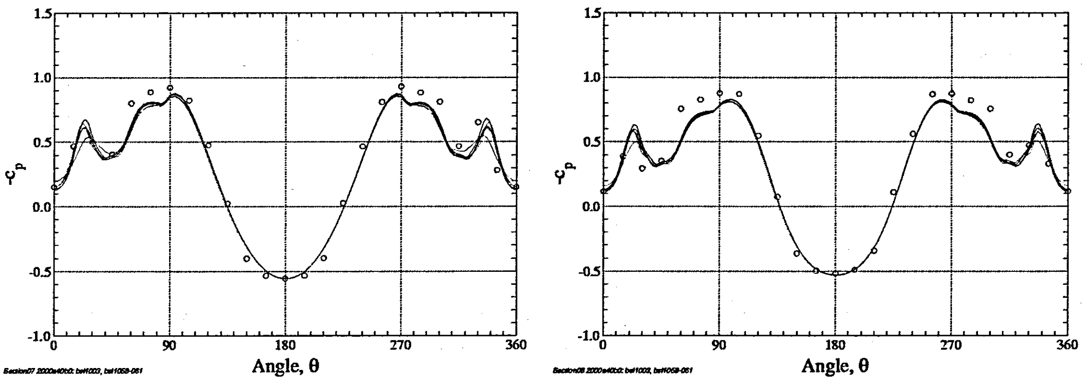

(e) Section 07 (f) Section 08

Figure B.7: *JAS-39 grid bsll, M=0.176, Re=4.06 × 10^6, α=40°. Circumferential c_p distributions, sections 03-08. Comparison of turbulence models.*

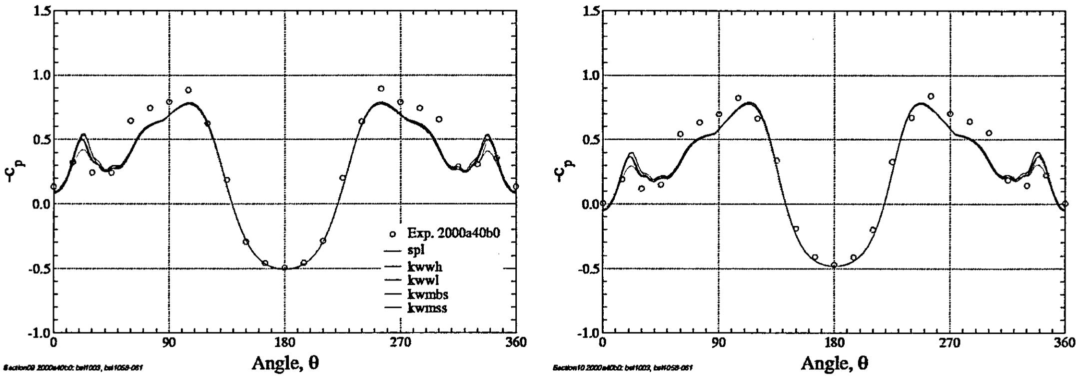

(a) Section 09

(b) Section 10

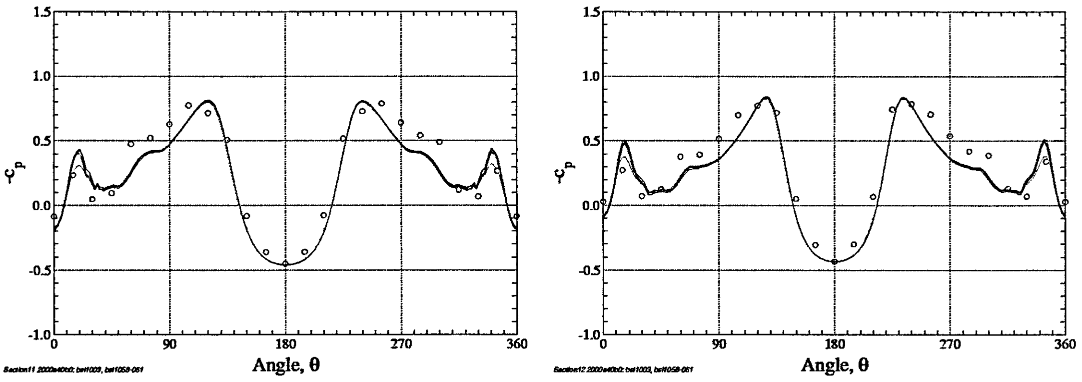

(c) Section 11

(d) Section 12

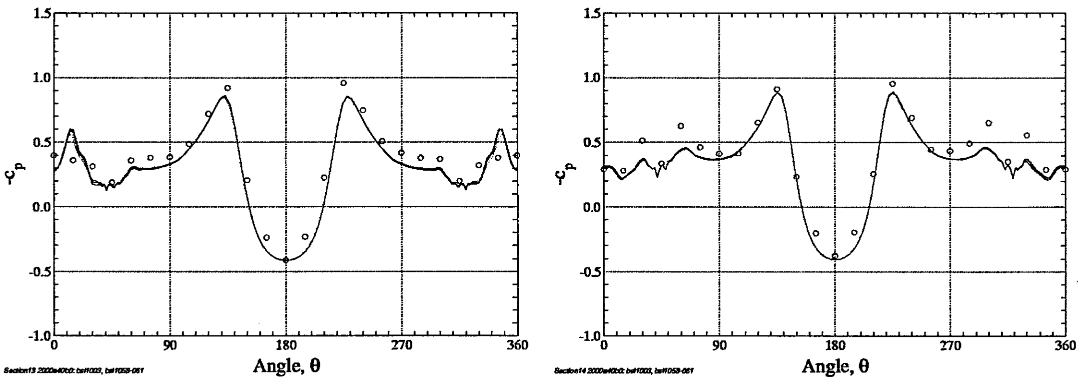

(e) Section 13

(f) Section 14

Figure B.8: *JAS-39 grid bsll, M=0.176, Re=4.06 × 10^6, α=40°. Circumferential c_p distributions, sections 09-14. Comparison of turbulence models.*